ATOMIC STRUCTURE AND NON-ELECTRONIC PROPERTIES OF SEMICONDUCTORS

Influence of native defects on polytypism in SiC

A. A. Lebedev

A. F. Ioffe Physicotechnical Institute, Russian Academy of Sciences, 194021 St. Petersburg, Russia

An analysis of experimental data on the influence of native defects of the crystalline lattice on polytypism in silicon carbide has been performed. A simple analytical expression, which links the degree of hexagonality of the polytype with the concentration of carbon and silicon vacancies, was obtained. The possible dependence of the model parameters on the experimental conditions is investigated. © *1999 American Institute of Physics.*
[S1063-7826(99)00107-6]

INTRODUCTION

It is well known that the term ''silicon carbide'' includes in fact an entire class of semiconductor compounds since SiC is able to crystallize in various modifications known as polytypes. SiC polytypes with the same chemical composition can differ significantly in their electrical properties; for example, their band gaps (E_g) are found within the range from 2.4 eV ($3C$-SiC) to 3.3 eV ($2H$-SiC). All this makes silicon carbide a promising material from the point of view of creating different types of heterostructures.

However, there is now no generally accepted theory of polytypism in SiC, although a large body of experimental data has accumulated on the dependence of various properties of SiC on the structure of the polytype. In our study we have made an effort, on the basis of the available experimental data, to obtain an analytical expression relating the stoichiometry of the polytype with its degree of hexagonality.

ANALYSIS OF THE EXPERIMENTAL DATA

All of the known polytypes of silicon carbide crystallize according to the laws of dense spherical packing and are binary structures composed of identical layers that differ in the order of their arrangement (cubic or hexagonal layer) and in the number of layers per unit cell. Polytypes are usually characterized using the Ramsdell notation,[1] which consists of a natural number equal to the number of layers per period in the direction perpendicular to the base plane, and an alphabetical character which characterizes the symmetry system of the Bravais lattice: C — cubic, H — hexagonal, and R — rhombohedral. Only in two SiC polytypes are the positions of all the atoms equivalent and correspond either to cubic ($3C$-SiC) or hexagonal ($2H$-SiC) sites of the crystalline lattice (see, e.g., Ref. 2). In all the remaining polytypes the atoms can be found at both types of sites and the polytypes differ as to the number of atoms at the hexagonal (N_h) and cubic (N_k) sites of the lattice. Therefore, to characterize the polytypes it is convenient to use the degree of hexagonality[3]

(D), which is defined as the ratio of the number of atoms at hexagonal sites to the total number of atoms per unit cell,

$$D = N_h / (N_h + N_k).$$

A study of SiC growth processes has shown that temperature exerts only a weak effect on the structure of SiC. It turns out that the crystal structure of the growing polytype depends much more strongly on the impurity composition of the growth zone. In Refs. 4–6 it was found that when impurities were added to the growth zone of the SiC layers, it was possible to obtain epitaxial films having a different polytype than that of the substrate. It was also found that varying the Si/C ratio in the growth zone has a substantial effect on heteropolytypic epitaxy. Increasing the Si concentration, for example, leads to an increase in the probability for the formation of $3C$-SiC or other polytypes with a low degree of hexagonality.

Vodakov *et al.*[6] demonstrated a link between the processes of heteropolytypic epitaxy and the stoichiometric composition of the various polytypes of SiC. Earlier it was shown that the Si/C ratio is not constant in all SiC polytypes—it decreases with increasing degree of hexagonality and is equal to 1.046, 1.022, and 1.001 for the polytypes $3C$, $6H$, and $4H$, respectively.[7] Data considered in Ref. 6 on diffusion and solubility of impurities in various SiC polytypes also point to different concentrations of the carbon vacancies V_C.

Vodakov *et al.*[6] explained the observed dependence by suggesting that bonds between the atoms at cubic sites become energetically more favorable as a result of an increase in strains in the lattice due to the growth of the concentration of carbon vacancies. This then leads to a change in the structure of the crystal and a transformation of the polytype. Thus, the influence of doping on heteropolytypic epitaxy can be explained by asserting that by introducing impurities that occupy carbon sites we decrease the concentration of carbon vacancies and stimulate growth of epitaxial films having a greater degree of hexagonality than the substrate. Upon introduction of impurities that occupy silicon sites, we increase

TABLE I. Values of $[V_{Si}]$, $[V_C]$, and D for various polytypes of SiC.

Row No.	Parameter	Polytype						Remarks
		4H	27R	15R	6H	8H	3C	
1	D_{th}	0.5	0.44	0.4	0.33	0.25	0	Refs. 2 and 3
2	$[V_{Si}], 10^{20}$ cm^{-3}	7.3	6	5	4	3	2	Ref. 7, x-ray data
3	$[V_C], 10^{20}$ cm^{-3}	7.3	10	12	14	16.6	23.5	
4	$[V_C]/[V_{C-4H}]$	1	1.37	1.64	1.92	2.27	3.22	
5	$[V_C]/[V_{C-4H}]$	1	1.2	1.8	2	3.2	4.5	Ref. 6, boron diffusion
6	$[V_C]/[V_{C-4H}]$	1	1.2	2.6	3	3.6	6.5	Ref. 6, boron solubility
7	$[V_C]/[V_{C-4H}]$	1		1.8	2	2.9	4.2	Ref. 6, nitrogen solubility
8	$\{[V_C]/[V_{C-4H}]\}_{av}$	1	1.26	2.07	2.23	3.0	4.6	
9	$[V_C^*], 10^{20}$ cm^{-3}	7.3	9.2	15.1	16.3	21.9	33.6	
10	D_{calc}	0.5	0.46	0.36	0.33	0.24	0.06	formula (3)

the concentration of carbon vacancies resulting in growth of films with a lower degree of hexagonality than the substrate. The possibility of heteropolytypic epitaxy of SiC shows also that the composition of the growth zone (i.e., the concentrations of silicon and carbon vacancies V_{Si} and V_C) has a much greater influence on the crystal structure of the growing layer than the polytype of the substrate.

Let us now consider the data in the literature on the stoichiometric composition of various polytypes of SiC. By comparing the density of SiC samples determined by x-ray analysis and in the usual way Sorokin et al.[7] determined the absolute values of the concentrations of the silicon and carbon vacancies V_{Si} and V_C in various polytypes of SiC (see Table I, rows 2 and 3, respectively). Vodakov et al.[6] measured the coefficients of boron diffusion (D_B) and also the solubility of boron and nitrogen (C_B and C_N) in the same polytypes. They concluded that these quantities are proportional to $[V_C]$ and that it is possible to judge the relative change in $[V_C]$ from their relative variation. Therefore, to average all the available data in the literature it is convenient to use the relative concentration of the carbon vacancies $[V_C]/[V_{C-4H}]$, i.e., the ratio of the concentration of the carbon vacancies in the given polytype, $[V_C]$, to the concentration of the carbon vacancies in the 4H polytype. Using the data of Ref. 6, we can write

$$[V_C]/[V_{C-4H}] \approx D_B/D_{B-4H} \approx C_B/C_{B-4H} \approx C_N/C_{N-4H}.$$

The values of $[V_C]/[V_{C-4H}]$ calculated using all the experimental data are listed in rows 4–7 of the table. Taking all the experimental data into account, we found the mean value of the relative concentration of the carbon vacancies using the formula $\{[V_C]/[V_{C-4H}]\}_{av} = (1/i)\Sigma([V_C]/[V_{C-4H}])_i$, where $i = 4$ is the total number of employed experimental dependences. Next we calculated the absolute value, using $[V_{C-4H}]$ from Ref. 7, as $[V_C^*] = [V_{C-4H}]\{[V_C]/[V_{C-4H}]\}_{av}$. The values obtained in this way are given in row 9.

As can be seen from the table, there is good agreement between the values of $[V_C]/[V_{C-4H}]$ obtained in Refs. 6 and 7. Nevertheless, the authors of Ref. 6 noted that the absolute concentration of electrically active vacancies in SiC can be less than that obtained in Ref. 7. According to their assumptions, a large fraction of the vacancies are joined together into electrically inactive clusters.[6,8]

MODEL

We will attempt to formalize the model proposed in Ref. 6. We consider a growing layer of SiC as a set of atoms, which, with some probability (α) can become attached to the cubic sites of the crystalline lattice. We can then write the number of cubic and hexagonal sites in the form

$$N_k = \alpha N, \quad N_h = (1-\alpha)N, \tag{1}$$

where N is the total number of atoms per unit volume.

We also take into account the experimental data presented above which indicate that the concentration of carbon and silicon vacancies has a fundamental influence on the crystal structure of the growing layer. We assume that the appearance of one carbon vacancy leads to the result that β_k neighboring atoms can be found only at cubic lattice sites and, correspondingly, in the case of the appearance of a silicon vacancy that β_h neighboring atoms can be found only at hexagonal lattice sites. For simplicity we assume that $\beta_k = \beta_h = \beta$. We can then write expression (1) in the form

$$N_k = \beta[V_C] + \alpha[N - (\beta+1)([V_C] + [V_{Si}])],$$
$$N_h = \beta[V_{Si}] + (1-\alpha)[N - (\beta+1)([V_C] + [V_{Si}])]. \tag{2}$$

We can thus easily obtain an expression for D:

$$D = \{\beta[V_{Si}] + (1-\alpha)[N - (\beta+1)([V_C] + [V_{Si}])]\}/$$
$$[N - ([V_C] + [V_{Si}])]. \tag{3}$$

Let us now determine the parameters needed for the calculation. From the known value of the density of SiC (3.21 g/cm^3) we obtain $N = 9.6 \times 10^{22}$. To determine α we substitute the values of $[V_C]$, $[V_{Si}]$, and D for 4H-SiC in Eq. (3) and obtain $\alpha = 0.5$. To determine the value of β we use the values of the same parameters for 6H-SiC and obtain $\beta = 25.5$. The values of D calculated using these values of α and β are listed in the table.

DISCUSSION

As can be seen from the table, a fair agreement is observed between the calculated and experimental values. To develop the proposed model further, it is important to ask whether the coefficients α and β are constant under various conditions of the experiment and whether they depend on D.

In our opinion, the parameter α should be affected by thermodynamic factors (pressure, temperature) which govern migration of atoms in the growth zone, and also by the orientation and polytype of the substrate. We may quite logically assume that as D decreases, α will increase. This may have to do with the fact that in polytypes with small D the concentration of carbon vacancies increases, and along with it the number of atoms for which a lattice site has been determined. Thus, a growing number of neighboring atoms will occupy cubic sites, which can lead to a lowering of the probability of incorporation into a hexagonal site of an atom not associated with a carbon vacancy, i.e., an increase in α.

On the other hand, as the concentration of carbon vacancies increases, the influence of individual vacancies will overlap, a coalescence of vacancies into complexes becomes possible, and the effective value of β may decrease. Thus, in the case of our calculation ($\beta = \text{const}$, $\alpha = \text{const}$) actual changes in β and α as $D \to 0$ will cancel out.

Note that the maximum discrepancy between the theoretical values[2,3] of D (D_{th}) and the values calculated according to formula (3) (D_{calc}) was nonetheless obtained for $3C$-SiC. This possibly has to do with the fact that formation of a $3C$ polytype corresponds to a phase transition between the hexagonal and cubic structure of SiC. It is probable that for $D \approx 0$ it is necessary to estimate the nature of the variation of α and β, taking into account results of percolation theory, as was done in order to estimate the parameters of ferromagnets near the phase transition point.[9,10]

It should also be borne in mind that the experimental data presented in Refs. 6 and 7 were obtained mainly on samples of SiC grown by the Lely method at high temperatures ($\sim 2500\,^{\circ}$C). It is well known that SiC samples obtained at lower temperatures ($\sim 2000\,^{\circ}$C, modified Lely method) possess lower structural perfection, having a high density of dislocations and other kinds of inclusions. There-fore, for a more complete description of processes of heteropolytypic transformation of SiC it is necessary to have experimental data on the stoichiometry of samples of the given type.

CONCLUSIONS

The analysis which we conducted here does not give a complete description of the polytypism of SiC, but is instead largely a generalization of the experimental data obtained previously. It does, however, clarify the possible directions of further experimental and theoretical study of this problem in silicon carbide. Since the study of polytypism is also important for some other wide-band semiconductors (GaN, ZnSe, and ZnS), the method outlined by us here can have a wide application upon its development.

[1] L. S. Ramsdell, Am. Mineral. **32**, 64 (1947).

[2] H. K. Henisch and R. Roy, *Silicon Carbide—1968* (Pergamon Press, Oxford, 1968).

[3] H. Jagodzinskii, Acta Crystallogr. **2**, 201 (1949).

[4] Yu. Vakhner and Yu. M. Tairov, Fiz. Tverd. Tela (Leningrad) **12**, 1543 (1970) [Sov. Phys. Solid State **12**, 1213 (1970)].

[5] Yu. A. Vodakov, E. N. Mokhov, A. D. Roenkov, and M. M. Anikin, Pis'ma Zh. Tekh. Fiz. **5**, 367 (1979) [Tech. Phys. Lett. **5**, 147 (1979)].

[6] Yu. A. Vodakov, G. A. Lomakina, and E. N. Mokhov, Fiz. Tverd. Tela (Leningrad) **24**, 1377 (1982) [Sov. Phys. Solid State **24**, 780 (1982)].

[7] N. D. Sorokin, Yu. M. Tairov, V. F. Tsvetkov, and M. A. Chernov, Kristallografiya **28**, 910 (1983) [Sov. Phys. Crystallogr. **28**, 539 (1983)].

[8] Yu. A. Vodakov and E. N. Mokhov, Inst. Phys. Conf. Ser. **137**, 197 (1994).

[9] E. F. Shender, Zh. Éksp. Teor. Fiz. **70**, 2251 (1976) [Sov. Phys. JETP **43**, 1174 (1976)].

[10] B. I. Shklovskiĭ and A. L. Efros, *Electronic Properties of Doped Semiconductors* (Springer-Verlag, New York, 1984).

Antistructural defects in PbTe-type semiconductors

V. F. Masterov, S. I. Bondarevskiĭ, F. S. Nasredinov, N. P. Seregin, and P. P. Seregin

St. Petersburg State Technical University, 195251 St. Petersburg, Russia

Mössbauer emission spectroscopy on the isotope ^{119m}Te(^{119m}Sn) is used to identify tin impurity centers in PbTe and PbS lattices. Using the emission variant of Mössbauer spectroscopy makes it possible to stabilize the tin impurity atoms in the anion sublattice, i.e., to obtain antistructural defects. The charge state of the tin impurity atoms displaced from the anion sublattice is found to depend on the position of the Fermi level. © *1999 American Institute of Physics.* [S1063-7826(99)00207-0]

In this paper we present the results of experimental observation of tin atoms which enter into the makeup of antistructural defects in PbTe-type compounds. For this purpose we used the emission variant of Mössbauer spectroscopy on the isotope ^{119m}Te(^{119m}Sn), which allowed us to stabilize the tin impurity atoms at foreign sites after a chain of radioactive decays of the mother nuclei.[1]

We obtained the isotope ^{119m}Te via the reaction ^{117}Sn($\alpha,2n$)^{119m}Te. To separate the carrier-free ^{119m}Te sample we used the procedure of anion exchange. Mössbauer sources were prepared by alloying samples of PbS or PbTe with the carrier-free ^{119m}Te sample so that the concentration of Sb impurity atoms formed after the decay of ^{119m}Te did not exceed 10^{17} cm^{-3}. The initial samples were *n*-type (with an excess of lead, carrier concentration $n \sim 10^{18}$ cm^{-3}) and *p*-type (with a chalcogen excess, carrier concentration $p \sim 10^{18}$ cm^{-3}).

Mössbauer spectra of ^{119m}Te(^{119m}Sn) were measured on an SM-2201 commercial spectrometer at 80 K with CaSnO$_3$ absorber (tin surface density 5 mg·cm^{-2}). The spectrum with such an absorber and a Ca^{119m}SnO$_3$ source turned out to be a single line with a full width at half-maximum $\Gamma = 0.79 \pm 0.01$ mm/s, which we assumed to be the instrument width of the spectral line. Typical spectra of PbS: ^{119m}Te and Pb^{119m}Te samples are shown in Figs. 1 and 2, and results of data reduction of the spectra are listed in Table I.

It can be seen that the experimental spectra of the *n*-type samples consist of a superposition of two lines: an intense line (spectrum I, the isomeric shift is due to ^{119m}Sn^0) and a less intense line (spectrum II, the isomeric shift is due to ^{119m}Sn^{2+}). The emission spectra of the *p*-type samples also consist of a superposition of two lines. For *p*-type PbTe the experimental spectrum is analogous to the spectrum for *n*-type PbTe whereas the spectrum for *p*-type PbS, in addition to the intense line I, also contains a less intense line III (the isomeric shift is due to ^{119m}Sn^{4+}).

The source of the Mössbauer γ rays for measuring these spectra was the ^{119m}Sn nucleus formed after electron capture (EC) at the outset in the ^{119m}Te nucleus, and then in the ^{119}Sb nucleus (see the inset in Fig. 1). An excited daughter atom is formed as a result of electron capture from the inner shell of the mother atom. Its excitation is removed either by radiative

transitions or by emission of Auger electrons, which gives rise to a spectrum of charges of the tin daughter ions. The ionized atom can be displaced from its normal lattice site, and the emission of an antineutrino as a result of electron capture transfers a recoil energy to the atom, which is also conducive for the appearance of displaced tin atoms.

An analysis of numerous Mössbauer studies of aftereffects of nuclear conversions shows that the daughter atom undergoes a transition to a stable charge state in a time less than several picoseconds. In other words, only the final shapes of stabilization of the daughter atoms appear in the Mössbauer emission spectra. The probability for the appearance of displaced atoms depends on the ratio of the recoil energy of the daughter nucleus E_R to the threshold energy of
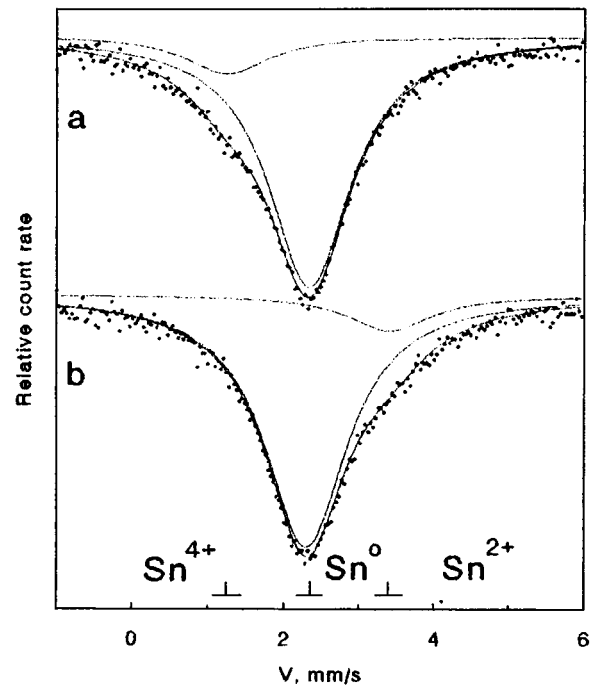

FIG. 1. Mössbauer emission spectra of ^{119m}Te(^{119m}Sn) at 80 K of *n*-PbS (a) and *n*-PbTe (b). The experimental spectra are broken down into components corresponding to ^{119m}Sn^0 and ^{119m}Sn^{2+}. The inset shows a decay diagram of ^{119m}Te and ^{119}Sb.

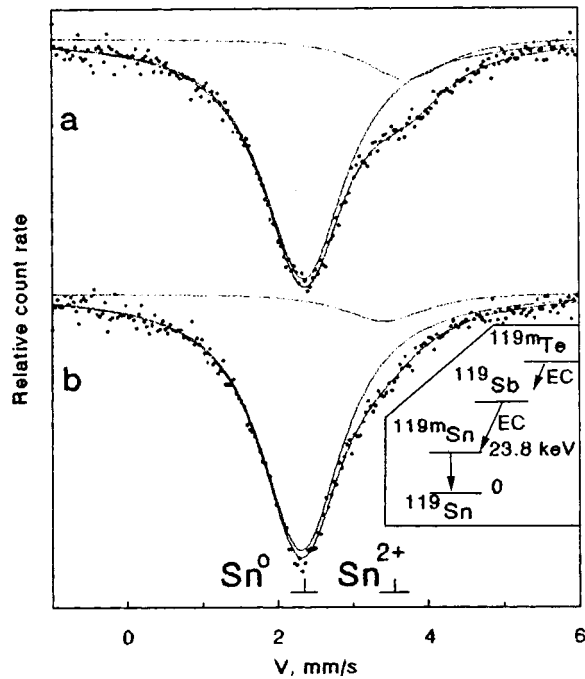FIG. 2. Mössbauer emission spectra of ^{119m}Te(^{119m}Sn) at 80 K of *p*-PbS (a) and *p*-PbTe (b). The experimental spectra are broken down into components corresponding to ^{119m}Sn^0, ^{119m}Sn^{2+}, and ^{119m}Sn^{4+}.

TABLE I. Parameters of Mössbauer emission spectra of ^{119m}Te(^{119m}Sn) in PbS and PbTe at 80 K.

Compound, conductivity type	Type of spectrum	Center	IS, mm/s	Γ, mm/s	S, %
n-PbS	I	^{119m}Sn^0	2.35	1.34	85
	II	^{119m}Sn^{2+}	3.72	1.45	15
n-PbTe	I	^{119m}Sn^0	2.31	1.32	90
	II	^{119m}Sn^{2+}	3.42	1.41	10
p-PbS	I	^{119m}Sn^0	2.34	1.36	87
	III	^{119m}Sn^{4+}	1.25	1.46	13
p-PbTe	I	^{119m}Sn^0	2.30	1.33	88
	II	^{119m}Sn^{2+}	3.41	1.40	12
Error			± 0.01	± 0.02	± 2

Note: IS — isomeric shift relative to CaSnO$_3$, Γ — full width of the spectrum at half-maximum, S — area under spectrum.

tellurium sites. The isomeric shifts of spectra II and III are typical for chalcogenides of bivalent and tetravalent tin, in which only chalcogenide atoms are found in the immediate vicinity of the tin atoms, and consequently these spectra correspond to tin daughter atoms—^{119m}Sn^{2+} (spectrum II) and ^{119m}Sn^{4+} (spectrum III), which arise after the decay of the ^{119m}Te^{2-} mother atoms and which are displaced due to the recoil energy from the anion and cation lattice sites, thereby forming isoelectronic substitution impurities.

According to Ref. 2, an isoelectronic tin impurity in PbS is electrically active and plays the role of a two-electron donor. This explains the dependence of the isomeric shift of the spectrum we observed for such centers on the conductivity type of the material: in *n*-type samples spectrum II is due to a neutral state of the donor center (^{119m}Sn^{2+}), and in *p*-type samples spectrum III is due to the doubly ionized state (^{119m}Sn^{4+}). In a PbTe lattice, an isoelectronic tin impurity is electrically inactive,[2] and this is confirmed by the absence, according to our observations, of a dependence of the isomeric shift due to these centers on the position of the Fermi level.

displacement of the atoms $E_d \simeq 25$ eV. To estimate the possibility of displacement of daughter atoms from their normal lattice sites due to the recoil energy, we calculated the maximum recoil energy for the probe nucleus ^{119m}Sn: the decay ^{119m}Te→^{119}Sb is accompanied by the recoil energy $E_R \simeq 1.4$ eV, and the decay ^{119}Sb→^{119m}Sn is accompanied by the recoil energy $E_R \simeq 24$ eV. The significant value of the second recoil energy gives reason to expect in the Mössbauer emission spectra on ^{119m}Te(^{119m}Sn) in PbS and PbTe samples the appearance of lines due to ^{119m}Sn atoms at the anion sites, and lines due to ^{119m}Sn atoms displaced from these sites.

On the basis of the isomeric shifts, spectrum I corresponds to tin daughter atoms having only metal (lead) atoms in their immediate environment. This means that it can be attributed to ^{119m}Sn^0 centers which are formed after the decay of the ^{119m}Te^{2-} mother atoms and which remain at the

[1] P. P. Seregin and P. V. Nistiryuk, *Application of the Mössbauer Effect and Photoelectron Spectroscopy in the Physics of Amorphous Semiconductors* [in Russian], Kishinev, Ştiinţa, 1991.
[2] V. F. Masterov, F. S. Nasredinov, S. A. Nemov, and P. P. Seregin, Fiz. Tekh. Poluprovodn. **31**, 291 (1997) [Semiconductors **31**, 302 (1997)].

Translated by Paul F. Schippnick

ELECTRONIC AND OPTICAL PROPERTIES OF SEMICONDUCTORS

Electrical properties of nuclear-doped indium antimonide

N. G. Kolin and D. I. Merkurisov

Branch of the State Scientific Center L. Ya. Karpov Physicochemical Scientific-Research Institute, 249020 Obninsk, Russia

S. P. Solov'ev

Atomic Energy Institute, 249020 Obninsk, Russia

The possibility of nuclear doping of indium antimonide over a wide range of concentrations ($5 \times 10^{14} - 10^{18}$ cm^{-3}) by irradiation with reactor neutrons is investigated; the effect of irradiation and subsequent heat treatments on the electrical parameters of the material is investigated. A comparative analysis of the quality of nuclear-doped and conventional InSb is used to demonstrate the possibility of the practical use of this nuclear-doped material. © *1999 American Institute of Physics.* [S1063-7826(99)00307-5]

The nuclear doping method applied to semiconductor materials has found wide application worldwide for silicon and to a lesser degree for germanium and some III–V compounds.[1] The possibilities of nuclear doping of indium antimonide were demonstrated in the 1960s.[2,3] A comparative study of the electrical properties of InSb irradiated by electrons, H$^+$ ions, and reactor neutrons during nuclear doping was reported in Ref. 4. However, there are no data in the literature on nuclear doping of indium antimonide as a practically realizable method.

In this paper we report the results of an experimental study of the possibility of nuclear doping of indium antimonide over a wide range of concentrations from $n \approx 5 \times 10^{14}$ to $n \approx 10^{18}$ cm^{-3} by irradiation with thermal (slow) reactor neutrons, investigate the effect of irradiation and subsequent heat treatments on the electrical characteristics of the material, and present a comparative analysis of the quality of nuclear-doped indium antimonide (NDIA) and indium antimonide doped metallurgically during growth.

As the starting material we used undoped InSb wafers and wafers doped with tellurium to a concentration $n \approx 1.6 \times 10^{15}$ cm^{-3} having a diameter of 30 to 50μm and thickness

1.5$-$2 mm, grown by the Czochralski method.

Irradiation was performed in vertical chambers of a VVR reactor at a temperature $T \leqslant 70\,°$C. We used two types of channels: channels in the reactor core with a slow-neutron flux density $\varphi_s \approx 5 \times 10^{13}$ cm$^{-2} \cdot$ s^{-1} and ratio of slow to fast ($E > 0.1$ MeV) neutron flux densities $\varphi_s / \varphi_f \approx 1$, and channels at the core periphery, where $\varphi_s \approx 1.3 \times 10^{12}$ cm$^{-2} \cdot$ s^{-1}, $\varphi_s / \varphi_f \approx 2$.

As is well known, when slow neutrons interact with atoms of matter, nuclear reactions take place with the formation of unstable isotopes which with time undergo β decay. As a result, atoms having atomic number one greater than the atoms of the irradiated material are formed. These atoms are the dopant impurities for the parent material.[1] Table I lists the main products of (n, γ) nuclear reactions initiated by slow neutrons in indium antimonide. Since the absorption cross section of the slow neutrons for the main isotope of indium In^{115} (≈ 200 barns) is much greater than for antimony, the final product of nuclear doping in indium antimonide, as in InAs and InP, is primarily tin atoms.

The large absorption cross section of In^{115} gives rise to a strong self-screening of InSb samples during irradiation. The

TABLE I. Products of n, γ nuclear reactions in InSb.

Element	Isotope	Isotope content, %	Slow neutron absorption cross section, barns	Half-life	Efficiency of nuclear doping n_{tr}/F_s	Reaction products (fractional amount)	Total reaction product
In	Natural		190 ± 10				
	In^{113}	4.23	58 ± 12	50.1 da	3.6×10^{-2}	Sn^{114} (0.980) Cd^{114} (0.010)	Tin (97.50%), tellurium (1.62%),
	In^{115}	95.77	200 ± 20	54 min	2.8	Sn^{116} (1.000)	cadmium (0.01%),
Sb	Natural		5.5 ± 1.0				other elements
	Sb^{121}	57.25	5.7 ± 0.5	2.8 da	4.8×10^{-2}	Te^{122}(0.969)	(0.87%)
	Sb^{123}	42.75	3.9 ± 0.3	21 min	2.5×10^{-2}	Te^{124}(0.031)	

slow-neutron flux density falls by a factor of $1/e$ at a distance of 1.4 mm, and indium is characterized by resonance absorption of neutrons with energy 1.46 eV with an absorption cross section equal to 2.2×10^4 barns. Resonance neutrons are strongly absorbed by the InSb surface and their density falls by a factor of $1/e$ at a depth on the order of several microns; therefore, in order to eliminate the influence of resonance neutrons, either the InSb samples were wrapped in indium foil or they were shaved on both sides to a depth of about 30μm after irradiation. Another peculiarity of indium-containing compounds is strong absorption of epithermal neutrons by indium atoms, leading to additional doping of the material.[4]

To calculate the tin concentration due to nuclear reactions initiated by slow neutrons, we used the formula

$$N_{Sn} = N_0 K \sigma F_s, \qquad (1)$$

where N_0 is the number of atoms of the material per unit volume, K is the percent content of the isotope, σ is the absorption cross section of the slow neutrons, F_s is the slow-neutron flux. A theoretical calculation using formula (1) and the data of Table I gives a value of the efficiency of nuclear doping (N_{Sn}/F_s) in indium antimonide equal to about 2.8. Our experimental results indicate that the irradiated samples of InSb should be stored for a time varying from 4–6 to 12–24 months, depending on the neutron flux, for the induced radioactivity to fall to an acceptable level.

The electrical properties of irradiated InSb are determined chiefly by three parameters:

– the initial concentration of impurities and growth defects;

– the concentration of impurities introduced into InSb as a result of nuclear reactions initiated by slow neutrons;

– radiation defects formed in InSb during irradiation.

The slow-neutron fluxes were chosen in such a way that the concentration of the impurities introduced as a result of nuclear transmutations would be not less than 3–5 times
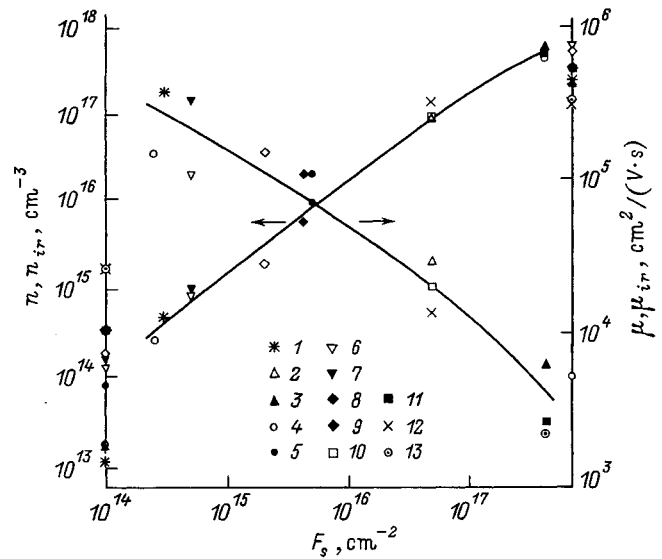

FIG. 1. Dependence of the concentration n_{ir} and mobility μ_{ir} of the majority charge carriers on the slow neutron fluxes F_s for InSb samples (the initial values of n and μ are indicated on the two vertical axes). The numbers assigned to the symbols in the figures correspond to the numbers of the samples in Table II.

higher than the concentration of the initial impurities with the aim of reducing the influence of the latter on the properties of the nuclear-doped material.

Figure 1 plots the dependence of the concentration and mobility of the charge carriers in the InSb samples listed in Table II on the slow-neutron flux. As can be seen, the charge-carrier concentration increases monotonically with increasing neutron flux and, in contrast to other semiconductors (GaAs, InP; Refs. 5 and 6), no decrease in the charge-carrier concentration is observed, nor any conversion of the conductivity type $n \rightarrow p$. This indicates that irradiation by reactor neutrons introduces primarily n-type impurity levels into the InSb samples, in good agreement with calculations of the limiting position of the Fermi level in strongly irradi-

TABLE II. Properties of initial and nuclear-doped samples of indium antimonide.

Sample number	n, 10^{14} cm^{-3}	μ, 10^5 cm^2/(V·s)	F_s, 10^{16} cm^{-2}	N^{th}, 10^{16} cm^{-3}	N^{csa}, 10^{16} cm^{-3}	N_{ir}, 10^{16} cm^{-3}	n_{ia}, 10^{16} cm^{-3}	μ_{ia}, 10^4 cm^2/(V·s)
1	0.10	4.00	0.03	0.09		0.05	0.05	39.0
2	0.15	3.76	4.80	13.6		8.60	10	5.00
3	0.15	3.76	43.20	122.7	113.6	54.0	100	1.70
4	0.16	0.05	0.03	0.07		0.02	0.05	17.0
5	0.75	6.50	0.50	1.42		0.90	0.81	13.5
6	1.20	6.50	0.05	0.14		0.08	0.12	26.5
7	1.50	6.00	0.05	0.14		0.10	0.11	28.0
8	1.70	6.14	0.20	0.57		0.18	0.52	17.2
9	3.10	4.70	0.42	1.20	2.10	0.54	0.90	12.0
10	3.10	4.70	4.80	13.6		9.10	10	5.00
11	3.10	4.70	43.2	122.7		45.0	90	2.00
12	16.0	2.80	4.80	13.6		13.0	17	4.00
13	16.0	2.90	43.2	122.7		43.0	100	1.50

Note: n, μ — initial values of the electron concentration and mobility; n_{ir} — electron concentration after irradiation; n_{ia} and μ_{ia} — concentration and mobility after irradiation and annealing at $T = 450°$ for 20 min; F_s — unperturbed flux of slow neutrons; N^{th} — calculated concentration of introduced impurity (for unperturbed F_s); N^{csa} — concentration of introduced impurity (Sn) from the chemical-spectral analysis data.
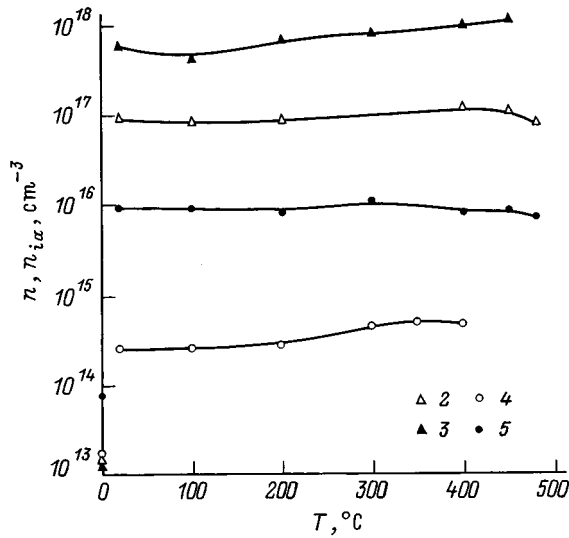
FIG. 2. Dependence of the concentration of the majority charge carriers on the temperature of isochronous anneal for InSb samples irradiated by different fluxes of the total spectrum of reactor neutrons (the initial concentrations are indicated on the vertical axis). The numbers assigned to the symbols correspond to the numbers of the symbols in Table II.
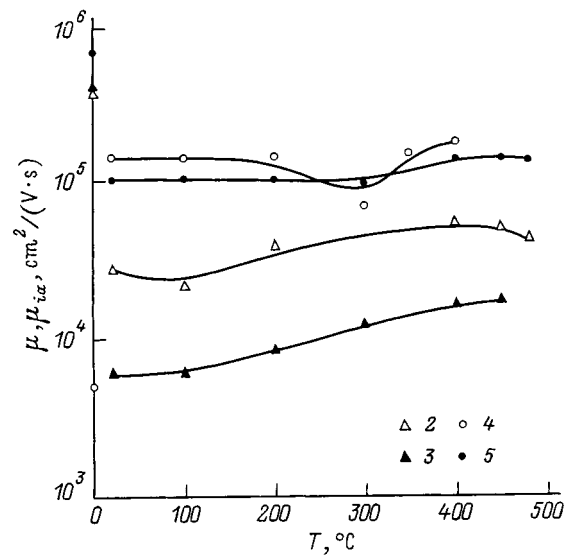

FIG. 3. Dependence of the concentration of the majority charge carriers on the temperature of isochronous anneal for InSb samples irradiated by different fluxes of the total spectrum of reactor neutrons (the initial concentrations are indicated on the vertical axis). The numbers assigned to the symbols correspond to the numbers of the symbols in Table II.

ated semiconductors.[7] The mobility of the charge carriers decreases as the neutron flux is increased, due to an increase in the concentration of the impurity and the number of radiation defects.

With the aim of revealing the mechanisms for the formation and annealing of radiation defects, we performed an isochronous anneal of the irradiated samples for 20 min in the temperature interval from 100 to 480 °C. An analysis of the results makes it possible to distinguish the influence of the impurities formed as a result of the nuclear transmutations from the influence of the introduced radiation defects on the electrical properties of InSb.

Figures 2 and 3 plot the dependence of the concentration and mobility of the charge carriers on the temperature of isochronous anneal for InSb samples with different initial charge-carrier concentrations. As can be seen, isochronous annealing does not lead to significant changes in the electrical parameters of irradiated InSb. The charge-carrier concentration after irradiation and the corresponding heat treatments remains essentially the same; i.e., almost all the impurity introduced by nuclear doping is found in the material in the electrically active state, which can be explained by the narrow band gap of indium antimonide (0.18 eV).

Small changes in the concentration and mobility of the charge carriers during heat treatment are observed at low and high doping levels. This is apparently due to the predominant influence of radiation defects in comparison with the influence of the introduced impurity at the given doping levels. At annealing temperatures greater than 450 °C the charge-carrier concentration and mobility are decreased, indicating a degradation of the quality of the material at temperatures near the melting point of InSb (525 °C).

Figure 4 plots the dependence of the mobility of the majority charge carriers on their concentration for InSb samples doped in different ways. It can be plainly seen that

at higher neutron fluxes and consequently higher charge-carrier concentrations, radiation defects, which are removed by heat treatment (consider the difference between curves *1* and *2*), make a progressively larger contribution to the variation of the mobility. A comparison of the theoretical and experimental dependences testifies to the high quality of nuclear-doped InSb, in particular, at high doping levels, which are difficult to attain metallurgically. The data on the
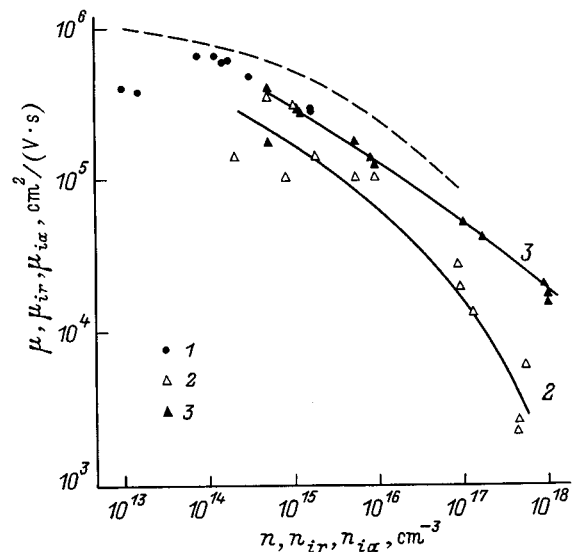

FIG. 4. Dependence of the mobility of the majority charge carriers on their concentration for InSb samples prepared by different means. The numbers assigned to the symbols and curves correspond to data for: *1* — the initial, unirradiated samples (μ), *2* — samples after irradiation by different fluxes of the total spectrum of reactor neutrons (μ_{ir}), *3* — samples after irradiation and annealing at 450 °C (μ_{ia}). The dashed curve corresponds to the theoretical dependence.

properties of nuclear-doped samples of InSb are summarized in Table II.

Experimental data, taken after irradiation and annealing of samples at 450 °C, allow us to derive an empirical formula for the dependence of the concentration of the majority charge carriers in nuclear-doped indium antimonide on the slow-electron flux

$$n_{tr} = 2.1 F_s. \tag{2}$$

The results obtained by us are a direct proof of the possibility of nuclear doping of InSb with tin over a wide range of concentrations. Nuclear-doped indium antimonide possesses good electrical properties, equal to or better than indium antimonide metallurgically doped during growth. At the same time, the extended storage time required to allow the induced radioactivity to fall to acceptable levels hinders the wide application of the method for industrial production of the material. The nuclear doping method can be applied to indium antimonide to dope concealed thin layers in multilayer semiconductor structures and at different stages of production in the fabrication of devices.

[1] L. S. Smirnov, S. P. Solov'ev, V. F. Stas', and V. A. Kharchenko, *Doping of Semiconductors by the Nuclear Reactions Method* [in Russian], Nauka, Moscow, 1981.

[2] Sh. M. Mirianashvili, D. I. Nanobashvili, and Z. G. Razmadze, Fiz. Tverd. Tela (Leningrad) **7**, 3566 (1965) [Sov. Phys. Solid State **7**, 2877 (1966)].

[3] L. K. Vodop'yanov and N. I. Kurdiani, Fiz. Tverd. Tela (Leningrad) **8**, 72 (1966) [Sov. Phys. Solid State **8**, 55 (1966)].

[4] V. N. Brudnyĭ, N. V. Kamenskaya, and N. G. Kolin, in *Electrical Properties of Strongly Irradiated InSb* [in Russian] (Publishing House of the Academy of Sciences of the USSR, Pavlodar, 1989), Pt. 2, p. 140.

[5] N. G. Kolin, L. V. Kulikova, V. B. Osvenskiĭ, S. P. Solov'ev, and V. A. Kharchenko, Fiz. Tekh. Poluprovodn. **18**, 2187 (1984) [Sov. Phys. Semicond. **18**, 1364 (1984)].

[6] V. N. Brudnyi, N. G. Kolin, and V. A. Novikov, Phys. Status Solidi A **132**, 35 (1992).

[7] V. N. Brudnyĭ and S. N. Grinyaev, Fiz. Tekh. Poluprovodn. **32**, 315 (1998) [Semiconductors **32**, 284 (1998)].

Translated by Paul F. Schippnick

Study of the polarization photoluminescence of thick epitaxial GaN layers

Yu. V. Zhilyaev, V. V. Krivolapchuk, and I. N. Safronov

A. F. Ioffe Physicotechnical Institute, Russian Academy of Sciences, 194021 St. Petersburg, Russia

Polarization photoluminescence spectra of gallium nitride were obtained. It follows from an analysis of the spectra that inhomogeneous broadening of the emission line having a half-width greater than 20 meV can be determined from the dispersion of the angles θ_c of the symmetry axes of the crystallites forming the epitaxial GaN layer, relative to the surface of the layer. Varying the angle of incidence, the focusing of the exciting laser beam, and the photoluminescence recording angle makes it possible to use polarization photoluminescence measurements for precision diagnostics of the quality of GaN layers. © *1999 American Institute of Physics.*
[S1063-7826(99)00407-X]

INTRODUCTION

At present, GaN is one of the most promising wideband materials because it can be used to create blue and ultraviolet lasers and high-temperature semiconductor devices.[1,2] To create device structures based on GaN it is very useful to have a GaN substrate. Accordingly, we used gas-phase epitaxy in a chloride system to grow thick (with thickness $d > 300\ \mu$m) layers of GaN (with würzite crystal structure— *wz*) on a sapphire substrate. After separating the GaN from the sapphire, we used these thick (essentially bulk) layers as substrates to fabricate the device structures. Photoluminescence in the ultraviolet is observed on thick GaN layers obtained in this way.

Since GaN has hexagonal structure, it may be expected that the spectral characteristics of the photoluminescence will depend on the mutual orientation of the symmetry axis ($\mathbf{C}_6$), the wave vector ($\mathbf{k}$), and the electric field vector ($\mathbf{E}$) of the light.[3] The aim of the present work is to investigate the spectral properties of the polarization photoluminescence of thick epitaxial GaN layers with würzite structure.

SAMPLES AND EXPERIMENT

The samples were epitaxial layers of GaN with *n*-type conductivity, growing on sapphire substrate with (0001) orientation. X-ray diffraction data show that in this case the $\mathbf{C}_6$ axis is oriented in the growth direction (perpendicular to the epitaxial layer). The thickness of the layers varied in the interval $200-400\ \mu$m. A diagram of the experiment is shown in Fig. 1. Excitation was produced using radiation from a pulsed nitrogen laser with wavelength $\lambda_{\mathrm{ex}} = 337$ nm (pulse repetition rate 100 Hz) with electric field vector in all cases perpendicular to the $\mathbf{C}_6$ axis ($\mathbf{E} \perp \mathbf{C}_6$). The angle between the excited laser beam and the normal to the sample plane was fixed at 42°. The laser beam was focused on a spot with diameter $L_{\mathrm{ex}} \approx 400\ \mu$m. Luminescence spectra were recorded at temperatures $T = 77$ and 300 K. The photoluminescence (PL) spectra were recorded in *s* and *p* polarizations with the help of an SDL-2 spectrometer in the photon-counting regime. This spectrometer introduces a polarization not ex-

ceeding 4% (in the spectral interval of interest), and therefore the measurements were performed without a depolarization wedge.

Photoluminescence spectra of GaN were recorded on a series of samples with the $\mathbf{C}_6$ axis perpendicular to the sample plane. For all samples at $T = 77$ and 300 K we recorded a series of spectra: the spatial orientation of the sample was fixed and the spectrum was recorded both in unpolarized light (with no polaroid in front of the spectrometer gap) and in linearly *s*- and *p*-polarized light (with a polaroid in front of the spectrometer gap). The sample was then rotated by 90° about the optical axis ($c - d$) (Fig. 1) and the procedure was repeated. Thus, for each sample we recorded a series of six spectra.

RESULTS AND DISCUSSION

In all cases there is one I_2 line in the photoluminescence spectra of the investigated samples, whose emission maximum at $T = 77$ K is located (depending on the specific sample) in the energy interval $3.461-3.479$ eV, and the full width of the line at half-maximum (FWHM) is found to lie within the limits $21-50$ meV. This emission line is attributed to annihilation of an exciton bound to a neutral donor.[4,5] At $T = 300$ K the energy of the emission maximum and the FWHM are equal to 3.407 eV and 98 meV, respectively. The typical form of the emission spectra at $T = 77$ and 300 K is shown in Figs. 2a and 2b. While examining the photoluminescence spectra we discovered that the emission on the observed line is polarized. The degree of polarization at the line maximum was found from the formula $P = (I_p - I_s)/(I_p + I_s)$ (I_p and I_s are the intensities of the radiation with *p* and *s* polarization) and for some samples reached 47%. We also observed a significant narrowing of the I_2 luminescence line in both the *s* and *p* components of the polarization (Fig. 2).

Since GaN has hexagonal structure, we can expect, as was shown in Ref. 6, an anisotropy in the orientation of the emitting dipoles and, consequently, a dependence of the spectral characteristics of the emission on the mutual orientation of the $\mathbf{C}_6$ symmetry axis, the wave vector $\mathbf{k}$, and the
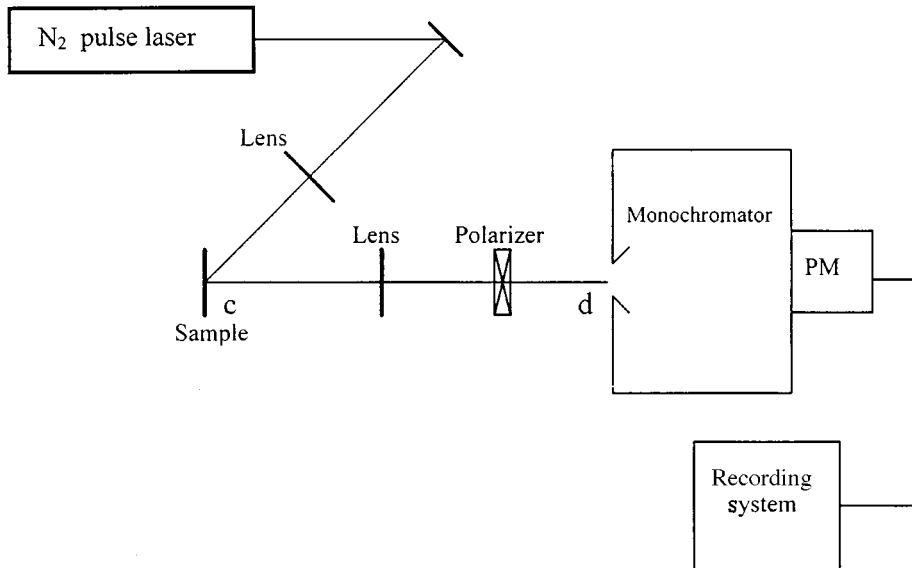
FIG. 1. Diagram of the experimental setup. PM — photomultiplier.
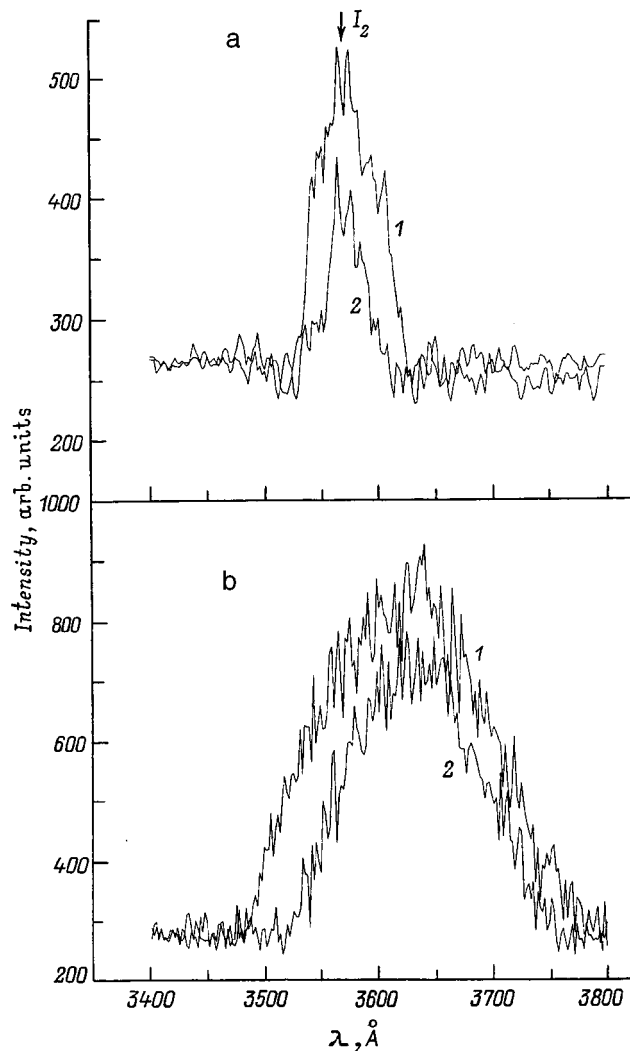

FIG. 2. Photoluminescence spectra of epitaxial GaN layers at $T=77$ (a) and 300 K (b). *1* — unpolarized, and *2* — polarized (s, p) luminescence.

electric field vector **E**. This means that the emission spectrum for $(\mathbf{k}, \mathbf{E}) \perp \mathbf{C}$ differs from the spectrum for $(\mathbf{k}, \mathbf{E}) \| \mathbf{C}$; i.e., the spectra are different depending on the chosen orientation of the linear polarization. To prove this assertion we examined the polarization emission spectra in a sample in which the $\mathbf{C}_6$ axis lay in the layer plane (anisotropic geometry of the experiment). In this case we observed a substantial difference in the intensities of the I_2 line of the s and p components of the polarization and marked narrowing of the photoluminescence line. Moreover, it became clear that the degree of polarization tracks the rotation of the sample by 90° about the $c-d$ axis perpendicular to the plane of epitaxial growth. This kind of photoluminescence anisotropy was investigated in Ref. 7. The authors of Ref. 7 showed that photoluminescence of GaN (wz) depends on the angle between the polarization vector and the direction of the $\mathbf{C}_6$ axis (φ_c). In this case we observed some change in the half-width of the photoluminescence line. It is natural to expect that in samples with the $\mathbf{C}_6$ axis perpendicular to the sample plane (isotropic geometry of the experiment), the polarization dependence of the photoluminescence intensity on the orientation of the linear polarization vector should be weak. However, in a number of the investigated samples we observed a significant (twofold) narrowing of the I_2 line when recording the photoluminescence in linearly polarized light. A comparison of series of spectra of different samples showed that the indicated narrowing of the I_2 line increases with increasing initial half-width of the line which was recorded without a polarizer.

Key to an understanding of such behavior of the photoluminescence line in isotropic geometry are the following circumstances: *1* — the polarization dependence of the line width on φ_c, observed in the case of anisotropic geometry of the experiment; *2* — the mosaic structure of the GaN epitaxial layers, made up of individual crystallites with characteristic dimensions $l \approx 1-10\,\mu$m. From the fact that the width of the emitting region ($L_{\text{ex}} \geqslant 400\,\mu$m) substantially exceeds the characteristic dimension of one crystallite it follows that

the observed photoluminescence line consists of the combined emission of a large number of crystallites (inhomogeneous line width). In this case the C_6 axes of the individual crystallites can form a ''fan'' (cone) of directions. It is clear that polarization behavior of the half-width of the line can be observed in the absence of averaging over the directions of the C_6 axes in this fan. Hence it follows that the fan is asymmetrical; i.e., the C_6 axes of the individual crystallites form a bundle diverted as a whole by an angle θ_c from the normal. The angle φ_c is formed in this case by the linear polarization vector and the direction of the projection of the resulting beam axis on the sample plane. In this case, the inhomogeneous line broadening is determined by the dispersion of the angle θ_c of the bundle of C_6 axes of the individual crystallites that contribute to the I_2 emission line. This allows us to conclude that the behavior of the half-width of the line (FWHM) in the case of isotropic geometry is analogous to the case of anisotropic geometry of the experiment considered above and described in Refs. 7 and 8. In the framework of this model a different value of the narrowing (in the *s* and *p* polarizations) of the I_2 line in different samples is explained by the initially different magnitude of the dispersion of the θ_c angles in these samples.

In summary, our study of the I_2 line allows us to conclude that the inhomogeneous broadening of this emission line having FWHM greater than $20\,\mathrm{meV}$ can be determined (provided $l < L_{\mathrm{ex}}$) from the dispersion of the angles θ_c of the symmetry axes of the crystallites that form the epitaxial GaN layer relative to the normal. The appearance of dispersion of the angles θ_c is probably due to the influence of deforma-tions present in the epitaxial GaN layers. Specific mechanisms of this influence require further detailed study. A methodological aspect of this problem is that in the analysis of the GaN photoluminescence spectra it is necessary to take their polarization characteristics into account. In addition, it follows from the results presented here that varying the angle of incidence, the focusing of the exciting laser beam, and the recording angle in the photoluminescence measurements makes it possible to use polarization measurements of the photoluminescence for precision diagnostics of the quality of GaN layers.

[1] H. Morkoc, S. Strite, G. B. Gao, M. E. Lin, B. Sverdlov, and M. Burns, J. Appl. Phys. **76**, 1363 (1994).
[2] M. Asif Khan, M. S. Shur, J. N. Kuznia, Q. Chen, J. Burm, and W. Shaff, Appl. Phys. Lett. **66**, 1083 (1995).
[3] Bao Oinncheng, Zhang Fungleng, Shi Ke, Dai Rensong, and Xu Xurong, Solid State Commun. **59**, 599 (1986).
[4] R. Dingle, D. D. Shell, S. E. Stokowski, and M. Ilegems, Phys. Rev. B **4**, 1211 (1971).
[5] W. Shan, T. J. Schmidt, X. H. Yang, S. J. Hwang, J. J. Song, and B. Goldenberg, Appl. Phys. Lett. **66**, 985 (1995).
[6] D. G. Thomas and J. J. Hopfield, Phys. Rev. **128**, 2135 (1962).
[7] K. Domen, K. Horino, A. Kuramata, and T. Tanahashi, Appl. Phys. Lett. **71**, 1996 (1997).
[8] I. Nikitina and V. Dmitriev, Inst. Phys. Conf. Ser. **147**, 431 (San Diego, 1997).

Translated by Paul F. Schippnick

Electrical properties of epitaxial indium arsenide and narrow band solid solutions based on it

T. I. Voronina, T. S. Lagunova, K. D. Moiseev, A. E. Rozov, M. A. Sipovskaya, M. V. Stepanov, V. V. Sherstnev, and Yu. P. Yakovlev

A. F. Ioffe Physicotechnical Institute, Russian Academy of Sciences, 194021 St. Petersburg, Russia
(Submitted December 3, 1998; accepted for publication December 8, 1998)
Fiz. Tekh. Poluprovodn. **33**, 781–788 (July 1999)

The electrical properties of epitaxial InAs and solid solutions based on it (InGaAsSb, InAsSbP, InAsGa, InAsP) have been investigated. It is shown that intentionally undoped crystals have n-type conductivity, which is determined by shallow donor impurities ($E_1 = 0.002 - 0.003$ eV) and structural defects ($E_2 = 0.02 - 0.03$ eV and $E_3 = 0.09 - 0.10$ eV). It is shown that growth of epitaxial InAs using the neutral solvent Pb and also rare-earth elements makes it possible to reduce the electron density by almost an order of magnitude (to levels as low as 3×10^{15} cm^{-3}) due to due to a decrease in the density of structural defects. © *1999 American Institute of Physics.* [S1063-7826(99)00507-4]

The interest that has been shown in epitaxial indium arsenide and narrow-band solid solutions similar to it in composition is based on the wide applications of these materials in optoelectronic technology. Devices based on it cover the spectral range from 2.7 to 6 μm. The electrical and photoelectric properties of epitaxial indium arsenide differ in many ways from those of Czochralski-grown InAs and have been widely studied, including by us.[1,2] We determined its energy spectrum, identified its natural structural defects, and proposed and realized methods for enhancing the quality of crystals of this material (i.e., decreasing the concentration of structural defects and increasing the mobility of current carriers). We also investigated the galvanomagnetic and photoelectric properties of some narrow-band solid solutions based on indium arsenide such as In$_x$GaAsSb ($x = 0.8 - 0.9$) and InAsSbP$_x$ ($x = 0.03 - 0.26$).[3–5]

In our study we have generalized our results on epitaxial indium arsenide and on solid solutions similar to it. We have also investigated new narrow-band materials in order to find general trends and ways to enhance the quality of crystals of this material.

RESULTS OF A STUDY OF EPITAXIAL INDIUM ARSENIDE

We examined epitaxial InAs films grown on indium-arsenide substrates ($n = 3 \times 10^{16}$ cm^{-3}) at temperatures in the range 550–650 °C. We investigated their galvanomagnetic properties (electron density n, Hall coefficient R, conductivity σ, and magnetic resistance $\Delta\rho/\rho$) and photoconductivity in the temperature interval $T = 77 - 300$ K. The epitaxial layers were quite thick (40–80 μm); therefore, for the electrical measurements the substrate was ground down.

All of the InAs samples grown by liquid-phase epitaxy had n-type conductivity, where the electron density grew and the electron mobility fell as the growth temperature was lowered. Electrical parameters of the epitaxial films prepared at different temperatures are listed in Table I. This table also lists values of the parameters for standard samples grown by

the Czochralski method. It can be seen that the electron density in the epitaxial films is always approximately an order of magnitude higher than in InAs crystals grown by the Czochralski method ($t = 940$ °C), while the mobility is lower by a factor of 2 or more. This stems from the fact that in crystals of indium arsenide grown by the Czochralski method the conductivity is determined only by shallow background impurities (S, Se, Te) with activation energy $E = 0.002$ eV (see Table I). In crystals grown by liquid-phase epitaxy at $t = 650 - 550$ °C, as a study of the photoconductivity and temperature dependence of the Hall coefficient has shown, there also exist impurities with activation energy $E_2 = 0.02 - 0.03$ eV, which are attributable to a breakdown of stoichiometry in the solution–melt that arises at lower growth temperatures. According to the phase diagram,[6] at such temperatures InAs crystallizes in a lattice with an arsenic deficiency. As a result, a donor structural defect of the type ''arsenic vacancy + trapped impurity'' arises (V_{As} + impurity), which increases the electron density in the epitaxial film. The relative concentrations of As and In and consequently the number of structural defects and the electron density in the crystal depend on the growth temperature, as confirmed by the data in Table I.

We have proposed a method for decreasing the concentration of structural defects in epitaxial indium arsenide by introducing the neutral solvent lead into the solution–melt,[1] which makes it possible to vary the relative concentrations of As and In in the solution–melt. Experimentally, we found (see Table II) that when the lead concentration was increased (up to 70 mole%), the electron density fell while the mobility grew by approximately a factor of 2. For lead concentrations greater than 80 mole%, the electron density continued to decrease at all growth temperatures but the mobility fell as well. We assume that this occurs because of growth of the degree of compensation since for equal quantities of As and In in the solution–melt at relatively low temperatures the probability arises of the formation of acceptor structural defects bound to indium vacancies. In this case, high-resistance

TABLE I.

Preparation method	Growth temperature, °C	Composition mole%		$T = 77$ K				
		In	As	$n \times 10^{-17}$ cm^{-3}	μ, cm^2/(V·s)	E_1, eV	E_2, eV	E_3, eV
Czochralski	940	50	50	0.27	34 500	0.002	none	none
LPE	650	91.7	8.3	3.8	15 200	0.001	0.015	none
LPE	600	94.8	5.2	9	6 620	0.002	0.015 0.02	none
LPE	550	95	5	33	6 080	0.002	0.015 0.02	0.1 0.2

films, which find wide application in practice as semi-insulating substrates, were produced. In such well-compensated samples it is possible to observe slopes in the temperature dependence of the Hall coefficient which correspond to deep donor impurities in InAs with activation energy $E_3 = 0.09 – 0.1$ eV. It is possible that this is yet another structural defect whose nature is still unclear.

It can be assumed that the use of lead in the solution–melt during the growth of InAs alters the concentration of not only the structural defects but also the concentration of the shallow background impurities, forming such compounds with them as PbS, PbTe, and PbSe.

Doping of InAs during epitaxial growth with rare-earth elements (ytterbium and gadolinium) also led to a decrease of the concentration of current carriers and a strong rise of the mobility. It is possible that rare-earth impurities actively bond to background impurities, forming neutral compounds with them.

The final result of doping with lead and rare-earth impurities is well illustrated by Fig. 1, which plots the theoretical dependence of the electron mobility in InAs on their concentration (dashed line) and also the results for epitaxial films of indium arsenide grown in the presence of lead and doped with rare-earth elements. The purest samples with high mobility (about 100 000 cm^2/(V·s), which is close to the theoretical mobility (curve *1*), were obtained by doping with rare-earth impurities. The presence of lead during doping with rare-earth elements lowers the mobility (curve *2*), although it gives samples with the lowest concentration of current carriers ($n = 3 \times 10^{15}$ cm^{-3}). Lead in the absence of rare-earth impurities (curve *3*) can also strongly lower the concentration and mobility of the crystals.

RESULTS OF A STUDY OF SOLID SOLUTIONS. UNDOPED SOLID SOLUTIONS

Ternary and quaternary solid solutions similar in composition to indium arsenide grown by liquid-phase epitaxy at $t = 550 – 650$ °C have been widely used to extend the optical range of operation of devices in the infrared. The width of the band gap in them can be both less than and greater than in InAs ($E_g^{\text{InAs}} = 0.41$ eV at $T = 77$ K). Thus, in the investigated solid solution In$_x$GaAsSb ($x = 0.8 – 0.92$) the width of the band gap $E_g < E_g^{\text{InAs}}$ while in InAsSbP$_x$ ($0.03 < x < 0.26$), InAsGa$_x$ ($x = 0.02 – 0.03$), and InAsP$_x$ ($x = 0.022 – 0.07$) $E_g > E_g^{\text{InAs}}$. Let us examine in more detail each of these solid solutions.

SOLID SOLUTION In$_x$GaAsSb

The quaternary solid solutions In$_x$GaAsSb with x varying over a wide interval have been in wide use for a long time, and therefore their electrical properties have been studied extensively.[7–9]

It is well known that these solid solutions have a broad region of immiscibility in the interval $0.2 < x < 0.8$. Therefore, they can be used only for small values of x ($x < 0.2$), where they are similar to GaSb, and for large values of x ($x = 0.8 – 0.9$), where they are similar to InAs.

Figure 2 plots the theoretical dependence of the width of the band gap E_g on x at $T = 77$ K over the entire interval of variation of x for the solid solutions In$_x$GaAsSb (Ref. 10) along with experimental points which we obtained by examining the photoconductivity in them. It can be seen that for $0.7 < x < 0.92$ E_g varies only weakly and is similar in value to E_g^{InAs} (0.3–0.32 eV), and for $0 < x < 0.22$ E_g falls from

TABLE II.

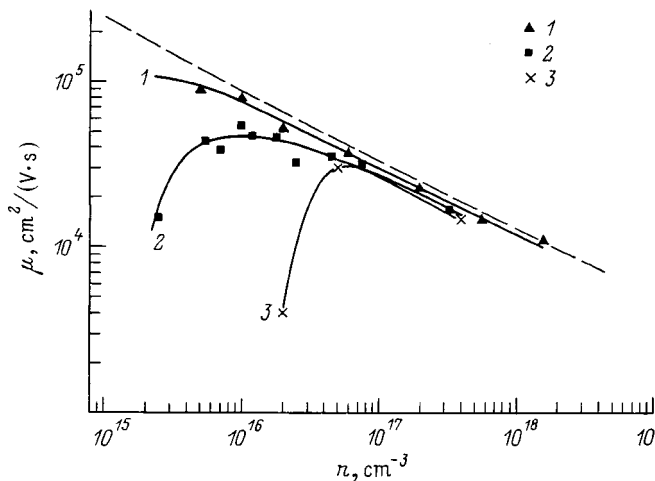| No.	t, °C	Composition of solution–melt, mole %			$T = 77$ K	
		In	As	Pb	$n \times 10^{-17}$ cm^{-3}	μ, cm^2/(V·s)
1	650	91.2	8.22	0	4	13 900
2		32.9	3.7	63.3	0.49	30 000
3		7.19	7.19	85.6	0.2	3 930
4	600	94.8	3.2	0	9	6 620
5		31.8	1.8	66.3	1.2	20 600
6		4.18	4.18	91.6	0.082	4 020
7	550	95	5	0	33	6 080
8		31.8	0.9	67.6	15	6 160
9		2.5	2.5	95	0.46	390
10	500	1.4	1.4	97.2	0.2	4 640

FIG. 1. Dependence of the mobility μ on the electron density n in InAs: dashed line—theory, *1*—samples doped with rare-earth elements, *2*—samples doped with rare-earth elements and lead, *3*—samples doped with lead.

0.78 to 0.56 eV. It may be noted that there exists a region of values of E_g which corresponds to the immiscibility region of the solid solution, where experimental points are absent since these solid solutions cannot be obtained by liquid-phase epitaxy.

Narrowband solid solutions $In_xGaAsSb$ similar in composition to InAs are interesting for the reason that on the basis of these solid solutions it is possible to obtain the so-called disconnected type-II heterojunctions which possess a number of unique electrical and photoelectric properties.[11] These solid solutions are used to create optoelectronic devices which play an essential role in connection with ecological problems and preservation of the environment.
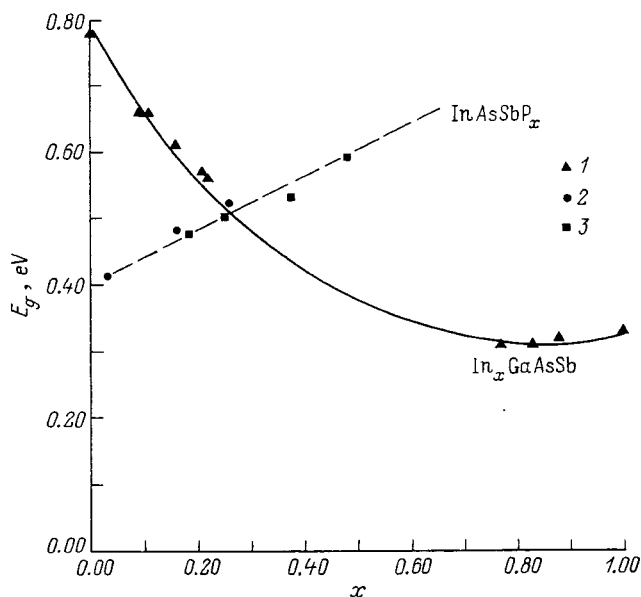
FIG. 2. Dependence of the width of the band gap E_g at $T = 77$ K on the composition of $In_xGaAsSb$ and $InAsSbP_x$ solid solutions. Curves—theory,[10,13] points: *1, 2*—our data, *3*—data of Ref. 14.

In this article we present the results of an experimental study of the galvanomagnetic properties (Hall coefficient, conductivity, mobility) and the photoconductivity at $T = 77–300$ K in InGaAsSb solid solutions similar in composition to InAs, obtained by liquid-phase epitaxy at $t = 550–650$ °C on GaSb and InAs substrates. All the solid solutions had n-type conductivity. The thickness of the samples was 3–6 μm. Since the substrate in this case cannot be removed, it was necessary in the galvanomagnetic measurements to isolate the epitaxial layer from the substrate by creating a potential barrier at the "film–substrate" boundary or to use high-resistance substrates.

We examined two types of films: isoperiodic GaSb and isoperiodic InAs films. The isoperiodic GaSb films were grown on an n-GaSb : Te substrate or on high-resistance p-GaSb obtained with the neutral solvent lead. In the first case there exists a high potential barrier at the boundary which allows one to perform measurements up to $T = 300$ K. Isoperiodic InAs crystals were grown on high-resistance p-InAs : Zn (with resistivity $100 \, \Omega \cdot$cm at $T = 77$ K). In these samples at high temperatures the conductivity of the substrate grew due to the transition to intrinsic conductivity; therefore, it was possible to measure the parameters in them only up to 200 K.

For convenience and ease of visualization, results of the measurements of the electrical parameters are summarized in Table III for all of the most typical undoped samples, of various composition, grown on both types of substrates. Let us consider the results for InGaAsSb. It can be seen from the table that in InGaAsSb on an n-GaSb : Te substrate the electron density is an order of magnitude greater than in the samples grown on p-InAs : Zn. This can be explained by diffusion of tellurium or zinc impurities from the substrate into the epitaxial film. Diffusion of tellurium also took place in the case of growth on such substrates of solid solutions which are similar in composition to GaSb and which have p-type conductivity.[7] In them tellurium created an acceptor structural defect ($V_{Ga} + Te$). In the given solid solution, tellurium apparently manifests itself simply as a shallow donor since no significant lowering of the mobility typical of the presence of defects is observed. Zinc, acting as an acceptor as it diffuses from the substrate into the epitaxial film, raises the degree of compensation of electrons in it by lowering their density and decreasing their mobility.

The electron activation energies listed in Table III were determined from the temperature dependence of the Hall coefficient (Fig. 3). On the curve for the solid solution $In_{0.85}GaAsSb$ three slopes, which correspond to the activation energies $E_1 = 0.002$ eV, $E_2 = 0.02–0.03$ eV, and $E_3 = 0.09–0.1$ eV, are observed. The deepest donor level, E_3, also showed up in an examination of the photoconductivity. It may be noted that the same activation energies were found for epitaxial films of indium arsenide: as was already noted, E_1 is due to shallow uncontrollable impurities, and E_2 and E_3 are due to structural defects.

THE SOLID SOLUTION $InAsSbP_x$

Baranov *et al.*[12] showed that in the system $InAsSbP_x$ grown on an InAs substrate by liquid-phase epitaxy it is

TABLE III.

Solid solution	x	Substrate	77 K		300 K		E_1, eV	E_2, eV	E_3, eV
			$n\times10^{-17}$, c^{-3}	μ, cm^2/(V·s)	$n\times10^{-17}$, cm^{-3}	μ, cm^2/(V·s)			
In$_x$GaAsSb	0.85	n-GaSb : Te	6	8750	74	3400	0.002	0.02	0.09
	0.85	n-GaSb : Te	6	8000	1.5	7300	0.003	0.025	0.08
	0.8	p-InAs : Zn	0.2	8900	⋯	⋯	⋯	⋯	⋯
	0.79	p-InAs : Zn	0.5	6300	⋯	⋯	⋯	⋯	⋯
InAsSbP$_x$	0.03	p-InAs : Zn	0.9	29 000	⋯	⋯	⋯	⋯	⋯
	0.16	p-InAs : Zn	8	14 000	⋯	⋯	⋯	⋯	⋯
	0.26	p-InAs : Zn	0.18	13 000	⋯	⋯	0.002	0.02	0.9–0.1
InAsGa$_x$	0.02	p-InAs : Zn	0.53	2600	⋯	⋯	0.002	0.015	0.07
	0.03	p-InAs : Zn	1.0	2500	6.6	650	0.001	0.033	0.2
	0.05	p-InAs : Zn	10	4000	5.2	3400	0.002	0.018	0.07
InAsP$_x$	0.02	p-InAs : Zn	2	2500	19	1200	0.002	0.035	0.2
	0.038	p-InAs : Zn	10	4300	14	3900	0.001	0.03	⋯
	0.053	p-InAs : Zn	14	3100	17	3200	0.002	0.03	⋯
	0.073	p-InAs : Zn	5.8	3000	11	2500	0.002	0.03	⋯

possible to obtain a continuous series of solid solutions with $0<x<0.39$, whose band gap partly overlaps the spectral range of the immiscibility region of InGaAsSb, which raises interest in these solid solutions. The dashed line in Fig. 2 plots the calculated dependence of the width of the band gap in InAsSbP$_x$ on the composition,[13] and the points represent experimental results obtained by us and other authors.[14]

We investigated the electrical and photoelectric properties of the solid solutions InAsSbP$_x$ over a wide range of the phosphorus content ($0.03<x<0.26$). Our aim was to determine the parameters and to examine the energy spectrum of this material.

Epitaxial films, isoperiodic with the InAs substrate, were obtained by liquid-phase epitaxy from the initial ingredients InP, InAs, In, and Sb. The growth temperature t for x

<0.15 was 650 °C, the film thickness was about 100 μm, and the substrate was ground down before the measurements were performed. For $x=0.26$ and $t=550$ °C the layers were thin (3–5 μm). In this case, we used strongly compensated p-InAs : Zn as the substrate, which is a semi-insulator up to 200 K.

Parameters of the solid solutions InGaAsP$_x$ for representative values of x are listed in Table III. Note that in thin films with the composition InGaAsP$_{0.26}$ grown on InAs : Zn substrates the electron density is significantly lower for low electron mobility than in thick films of other compositions. We can assume that zinc which diffuses from the substrate compensates for the donors in the film. We observed an analogous picture in the solid solution InGaAsSb. The activation energies of the impurities were determined from the temperature dependences of the Hall coefficient and the photoconductivity. Figure 3 plots the dependence $R(T)$ for the solid solution InAsSbP$_{0.26}$. Three slopes are distinctly visible in the temperature dependence corresponding to the activation energies $E_1=0.002$ eV, $E_2=0.02$ eV, and $E_3=0.09$–0.1 eV. As can be seen, the same values were obtained as in indium arsenide and in the solid solution InGaAsSb.

THE TERNARY SOLID SOLUTIONS InAsGa$_x$ ($x=0.02-0.05$) AND InAsP$_x$ ($x=0.022-0.07$)

These solid solutions, which are very similar in composition to indium arsenide, have a band gap that is not much wider than that of InAs. According to the calculations, at $T=77$ K it is $E_g=0.448$ eV for InAsGa$_x$ and $E_g=0.415$ eV for InAsP$_x$. Interest in these materials stems from the search for crystals with lower electron affinity than in InAs and E_g close to the band gap of indium arsenide, with the aim of obtaining structures with a disconnected type-II heterojunction that contains a two-dimensional electron channel.

Ternary solid solutions InAsGa and InAsP were grown by liquid-phase epitaxy at $t=590$ °C on p-InAs : Zn substrates, with which they were not isoperiodic (the lattice mismatch $\Delta a/a$ varied from 0.1 to 0.2%). The parameters of these solid solutions are listed in Table III, and the tempera-
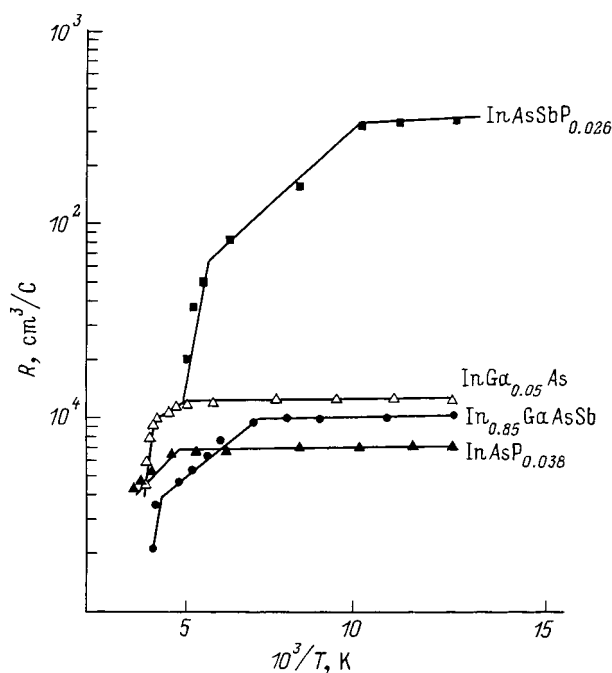

FIG. 3. Temperature dependence of the Hall coefficient R for different solid solutions.

TABLE IV.

Solid solution	Substrate	Impurity	Impurity concentration, mole	$T = 77$ K	
				$n \times 10^{-17}$, cm^{-3}	μ, cm^2/(V·s)
InAsSbP$_{0.26}$	p-InAs : Zn	...	...	0.18	13 500
		Te	2.5×10^{-4}	0.6	8 100
			5×10^{-4}	1.5	6 000
			4.6×10^{-3}	25	3 600
			9.2×10^{-3}	60	3 000
		Sn	1.8×10^{-2}	0.12	6 150
			3.2×10^{-2}	0.31	6 850
			2.5×10^{-1}	3.3	4 780
			6.2×10^{-1}	12	3 330

ture dependence of the Hall coefficient is plotted in Fig. 3. It is interesting that the electron density in all the investigated crystals was high (10^{17}–10^{18} cm^{-3}) while the mobility was low. The activation energies in these ternary solid solutions were similar to the activation energies of impurities in InAs and in the quaternary solid solutions (Fig. 3).

DOPING OF SOLID SOLUTIONS WITH DONOR IMPURITIES

To extend the range of current carrier concentrations in the solid solutions we doped some of them with donor impurities (Te, Sn).

The solid solution In$_{0.85}$GaAsSb, grown on a n-GaSb : Te substrate, was doped with tellurium. The electron density in this case grew linearly from 2.0×10^{17} to 10^{19} cm^{-3}, and the mobility fell from 11000 to 3000 cm^2/(V·s).

Thesolidsolution InAsSbP$_{0.26}$, grown on a p-InAs : Zn substrate, was doped with tellurium and tin. The results are summarized in Table IV, from which it can be seen that doping with tellurium raises the electron density from 2×10^{16} to 10^{19} cm^{-3} as the tellurium concentration increases from 10^{-4} to 10^{-2} mole %.

In the case of doping of InAsSbP with tin this impurity manifested its amphoteric properties: at low tin concentrations the number of acceptors and the number of donors in the crystal grew. Therefore, the electron density first decreased slightly, but at tin concentrations greater than 0.01 mole% the electron density grew rapidly and reached 10^{18} cm^{-3}. As measurements of the temperature dependence of the Hall coefficient and the photoconductivity in tellurium- and tin-doped samples showed, impurities in them with activation energy $E_1 = 0.002$–0.003 eV are preserved, but the defect with activation energy $E_2 = 0.02$–0.03 eV disappears, which suggests a possible curing by tellurium and tin.

In order to estimate the degree of perfection of the various n-type solid solutions examined in this study, we compared the dependence of the electron mobility on the electron density in them with the theoretical dependence $\mu(n)$ for indium arsenide, as we did in the case of doping of InAs by rare-earth impurities or by using lead solvent. The dashed curve in Fig. 4 plots the theoretical dependence for InAs;

experimental curves for all the investigated ternary and quaternary n-type solid solutions, both undoped and tellurium-doped, are also shown.

It can be seen from the figure that the dependence $\mu(n)$ for the solid solutions differs significantly from the theoretical dependence for InAs. Closest to the theoretical dependence $\mu(n)$ is the dependence for InGaAsSb grown on n-GaSb : Te (curve *1*), but for the same solid solution grown on p-InAs : Zn it is located significantly lower (curve *2*), which suggests that this material is highly imperfect (it has clusters of impurities and defects, the so-called ''mobility killers,'' and other flaws[8]). This dependence has roughly the same form for InAsSbP grown on the same substrate (curve *3*). As studies of transverse and longitudinal magnetoresistance in these crystals have shown, there do indeed exist clusters of impurities, whose fraction can reach 47% of the entire volume of the crystal in the undoped samples. Their appearance is possibly connected with zinc diffusion from the substrate during epitaxial growth.

Taking into account all the factors mentioned above, we conclude that to obtain solid solutions with a high mobility it
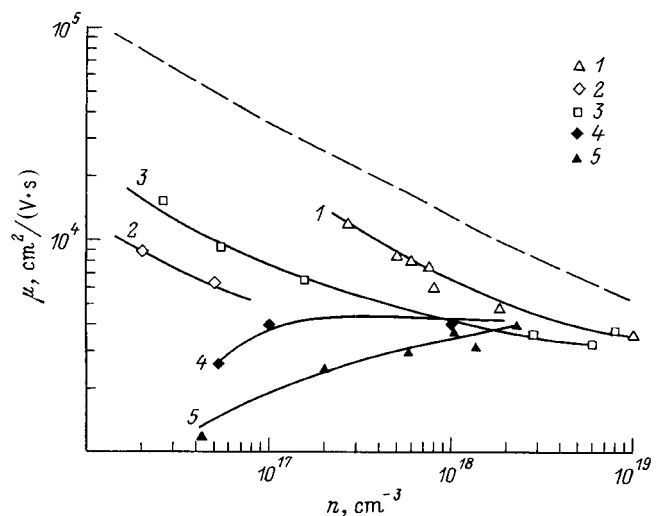

FIG. 4. Dependence of the mobility μ on the electron density n in the solid solutions: dashed curve—theoretical dependence for InAs, points—experiment: *1*—InGaAsSb on a n-GaSb:Te substrate, *2*—InGaAsSb on p-InAs:Zn, *3*—InGaAsP on p-InAs:Zn, *4*—InGaAs on p-InAs:Zn, *5*—InAsP on p-InAs.

TABLE V.

Solid solution	Substrate	Impurity	Impurity concentration, mole%	Conductivity type	$T = 77$ K	
					$n \times 10^{-17}$, cm^{-3}	μ, cm^2/(V·s)
In$_{0.85}$GaAsSb	*p*-GaSb : Te	...	...	n	5.6	3700
		Mn	6.6×10^{-3}	*n*	4	2270
			1.9×10^{-2}	*n*	2.2	890
			5.7×10^{-2}	*p*	8	20
			9.1×10^{-2}	*p*	13	59
			1.9×10^{-1}	*p*	40	60
			3.4×10^{-1}	*p*	170	50

is desirable to use either high-resistance substrates doped with lead or GaSb : Te substrates instead of InAs : Zn substrates.

The electron mobility in the undoped ternary solid solutions InAsGa$_x$ and InAsP$_x$ with different *x*, grown on *p*-InAs : Zn substrates (Fig. 4, curves *4* and *5*), is significantly lower than in the investigated quaternary solid solutions. In our view, this has to do with the fact that these epitaxial films are not isoperiodic with InAs (the lattice mismatch $\Delta a/a = 0.1 - 0.2\%$).

DOPING OF SOLID SOLUTIONS WITH ACCEPTOR IMPURITIES

Acceptor impurities, such as manganese and zinc, are usually used to obtain *p*-type solid solutions. The most promising is manganese since zinc diffuses strongly from the growing film to the substrate during doping, distorting the results. We investigated the manganese-doped solid solution In$_{0.85}$GaAsSb, grown on *n*-GaSb : Te and *p*-GaSb(Pb) substrates. The parameters of these manganese-doped solid solutions are listed in Table V.

Manganese doping leads first to a decrease in the electron density, and then to overcompensation and production of *p*-type material (see Fig. 5 for the InGaAsSb layers grown on *n*-GaSb : Te). We were able to obtain solid solutions with carrier concentration $p = 10^{19}$ cm^{-3} and mobility 50–100 cm^2/(V·s). It is interesting to note that sign inversion of the Hall coefficient (transition of the conductivity from *n*-type to *p*-type) in samples grown on *n*-GaSb : Te substrates (Fig. 5, curve *2*) takes place later at high manganese concentrations than in samples grown on *p*-GaSb(Pb) substrates. This can be explained by an increase in the electron density in the solid solution due to tellurium diffusion from the substrate.

A study of the photoconductivity in *p*-type manganese-doped InGaAsSb samples revealed the presence of peaks in the region of the impurity conductivity, associated with excitation of electrons from the valence band to levels with $E_2 = 0.03 - 0.04$ eV and $E_3 = 0.09 - 0.1$ eV, regardless of the type of substrate, which confirms our conclusion that they are associated with natural structural defects in this solid solution. In the spectral dependence we also observed a peak associated with excitation of electrons from a shallow acceptor level $E_A = 0.025 - 0.028$ eV, which is probably due to the manganese impurity in this solid solution.

CONCLUSIONS

Summarizing our discussion above, we can draw the following conclusions.

1. All of the epitaxial layers of indium arsenide, grown at different epitaxy temperatures (650–550 °C), are crystals with *n*-type conductivity. As the epitaxy temperature is lowered, the electron density grows by almost two orders of magnitude in comparison with the current carrier concentration in InAs crystals grown by the Czochralski method (2×10^{16} cm^{-3}) while the mobility falls by almost an order of magnitude.

While the conductivity is determined by shallow impurities with activation energy $E_1 = 0.002 - 0.003$ eV in InAs crystals, in epitaxial layers it is also governed by structural defects with activation energies $E_2 = 0.02 - 0.03$ eV and $E_3 = 0.09 - 0.1$ eV due to deviations from stoichiometry in the solution–melt toward lower arsenic concentrations by almost an order of magnitude.

2. We have achieved a substantial decrease in the current-carrier concentration (by almost an order of magnitude) and increase in the mobility in epitaxial layers of in-
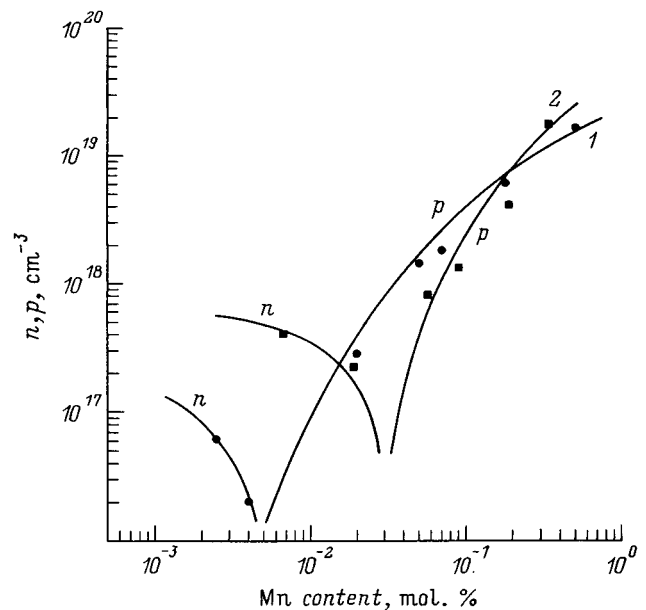

FIG. 5. Dependence of the current carrier concentration in InGaAsSb layers on the level of manganese doping: *1*—on a GaAs:Te substrate, *2*—on a *p*-GaSb(Pb) substrate.

dium arsenide due to use of the neutral solvent (lead), which makes it possible to reduce the nonstoichiometry (vary the ratio of the In and As concentrations in the solution). We achieved a decrease in the electron density in InAs epitaxial layers as a result of growing from solution–melts doped with rare-earth elements (ytterbium and gadolinium), which probably bind to background impurities in the initial solution. We obtained epitaxial layers with $n = 6 \times 10^{15}$ cm^{-3} and mobility about 100 000 cm^2/(V·s).

3. All of the investigated solid solutions, both with band gap E_g greater than that of indium arsenide (InAsSbP, In-GaAs, InAsP) and with band gap less than that of indium arsenide (InGaAsSb), have n-type conductivity; here the energy spectrum of the impurities in all the investigated crystals is similar to the energy spectrum of epitaxial InAs and consists of levels with energies $E_1 = 0.002 - 0.003$ eV, $E_2 = 0.02 - 0.03$ eV, and $E_3 = 0.09 - 0.1$ eV.

4. Doping of solid solutions with the donor impurities Te and Sn makes it possible to obtain layers with current-carrier concentrations in the interval $10^{16} - 10^{19}$ cm^{-3} and mobilities in the interval $8000 - 3000$ cm^2/(V·s). In crystals doped with donor impurities we observed curing of the structural defects with $E_2 = 0.02 - 0.03$ eV. Doping of solid solutions with acceptor impurities (Mn) leads to overcompensation and production of crystals with p-type conductivity and with hole density $p = 10^{19}$ cm^{-3} and mobility 50 cm^2/(V·s).

[1] A. N. Baranov, T. I. Voronina, A. A. Gorelenok, T. S. Lagunova, A. M. Litvak, M. A. Sipovskaya, S. P. Starosel'tseva, V. A. Tikhomirova, and V. V. Sherstnev, Fiz. Tekh. Poluprovodn. **26**, 1612 (1992) [Sov. Phys. Semicond. **26**, 905 (1992)].

[2] A. N. Baranov, T. I. Voronina, T. S. Lagunova, M. A. Sipovskaya, V. V. Sherstnev, and Yu. P. Yakovlev, Fiz. Tekh. Poluprovodn. **27**, 421 (1993) [Semiconductors **27**, 236 (1993)].

[3] T. I. Voronina, T. S. Lagunova, M. P. Mikhaĭlova, M. A. Sipovskaya, V. V. Sherstnev, Yu. P. Yakovlev, Fiz. Tekh. Poluprovodn. **25**, 421 (1991) [Sov. Phys. Semicond. **25**, 390 (1991)].

[4] T. I. Voronina, T. S. Lagunova, N. A. Prokof'eva, T. B. Popova, M. A. Sipovskaya, V. V. Sherstnev, and Yu. P. Yakovlev, Fiz. Tekh. Poluprovodn. **25**, 1639 (1991) [Sov. Phys. Semicond. **25**, 989 (1991)].

[5] T. I. Voronina, T. S. Lagunova, K. D. Moiseev, M. A. Sipovskaya, I. N. Timchenko, and Yu. P. Yakovlev, Fiz. Tekh. Poluprovodn. **27**, 1777 (1993) [Semiconductors **27**, 978 (1993)].

[6] A. N. Baranov, A. A. Gorelenok, A. M. Litvak, V. V. Sherstnev, and Yu. P. Yakovlev, Zh. Neorg. Khim. **37**, 448 (1992).

[7] A. N. Baranov, A. N. Dakhno, B. E. Dzhurtanov, T. S. Lagunova, M. A. Sipovskaya, and Yu. P. Yakovlev, Fiz. Tekh. Poluprovodn. **24**, 98 (1990) [Sov. Phys. Semicond. **24**, 59 (1990)].

[8] A. N. Baranov, T. I. Voronina, A. N. Dakhno, B. E. Dzhurtanov, T. S. Lagunova, M. A. Sipovskaya, and Yu. P. Yakovlev, Fiz. Tekh. Poluprovodn. **24**, 1072 (1990) [Sov. Phys. Semicond. **24**, 676 (1990)].

[9] T. I. Voronina, B. E. Dzhurtanov, T. S. Lagunova, and Yu. P. Yakovlev, Fiz. Tekh. Poluprovodn. **28**, 2001 (1994) [Semiconductors **28**, 1103 (1994)].

[10] J. C. De Winter, M. A. Pollack, A. K. Srivastava, and J. L. Zyskind, J. Electron. Mater. **4** 729 (1985).

[11] M. A. Afrailov, A. N. Baranov, A. P. Dmitriev, M. P. Mikhaĭlova, Yu. P. Smorchkova, I. N. Timchenko, V. V. Sherstnev, Yu. P. Yakovlev, and I. N. Yassievich, Fiz. Tekh. Poluprovodn. **24**, 1397 (1990) [Sov. Phys. Semicond. **24**, 876 (1990)].

[12] A. N. Baranov, B. E. Dzhurtanov, A. M. Litvak, N. A. Charikov, A. G. Chernyavskiĭ, V. V. Sherstnev, and Yu. P. Yakovlev, Zh. Neorg. Khim. **35**, 3008 (1990).

[13] E. P. Gertner, D. T. Cheung, A. N. Andrews, and J. T. Longo, J. Electron. Mater. **6**, 163 (1977).

[14] T. Fukui and J. Horikoshi, Jpn. J. Appl. Phys. **20**, 587 (1981).

Translated by Paul F. Schippnick

Hubbard energy of two-electron tin centers in $PbS_{1-z}Te_z$ solid solutions

V. F. Masterov,[†] F. S. Nasredinov, S. A. Nemov, P. P. Seregin, and N. P. Seregin

St. Petersburg State Technical University, 195251 St. Petersburg, Russia
(Submitted December 24, 1998; accepted for publication December 28, 1998)
Fiz. Tekh. Poluprovodn. **33**, 789–790 (July 1999)

It is shown by Mössbauer spectroscopy of the isotope ^{119}Sn that an isovalent tin impurity in $PbS_{1-z}Te_z$ solid solutions is a two-electron donor with a negative correlation energy, where the energy levels associated with tin centers are situated against the background of the valence band continuum. The Hubbard energy U is estimated for impurity tin atoms in $PbS_{1-z}Te_z$ ($|U|>0.2$ eV), which is found to be substantially higher than for analogous tin centers in $PbS_{1-z}Se_z$ solid solutions ($|U|=0.058$ eV). © *1999 American Institute of Physics.*
[S1063-7826(99)00607-9]

According to Mössbauer spectroscopy data on the isotope ^{119}Sn, tin in PbS and PbSe and their solid solutions $PbS_{1-z}Se_z$ is a two-electron donor with a negative correlation energy (Hubbard energy).[1] In PbS the energy levels generated by tin centers lie in the lower half of the band gap, whereas in $PbS_{1-z}Se$ solid solutions the tin levels drop as z is increased, and for $z>0.7$ they enter the valence band (but remain above the levels generated by sodium and thallium acceptor centers, which are used to control the position of the chemical potential in $PbS_{1-z}Se_z$ solid solutions.[1]

Attempts to observe the electrical activity of tin centers in PbTe have been unsuccessful because the energy levels of tin are situated against the background of states of the valence band below the attainable values of the chemical potential in this material. In $PbS_{1-z}Te_z$ solid solutions the tin levels ''rise up'' from the depth of the valence band, and it is possible to observe phenomena associated with change in the charge state of tin.[1] Here we give the results of a determination of the positions of the energy levels of tin in $PbS_{1-z}Te_z$ solid solutions and the Hubbard energy. The preparation of the samples for the investigations and the procedure for measuring the ^{119}Sn Mössbauer spectra are described in Ref. 1.

Figure 1 shows the ^{119}Sn Mössbauer spectra of $Pb_{1-x-y}Sn_xA_yS_{1-z}Te_z$ solid solutions at a temperature $T=80$ K. For partially compensated samples ($0<y<2x$) the ^{119}Sn Mössbauer spectra at $T=80$ K comprise the superposition of two lines, whose isomeric shifts correspond to Sn^{2+} and Sn^{4+}; the fraction of Sn^{4+} centers $P=N(Sn^{4+})/\{N(Sn^{2+})+N(Sn^{4+})\}$ [$N(Sn^{2+})$ and $N(Sn^{4+})$ are the densities of Sn^{2+} and Sn^{4+} centers, respectively] is proportional to $[N(A)-p]$, where $N(A)$ and p are the densities of acceptors and holes in the samples. The latter varied between the limits $10^{19}-10^{20}$ cm^{-3} and did not depend on the temperature in the range from 80 K to 295 K, indicating that in $PbS_{1-z}Te_z$ solid solutions the chemical potential associated with partially ionized tin donor levels is below the top of the valence band.

Consequently, tin in $PbS_{1-z}Te_z$ is a two-electron donor: Sn^{2+} and Sn^{4+} ions correspond to neutral ($[Sn]^0$) and doubly ionized ($[Sn]^{2+}$) tin centers. The electronic states associated with tin are situated against the background of states of the valence band, but have a higher energy than the acceptor states of thallium and sodium impurities. The absence of states corresponding to singly ionized tin centers in the Mössbauer spectra indicates that the Hubbard energy $U<0$ for two-electron tin centers in $PbS_{1-z}Te_z$.

A similar situation has been encountered for $PbS_{1-z}Se_z$ solid solutions.[2] For these solid solutions, which simultaneously contained Sn^{2+} and Sn^{4+} centers, the isomeric shifts of the Sn^{2+} and Sn^{4+} lines depended on the temperature at which the spectra were measured: Elevation of the temperature from 80 K to 295 K was accompanied by merging of the
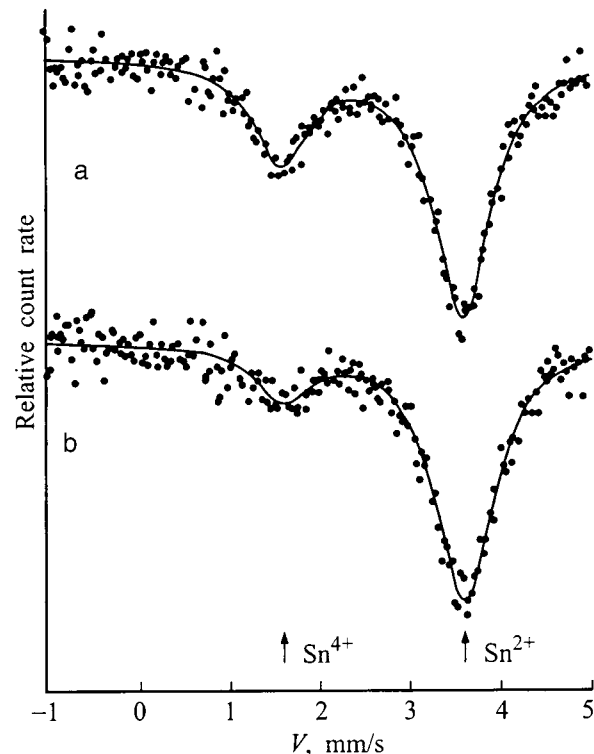

FIG. 1. Mössbauer spectra of ^{119}Sn at $T=80$ K for the solid solutions $Pb_{0.95}Sn_{0.03}Tl_{0.02}S_{0.2}Te_{0.8}$ (a) and $Pb_{0.95}Sn_{0.03}Tl_{0.02}S_{0.15}Te_{0.85}$ (b). The positions of the Sn^{4+} and Sn^{2+} spectra are shown.
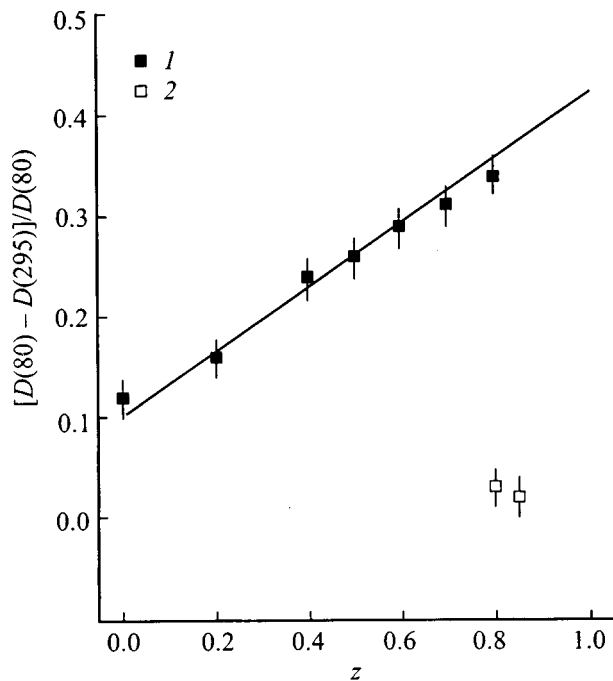
FIG. 2. Dependence on z of the relative change in the distance between the Sn^{2+} and Sn^{4+} lines when the temperature is raised from 80 K to 295 K for solid solutions $Pb_{0.96}Sn_{0.02}Na_{0.01}Tl_{0.01}S_{1-z}Se_z$ (*1*) and $Pb_{0.95}Sn_{0.03}Tl_{0.02}S_{0.2}Te_{0.8}$ (*2*). $D(80)$ and $D(295)$ denote the distances (in mm/s) between the Sn^{2+} and Sn^{4+} lines at 80 K and 295 K, respectively.

Sn^{2+} and Sn^{4+} lines (Fig. 2). Such temperature dependences of the isomeric shifts are characteristic of electron exchange between two charge states of a Mössbauer atom, when the lifetime of each state is commensurate with the lifetime of the Mössbauer level (this time is of the order of 20 ns for ^{119}Sn). For $z > 0.7$ the process activation energy E_0 does not depend on z; an analysis in Ref. 2 suggests that the activation energy of the indicated process in the case of tin levels situated against the background of the valence band is governed entirely by the Hubbard energy: $E_0 = -U/2$.

For $PbS_{1-z}Te_z$ solid solutions containing neutral and ionized tin centers the isomeric shifts of the Sn^{2+} and Sn^{4+} lines exhibit a far weaker temperature dependence than has been observed for $PbS_{1-z}Se_z$ solid solutions (Fig. 2). An estimate of the activation energy of electron exchange between neutral and ionized tin centers in $PbS_{1-z}Te_z$ gives $E_0 > 0.1$ eV, i.e., for the Hubbard energy we have $|U| > 0.2$ eV. This value is much higher than the value $|U| = 0.06$ eV obtained for analogous centers in $PbS_{1-z}Se_z$.

A comparison of the estimates for the Hubbard energy leads to conclusions about its nature, i.e., in our case about the source of the energy gain when the second electron is stripped from the tin center, relative to the first. First of all, this gain could hardly be associated with delocalized states of the valence zone, because for $PbS_{1-z}Se_z$ solid solutions the dependence of E_0 on z vanishes when the tin levels move into the valence band. This means that the delocalized states of the valence band and the electronic states of the tin atoms are separated in space, while the Hubbard energy is determined by the nearest-neighbor environment of the latter. Second, the Hubbard energy depends on the chemical nature of the chalcogen in the environment of the tin atoms. In the composition where the Hubbard energy was estimated, they are Se^{2-} for $PbS_{1-z}Se_z$ and Te^{2-} for $PbS_{1-z}Te_z$. The most probable cause of the onset of a negative Hubbard energy could be a shift of the ligand ions toward the central ion (in our case the Se^{2-} or Te^{2-} ions toward the Sn^{4+} ion) after detachment of the second electron. However, this effect should produce a greater energy gain for smaller-size ligands (i.e., for Se^{2-} as opposed to Te^{2-}). Our observed ratio of the Hubbard energies implies a different origin. The source in this case could be, for example, an increase of the covalent contribution to the tin-chalcogen binding energy in the ionization of tin.

†Deceased.

[1] V. F. Masterov, F. S. Nasredinov, S. A. Nemov, and P. P. Seregin, Fiz. Tekh. Poluprovodn. **30**, 840 (1996) [Semiconductors **30**, 450 (1996)].
[2] V. F. Masterov, F. S. Nasredinov, S. A. Nemov, and P. P. Seregin, Fiz. Tekh. Poluprovodn. **31**, 227 (1997) [Semiconductors **31**, 181 (1997)].

Translated by James S. Wood

Investigation of MOVPE-grown GaN layers doped with As atoms

A. F. Tsatsul'nikov, B. Ya. Ber, A. P. Kartashova, Yu. A. Kudryavtsev, N. N. Ledentsov,
V. V. Lundin, M. V. Maksimov, A. V. Sakharov, A. S. Usikov, and Zh. I. Alfërov

A. F. Ioffe Physicotechnical Institute, Russian Academy of Sciences, 194021 St. Petersburg, Russia

A. Hoffmann

Technische Universität Berlin, D-10623 Berlin, Germany
(Submitted December 28, 1998; accepted for publication December 30, 1998)
Fiz. Tekh. Poluprovodn. **33**, 791–794 (July 1999)

Conditions are investigated for the injection of arsenic into gallium nitride layers grown by metal-organic vapor-phase epitaxy. It is shown that the deposition of GaAs on a GaN surface relieves stresses in the GaN layer. The high-temperature overgrowth of a thin GaAs layer by a GaN layer causes As atoms to diffuse into the GaN, produces a thick, homogeneously doped GaN:As region, and creates a bright band in the photoluminescence spectrum with a maximum at ~2.5 eV. © *1999 American Institute of Physics.* [S1063-7826(99)00707-3]

Considerable attention has recently been given to the fabrication of light-emitting devices that operate in the visible and ultraviolet regions of the spectrum. This interest is largely attributable to the sweeping potential of such devices for applications in color television and in memory units. The greatest progress was in the use of structures based on the system InGaN–GaN, which permits the radiation energy to be varied within the range $\hbar\omega = 1.96 - 3.5$ eV. This system has provided the basis for the construction of light-emitting diodes operating from the green to the UV region of the spectrum. However, the fabrication of green-emitting lasers requires a higher content of InN (more than 35 mole %) in the active zone of InGaN. But then the excessive mismatch of the lattice parameters with GaN creates difficulties in the growth of such layers, leads to deterioration of the structural and, hence, optical characteristics of the active zone of In-GaN, and results in degradation of the device characteristics. These obstacles necessitate the use of alternative methods for solving the problem of extending the optical range of GaN-based devices.

One way to solve the problem is by the monitoring and regulation of self-organization processes in constrained systems. For In-containing systems these effects produce local regions of elevated In content and can be used to achieve major modifications of their optical properties. The formation of InGaAs quantum dots with diameters ~100 Å, which are capable of shifting the photoluminescence line to a wavelength $\lambda \approx 1.3$ μm, has been demonstrated in a conventional InGaAs-AlGaAs system; the same shift has been impossible to achieve using InGaAs-based quantum wells.[1] Numerous studies of InGaN quantum wells have shown that their optical properties are governed by recombination processes in local regions of elevated In content.[2] For the system InAlN-GaN this kind of phase separation has made it possible to generate optical radiation in the red region of the spectrum.[3]

In addition to InGaN-GaN, the constrained GaAsN-GaN system has received attention in recent studies.[4] It is characterized by a greater mismatch of the lattice parameters

(~25% between GaAs and GaN) than in InGaN-GaN (~12% between InN and GaN). However, theoretical calculations show that the decrease in the width of the band gap with the introduction of GaAs (~150 meV for 1% GaAs) greatly exceeds the analogous value for InN (~25 meV for 1% InN). Consequently, even slight additives of GaAs can significantly lower the energy of the optical transition. It has also been shown that the introduction of As improves the transport and optical characteristics of GaN layers.[5]

Here we report an investigation of the injection of As into GaN epilayers grown by metal-organic vapor-phase epitaxy (MOVPE) (organometallic compound hydride epitaxy). We intend to show that the deposition of GaAs on the surface of a GaN layer and its subsequent removal lead to stress relief and partial relaxation of the GaN layer. The deposition of a thin GaAs layer between GaN layers results in the formation of local GaN:As regions due to the emergence of a new band in the photoluminescence spectra, its maximum occurring at an energy $\hbar\omega \approx 2.5$ eV.

The GaN:As samples were grown on (0001)-oriented sapphire α-Al$_2$O$_3$ substrates in a horizontal reactor with inductive heating and a reduced pressure of 200 mbar. The vapor carrier was hydrogen or argon, the source of the group III element was trimethyl gallium (TMG), and the nitrogen source was ammonia. Tertiary butylarsine (TBA) or a 10% mixture of arsine (AsH$_3$) with hydrogen provided the source of arsenic. The resulting structures were investigated by secondary ion mass spectroscopy (SIMS) and photoluminescence, which was excited by an He-Cd laser with a pump power density of 25 W/cm^2 and was controlled by a cooled photoelectric multiplier. The surface morphology and the thickness of the layers were investigated by means of a scanning electron microscope.

The MOVPE preparation of GaAsN solid solutions has the distinctive feature that the growth of GaAs and the growth of GaN take place under different conditions. Typical growth temperatures for GaAs are $T_s = 600 - 750$ °C for a ratio of group III to group V components in the vapor phase
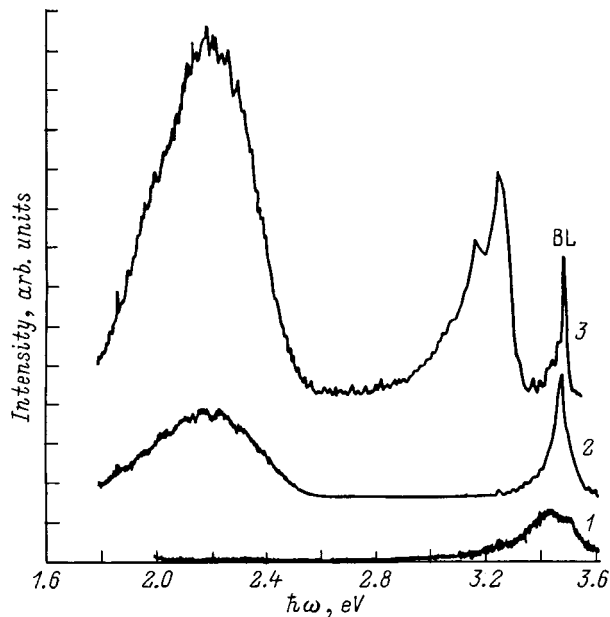
FIG. 1. Photoluminescence spectra of GaN layers grown in a TBA flux at various temperatures: (*1*) $T_s = 800\,°C$; (*2*) $840\,°C$; (*3*) $1040\,°C$. Measurement temperature $T = 77$ K.
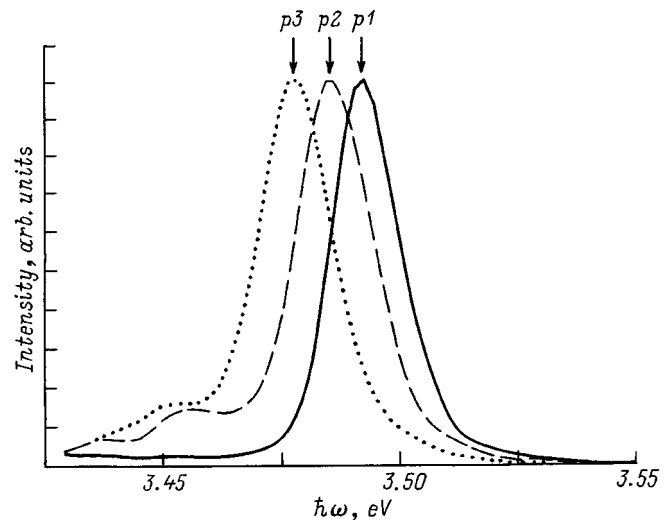

FIG. 2. Photoluminescence spectra of a GaN layer after etching of the GaAs layer from its surface. The spectra are recorded at different points of the sample surface with different effective thicknesses of the deposited GaAs. Measurement temperature $T = 77$ K.

equal to 30–100, as opposed to the analogous parameters for the preparation of high-quality GaN epilayers: $T_s = 1030 - 1080\,°C$ at a III-V ratio of 2000–5000 (Ref. 6). In the initial stage of our project, therefore, we began the investigation of the injection of As into GaN by growing GaN layers at various growth temperatures in a TBA flux of $(1.5 - 15) \times 10^{-4}$ mole/min. The procedure entailed, first, the growth of a virgin (not intentionally doped) GaN layer of thickness $2.5 - 3$ μm on a sapphire substrate[7] and then the additional injection of TBA into the reactor. Figure 1 shows the photoluminescence spectra of these samples. It is evident from the figure that lowering the temperature under the stated conditions does not significantly alter the edge photoluminescence intensity (BL), whereas the defect-induced blue line with a maximum at $\hbar\omega = 3.25$ eV vanishes from the photoluminescence spectrum. Consequently, the optical properties of the GaN layers do not suffer any appreciable degradation. On the other hand, the emergence of new photoluminescence lines due to the injection of As atoms is not observed. No changes were observed in the photoluminescence spectra of samples grown at lower TBA fluxes.

This result can be explained as follows. The growth of the GaAs layer (instead of a GaN + As layer) on a GaN layer with the injection of an ammonia flux into the reactor has shown that the growth rate of GaAs at identical growth temperatures ($T_s = 800\,°C$) and TMG fluxes is almost an order of magnitude higher than the growth rate of GaN. This means that the thermal decomposition of TBA produces a quantity of reactable arsenic or its compounds in the vapor phase far in excess of the quantity of reactable nitrogen generated by the decomposition of ammonia. Processes of interaction in the vapor phase between the components of group V elements involving TMG probably results in the formation

of stable polymer products, which lower the growth rate and obstruct the injection of As.

In the next stage of our investigations we used a 10% mixture of arsine with hydrogen as the arsenic source. The use of AsH_3 was conducive to more controlled growth of GaAs layers on GaN. Initially a GaAs layer of thickness ~ 0.6 μm was grown on a GaN surface. The GaAs layer had a polycrystalline structure owing to the large mismatch of the lattice parameters of GaAs and GaN. The thickness of the GaAs layer differed in different parts of the sample. After etching of the GaAs in an etchant $H_2SO_4 : H_2O_2 : H_2O = 5:1:1$ we investigated the photoluminescence of the GaN at different points of the structure surface (*p*1, *p*2, *p*3) characterized by different thicknesses of the initially deposited GaAs layer (Fig. 2). The effective thickness of the GaAs layer decreased from point *p*3 to point *p*1. Clearly, the deposition and subsequent etching of the GaAs significantly reduced the photoluminescence line on the long-wavelength side, the position of the *p*3 band essentially coinciding with the position of the free-exciton photoluminescence line in the unconstrained GaN. The total photoluminescence intensity scarcely changed in this case. Consequently, the deposition of GaAs leads to partial relaxation of the GaN epilayer. The effective thickness of the GaN relaxation layer is not smaller than the thickness at which the He-Cd laser beam is absorbed: $d \simeq 0.3$ μm.

Since the growth of GaN + As layers simultaneously in ammonia and arsine fluxes also failed to yield the expected results, we employed a different technique for the injection of As into GaN, based on the formation of thin GaAs layers in a GaN host. For this purpose we grew samples in which thin GaAs layers (30 nm and 60 nm) deposited on the GaN surface at $730\,°C$ were overgrown by a GaN layer of thickness ~ 50 nm at $1030\,°C$. It is important to note that at the indicated growth temperatures the GaN is thermally unstable in a hydrogen ambient without an ammonia flux.[8] The GaAs layer and the subsequent GaN layer were therefore grown in
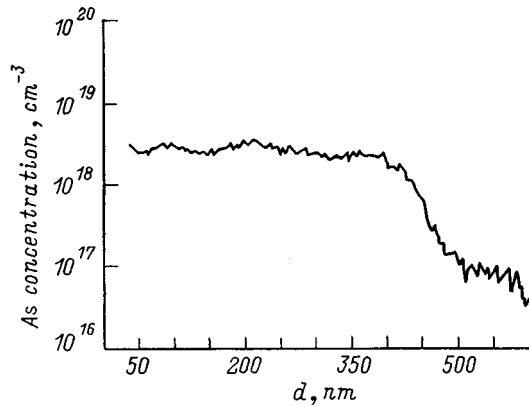
FIG. 3. SIMS profile of a structure with an intermediate GaAs layer of thickness 60 nm in GaN.
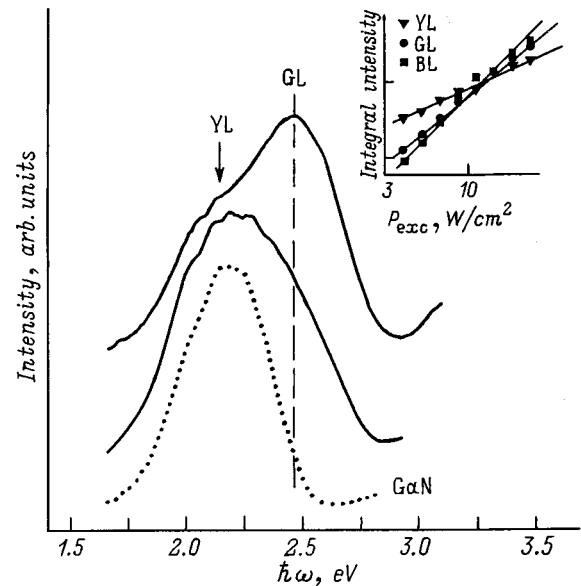

FIG. 4. Photoluminescence spectra of GaN layers with different thicknesses of the deposited GaAs layer. Inset: dependence of the total intensities of the lines YL, GL, and BL on the intensity of the exciting light beam P_{exc}. Measurement temperature $T = 77$ K.

an argon ambient. Figure 3 shows the SIMS profile of such a sample with a GaAs layer of thickness 60 nm. It is evident that a GaN:As layer of thickness ~400 nm with an average density of As atoms ~3×10^{18} cm^{-3} is formed instead of a thin GaAs layer in the given structure. We can therefore conclude that the diffusion of As atoms either during deposition of the GaAs layer or during high-temperature overgrowth resulted in the formation of a thick As-doped GaN layer. Figure 4 shows the photoluminescence spectra of the investigated structure in the interval $\hbar\omega = 1.5 - 3$ eV. The spectra of these structures acquire a new line (GL) with a maximum at ~2.45 eV (Ref. 9), whose intensity increases as the effective thickness of the deposited GaAs layer increases. It must be noted that this line does not occur in the photoluminescence spectra of samples grown at a low temperature (Fig. 1) and is therefore specifically attributable to the injection of As rather than to defects formed as a result of the low growth temperature. The dependence of the total GL intensity on the pump power density P_{exc} is described by the relation $I_{GL} \sim P_{exc}^{1.7}$ (see the inset in Fig. 4), which is typical for impurity-induced photoluminescense (line intensity YL $I_{YL} \sim P_{exc}$) and closely resembles the behavior of the photoluminescence edge (BL edge intensity, $I_{BL} \sim P_{exc}^2$). We can therefore assume that the GL is attributable to recombination processes in local GaN:As regions.

We have thus investigated the conditions for the injection of As into GaN layers during MOVPE growth. We have shown that the deposition of GaAs on a GaN surface reduces

stresses and leads to partial relaxation of the GaN surface layer. The subsequent overgrowth of the thin GaAs layer by a GaN layer at high temperature produces local GaN:As regions due to the emergence of a new band in the photoluminescence spectrum with a maximum at ~2.5 eV.

[1] D. L. Huffaker, G. Park, Z. Zou, O. B. Shchekin, and D. G. Deppe, Appl. Phys. Lett. **73**, 2564 (1998).

[2] Y. Narukawa, Y. Kawakami, M. Funato, S. Fujita, S. Fujita, and S. Nakamura, Appl. Phys. Lett. **70**, 981 (1997).

[3] S. Yamaguchi, M. Kariya, S. Nitta, T. Takeuchi, C. Wetzel, H. Amano, and I. Akasaki, Appl. Phys. Lett. **73**, 830 (1998).

[4] L. Bellaiche, S.-H. Wei, and A. Zunger, Appl. Phys. Lett. **70**, 3558 (1997).

[5] L. J. Guido, P. Mitev, M. Gherasimova, and B. Gaffey, Appl. Phys. Lett. **72**, 2005 (1998).

[6] R. D. Dupuis, J. Cryst. Growth **178**, 56 (1997).

[7] W. V. Lundin, A. S. Usikov, and U. I. Ushakov, M. V. Stepanov, B. V. Pushnyi, N. M. Shmidt, V. Tret'yakov, M. V. Maximov, and A. V. Sakharov, in *Seventh European Conference on Metal-Organic Vapour Phase Epitaxy and Related Growth Techniques, EW MOVPE VII, Workshop Booklet* (Berlin, 1997), F10.

[8] J. C. Zolper, M. H. Crawford, J. Howard, J. Ramer, and S. D. Hersee, Appl. Phys. Lett. **68**, 200 (1996).

[9] X. Li, S. Kim, E. E. Reuter, S. G. Bishop, and J. J. Coleman, Appl. Phys. Lett. **72**, 1990 (1998).

Translated by James S. Wood

SEMICONDUCTORS STRUCTURES, INTERFACES AND SURFACES

Photolectric effects in silicon switching structures utilizing rare-earth fluorides

V. A. Rozhkov*) and M. B. Shalimova

Samara State University, 443011 Samara, Russia

The photoelectric characteristics of silicon metal-insulator-semiconductor switching structures are investigated; cerium, dysprosium, and erbium fluorides are used for the insulator layer. It is shown that the photoelectric characteristics of the structures in the low-resistance state are similar to those of a metal-(tunneling insulator)-semiconductor structure; in particular, a mechanism of injection amplification of the photocurrent comes into play. © *1999 American Institute of Physics.* [S1063-7826(99)00807-8]

INTRODUCTION

The phenomenon of memory switching of the electrical conductivity, discovered comparatively recently[1–3] in structures with thin-film fluorides of rare-earth (RE) elements, opens new pathways to the design of various types of switches, reprogrammable memory elements, controls, and other functional devices. In structures utilizing RE fluorides this phenomenon is typified by a broad range of variation (as much as $10^6 - 10^7$-fold) of the resistance between the high-resistance and low-resistance states, fast switching times (fractions of a microsecond), low switching energies ($\sim 10^{-8}$ J), high radiation immunity, and a virtually unlimited number of switching cycles for the optimal choice of switching regime. The latter properties make it necessary to investigate the basic properties of the memory switching effect in these structures, along with the characteristics of the high-resistance and low-resistance states. Accordingly, in the present article we report a study of the special characteristics of photoelectric effects in silicon switching structures utilizing RE fluoride insulator layers.

OBJECTS AND PROCEDURE OF THE INVESTIGATIONS

Samples with a metal-insulator-semiconductor (MIS) structure were chosen for the experiments. Rare-earth fluoride insulator films of thickness $\sim 0.25 - 0.45$ μm were prepared by the thermal spraying of powdered CeF_3, DyF_3, and ErF_3 in vacuum. The substrates for the MIS structures were KÉF-5(111) *n*-type or KDB-4.5(100) *p*-type single-crystal silicon wafers.

The photoelectric characteristics of the silicon MIS structures with RE fluorides were investigated both in steady illumination and in illumination of the structures by monochromatic radiation pulses of various durations. The structures used for the measurements came with upper aluminum contacts having an area $A = 2.45 \times 10^{-3}$ cm^2. The structures were irradiated by an LGN-215 laser with a wavelength $\lambda = 0.63$ μm and a beam cross section of 2.54×10^{-2} cm^2. The intensity of the incident radiation was varied by means

of auxiliary light filters and had values $I = 7.6 \times 10^{16} - 4.8 \times 10^{18}$ kW/(cm$^2 \cdot s$). The source of the pulsed monochromatic radiation with a wavelength $\lambda = 0.93$ μm was an AL-106A gallium arsenide light-emitting diode. The radiation intensity from the AL-106A LED at the wavelength $\lambda = 0.93$ μm, determined by means of a calibrated LFD-2-A photodiode, was $I = 3 \times 10^{17}$ kW/(cm$^2 \cdot s$). A 40-W incandescent lamp with a tungsten filament was also used.

Figure 1 shows typical switching current-voltage (*I-V*) curves for the investigated MIS structure prepared on *n*-type silicon substrates. Investigations have shown that the MIS structures can exist in two stable states with significantly different resistances and *I-V* curves. The as-prepared samples
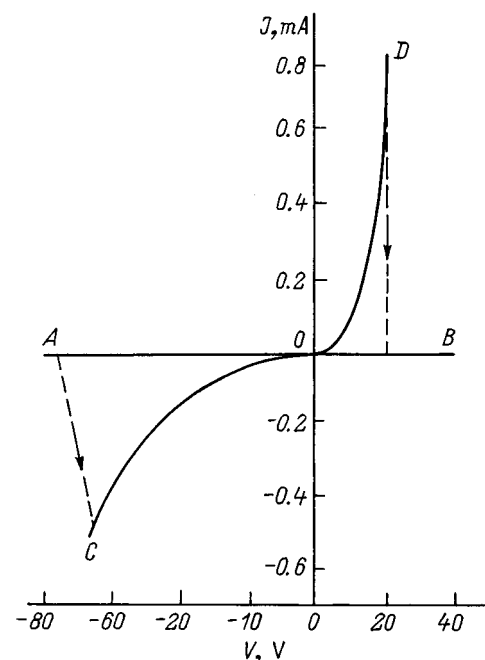

FIG. 1. Current-voltage characteristics of a silicon MIS structure utilizing a rare-earth fluoride element: (AOB) high-resistance state; (COD) low-resistance state.

are in a state with a high resistance of $(2-4)\times10^{11}\,\Omega$ (Fig. 1, line AOB) as long as the voltage, its polarity corresponding to the depletion of majority carriers from the surface of the semiconductor, does not exceed a threshold value $V_{th}=5-200\,V$ (depending on the thickness of the insulator and its degree of perfection). When the threshold voltage is exceeded, the resistance of the sample drops abruptly, switching it into a low-resistance state of $10^4-10^5\,\Omega$ (Fig. 1, branch COD). The structures are switched back to the original high-resistance state upon reversal of the polarity of the voltage, when the current through the sample attains a value of $100-600\,\mu A$. The reverse switching voltage for different samples now lies in the range $V_0=3-20\,V$. The structures exhibit reproducibility through multiple (more than 10^4) switchings from one state to the other and back again under both constant and pulsed voltages, both states persisting for a long time (more than 30 days) at room temperature with the voltage off.

RESULTS OF THE INVESTIGATIONS AND DISCUSSION

Investigations have shown[2] that the conducting channel formed in a RE fluoride film in the low-resistance state has a positive temperature coefficient of the resistance combined with the low resistivity typical of metals. We can assume on the basis of this condition that the conducting channel consists mainly of the metal phase. Estimates of the radius of the conducting channel from the leakage resistance of the silicon substrates give values of $1-5\,\mu m$.

An analysis of the experimental data shows that when silicon MIS structures utilizing a RE fluoride insulator switches to the low-resistance state, their electrical characteristics change considerably, exhibiting dependences similar to those typical of metal-tunnel insulator-semiconductor (MTIS) structures.[4,5] Figure 2 shows the reverse branches of the I-V curves of Al–CeF$_3$–n-Si structures in the low-resistance state, measured in steady illumination. The I-V curves of illuminated MIS structures with RE fluorides in the
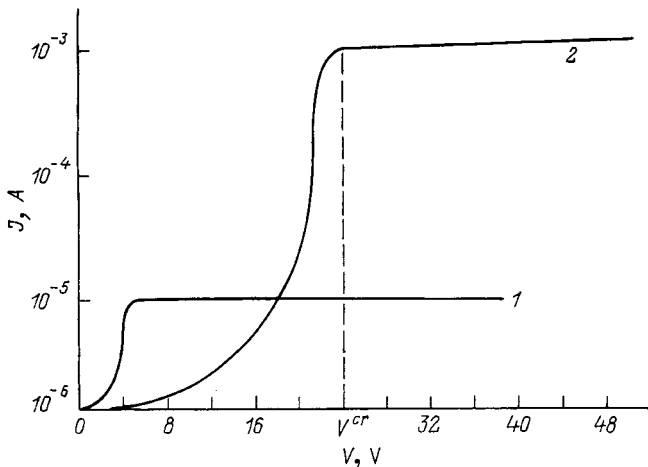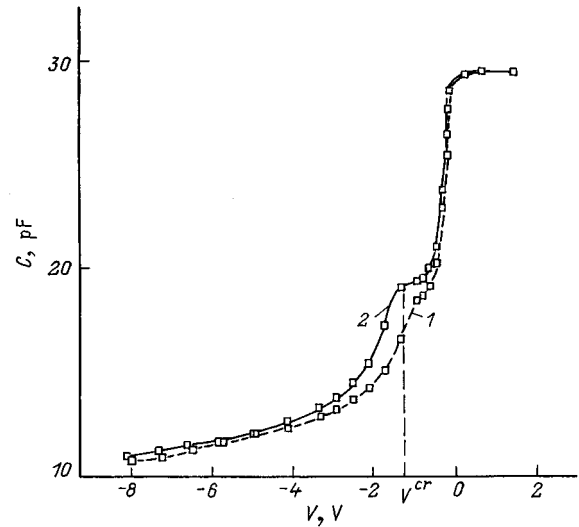

FIG. 3. Capacitance-voltage characteristic of an Al–CeF$_3$–p-Si MIS structure in the low-resistance state in darkness (1) and exposed to light (2).

low-resistance state have two distinctive segments. In the initial segment at $V<V^{cr}$ the current through the structure is limited by the leakage current through the insulator. At $V>V^{cr}$ the photocurrent goes to saturation and the applied voltage drops across the space charge region.

Figure 3 shows capacitance-voltage (C-V curves) of an Al–CeF$_3$–n-Si structure in the low-resistance state in darkness and in illumination by an incandescent lamp. The investigations show that the increase in the rate of generation of minority carriers in the illuminated structure leads to saturation of the surface density of minority carriers. In this case the transition of the C-V curve into the nonequilibrium depletion regime, when the silicon region contains a depletion layer whose thickness increases as the voltage on the structure is increased, takes place at higher reverse bias voltages ($V>V^{cr}$) than in darkness.

The general neutrality equation for an MTIS structure, taking into account the distribution of the voltage V applied to the structure, the voltage drops in the insulator (dielectric) V_d and in the semiconductor V_S, and the voltage across the load resistance V_L, can be written in the form (for an MIS structure with an n-type substrate) (Refs. 6 and 7)

$$V=\frac{kT}{q}y_S-V_L-\frac{qn_0L_D}{C_d}\left(\frac{p_S}{n_0}-y_S-1\right)^{1/2}\mp V_{FB},\qquad(1)$$

where V_{FB} is the flat-band potential, the plus sign corresponds to enriching initial band bending, $y_S=qV_S/kT$ is the dimensionless surface potential, C_d is the specific capacitance of the insulator, n_0 is the density of electrons in the bulk of the semiconductor, p_S is the surface density of holes, and $L_D=(\varepsilon_0\varepsilon_S kT/2q^2n_0)^{1/2}$ is the Debye shielding length.

An analysis shows[6,7] that for a certain reverse bias V^{cr} the surface density of minority carriers (holes) p_S in an MTIS structure saturates, and a further increase in the gate voltage does not increase the charge of the inversion layer. The saturation condition is written in the form[6,7]

FIG. 2. Current-voltage characteristics of an Al–CeF$_3$–Si structure in the low-resistance state, illuminated by a steady light source ($\lambda=0.63\ \mu m$). Luminous flux density: (1) 7.6×10^{16} kW/(cm$^2\cdot s$); (2) 2.5×10^{18} kW/(cm$^2\cdot s$).

$$V^{\mathrm{cr}}=\frac{kT}{q}y_S-\frac{qn_0L_D}{C_d}\left(\frac{4I^*}{\bar{D}_pV_pn_0}-y_S\right)^{1/2}-V_L\mp V_{FB},\quad(2)$$

where I^* is the light-generated flux of electron-hole pairs, V_p is the thermal velocity of holes, and $\bar{D}_p$ is the hole tunneling transmissivity.

Using the procedure described in Ref. 7, for the investigated structures we obtain the following values of the voltage drops on different regions of the structure at V^{cr}. The voltage drop across the depletion layer is

$$V_S=\frac{kT}{q}y_S\approx-0.6\,\mathrm{V};$$

the voltage drop across the insulator is

$$V_d=\frac{qn_0L_D}{C_d}\left(\frac{4I^*}{D_pV_pn_0}-y_S\right)^{1/2}\approx1.4-10.7\,\mathrm{V}.$$

The following quantities, consistent with the given experiment, are used for the estimates:

$$I=7.6\times10^{16}-4.8\times10^{18}\,\mathrm{kW/(cm^2\cdot s)},$$

$$I^*=8.4\times10^{14}-5.3\times10^{16}\,\mathrm{cm^{-2}s^{-1}};$$

$$\bar{D}_p=10^{-9};\quad C_d=2\times10^{-8}\,\mathrm{F/cm^2};\quad V_p=10^7\,\mathrm{cm/s};$$

$$n_0=9\times10^{14}\,\mathrm{cm^{-3}};\quad L_D=9.68\times10^{-6}\,\mathrm{cm}.$$

The specific capacitance of the insulator C_d in the given structures is approximately two orders of magnitude smaller than in MTIS structures with identical thickness of the tunneling-thin insulator over the entire area of the structure. This characteristic is associated with the local nature of the variations occurring in the insulator layer beneath the upper sprayed-on contact after switching of the MIS structure into the low-resistance state. The thickness of the tunneling-thin insulator layer d was estimated from the difference in the capacitances of the MIS structure in the high-resistance and low-resistance states equal to $1-15$ pF. Experimental studies have shown that the tunneling-thin insulator layer of thickness $d=10-40$ Å is formed only in the region of a conducting channel of small radius $\sim1-5$ μm at the interface between the semiconductor and the material of the conducting channel; the rest of the insulator beneath the contact remains unchanged and preserves the original thickness $\sim0.25-0.45$ μm.

The experimentally determined value of V^{cr} is $0.5-37$ V, where now the voltage drop across the load resistance $R_L=2-10\,\mathrm{k}\Omega$ is equal to $V_L=0.1-20$ V. It follows from Eq. (2) that the absolute value of V^{cr} increases with intensity of the incident radiation I^*, as indeed we have observed experimentally (Fig. 2).

Under the experimental conditions, therefore, we encounter the situation where a substantial part of the voltage applied to the MTIS structure falls across the insulator. A specific energy band diagram of the MIS structure (with a tunneling-thin insulator) can be achieved in this case, with internal amplification of the photocurrent. The investigated case is characterized by an increase in the current of electrons tunneling from the metal into the semiconductor as the

reverse bias and the illumination intensity are increased (for MTIS structures with an n-type substrate). The photocurrent of majority carriers becomes commensurate with or greater than the current of minority carriers, signifying an amplification regime.

Data obtained for various illumination intensities from measurements of the saturation photocurrent give a maximum current-power sensitivity ~0.7 A/W at a wavelength of 0.63 μm. The parameters of the investigated structures are nonoptimal in this case: Part of the surface of the structure is covered by the measurement probe, and approximately 40–90% of the radiation incident on the structure is reflected by the metal electrode. For photoelectric devices with optimal parameters and zero photocurrent amplification the maximum current-power sensitivity for the given wavelength is 0.4 A/W. This result indicates amplification of the photocurrent in the investigated structures.

We have investigated the form of the photoresponse kinetics of MIS structures utilizing RE fluorides in the low-resistance stage with illumination of the structures by monochromatic radiation pulses of various durations. We have established that the kinetic characteristics of the photocurrent $J_{\mathrm{ph}}(t)$ with a reverse bias $V=-32$ V applied to the structure are well approximated by hyperbolic functions of the form

$$J_{\mathrm{ph}}(t)=qI^*M_{\mathrm{ph}}A\begin{cases}1-\dfrac{1}{(1+t/\tau_d)^2},\\[2mm]\dfrac{1}{(1+t/\tau_d)^2},\end{cases}\quad(3)$$

where the first equation corresponds to illumination being turned on at the time $t=0$, the second equation corresponds to its being turned off at $t=0$, $M_{\mathrm{ph}}=(J_n+J_p)/J_p$ is the gain of the photocurrent for structures with an n-type substrate, J_n is the photocurrent of majority carriers (electrons), J_p is the photocurrent of minority carriers (holes), and τ_d is a characteristic relaxation time, which is given by the expression

$$\tau_d=\frac{2L_D(n_0)^{1/2}}{[S_{pe}^0\exp(y_S^0)I^*]^{1/2}}.\quad(4)$$

Here

$$S_{pe}=\left(\frac{1}{4}V_p\bar{D}_p\right)\exp(-y_S)$$

is the effective rate of emission of holes from the semiconductor into the metal; the superscript 0 corresponds to nonillumination at the initial time.

We know[8,9] that the nature of the photoresponse kinetics of MTIS structures can differ. If the rate of tunneling transport of charge carriers through the insulator is greater than their recombination rate, the factors governing the photoresponse time in the structure are the same as in $p-n$ junctions. In structures where the photoresponse time is governed by the accumulation time of minority carriers in the surface potential well, amplification of the photocurrent, which is detected from the specific form of the photoresponse kinetics and a rise in the photocurrent, can be observed. In the latter case the relaxation time decreases as the illumination inten-
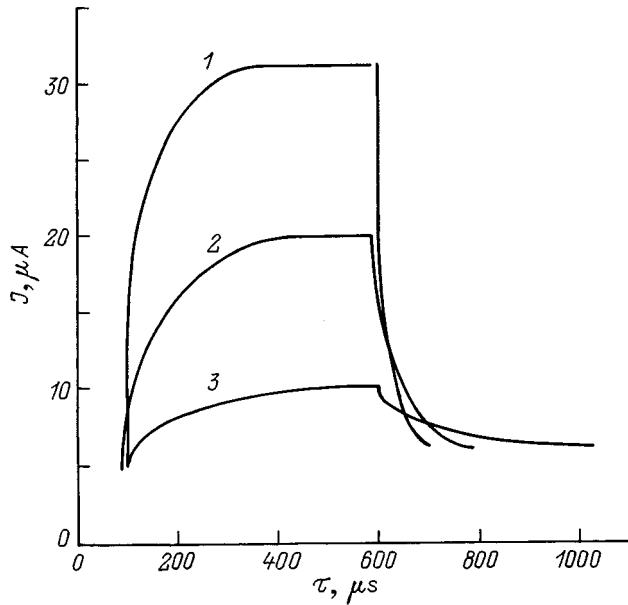
FIG. 4. Oscillograms of the photoresponse of an Al–DyF$_3$–p-Si MIS structure in the low-resistance state for various radiation intensities at the wavelength $\lambda = 0.93$ μm: (*1*) I_1; (*2*) I_2; (*3*) I_3; $I_1 > I_2 > I_3$.

FIG. 5. Photoresponse kinetics of an Al–CeF$_3$–p-Si MIS structure in the low-resistance state, illuminated by radiation pulses of different durations: (a) $\tau = 700$ μs; (b) $\tau = 25$ μs. The arrows indicate the values of the photocurrents: (a) $J_{\mathrm{ph}}(\infty)$; (b) $J_{\mathrm{ph}}(0)$.

sity is increased, corroborating the photoresponse oscillograms shown in Fig. 4 for MIS structures with RE fluorides in the low-resistance state.

A previous analysis[9] of relaxation effects in MTIS structures shows that the total current density through an MTIS structure with an n-type substrate depends on the sum of the displacement current and the ohmic current density of minority carriers (holes):

$$J_{\mathrm{ph}}(t) = \varepsilon_0 \varepsilon_S \frac{dE_S}{dt} + q S_{pe} \Delta p^*(t), \qquad (5)$$

where E_S is the electric field on the surface of the semiconductor, and Δp^* is the light-induced increment of the surface nonequilibrium hole density. When the photocurrent is amplified, the presence of a current of majority carriers must be taken into account in Eq. (5); for MTIS structures with an n-Si substrate the current in question is electronic. The current density is then described by the relation

$$J_{\mathrm{ph}}(t) = \varepsilon_0 \varepsilon_S \frac{dE_S}{dt} + q M_{\mathrm{ph}} S_{pe} \Delta p^*(t). \qquad (6)$$

For large photocurrent gains $M_{\mathrm{ph}} \gg 1$ the first term on the right-hand side of Eq. (6) can be disregarded, whereupon the equation of continuity for the flux of minority carriers can be taken into account to obtain Eq. (3), which describes the kinetic characteristics of the investigated MIS structures in the low-resistance state. It is assumed here that inversion of the conductivity takes place, and that the minority carriers are nondegenerate on the surface of the semiconductor.[9] The experimental photoresponse characteristics are therefore in agreement with the theoretical relations.

An investigation of the kinetic photoresponse characteristics shows that capacitive current segments associated with the switching off and on of illumination are discernible
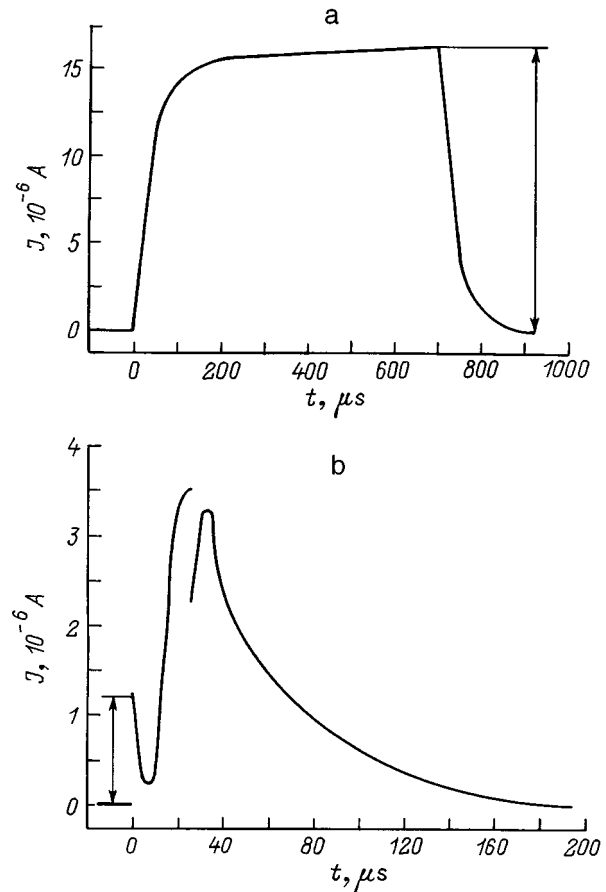
on the photoresponse oscillograms. Figure 5a shows a total oscillogram of the photocurrent for an Al–CeF$_3$–n-Si structure in the low-resistance state illuminated by a rectangular light pulse with a constant voltage $V = -32$ V applied to the structure. Figure 5b shows the same characteristic for an illuminating pulse of shorter duration, providing a means for examining in closer detail the initial and final current spikes of a purely capacitive character. This current is described by the expression $J_{\mathrm{ph}}(0) = qAI^* = 1.3$ μA and is equal to the minority carrier photogeneration current. It stabilizes in a time much shorter than τ_d and is determined by the larger of the quantities: the carrier transit time through the space charge region or the product RC (where R is the load resistance, and C is the capacitance of the structure and the connecting wires). The saturation photocurrent $J_{\mathrm{ph}}(\infty)$ is greater than $J_{\mathrm{ph}}(0)$, implying the onset of the photocurrent amplification regime. The possibility of separating the majority and minority carrier currents in time enables us to calculate directly from the photocurrent kinetics the gain of the photocurrent in the structure as the ratio of the total amplitude of the photoresponse $J_{\mathrm{ph}}(\infty)$ representing the sum of the majority and minority carrier currents to the amplitude of the initial segment of the photocurrent $J_{\mathrm{ph}}(0)$. For the characteristic shown in Fig. 5 the gain is $M_{\mathrm{ph}} = 13$. The maximum photo-

current gain is $M_{ph}=49$ and $M_{ph}=34$ for structures utilizing p-type and n-type silicon, respectively.

At an illumination intensity $I=3\times10^{17}\,\mathrm{kW/(cm^2 \cdot s)}$ the maximum current-power sensitivity is 0.5 A/W at a wavelength of 0.93 μm. The allowance for light losses in reflection from the surface of the investigated structure for the quantum efficiency in silicon $\eta\approx0.3$ gives a value of the photocurrent of electron-hole pairs generated by light per unit time $I^*=3.3\times10^{15}\,\mathrm{cm^{-2}\cdot s^{-1}}$. Accordingly, the capacitative current is $J_{ph}(0)=qAI^*=1.3\times10^{-6}$ A, which agrees with the experimental results. It must be noted that Eq. (3) describes only the ohmic through current, which is equal to zero when the illumination is turned on at the initial time. The relaxation time can be determined from the photoresponse kinetics of silicon MIS structures utilizing RE fluorides in the low-resistance state: $\tau_{rel}=50-450\,\mu$s for p-type and $\tau_{rel}=30-180\,\mu$s for n-type Si samples. Since

$$S^0_{pe}\exp(y^0_S)=\frac{1}{4}\bar{D}_p V_p , \qquad (7)$$

we obtain the following relation by substituting Eq. (7) into (4):

$$\bar{D}_p=\frac{16L^2_D n_0}{\tau^2_d V_p I^*}. \qquad (8)$$

Equation (8) can be used to determine the hole tunneling transmissivity $\bar{D}_p$ for a structure with an n-type substrate and the electron tunneling transmissivity $\bar{D}_n$ for a structure with a p-type substrate. The tunneling transmissivities determined in this way lie in the intervals $\bar{D}_n=2.7\times10^{-11}-2.2\times10^{-8}$ and $\bar{D}_p=1.7\times10^{-10}-4.7\times10^{-8}$. According to Eq. (8), the relaxation time increases as the tunneling transmissivity for minority carriers decreases.

In the situation investigated here the conducting channel formed in the insulator film in the low-resistance state is simultaneously the upper current input contact to the MTIS structure and influences its photoelectric characteristics. As mentioned previously,[10] the replacement of the metal electrode in an MTIS structure by a highly doped semiconductor produces a semiconductor-tunneling insulator-semiconductor (STIS) structure. The amplification effect can now be achieved only in isotypical STIS structures, because the tunneling current of majority carriers is obstructed in anisotypical STIS structures. Since photocurrent amplification in the investigated MIS structures in the low-resistance state occurs on structures with both p-type and n-type substrates, it is justified to assume that the material of the conducting channel has a metallic nature.

The reported investigations thus demonstrate the feasibility of using silicon MIS structures with RE fluorides as electrical switches and photodetectors with internal amplification of the photocurrent.

*)E-mail: rozhkov@ssu.samara, ru

[1] V. A. Rozhkov and M. B. Shalimova, Pis'ma Zh. Tekh. Fiz. **18**(5), 74 (1992) [Sov. Tech. Phys. Lett. **18**, 157 (1992)].

[2] V. A. Rozhkov and M. B. Shalimova, Fiz. Tekh. Poluprovodn. **27**, 438 (1993) [Semiconductors **27**, 245 (1993)].

[3] V. A. Rozhkov and N. N. Romanenko, Pis'ma Zh. Tekh. Fiz. **19**(22), 6 (1993) [Tech. Phys. Lett. **19**, 704 (1993)].

[4] V. A. Rozhkov and M. B. Shalimova, Pis'ma Zh. Tekh. Fiz. **24**(16), 92 (1998) [Tech. Phys. Lett. **24**, 663 (1998)].

[5] V. A. Rozhkov and M. B. Shalimova, Fiz. Tekh. Poluprovodn. **32**, 1349 (1998) [Semiconductors **32**, 1201 (1998)].

[6] A. Ya. Vul', S. V. Kozyrev, and V. I. Fedorov, Fiz. Tekh. Poluprovodn. **15**, 142 (1981) [Sov. Phys. Semicond. **15**, 83 (1981)].

[7] A. Ya. Vul', V. I. Fedorov, Yu. F. Biryulin, Yu. S. Zinchik, S. V. Kozyrev, I. I. Saĭdashov, and K. V. Sanin, Fiz. Tekh. Poluprovodn. **15**, 525 (1980) [Sov. Phys. Semicond. **15**, 297 (1980)].

[8] A. Ya. Vul', A. T. Dideĭkin, and S. V. Kozyrev, in *Photodetectors and Phototransducers* [in Russian], Nauka, Leningrad (1986), p. 105.

[9] A. Ya. Vul', A. T. Dideĭkin, Yu. S. Zinchik, K. V. Sanin, and A. V. Sachenko, Fiz. Tekh. Poluprovodn. **17**, 1471 (1983) [Sov. Phys. Semicond. **17**, 933 (1983)].

[10] A. Ya. Vul' and A. V. Sachenko, Fiz. Tekh. Poluprovodn. **17**, 1361 (1983) [Sov. Phys. Semicond. **17**, 865 (1983)].

Translated by James S. Wood

Fabrication and properties of In$_2$O$_3$/CdS/CuInSe$_2$ heterostructures

V. Yu. Rud'*)

St. Petersburg State Technical University, 195251 St. Petersburg, Russia

Yu. V. Rud'

A. F. Ioffe Physicotechnical Institute, Russian Academy of Sciences, 194021 St. Petersburg, Russia
(Submitted December 21, 1998; accepted for publication December 23, 1998)
Fiz. Tekh. Poluprovodn. **33**, 801–804 (July 1999)

Heterostructures are prepared by the vacuum thermal evaporation of CdS⟨In⟩ onto heated
p-CuInSe$_2$ substrates. An In$_2$O$_3$ layer is deposited on the wide-gap component of each structure
by magnetron sputtering. The photosensitivity of the heterostructures in ambient light and
in linearly polarized radiation is investigated. The photosensitivity of higher-quality structures
attains 80 mA/W at $T = 300$ K. The heterostructures exhibit induced photopleochroism,
and the laws governing its angular and spectral dependences are discussed. It is concluded that
the prepared heterostructures have possible applications as narrowly selective
photoanalyzers of linearly polarized radiation.   © *1999 American Institute of Physics.*
[S1063-7826(99)00907-2]

Ternary A$^{\mathrm{I}}$B$^{\mathrm{III}}$C$_2^{\mathrm{VI}}$ semiconductors with a chalcopyrite lattice are finding ever-increasing applications in designs of various types of high-efficiency photoconversion devices.[1–3] A CdS/CuInSe$_2$ barrier has already demonstrated the capability of achieving 18% solar cell efficiency.[4] In this paper we give the results of first-time investigations of the polarization photosensitivity of such heterostructures fabricated with an In$_2$O$_3$ antireflection coating.

Polycrystalline CuInSe$_2$ ingots prepared by direct fusion of the 99.999 wt. % pure raw elements were used to build the heterostructures. The synthesis operation took place in evacuated quartz cells, and an electrically homogeneous substance with a free-hole density of approximately 2 $\times 10^{16}$ cm^{-3} and a Hall mobility of 25 cm^2/(V·s) at $T = 300$ K was obtained by dosing the composition with excess selenium. The unit cell parameters of the grown crystals matched the established values for CuInSe$_2$ (Ref. 4).

The synthesized dense CuInSe$_2$ ingots (up to 10 cm in length and up to 12 mm in diameter) were cut into disks, whose surfaces were polished mechanically, then chemically, and were carefully washed and dried. Cadmium sulfide layers were deposited by thermal spraying in vacuum from a powdered mixture of CdS and InS in suitable proportion. The layers were deposited on heated (400−450 °C) CuInSe$_2$ substrates. This technique produced CdS layers with free-electron densities from 10^{18} cm^{-3} to 10^{19} cm^{-3} at thicknesses of 3−4 μm. The attained doping level of the layers involved the dissolution of indium in the CdS. Layers of In$_2$O$_3$ approximately 1 μm thick were deposited on the surface of the CdS by the magnetron sputtering of a pure indium target in an oxygen-containing atmosphere. A gold finger array was then deposited on the In$_2$O$_3$ surface by vacuum evaporation and a solid gold layer of thickness up to 2 μm was deposited on the back surface of the disks. The active area of the resulting heterostructures attained 1−1.2 cm^2.

Figure 1 shows a typical steady-state current-voltage

(I–V) characteristic of one of the finished heterostructures; the direction of the through current always corresponds to positive polarity of the external bias on the p-CuInSe$_2$. The forward branch of the I–V characteristic at $U > 1$ V obeys the equation

$$I = (U - U_0)/R_0, \tag{1}$$

where R_0 is the residual resistance, and U_0 is the cutoff voltage. For our heterostructures we have $R_0 = 200 - 500$ Ω and $U_0 = 0.8$ V at $T = 300$ K. The reverse current of the heterostructures increases directly as the voltage up to 1 V, and then soft breakdown sets in at $U > 1$ V.

The illumination of a heterostructure from the In$_2$O$_3$ side induces the photovoltaic effect, positive polarity of the photovoltage corresponding to p-CuInSe$_2$, consistent with the direction of rectification. The voltage photosensitivity of superior heterostructures attains 10 V/W, and the current photosensitivity attains 80 mA/W at $T = 300$ K.

Figure 2 shows typical spectral curves of the relative quantum efficiency of photoconversion η for selected heterostructures in ambient light at $T = 300$ K. The long-wavelength edge of the photosensitivity for all the heterostructures is exponential and corresponds to a steep slope $s = \partial(\ln \eta)/\partial(\hbar\omega)$, which varies in the interval $60 - 120$ eV^{-1} for our heterostructures, corresponding to the character of meson transitions in CuInSe$_2$ (Ref. 5). The energy position of the long-wavelength edge of the photosensitivity η for the investigated structure lies within the neighborhood of the band gap E_G of CuInSe$_2$ and can be identified with direct meson transitions in this semiconductor.[6] However, the spectral profile of the short-wavelength decay of the photosensitivity ($\hbar\omega > E_G$) in our heterostructures differs considerably (Fig. 2, curves *1–4*), producing variations in the width (FWHM) $\delta_{1/2}$ of the spectral bands of η from 20 meV to 400 meV in different heterostructures. For heterostructures with the broadest-band photosensitivity spectrum (Fig. 2,
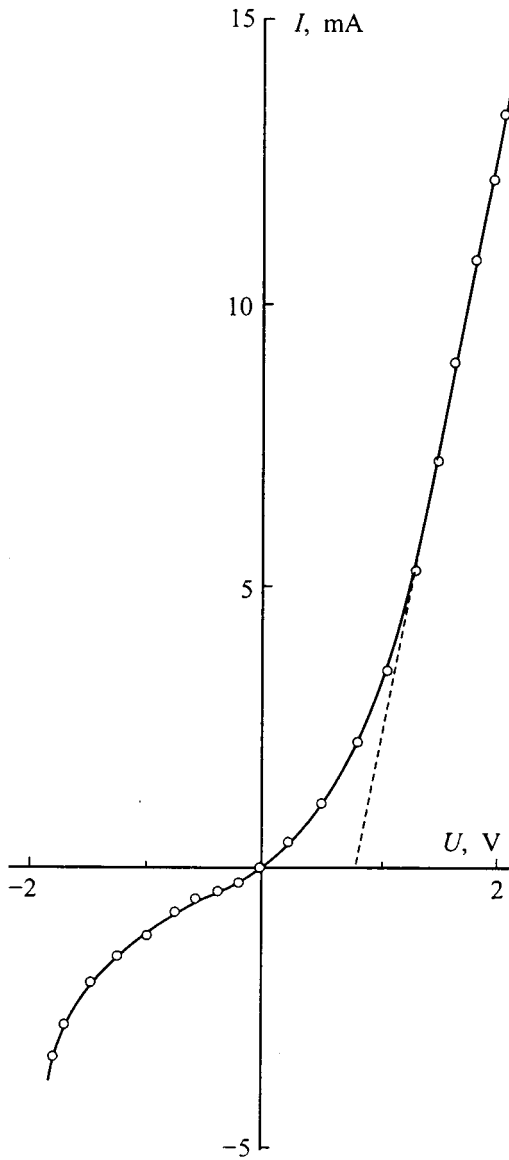
FIG. 1. Steady-state I–V characteristic of an In_2O_3 /CdS/CuInSe$_2$ hetero-structure at $T=300$ K. Positive polarity of the external bias corresponds to CuInSe$_2$.

FIG. 2. Spectral curves of the relative quantum efficiency of photoconversion of In_2O_3/CdS/CuInSe$_2$ heterostructures at $T=300$ K. Samples: (*1*) No. 6; (*2*) No. 1; (*3*) No. 7; (*4*) No. 10-1. Illumination by unpolarized radiation from the In_2O_3 side. Density of electrons in the CdS layers at $T=300$ K: (*1*) $n=2\times10^{-19}$ cm^{-3}; (*2*) 0.8×10^{-19} cm^{-3}; (*3*) 0.5×10^{-19} cm^{-3}; (*4*) 0.15×10^{-19} cm^{-3}.

curve *4*) the energy position of the absolute maximum $\hbar\omega_m$ coincides with the value of E_G for CuInSe$_2$ (Ref. 4).

As the short-wavelength decay of η intensifies and $\delta_{1/2}$ decreases accordingly, the absolute photosensitivity maximum shifts toward longer wavelengths. We notice that once $\hbar\omega_m$ becomes smaller than the value of E_G for CuInSe$_2$, the short-wavelength decay of η becomes practically exponential up to photon energies close to E_G (Fig. 2, curves *1–3*). Bearing in mind that the geometrical parameters of the wide-gap components in the investigated heterostructures are similar, we have a basis for linking the steep short-wavelength decay of η to predominant localization of the active zone of the heterostructure in the CuInSe$_2$ as a result of differences in the doping levels of the substrates and the CdS⟨In⟩. The short-wavelength decay of the photosensitivity for the η spectra in Fig. 2 was found to decrease with decreasing density of electrons in the CdS⟨In⟩ layers.
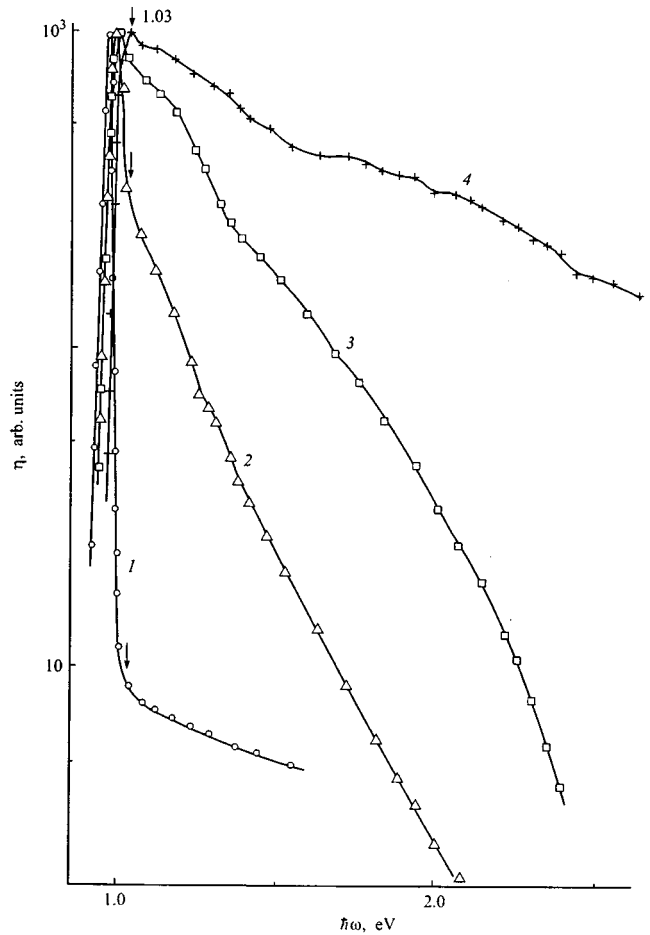
When a heterostructure is illuminated by linearly polarized radiation along the normal to the frontal plane of the In_2O_3 (angle of incidence $\Theta=0°$), the photosensitivity of all the synthesized heterostructures is independent of the position of the electric field vector of the light wave relative to the plane of incidence of the radiation over the entire range of photosensitivity (Fig. 3). This fact is dictated by the poly-crystalline character of the substrates and the n-CdS layers, which washes out the natural photopleochroism of the semiconductors.[5] Under off-normal conditions, $\Theta>0°$, a difference occurs in the photocurrents for the p and s polarizations, $i^p>i^s$ (Fig. 3, curves *1, 1'* and *2, 2'*). As a result, the induced photopleochroism

$$P_I=(i^P-i^S)/(i^P+i^S) \qquad (2)$$

acquires a nonzero value over the entire photosensitivity range. The dependence of P_I on the angle of incidence Θ in the investigated heterostructures is characterized by a square law $P_I\sim\Theta^2$ over the entire photosensitivity range (Fig. 3, curves *3* and *4*), which is consistent with Ref. 7 and permits P_I to be smoothly controlled by varying Θ.
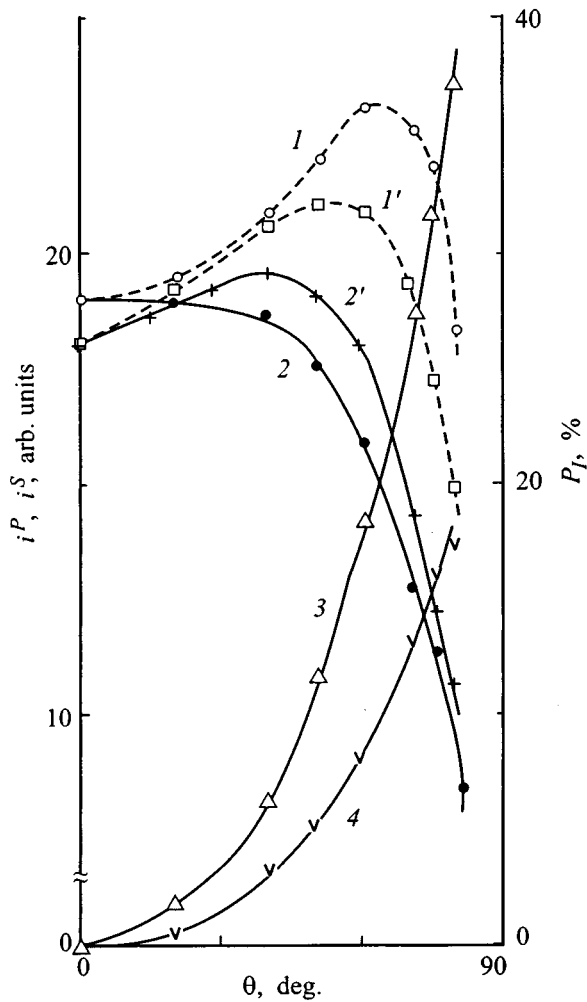
FIG. 3. Dependence of the photocurrents i^p (*1, 1'*) and i^s (*2, 2'*) and the induced photopleochroism (*3, 4*) on the angle of incidence of linearly polarized radiation for $In_2O_3/CdS/CuInSe_2$ heterostructures at $T = 300$ K. Sample No. 7, wavelengths: (*1, 2, 3*) $\lambda = 1.160$ μm (*1', 2', 4*) $\lambda = 0.994$ μm.

FIG. 4. Spectral curves of the induced photopleochroism of $In_2O_3/[1]CdS/[1]CuInSe_2$ heterostructures at $T = 300$ K, $\Theta = 75°$. Samples: (*1*) No. 7; (*2*) No. 3; (*3*) No. 10-1.

Figure 4 shows typical spectral curves of the induced photopleochroism for several heterostructures. It follows from this figure that the induced photopleochroism of such structures can exhibit oscillations or remain constant. The presence of oscillations and variations of P_I among the investigated heterostructures having the same air/In_2O_3 interface, across which radiation enters into the active zone of the heterostructure, comes into conflict with the analysis in Ref. 7. An estimate of the induced photopleochroism on the basis of Ref. 7 and the refractive index $n = 2.14$ for In_2O_3 (Ref. 8) in such structures yields a value of 36–38% ($\Theta = 75°$). The experimental values of P_I come close to this limit only in the long-wavelength region and only for certain representatives of our structures (Fig. 4). Similar features have been observed previously in other types of heterostructures and attributed to interference effects.[3,9–12] The occurrence of photopleochroism oscillations for the heterostructures in the present study is most likely associated with the interference of radiation in the In_2O_3 layers. The differences in the amplitudes of the oscillations and the energy positions of the extrema of P_I (Fig. 4) in this case are indicative of oscilla-
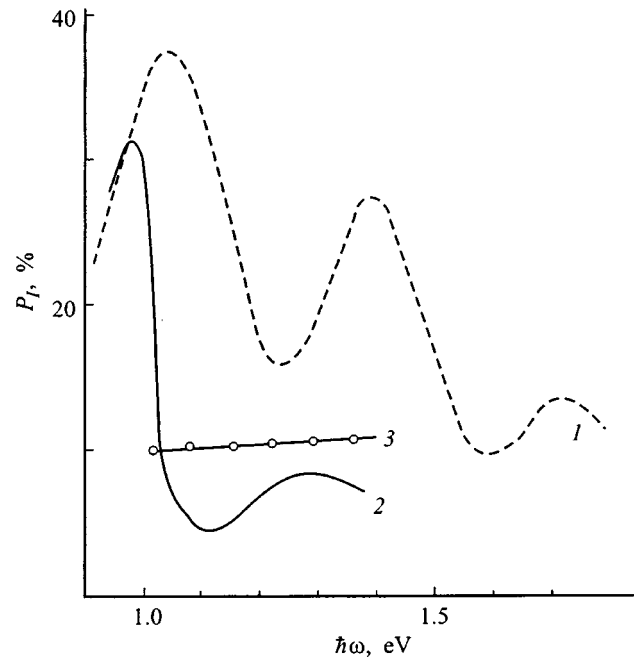
tions of the parameters of the transmission-enhancing (antireflection) layers in such heterostructures.

It is important to emphasize that only in the vicinity of energies corresponding to maxima of P_I are the angular dependences of the photocurrents qualitatively consistent with the results of analysis of the transmission of a light wave across an interface between two media on the basis of the Fresnel equations.[13,14] In this case, as the angle Θ increases, the photocurrent i^p increases at first, passes through a maximum in the vicinity of the pseudo-Brewster angle, and only then does it decrease, where i^s decreases monotonically as the angle of incidence increases (Fig. 3, curves *1* and *1'*). The attendant increase in i^p characterizes In_2O_3 layers as reasonably perfect and indicates a reduction of losses in reflection of the *p* wave. The observed differences in the angular dependences of the photocurrents have the effect that their polarization difference $\Delta i = i^p - i^s$ and, hence, the coefficient P_I itself reach their maximum values.

With an increase in the distance of the incident photon energy from the point corresponding to the maximum of the P_I spectra (Fig. 4, curves *1* and *2*) the angular dependence of i^s exhibits a fundamental departure from the position of i^s predicted on the basis of the Fresnel equations (Fig. 3, curve *2*). The differences are greatest in the vicinity of the energy of the minimum in the P_I spectrum and lie in the fact that the photocurrent i^s, coming into closest approach to i^p, exhibits an angular dependence with a maximum, similar to i^p. The emergence of the P_I minima indicates a reduction of reflection losses not only for the *p* wave, but also for the *s* wave. This merging of i^p and i^s (Fig. 3, curves *2* and *2'*) naturally causes the induced photopleochroism, like Δi, to attain a minimum.

For heterostructures with an essentially constant value of P_I in their photosensitivity range (Fig. 4, curve *3*) the angular dependences of the photocurrents i^p and i^s are the same as in the vicinity of the energy of the P_I minimum for the case discussed above. This means that the antireflection conditions in such heterostructures, in contrast with the structures discussed above, can be satisfied over a broad range of the spectrum.

In closing, we note that the maximum azimuthal photosensitivity in the prepared structures attains $60 \, \text{mA}/(\text{W} \cdot \text{deg})$ at $T = 300$ K, which is an order of magnitude higher than without the antireflection coating.[15] Similarly, the deposition of an antireflection coating for our heterostructures helps to achieve a narrowly selective photodetection regime ($\delta_{1/2} = 20 - 40$ meV), where the width of the band and its energy position are controlled by the parameters of the heterostructure. It is also important to note the potential application of polarization photoelectric spectroscopy for diagnostics of the prepared heterostructures and, accordingly, selection of the required technological regimes for their fabrication.

*⁾E-mail: rudvas@uniys.hop.stu.neva.ru

[1] A. M. Gabor, J. R. Tuttle, D. S. Albin, M. A. Contreras, R. Noufi, and A. M. Herman, Appl. Phys. Lett. **65**, 198 (1994).
[2] H. W. Schock, Appl. Surf. Sci. **92**, 606 (1996).
[3] V. Yu. Rud', Yu. V. Rud', T. Walter, and H. W. Schock, Inst. Phys. Ser. No. 152: in *Proceedings of the 11th International Conference on Ternary and Multinary Compounds, ICTMS-11*, Univ. of Salford, Sept. 8–12, 1997, edited by R. D. Tomlinson *et al. (IOP Publ. Ltd., 1998), p. 971.*
[4] L. Stolt, J. Hedström, J. Kessler, M. Ruckh, K.-O. Velthaus, and H. W. Schock, Appl. Phys. Lett. **62**, 597 (1993).
[5] J. L. Shay and J. H. Wernick, *Ternary Chalcopyrite Semiconductors: Growth, Electronic Properties, and Applications* (Pergamon Press, Oxford-New York, 1975).
[6] F. P. Kesamanly, V. Yu. Rud', and Yu. V. Rud', Fiz. Tekh. Poluprovodn. **30**, 1921 (1996) [Semiconductors **30**, 1001 (1996)].
[7] G. A. Medvedkin and Yu. V. Rud', Phys. Status Solidi A **67**, 333 (1981).
[8] *Current topics in Materials Science*, edited by E. Kaldis (North-Holland, Amsterdam, 1980), p. 76.
[9] V. Rud', Yu. Rud', T. Walter, and H. W. Schock, in *Abstracts of the Fifth International Conference ''POLYSE'98, Polycrystalline Semiconductors — Bulk Materials, Thin Films, and Devices''* (Schwäbisch Gmünd, Germany, 1998), p. 37.
[10] V. M. Botnaryuk, L. V. Gorchak, S. D. Raevskiĭ, V. Yu. Rud', Yu. V. Rud', and D. A. Shcherban', Zh. Tekh. Fiz. **68**(3), 72 (1998) [Tech. Phys. **43**, 546 (1998)].
[11] V. M. Botnaryuk, V. V. Bel'kov, Yu. V. Zhilyaev, S. D. Raevskiĭ, V. Yu. Rud', Yu. V. Rud', and L. M. Fedorov, Fiz. Tekh. Poluprovodn. **32**, 1206 (1998) [Semiconductors **32**, 1077 (1998)].
[12] V. Yu. Rud', in *Proceedings of the Third St. Petersburg Assembly of Young Scientists and Specialists* (St. Petersburg, 1998), p. 76.
[13] G. S. Landsberg, *Optics* [in Russian], Vysshaya Shkola, Moscow, 1976.
[14] I. S. Gorban', *Optics* [in Russian], Vishcha Shkola, Kiev, 1979.
[15] N. N. Konstantinova, M. A. Magomedov, V. Yu. Rud', and Yu. V. Rud', Jpn. J. Appl. Phys. **32-3**, 106 (1993).

Translated by James S. Wood

Production and investigation of AgIn$_5$S$_8$/(InSe, GaSe) heterojunctions

I. V. Bodnar'

Belarus State University of Information Science and Radio Electronics, 220027 Minsk, Belarus

V. F. Gremenok

Institute of Solid-State and Semiconductor Physics, Academy of Sciences of Belarus, 220072 Minsk, Belarus

V. Yu. Rud'*)

St. Petersburg State Technical University, 195251 St. Petersburg, Russia

Yu. V. Rud'

A. F. Ioffe Physicotechnical Institute, Russian Academy of Sciences, 194021 St. Petersburg, Russia

It is shown that photosensitive AgIn$_5$S$_8$/(InSe, GaSe) heterojunctions can be fabricated using bulk crystals grown from the melt and from the vapor phase or polycrystalline thin films of the ternary compound prepared by pulsed laser evaporation. The spectral curves of the photosensitivity of the heterojunctions are investigated as a function of the photodetection geometry. It is concluded that the resulting structure have a promising potential as wideband and selective photodetectors. © *1999 American Institute of Physics.* [S1063-7826(99)01007-8]

INTRODUCTION

Ternary A^{I}B^{III}C$_2^{VI}$ semiconductors are enjoying ever-growing applications as components of highly efficient ($\eta \approx 18\%$), stable solar cells.[1–3] The parameters of these materials are controlled primarily by varying the composition of solid solutions of the compounds.[4,5] In sections of A^{I}–B^{III}–C$_2^{VI}$ systems, however, together with A^{I}B^{II}C$_2^{VI}$ compounds there exist ordered phases with the general formulas A^{I}B$_3^{II}$C$_5^{VI}$ and A^{I}B$_5^{II}$C$_8^{VI}$ (Refs. 3, 6, and 7, which should also be treated as an effective approach to the synthesis of materials with the required properties. The physical properties of these phases have not been adequately studied to date, and for this reason their practical potential has not been revealed to the fullest.

The present paper is aimed in this direction and represents a feasibility study of the fabrication of photosensitive structures utilizing one such phase, AgIn$_5$S$_8$, prepared in the form of bulk crystals and thin films. Here we give the results of first investigations of the photoelectric properties of several types of AgIn$_5$S$_8$ heterojunctions and discuss their possible applications.

EXPERIMENTAL PART

Single crystals of AgIn$_5$S$_8$ were grown by two different techniques. One was based on the oriented crystallization of a melt of stoichiometric composition.[8] Such crystals in the virgin state have n-type conductivity with an electron density of $(2–5)\times10^{19}$ cm^{-3} and a Hall mobility of $40–60$ cm^2/(V·s) at a temperature of 300 K. The second preparation technique involved a vapor-transport process using iodine as the carrier and was capable of producing crystals having a natural prismatic faceting with average dimensions

of $5\times3\times3$ mm. These crystals also had n-type conductivity with an electron density $\sim6\times10^{18}$ cm^{-3} and a mobility of $10-20$ cm^2/(V·s).

Single-phase AgIn$_5$S$_8$ thin films with thicknesses of $0.6-0.8$ μm were prepared by pulsed laser evaporation of the bulk crystals onto glass substrates, whose temperature was maintained close to 780 K during deposition.[9] Like the bulk crystals, the films had n-type conductivity.

To create photosensitive AgIn$_5$S$_8$ structures, we explored the possibilities of forming direct optical contact of the surfaces of the bulk crystals and the thin films with the surfaces of natural chips of layered InSe and GaSe semiconductor materials.[10] These crystals were grown by the oriented crystallization of corresponding III–VI melts of near-stoichiometric composition and had n-type conductivity with an electron density $n\approx10^{14}$ cm^{-3} at 300 K. After grinding and polishing, the surfaces of the bulk AgIn$_5$S$_8$ crystals were treated in a polishing etchant, whereas after deposition of the thin films on glass their outer surfaces were mirror-smooth, and further treatment was unnecessary. Indium was used for the ohmic contacts to the AgIn$_5$S$_8$ and III–VI semiconductors. The AgIn$_5$S$_8$ and III–VI wafers joined in direct optical contact were placed in a special holder, which fixed the position of this contact and permitted the structures to be illuminated from either the AgIn$_5$S$_8$ or the III–VI side. The spectral dependences of the relative quantum efficiency of photoconversion η, calculated as the ratio of the short-circuit photocurrent to the number of incident photons, were measured in constant and modulated (at 20 Hz) radiation using an SPM-2 monochromator with a quartz prism. A spectral resolution ≈0.5 meV was achieved in the reported measurements.

TABLE I. Photoelectric properties of heterojunctions at 300 K.

Preparation of AgIn₅S₈ by:	d, μm	R_0, Ω	Illumination from AgIn₅S₈ side				Illumination from InSe side			
			S_U, V/W	$\hbar\omega$, eV	S, eV^{-1}	$\delta_{1/2}$, meV	S_U, V/W	$\hbar\omega$, eV	S, eV^{-1}	$\delta_{1/2}$, meV
Laser evaporation onto glass	0.65	4×10^3	15	1.25	70	840	5	1.215	66	40
Oriented crystallization	140	6×10^7	30	1.252	58	560	10	1.215	60	25
Vapor-phase method	80	2×10^9	31	1.82	45	180	3	1.21	50	50

RESULTS AND DISCUSSION

Investigations of the steady-state current-voltage (I–V) curves of the heterojunctions made from n-type AgIn₅S₈ thin films and n-type III–VI wafers consistently disclosed rectification. The forward conducting direction in such heterojunctions corresponds to positive polarity of the III–VI semiconductors, and the rectification factor at voltages $U\approx2$ V does not exceed 10 in the best structures. The forward branch of the I–V curve at $U>2$ is characterized by the relation

$$U = U_0 + I \cdot R_0, \qquad (1)$$

where the cutoff voltage is $U_0\approx0.2-0.6$ V, and the residual resistance R_0 (see Table I) depends heavily on the method used to prepare the ternary compound. This dependence suggests an interrelationship between the electrical properties of the compound and the technological conditions.

Illumination of the investigated heterojunctions induces a photovoltaic effect, where the sign of the photovoltage is independent of the illumination geometry and is preserved over the entire photosensitivity range of such heterojunctions. This fact justifies the assumption that the only active zone in such structures is the heterointerface formed by the optical contact created between the ternary and binary chalcogenides. Table I gives the values of the maximum voltage photosensitivity S_U for AgIn₅S₈/InSe heterojunctions. It is evident that the photosensitivity in such heterojunctions is higher in illumination from the AgIn₅S₈ side, consistent with the ratio between the widths of the band gaps E_G of these semiconductors.[11] For AgIn₅S₈/GaSe structures we have attained similar values of S_U, the only difference being that now the photosensitivity begins to dominate in illumination of the heterojunction from the GaSe side. This result is mainly attributable to the interrelationship between the fundamental properties of the phases.

Typical spectral curves of the relative quantum efficiency of photoconversion η for AgIn₅S₈/InSe heterojunctions exhibit a dependence not only on the photodetection geometry, but also on the technological conditions attending the preparation of the ternary compound (Figs. 1 and 2 and Table I). For example, when a heterojunction is illuminated from the InSe side, the long-wavelength edge of η is exponential in all the structures and has a slope $S = \delta(\ln\eta)/\delta(\hbar\omega)$, since it is determined by direct interband transitions in the InSe.[10] The abrupt drop of *eta* on the short-wavelength side for $\hbar\omega>1.215$ eV is attributable to the influence of radiation absorption in the InSe. It is typical of all

heterojunctions of this type and does not depend on the AgIn₅S₈ growth technology. When an AgIn₅S₈/InSe heterojunction is illuminated from the AgIn₅S₈ side, owing to the elimination of absorption in the InSe, the long-wavelength edge of the photosensitivity curve shifts into the short-wavelength spectral region, and the photosensitivity maximum is attained at $\hbar\omega\approx E_g$ (InSe). The width (FWHM) $\delta_{1/2}$ of the η spectra increases significantly in this photodetection geometry (Figs. 1 and 2, curves *2* and *3*, and Table I). Con-
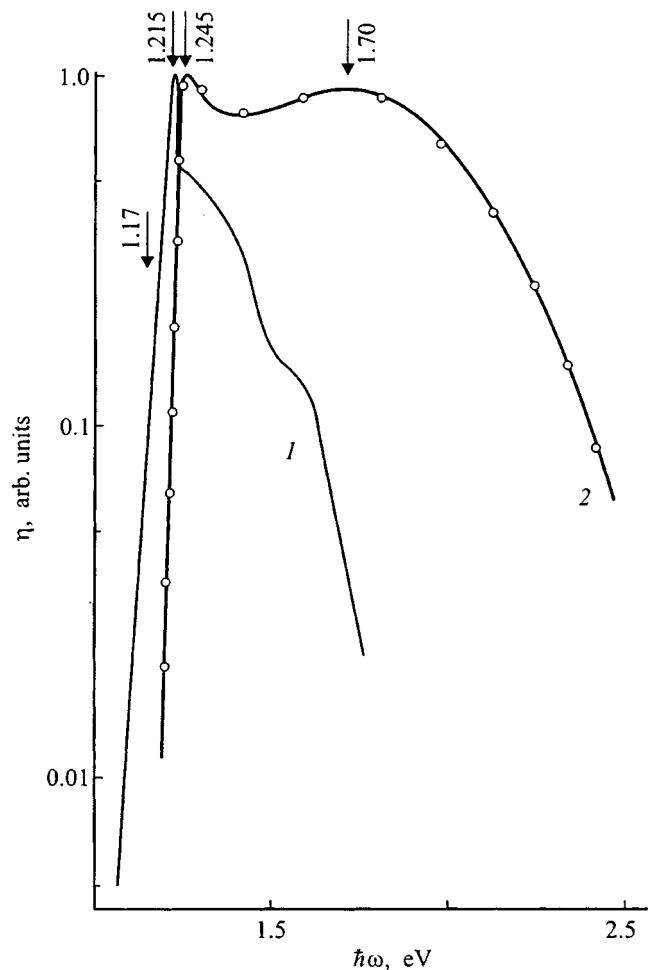

FIG. 1. Spectral curve of the relative quantum efficiency of photoconversion η of a thin-film AgIn₅S₈/InSe heterojunction at 300 K, illuminated from: (*1*) the InSe side; (*2*) the AgIn₅S₈ side. The film was prepared by laser evaporation.
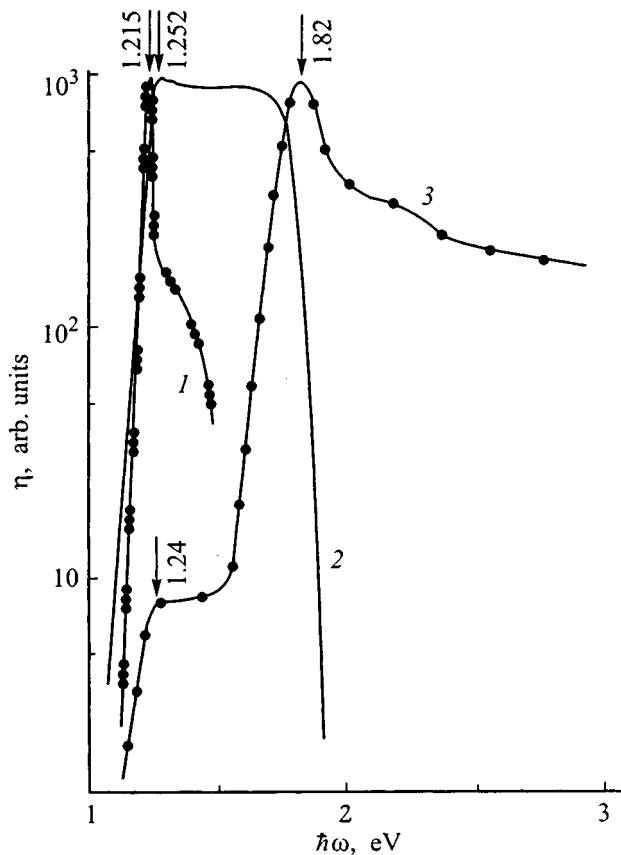
FIG. 2. Spectral curves of η for a bulk-crystal $AgIn_5S_8$/InSe heterojunction at 300 K, illuminated from: (*1*) the InSe side; (*2*) the $AgIn_5S_8$ side. The crystal was prepared by: (*1, 2*) oriented crystallization; (*3*) the vapor-phase method.

FIG. 3. Spectral curves for bulk-crystal $AgIn_5S_8$/GaSe (*1, 2*) and thin-film $AgIn_5S_8$/GaSe (*3*) heterojunctions. The crystal was prepared by the vapor-phase method, and illumination is from: (*1*) the side of the $AgIn_5S_8$ thin film; (*2*) the GaSe side.

sequently, the window effect typical of near-perfect heterojunctions occurs in our prepared structures.[11]

The widest-band photosensitivity is attained in heterojunctions prepared from $AgIn_5S_8$ thin films (Fig. 1, curve *2*). The maximum of η in such heterojunctions, $\hbar\omega\approx1.7$ eV, is close to the gap E_G of bulk crystals of the ternary compound.[8] For this reason, the short-wavelength decay of η in the illumination of $AgIn_5S_8$/InSe structures from the $AgIn_5S_8$ side must be attributed to the influence of absorption in the laser-evaporated $AgIn_5S_8$ thin film.

The short-wavelength decay of η for $\hbar\omega>1.7$ eV becomes steeper In heterojunctions utilizing bulk $AgIn_5S_8$ crystals grown by oriented crystallization (Fig. 2, curve *2*). This situation is induced by a marked increase in absorption in the $AgIn_5S_8$ crystal when its thickness is increased more than 10^3-fold relative to the laser-deposited film. We also emphasize the coincidence of the energy positions of the short-wavelength decays of η in such heterojunctions, leading to the important conclusion that the gaps E_G in the bulk $AgIn_5S_8$ crystal and in the thin film prepared from it are close to one another.

For heterojunctions of this type with a bulk $AgIn_5S_8$ crystal obtained from the vapor phase the spectral profile of η exhibits a major change (Fig. 2, curve *3*) from the one discussed above. In fact, the photosensitivity in such heterojunctions illuminated from the $AgIn_5S_8$ side, in contrast with
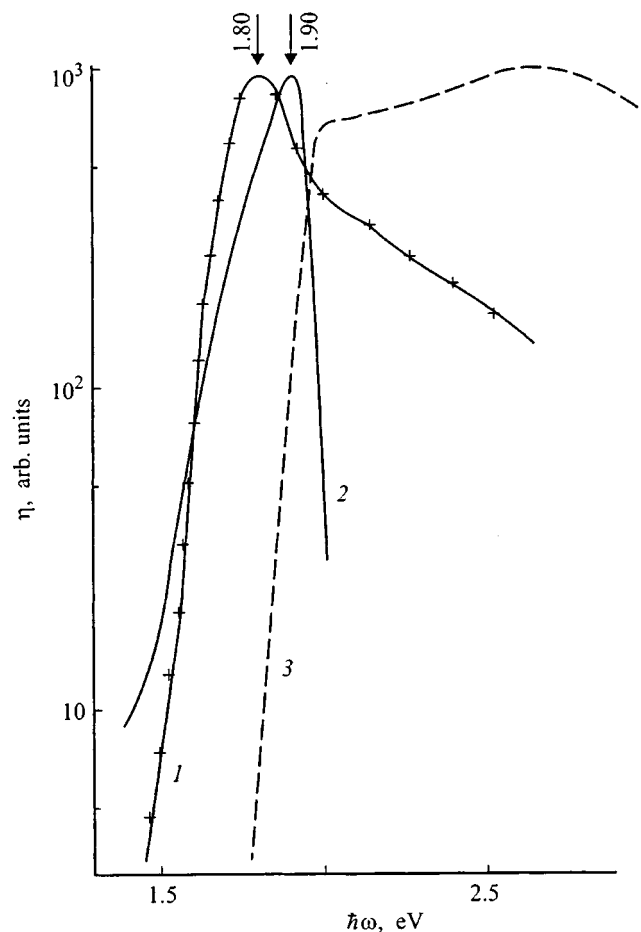
the previous types of structures (Figs. 1 and 2, curves *2*), dominates in such heterojunctions with illumination from the $AgIn_5S_8$ side, whereas the contribution of absorption of the narrow-gap component InSe is reduced more than 10^2-fold (Fig. 2, curves *2* and *3*). It is also important to note that the maximum of η in heterojunctions utilizing the highest-resistance vapor-phase crystals, $\hbar\omega=1.82$ eV, corresponds to the interval of abrupt decay of the photosensitivity of heterojunctions made from the lower-resistance $AgIn_5S_8$. The observed transformation in the spectra of η, depending on the technology of preparation of the ternary compound (Figs. 1 and 2), can be qualitatively explained by taking into account the variation of the electrical properties of $AgIn_5S_8$, which causes an ever-greater portion of the active zone of the heterojunction to be localized in the bulk of the $AgIn_5S_8$ as the resistance of the latter increases relative to the InSe.

When InSe is replaced by the wider-gap compound GaSe, the role of the wide-gap component begins to be taken over by gallium arsenide. Figure 3 shows typical spectra of η for $AgIn_5S_8$/GaSe heterojunctions. In a structure made from vapor-phase crystals and illuminated from the $AgIn_5S_8$ side the photosensitivity spectrum (Fig. 3, curve *1*) is similar to the characteristic spectrum for $AgIn_5S_8$/InSe (Fig. 2, curve

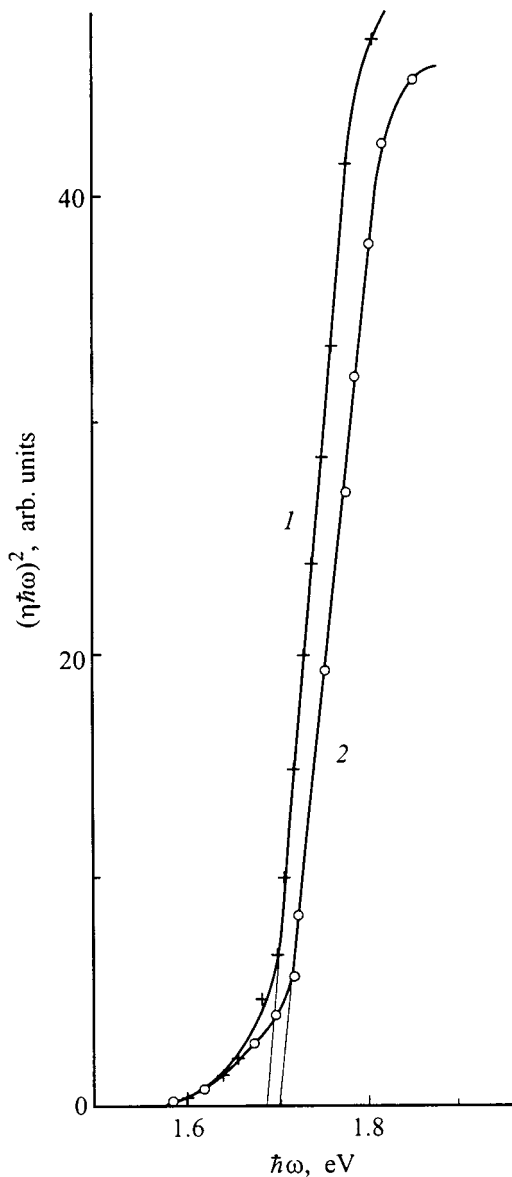erojunctions and exhibit satisfactory agreement with E_G for $AgIn_5S_8$ (Ref. 8). In heterojunctions utilizing laser-deposited $AgIn_5S_8$ films, the cutoff energy for both photodetection geometries is determined by interband transitions in the GaSe (Fig. 3, curve *3*), owing to the substantial difference in the doping levels of the contacting substances and, accordingly, the predominant localization of the active zone in the GaSe.

It should be noted that the photoelectric parameters of the prepared heterojunctions do not exhibit any degradation effects and can be used for nondestructive diagnostics of the homogeneity of the photoelectric parameters of the new semiconductor $AgIn_5S_8$ by decreasing the area of the III–VI wafer and positioning it at different points of the surface of films and bulk crystals of the semiconductor.[13]

Polarization studies of the sensitivity of $AgIn_5S_8$/III–VI thin-film heterojunctions show that natural photopleochroism is not observed in such structures, and that the polarimetric photodetection regime can be implemented in structures prepared on specially oriented single crystals or with the oblique incidence of radiation.[5]

Consequently, easily fabricated $AgIn_5S_8$/III–VI structures have potential practical applications as finely selective, wideband photodetectors of natural radiation.

*)E-mail: rudvas@uniys.hop.stu.neva.ru

[1] H. W. Schock, in *Proceedings of the 12th Photovoltaic Solar Energy Conference and Exhibition*, Amsterdam, edited by R. Hill *et al.* (H. S. Stephen Assoc., Bedford, UK, 1994), p. 944.

[2] T. Negami, in *Abstracts of the Fifth International Conference ''POL-YSE'98, Polycrystalline Semiconductors — Bulk Materials, Thin Films, and Devices''* (Schwäbisch Gmünd, Germany, 1998), p. 18.

[3] T. Walter, D. Braunger, H. Dittrich, C. Koble, R. Herberholz, and H. W. Schock, Sol. Energy **41/42**, 355 (1996).

[4] D. Schmid, M. Ruck, and H. W. Schock, Sol. Energy Mater. Sol. Cells **41/42**, 281 (1996).

[5] V. Yu. Rud', Yu. V. Rud', T. Walter, and H. W. Schock, Inst. Phys. Conf. Ser. **152**, 971 (1998).

[6] A. N. Tiwari, S. Blunier, M. Filzmoser, H. Zogg, D. Schmid, and H. W. Schock, Appl. Phys. Lett. **65**, 3347 (1994).

[7] K. Wakamura, S. Endo, and T. Irie, Cryst. Res. Technol. **31-S2**, 923 (1996).

[8] N. S. Orlova, I. V. Bodnar', and E. A. Kudritskaya, Neorg. Mater. **34**, 13 (1998).

[9] V. F. Gremenok, E. P. Zaretskaya, I. V. Bodnar, and I. V. Victorov, Cryst. Res. Technol. **31-S2**, 485 (1996).

[10] *Physicotechnical Properties of Semiconducting Materials: Handbook* [in Russian], Nauka, Moscow, 1975.

[11] I. V. Bodnar, V. Yu. Rud', and Yu. V. Rud', Cryst. Res. Technol. **31-S1**, 261 (1996).

[12] S. M. Sze, *Physics of Semiconductor Devices* (Wiley-Interscience, New York, 1981).

[13] N. M. Mekhtiev, Yu. V. Rud', and É. Yu. Salaev, Fiz. Tekh. Poluprovodn. **12**, 1566 (1978) [Sov. Phys. Semicond. **12**, 924 (1978)].

Translated by James S. Wood

FIG. 4. Photosensitivity of $AgIn_5S_8$/InSe (*1*) and $AgIn_5S_8$/GaSe (*2*) heterojunctions at 300 K. Illumination is from the $AgIn_5S_8$ side, and the $AgIn_5S_8$ crystal was prepared by the vapor-phase method.

3), because it is governed mainly by absorption in the same $AgIn_5S_8$ wafer. Despite differences in the atomic composition of the III–VI semiconductors used, the long-wavelength edge of the photosensitivity for such heterojunctions (Fig. 4) straightens out in the characteristic coordinates for direct optical transitions,[12] $(\eta\hbar\omega)^2 - \hbar\omega$, and the cutoff energies extrapolated to $\hbar\omega=0$ are close together for the compared het-

Zinc telluride epilayers and CdZnTe/ZnTe quantum wells grown by molecular-beam epitaxy on GaAs(100) substrates using solid-phase crystallization of an amorphous ZnTe seed layer

V. I. Kozlovskiĭ,*) A. B. Krysa, Yu. G. Sadof'ev, and A. G. Tur'yanskiĭ

P. N. Lebedev Physics Institute, Russian Academy of Sciences, 117924 Moscow, Russia

The deposition of an amorphous ZnTe seed layer of thickness 10 nm and its subsequent solid-phase crystallization are implemented prior to the start of molecular-beam epitaxy of ZnTe layers on GaAs(100) substrates. RHEED patterns from the growth surface of the samples during epitaxy confirm that the formation of three-dimensional nucleation centers is successfully eliminated by this technique, and two-dimensional growth in the early stage of epitaxy is achieved. Cathodoluminescence and x-ray structural analyses indicate a higher quality on the part of ZnTe layers grown with the application of an amorphous ZnTe layer. Quantum-well ZnCdTe/ZnTe structures that emit efficiently in the green region of the spectrum can be grown by optimizing the epitaxy regimes. © *1999 American Institute of Physics.*
[S1063-7826(99)01107-2]

Structures based on ZnTe and CdTe hold considerable promise for applications in a number of optoelectronic devices. One deterrent to the acceptance of such structures is a severe mismatch of the lattice parameter a with the commonly used GaAs substrates (the mismatch $\Delta a/a = 7.6\%$ for ZnTe/GaAs). In the presence of a large mismatch we encounter either an island mechanism of film nucleation (Volmer–Weber mechanism) or the Stransky–Krastanov mechanism, whereby an elastically stressed pseudoamorphous film is formed during the initial stage of growth until a certain critical thickness is attained. However, the attainment of above-critical thicknesses is accompanied by relaxation of the elastic stresses due to the generation of a network of misfit dislocations. In local zones containing misfit dislocations the elastic energy of the film and its chemical potential decrease, so that the dislocations begin to act like effective sinks for adatoms of the substance in question, disrupting the growth planarity.[1] Moreover, the gradient of the chemical potential in the plane of the growing film can serve as a driving force for directional mass transfer from pseudoamorphous zones into dislocation zones. In this event the dislocation-free zones can be completely dissolved, and in their place are bare substrate zones uncovered by film material. As a rule, uncorrelated networks of misfit dislocations are generated on the areas of neighboring islands. Upon coalescence of the islands, the ends of the dislocation lines bend and grow into the bulk of the film.[2]

Consequently, when either of the above-mentioned film nucleation mechanisms is operative, in the initial stage of growth the islands are surrounded by zones depleted of the deposited material, i.e., the coating is not continuous. The diameters of islands formed at active growth centers can greatly exceed the average island diameter. These considerations impart a coarse microprofile to the grown film and lead to the generation of extended structural defects, which permeate the bulk of the film.[3–7]

One possible way to improve the quality of the heteroepilayers near the interface for a sizable difference in the lattice parameters of the joined materials is to employ solid-phase epitaxy in the initial growth stage. A thin seed layer of amorphous material is deposited on the substrate at a reduced temperature, and it is then crystallized at a higher temperature. This operation produces a continuous, homogeneous coating with a crystalline, albeit imperfect structure. The film growth process is then continued with the substrate at the usual temperature for heteroepitaxy. The twofold effect of the technique is to improve the surface morphology of the heteroepitaxial film by virtue of the formation of a continuous, homogeneous coating early in the process when the film has an ultimately small thickness, and also to lower the density of extended structural defects growing into the bulk of the film. The above-described two-stage growth scheme has been used successfully in the heteroepitaxy of GaAs on Si ($\Delta a/a = 4\%$) (Refs. 8 and 9) and is widely used in the heteroepitaxy of GaN on a sapphire substrate ($\Delta a/a = 13\%$) (Refs. 10–12).

Despite the extreme difference in the lattice parameters of ZnTe and GaAs, none of the sources available to us in the literature report the application of solid-phase epitaxy in the initial stage of growth of a ZnTe layer on a GaAs substrate for the reduction of structural defects and morphological flaws. In this paper we describe a feasibility study of improving the quality of ZnTe films and CdZnTe/ZnTe quantum wells on GaAs(100) substrates grown by molecular-beam epitaxy (MBE) using an amorphous seed layer of ZnTe, which is subsequently crystallized. On films prepared by this technique we have investigated the dependence of the cathodoluminescence of ZnTe on the type of reconstruction of the growth surface.

The structures were grown on a Katun MBE apparatus after a major modification of the molecular beam generating system and the installation of an ionic manometer to monitor the equivalent pressures of the beams. The films were grown by evaporating the elements Zn, Cd, and Te from separate sources. After the removal of oxides from the GaAs surface by heating to a temperature of $550-580\,°C$ the substrate was cooled to room temperature, and an amorphous seed layer of ZnTe of thickness 10 nm was deposited on it. This layer was heated to a temperature of $350-380\,°C$ in a flux of Te (or Zn) molecules with an effective pressure of $(2-3)\times10^{-7}$ Torr and was kept until it had completely crystallized. Annealing of the samples without the application of a Te (or Zn) molecular beam to the surface causes the film to be desorbed until the crystallization process is terminated. Further growth of the structures took place at a temperature of $320-350\,°C$ and a growth rate of 0.2 nm/s. The epitaxy was monitored by reflection high-energy electron diffraction (RHEED). For comparison, samples were also grown without the seed amorphous layer. We were unable to pinpoint the pseudoamorphous growth stage by the RHEED method, possibly because of the small critical thickness (~1 nm). The grown structures were investigated by cathodoluminescence and x-ray diffractometry. The cathodoluminescence spectra were recorded at a temperature $T=20-30$ K, an electron energy $E_e=3-30$ keV, and a current density $j_e=10^{-5}$ A/cm^2. The x-ray measurements were performed on a DRON-3 x-ray diffractometer using a two-crystal configuration. The characteristic $CuK_{\alpha1}$ line was isolated from the spectrum of a fine-focus tube with a copper anode by means of a Si(111) crystal monochromator. The radius of the focal spot of the diffractometer was increased to 350 mm to improve the angular resolution.

Figure 1 shows a time comparison of RHEED patterns from the surface of samples without (a–d) and with (e–h) the use of an amorphous buffer layer. After oxide removal the RHEED pattern of the GaAs substrate (a) contains relatively elongated reflections, indicating that the substrate has a single-crystal character and that the surface is very nearly atomically smooth. The RHEED pattern (b and c) becomes spotty with the initiation of epitaxy. This behavior is inherent in three-dimensional growth. Subsequently, after the first 10 min of growth, a gradual improvement of the surface structure is observed in that the reflections are elongated into bands. However, even after 20 min of growth (d), when the film attains a thickness of more than 0.2 μm, the RHEED pattern is still spotty.

The deposition of a thin ZnTe seed layer at room temperature completely eradicates the diffraction reflections, and the RHEED pattern shows up as uniform illumination of the screen (diffuse scattering background) due to the amorphous structure of the layer. Dotted reflections are formed as the structure is heated (e), exhibiting greater contrast with increased heating time. If the crystallization procedure is accurately performed, it is possible to achieve the formation of elongated reflections and to see signs of their merging into bars. However, even if the latter effect is not successfully achieved during annealing of the seed layer, with the start of epitaxy (f and g) the reflections stretch out far more quickly
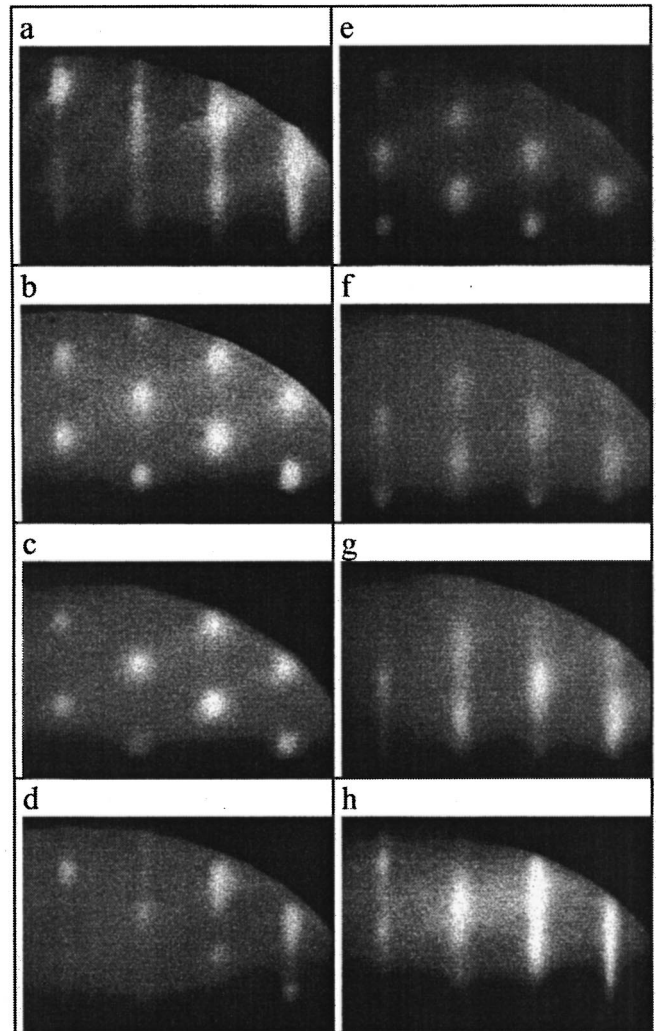

FIG. 1. RHEED patterns from the surfaces of the GaAs substrate after the removal of oxides and before the start of epitaxy (a) and from ZnTe films without (b–d) and with (e–h) the application of an amorphous ZnTe seed layer (b–d) at various times after the start of epitaxy: (e) 0 min (after solid-phase crystallization of the seed layer); (b, f) 4 min; (c, g) 9 min; (h) 12 min; (d) 20 min.

into lines than in growth without the amorphous layer. Two-dimensional layer-by-layer growth begins at a film thickness ~30 nm, and after just 12 min of growth (h) the RHEED pattern exhibits a high structural quality on the part of the growth surface.

Rocking curve measurements confirm that the structure of the films is improved when a seed layer is used. After a correction for instrumental distortion, introduced by means of a convolution algorithm, the half-widths of the rocking curves for films of thickness 2.5 μm with and without a seed layer are $116''$ and $200''$, respectively.

The cathodoluminescence spectra of ZnTe epitaxial films of thickness 1.5 μm grown under identical conditions except in the initial stage of epitaxy are compared in Fig. 2. The strongest lines in the cathodoluminescence spectra occur at $\lambda=521$ nm and 522.5 nm, corresponding to resonances in the reflection spectrum. We attribute them to the emission of free excitons with heavy (X_{hh}) and light (X_{lh}) holes, respec-
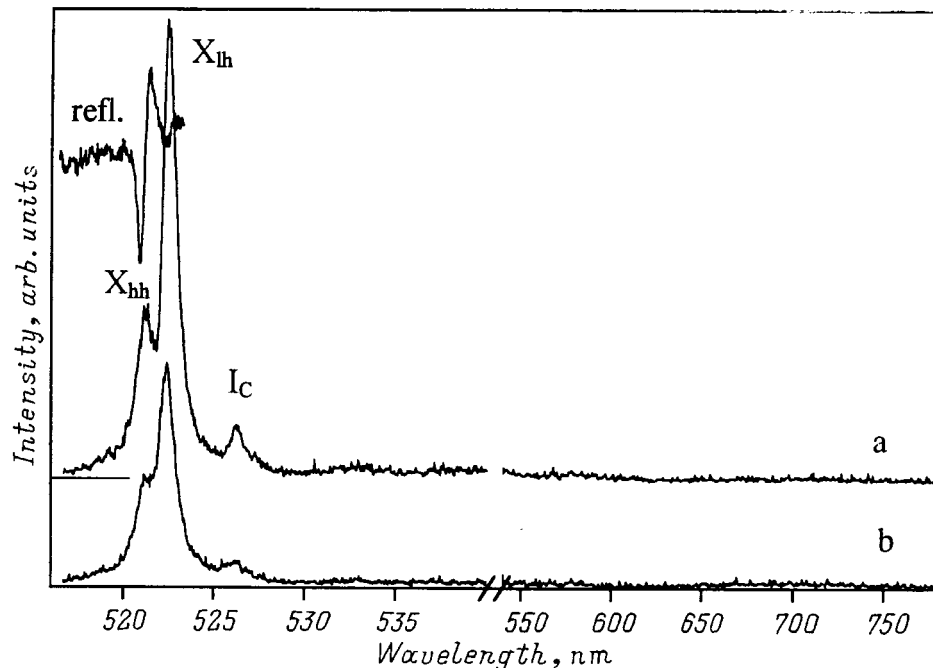
FIG. 2. Cathodoluminescence spectra of ZnTe films of thickness 1.5 μm, grown with (a) and without (b) the application of an amorphous seed layer, $E_e = 10$ keV, $T = 20$ K. The curve labeled "refl." represents the reflection spectrum of the ZnTe film with the application of an amorphous seed layer.

tively. The splitting obtained here (7 meV) is close to that observed in Ref. 13 for a similar film thickness and is explained by the tensile stress of the film due to a difference in the thermal expansion coefficients. Moreover, the spectrum contains an I_C line, which has been observed in ZnTe/GaAs epitaxial films prepared by different techniques[13] and in proton-irradiated bulk ZnTe single crystals,[14] where it was identified with native defects.

A comparison of the spectra shows that narrower exciton emission lines are observed for a sample grown with the application of an amorphous seed layer, and the total radiation intensity is twice that obtained for a sample grown without the amorphous seed layer. The influence of the seed layer on cathodoluminescence diminishes when the thickness of the epilayer increases to 3 μm. But a decrease in the thickness of the epilayer to 0.2 μm all but eliminates cathodoluminescence, even for samples grown with a seed layer, evidently because of a marked increase in the density of defects that compensate for the mismatch of the crystal lattices of the epilayer and the substrate near the interface.

Next we investigated the cathodoluminescence of ZnTe epilayers grown with the application of a seed layer as a function of the deviation of the elemental composition of the growth surface from stoichiometry during epitaxy. An excess of one of the original elements was determined from the type of surface reconstruction with the aid of the RHEED pattern. Figure 3 shows the cathodoluminescence spectra at 30 keV of ZnTe films of thickness 2.6 μm with different surface reconstructions: (a) (2×1), corresponding to tellurium enrichment of the surface; (b) $c(2 \times 2)$, corresponding to zinc enrichment of the surface; (c) $(2 \times 1) + c(2 \times 2)$, which is the closest to a stoichiometric surface composition. Together with exciton emission, long-wavelength ("deep" line) emission through deep levels is present in the spectrum. This emission is attributed to the recombination of charge carriers
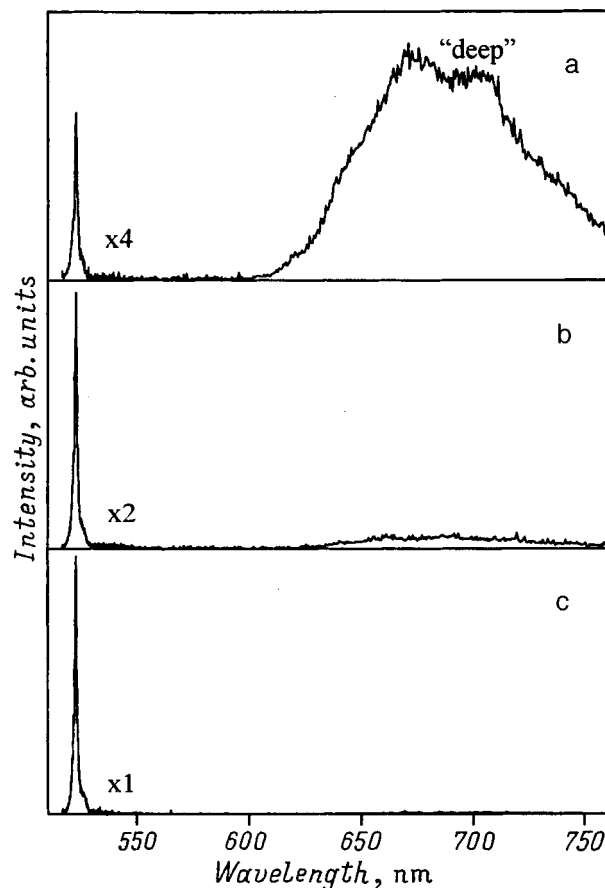
FIG. 3. Cathodoluminescence spectra of ZnTe films of thickness 2.6 μm, grown with the application of an amorphous seed layer, $E_e = 30$ keV, $T = 30$ K, for three different reconstructions of the growth surface during epitaxy: (a) (2×1), corresponding to Te enrichment; (b) $c(2 \times 2)$, corresponding to Zn enrichment; (c) $(2 \times 1) + c(2 \times 2)$, corresponding to a surface of stoichiometric composition.
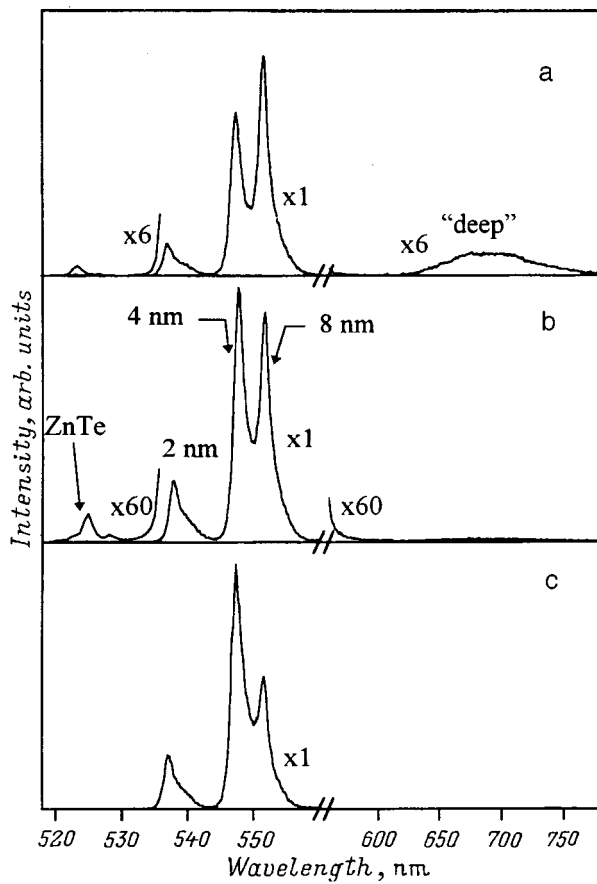
FIG. 4. Cathodoluminescence spectra of a structure containing (in the order of increasing distance from the substrate) a crystallized ZnTe seed layer, a ZnTe buffer layer of thickness 1.5 μm, three $Cd_{0.12}Zn_{0.88}Te$ quantum wells of thickness of 8 nm, 4 nm, and 2 nm with ZnTe barriers of thickness 30 nm, and a ZnTe coating layer of thickness 5 nm, at $T = 20$ K for various electron energies and corresponding excitation depths: (a) 30 keV, 2.5 μm; (b) 10 keV, 0.25 μm; (c) 3 keV, 0.03 μm.

at complexes containing native defects, and its presence is associated with structural imperfections of the epitaxial film.[15] The observed deep-line structure is caused by the interference of radiation along the thickness of the film. When E_e is decreased from 30 keV to 3 keV and, accordingly, the cathodoluminescence excitation depth z_0 decreases from 2.5 μm to 0.03 μm, the intensity of the long-wavelength emission decreases considerably, indicating a concentration of the corresponding centers near the ZnTe/GaAs interface.

It follows from the spectra in Fig. 3 that the maintenance of a surface of stoichiometric composition during epitaxy produces a film that emits the strongest radiation in the exciton region of the spectrum and the weakest deep line. The measured ratio of the equivalent pressures of the molecular beams for this case, $p(Te_2)/p(Zn) = 2$, can be regarded as the optimum for the MBE growth of ZnTe films.

The application of an amorphous ZnTe seed layer and its subsequent solid-phase crystallization before the start of epitaxy have enabled us to produce quantum-well CdZnTe/ZnTe structures with a high radiation efficiency. Figure 4 shows cathodoluminescence spectra of a structure containing (in the order of increasing distance from the substrate) a crystallized ZnTe seed layer, a ZnTe buffer layer of thick-

ness 1.5 μm, three $Cd_{0.12}Zn_{0.88}Te$ quantum wells having thicknesses of 8 nm, 4 nm, and 2 nm with ZnTe barriers of thickness 30 nm and a ZnTe coating layer of thickness 5 nm. The spectrum contains high-intensity, well-resolved emission lines with maxima at $\lambda_{max} = 537$ nm, 547.4 nm, and 551.6 nm and half-widths $\Delta \approx 9.6$ meV, 9.5 meV, and 7.7 meV, which are attributable to emission from quantum wells having widths of 2 nm, 4 nm, and 8 nm, respectively. When E_e is increased from 3 keV to 30 keV (increasing z_0 from 0.03 μm 2.5 μm), the fraction of carriers collected by the 8-nm quantum well from the direction of the ZnTe buffer layer increases. The latter event causes the emission from this quantum well to become stronger than the emission from the other quantum wells. The emission intensity of excitons and of the deep centers of the ZnTe buffer layer also increases in this case. However, even for $E_e = 30$ keV, when the structure is excited over its entire thickness, including the most defective region near the GaAs substrate, the intensity of the exciton and long-wavelength emission from the buffer is approximately two orders of magnitude lower than the intensity of the quantum well emission. This result attests to the effective collection of carriers in the quantum well.

We have thus shown that the technique of using an amorphous ZnTe seed layer with its subsequent solid-phase crystallization can be used to eliminate the formation of three-dimensional nucleation centers and to achieve the two-dimensional growth of ZnTe on GaAs substrates in the very first stage of MBE. This increases the intensity of exciton emission and decreases the half-width of the sample rocking curve. We have also investigated the dependence of the cathodoluminescence of the ZnTe layers on the ratio of the Zn and Te fluxes. The optimum ratio of the equivalent pressures of the molecular beams is $p(Te_2)/p(Zn) = 2$. Quantum-well CdZnTe/ZnTe structures emitting efficiently in the green region of the spectrum can be created by optimizing the epitaxy regimes.

*)E-mail: vikoz@sgi.lpi.msk.su

[1] S. M. Pintus, S. I. Stenin, A. I. Toropov, and E. M. Trukhanov, IFP SO AN SSSR/NGU Preprint No. 5-86 [in Russian], Institute of Semiconductor Physics, Siberian Branch of the Russian Academy of Sciences, and Novosibirsk State University, Novosibirsk, 1986.

[2] Yu. B. Bolkhovityanov, Yu. D. Vaulin, A. K. Gutakovskiĭ, S. I. Penin, and V. I. Yudaev, Izv. Akad. Nauk SSSR, Ser. Fiz. **44**, 1238 (1980).

[3] F. Kitagava, T. Mishima, and K. Takahashi, J. Electrochem. Soc. **127**, 937 (1980).

[4] J. P. Faurie, J. Reno, S. Sivananthan, I. K. Sou, X. Chu, M. Boukerche, and P. S. Wijewarnasuriya, J. Vac. Sci. Technol. B **4**, 585 (1986).

[5] Y. Hishida, H. Ishii, T. Toda, and T. Niina, J. Electron Spectrosc. Relat. Phenom. **95**, 517 (1989).

[6] T. Karasawa, K. Ohkava, and T. Mitsuyu, J. Cryst. Growth **95**, 547 (1989).

[7] T. Karasawa, K. Ohkava, and T. Mitsuyu, Appl. Phys. Lett. **54**, 117 (1989).

[8] S. Nishi, H. Inomata, M. Akiyama, and K. Kaminishi, Jpn. J. Appl. Phys. **24**, 391 (1985).

[9] Y. Fukuda and Y. Kohama, J. Cryst. Growth **81**, 451 (1986).

[10] H. Morkoc, S. Strite, G. B. Gao, M. E. Lin, B. Sverdlov, and M. Burns, J. Appl. Phys. **76**, 1363 (1994).

[11] J. N. Kuznia, M. Asif Khan, D. T. Olson, R. Kaplan, and J. Freitas, J. Appl. Phys. **73**, 4700 (1993).

[12] S. Nakamura, Jpn. J. Appl. Phys. **30**, L1705 (1991).

[13] G. Kudlek and J. Gutowski, J. Lumin. **52**, 55 (1992).

[14] V. I. Kozlovskiĭ and A. B. Krysa, Fiz. Tverd. Tela (St. Petersburg) **35**, 3087 (1993) [Phys. Solid State **35**, 1519 (1993)].

[15] Y. Biao, M. Azoulay, M. A. Georg, A. Burger, W. E. Collins, E. Siberman, C.-H. Su, M. E. Volz, F. R. Szofran, and D. C. Gilles, J. Cryst. Growth **138**, 219 (1994).

Translated by James S. Wood

Distribution of the electric field in high-resistivity MSM structures illuminated by nonmonochromatic light

B. I. Reznikov

A. F. Ioffe Physicotechnical Institute, Russian Academy of Sciences, 194021 St. Petersburg, Russia
(Submitted November 17, 1998; accepted for publication December 30, 1998)
Fiz. Tekh. Poluprovodn. **33**, 815–823 (July 1999)

The sensitivity of the electric field distribution to the spectrum of the incident radiation in highly biased, high-resistivity, semiconductor structures of the MSM (metal-semiconductor-metal) type illuminated by nonmonochromatic light is investigated theoretically. It is shown that in the presence of deep impurity levels the field distribution depends strongly on the spectral composition of the incident light. The frequency interval corresponding to optical thicknesses of the order of unity is found to significantly influence the space charge in the bulk of the structure and the electric field distribution $E(x)$, even when the fraction of energy in this region of the spectrum relative to the total flux is extremely minimal. The trapping of holes by a deep impurity level in the bulk of the structure forms a positive space charge and produces qualitatively new field distributions, which increase near the dark electrode with a positive curvature of the function $E(x)$. The impurity trapping of electrons near the illuminated anode imparts a negative space charge to the impurity levels. This phenomenon induces a substantial increase of the field in the electrode sheath and forms in the vicinity of the anode a region wherein the field varies only slightly. All the prominent features disclosed by the calculations in the electric field distributions are observed in experiment. © *1999 American Institute of Physics.* [S1063-7826(99)01207-7]

1. INTRODUCTION

1.1. The relaxation of the electric field and current in a high-resistivity metal-semiconductor-metal (MSM) structure subjected to an applied voltage and illumination poses a fundamental problem characterized by the interaction of numerous nonlinear effects, which produce an enormous diversity of relaxation laws and steady-state solutions. One of the most intriguing effects is the generation of a light-induced space charge and the redistribution of the latter, accompanied by a change of the electric field.

Experimental work has stimulated various applications of the effect in semiconductor electronics. In particular, it has been established that the photosensitivity and spatial resolution of space-time light modulators and devices for the writing of volume holograms depend on the magnitude and distribution of the space charge of photoelectrons captured by deep traps as the optical image is recorded.[1] Electric field measurements in $Bi_{12}GeO_{20}$ crystals have exhibited their dependence on the energy absorbed in the crystal and the wavelength of the incident light.[2] It was determined that the field in a crystal becomes increasingly nonuniform as the absorbed energy increases. The quantity $\tilde{E} = E/E_e$ ($E_e = V/d$, where d is the diameter of the structure) decreases near the illuminated electrode (cathode) and increases in the opposite part of the structure. The formation of space charge regions of opposite sign imparts a minimum to $\tilde{E}$ in the crystal. The sign of the total charge in the crystal and the form of the field distribution depend on the wavelength of the incident light. For shorter-wavelength radiation ($\lambda = 0.45$ μm) a nonmonotonic field distribution is formed with clearly defined space charge regions of both signs, but when the wavelength increases ($\lambda = 0.65$ μm, a uniform, diminishing field distribution is formed around the cathode, while the field in the bulk of the crystal is essentially uniform. Experimental studies of the transient photocurrent and field distribution in $Bi_{12}SiO_{20}$ and $Bi_{12}GeO_{20}$ crystals over a wide range of the light absorption coefficient α have also indicated a qualitative difference in the field distributions accompanying strong absorption ($\alpha \simeq 10^4$ cm^{-1}; Ref. 3) and weak absorption ($\alpha \simeq 0.5$ cm^{-1}; Ref. 4). In the first case the field $\tilde{E}$ increases directly as $\sqrt{x}$, where x is the distance from the illuminated electrode, as in the space charge-limited current regime.[5] In the second case the field drops sharply in a tight region around the electrode and then remains constant all the way to the positive electrode. Theoretical studies (see, e.g., Ref. 6) based on a monopolar drift model have described the evolution of the field during the radiative transport of electrons from trapped donors and have accounted for the experimental relations reported in Refs. 2–4 It was established that for intermediate absorption coefficients the region where the field increases by the square-root law, $E \sim \sqrt{x}$, extends to the dark electrode, and a low-field region is formed at a certain distance from the illuminated electrode. The measured $E(x)$ curves therefore comprise a combination of limiting cases, first investigated by Mott and Gurney,[5] of the field distribution at a metal-insulator interface. The theoretical and experimental results obtained in this research stage are surveyed in Ref. 7.

In ambient light the generation of two types of free photocarriers produces an even greater diversity of fields, even in pure crystals. The results of a numerical simulation of

transient processes in metal-insulator-semiconductor-insulator-metal (MISIM) structures[8] show that the steady-state electric field distributions are extremely different from the classical square-root law $E \sim \sqrt{x}$, and the type of distribution is governed by the space charge in the vicinity of the illuminated anode. The latter quantity is controlled both by the surface carrier recombination rate and by the light absorption coefficient. The published results demonstrate the appreciable influence of the optical thickness of the incident radiation on the field distributions.

1.2. Another trend in research on the electric fields is related to the application of wide-gap, high-resistivity, compensated crystals (such as CdTe, HgI$_2$, and C) as the element base of radiation detectors[9] and light-controlled optoelectronic devices designed for fiber-optic communication lines, data processing systems, and systems for the recording of optical image signals.[10] The operation of these devices is based on the variation of the electric field distribution when the structure is illuminated. The results of measurements of the steady-state photocurrent and field distributions, along with the transient characteristics of ''pure'' high-resistivity (semi-insulating) crystals ($N_t \lesssim 10^{13}\,\text{cm}^{-3}$) (Refs. 11 and 12) and crystals containing a high density of impurity levels ($N_t \simeq 10^{15}\,\text{cm}^{-3}$) (Ref. 13), have revealed several new experimental factors associated with the distribution of electric fields and with the dependence of the current on the luminous intensity. The outcome of this work has been a drive to explain the sum-total of the experimental data within the framework of a unified approach.[14–18] We now give a brief interpretation of certain basic experimental principles.

1. The dark fields in symmetric MSM structures with a constant potential difference specified on their contacts are close to uniform distributions. This result indicates a low effective charge density ep_d in the nonilluminated structures, i.e., $4\pi ep_d/(\varepsilon V/d) \ll 1$, which gives the estimate $p_d \lesssim 3 \times 10^9\,\text{cm}^{-3}$.

2. The increase in the dark field near the anode when the thickness of the dielectric layer at the positive contact increases indicates the presence of a moderate density of deep impurity levels in the crystal and their ''decompensation'' as the rate of hole exchange across the interface varies.[15]

3. The illumination of the structure by ambient light alters the field distribution. The ratio $\tilde{E} = E/E_e$ decreases near the illuminated surface and increases at the dark electrode. As the luminous intensity is increased, the deformation of the field distribution increases and tends to saturation.

4. A characteristic detail of the distributions $\tilde{E}(x)$ is the presence of a low-space-charge region inside the structure (within roughly 2/3 of the thickness) and a weak dependence of the field in this region on the luminous intensity (see Figs. 4a and 4b in Ref. 11). In the cathode part of the structure, illuminated from the anode side, the field increases with acceleration, i.e., the field distribution $\tilde{E}(x)$ has a positive curvature: $d^2\tilde{E}/dx^2 > 0$.

5. The current-intensity dependence is sublinear in pure crystals.

The main phenomenon observed in Refs. 11 and 12 — shielding of the field at the illuminated electrode — is similar to the results of Ref. 2, but the measured coordinate dependence of the field is qualitatively new in comparison with what had been observed previously[2–4] and departs from the classical square-root law describing the increase of the field.[5] A theoretical investigation based on the model of a pure crystal illuminated by ambient light has fully explained the above-noted principles 3 and 5 and has revealed a new phenomenon: structural transformation of the field by the space charge of free photogenerated carriers.[14] The investigation has confirmed that the current-intensity dependence is sublinear without bulk recombination or the capture of carriers by trapping levels and is solely attributable to weakening of the external field by the field of free photogenerated carriers. The latter consideration fundamentally distinguishes the given phenomenon from the transformation of the field due to space charge redistribution in the transfer of electrons from trapped donors.[6] However, this model has not explained the entire set of experimental principles 1, 2, and 4, which combine an almost uniform dark distribution and an increase of the field in the cathode part of the structure with a positive curvature of the distribution in illumination. Moreover, the origin of the positive space charge in the vicinity of the cathode is fundamentally impossible to explain on the basis of a pure crystal model with strong absorption of radiation. In pure, highly biased crystals the total current essentially coincides with the hole drift current, $j \simeq e\mu_p pE$, and its invariance implies that the field increases for a negative curvature of the distribution (see Ref. 16 for more details). The problem is not solved by taking into account the space charge of deep trapping levels. Owing to the trapping of photogenerated holes by an impurity near the anode, the cathode space charge decreases, and the field at the cathode increases even more slowly than for a pure crystal.[17,15]

2. THE BASIC PHYSICAL CONCEPT

Does a physical mechanism exist to support the increase in the field near the cathode when its distribution has a positive curvature? Published results[15,18,16,19] show that such distributions are possible both in darkness and in light within definite ranges of the surface barrier height, impurity concentration, and impurity capture cross sections. They are produced exclusively by dark generation-recombination processes, which impart continuity to the electron density in the bulk of the crystal and on its surface in the presence of inefficient diffusion. A positive space charge occurs in the dark generation of electrons by an impurity, so that the degree of filling of impurity centers falls below the equilibrium value.[18] In cases where the impurity concentration and its space charge exceed the free-carrier charge, the field increases with acceleration, i.e., $d^2E/dx^2 > 0$.

Because the degree of filling of an impurity with electrons in the bulk does not change in illumination in the presence of strong absorption (see Fig. 5 in Ref. 18), the given mechanism can influence the nature of the electric fields in the unique instance when illumination generates additional carriers in the bulk. A number of facts suggest that the spectrum of the incident radiation in the experiments described in Refs. 11 and 12 contains something other than a highly ab-

sorbed component. First, the measured field distributions in the presence of weak absorption differ very little from those obtained by illumination in ''ambient'' light (Ref. 12, p. 64). Second, in these experiments the spectrum of the particular source of illumination comprises a bell-shaped distribution with a maximum at $\lambda = 0.8$ μm (1.56 eV) and with a width of approximately 0.1 eV, defined at the points where the spectral density drops by two orders of magnitude, and it probably contains frequencies corresponding to higher as well as lower values of the absorption coefficient. Assuming that the generation of holes in the bulk and their trapping by an impurity are, from the standpoint of the magnitude and sign of the space charge, equivalent to the thermal generation of electrons by the impurity, it is reasonable to expect that for high-resistivity semiconductors having a low self-charge this process will contribute significantly to the magnitude and distribution of the space charge in the structure and emerge as an inseparable part of the physical model.

The objective of the present study is to investigate the photoelectric effect in high-resistivity semiconductors when the structures are illuminated by nonmonochromatic radiation and to ascertain the role of the long-wavelength part of the spectrum on the distribution of the electric field. This problem has not been treated to date. In the papers known to us where the complete system of equations of the drift-diffusion approximation is used (see, e.g., Refs. 8, 20, and 21) and in papers that simulate the photoelectric effect in high-resistivity structures,[14,17,18,22] the generation function has been regarded as constant or has been written in the standard form corresponding to monochromatic radiation, $G(x) = \alpha I_i \exp(-\alpha x)$, where α is the absorption coefficient. Our second objective is to estimate model parameters than can be used to determine quantitative characteristics close to those observed in experiment. The determination of these quantities actually reduces to the solution of an ill-posed nonlinear inverse problem and is a complicated procedure, because an entire series of experimental principles must be satisfied simultaneously.

3. STATEMENT OF THE PROBLEM

We consider a highly biased, high-resistivity p-type semiconductor, $0 \leqslant x \leqslant d$, which has a density of equilibrium holes in the bulk p_* and which, in addition to shallow donors and acceptors, contains a deep impurity level subject to Shockley–Read statistics. Illumination takes place through a semitransparent anode at $x = 0$. A voltage V much higher than the semiconductor-metal contact potential is applied to the structure. The distribution of the densities of electrons $n(x)$ and holes $p(x)$ and of the electric field $E(x)$ are described by a system that includes the equation of continuity, the Poisson equation, and an equation describing the variation of the degree of filling of the deep impurity level by electrons. The boundary conditions describe the carrier exchange across the metal-semiconductor interface. The intensity of the exchange is specified by the surface recombination rates of electrons and holes $s_{n,p}$ and by the tunneling transmissivities of the interfaces for electrons and holes $T_{n,p}$. The mathematical statement of the problem is exactly

the same as described in Ref. 22, except that the expression for the electron-hole pair generation function incorporates the arbitrary forms of the spectrum of the incident radiation and the absorption spectrum $\alpha(h\nu)$:

$$G(x) = (1 - R) \int_0^\infty \alpha(h\nu) \frac{dI}{dh\nu} e^{-\alpha(h\nu)x} dh\nu \qquad (1)$$

(the reflection coefficient R is assumed to be constant).

The numerical method is described in Ref. 22. Parameters of the structure close to those used in experiment are specified. In particular, it is assumed that $d = 0.25$ cm and $V = 400$ V. The density of equilibrium holes in the bulk is varied in the interval $p_* = 10^8 - 10^{11}$ cm^{-3}. The surface recombination rates and tunneling transmissivities of the interfaces are set equal to $s_n = s_p = 10^6$ cm/s and $T_n = T_p = 1$. The parameters of CdTe are taken from Refs. 23 and 24. The absorption spectrum $\alpha(h\nu)$ is approximated by equations analogous to those in Ref. 25. The values of the absorption coefficient $\alpha(E_g)$ at a photon energy equal to the width of the band gap E_g and the characteristic energies are specified on the basis of data in Ref. 26. For the assumed dependence $\alpha(h\nu)$ at frequencies $h\nu \lesssim E_g$ a range of optical thicknesses of the order of $\alpha d = 1$ corresponds to $h\nu \approx 1.41$ eV $\pm kT$.

4. DARK FIELDS

The nearness of the dark fields to a uniform distribution indicates a high degree of compensation of the free and bound charges. This effect is achieved as a result of controlling the flux of holes across the metal-semiconductor interface by choosing the height of the Schottky barrier for holes equal to $E_g - e\varphi_{B_n}$, where φ_{B_n} is the barrier height for electrons. The critical value corresponding to charge compensation is attained under the condition $p_0 = p_*$ and depends on the hole tunneling transmissivity of the interface T_p (Ref. 15):

$$e\varphi_{\text{cr}} = E_g - kT \ln \frac{N_v/p_*}{1 + v_{\text{dr}}^p/V_p^T}, \qquad (2)$$

where $v_{\text{dr}}^p = \mu_p E_e$ is the hole drift velocity, and $V_p^T = V_p T_p$ is the rate of exchange across the interface. The variation of any one quantity (φ_{B_n}, T_p, or p_*) leads to decompensation of the free and bound charges and the emergence of a nonuniform field in the crystal.

Different values of φ_{B_n} correspond to different signs and values of the derivative dE/dx. In pure crystals with low heights $\varphi_{B_n} < \varphi_{\text{cr}}$ the derivative $dE/dx < 0$, and the field is almost uniform, owing to the smallness of the space charge in the structure, which is proportional to the difference $p - p_*$. When the condition $\varphi_{B_n} = \varphi_{\text{cr}}$ holds, as it does for $p_0 = p_*$, the field $E(x) = E_e$ throughout the entire structure, whereas for $\varphi_{B_n} > \varphi_{\text{cr}}$ the derivative dE/dx is positive. For the chosen values of the parameters and $p_* = 10^9$ cm^{-3} we have $e\varphi_{\text{cr}} \approx 0.923$ eV. In the range $\varphi_{B_n} > \varphi_{\text{cr}}$, which corresponds to the strong inequality $p_0 \gg p_*$, the field distribution becomes sensitive to the choice of numerical value of φ_{B_n}.

In a crystal containing deep impurity levels the field exhibits a much greater sensitivity of the dependence $E(x)$ to the choice of φ_{B_n} (see Fig. 1 in Ref. 15). The behavior of the derivative of the distribution $E(x)$ at $x=0$, $(dE/dx)_0$, which depends on the barrier height φ_{B_n}, is qualitatively the same as in the pure crystal. The derivative $(dE/dx)_0$ increases with φ_{B_n} and is equal to zero for $\varphi_{B_n}=\varphi_{cr}=0.923$ V. For $\varphi_{B_n}<\varphi_{cr}$ $(p_0, p\ll p_*)$, however, the degree of filling of the impurity with electrons is greater than the equilibrium value, and a region of negative space charge forms near the anode. For sufficiently high impurity concentrations and values of φ_{B_n} smaller than φ_{cr} by a factor of several times kT the field at the anode has a value $\tilde{E}\gg 1$, and the field moves away from the cathode part of the structure. We note that a decrease in the interface tunneling transmissivity (e.g., by virtue of an increase in the thickness of the insulator film) obstructs the hole flux across the interface and, hence, has the same effect as lowering the Schottky barrier.[15] The equality of the critical values of φ_{B_n} for the pure crystal and for the crystal containing an impurity is attributable to the fact that for $p_0=p_*$ the degree of filling of the impurity is equal to the impurity value, and the total nonequilibrium charge of the impurity centers is equal to zero.

Consequently, the height of the Schottky barrier φ_{B_n} can be determined from the specified values of p_* and T_p in accordance with the condition of uniformity of the dark field.

5. STEADY-STATE FIELD DISTRIBUTIONS IN PURE CRYSTALS

Two types of incident radiation spectra have been investigated: a step function of infinitesimally narrow frequency width with a variable photon energy (monochromatic radiation) and a Gaussian distribution (nonmonochromatic radiation). In the first case the energy of an incident light photon uniquely determines the absorption coefficient. In the second case the dependence of the absorption spectrum on the frequency (energy of an incident light photon) is taken into account. Both spectral curves are characterized by the position of the maximum $h\nu_m$ and the total flux density I_i of photons entering the semiconductor over the entire spectrum. The luminous intensity I_i is assumed to be independent of the time, and the duration of the illumination is assumed to be much longer than the field and current relaxation times.

The distribution of the field when the structure is illuminated by monochromatic light $(I_i=10^{16}\,\mathrm{cm}^{-2}\cdot\mathrm{s}^{-1})$ with various photon energies (various absorption coefficients) is shown in Fig. 1. It is evident from the figure that for optical thicknesses $\delta_0=\alpha d\gg 1$ the field distribution comes close to the square-root dependence $\tilde{E}\sim\sqrt{X}$. A decrease in the photon energy promotes more uniform emission, causes the space charge in the structure to decrease, and makes the field tend to a uniform distribution with a small positive curvature. Similar results are obtained for a Gaussian distribution of the spectral density with a fixed pulse half-width. The shift of the maximum of the distribution toward weaker absorption is analogous to a decrease in the photon energy.
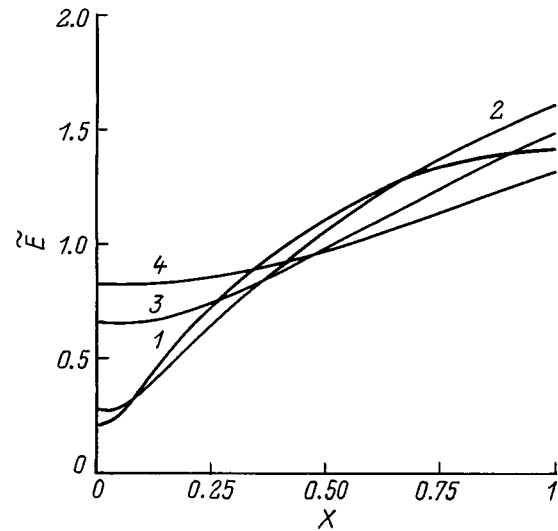

FIG. 1. Electric field distribution in pure crystals, $\tilde{E}=E/E_e=f(X)$ ($X=x/d$) in illumination by monochromatic light: (*1*) $h\nu=1.45$ eV, $\delta_0=\alpha d=14$; (*2*) 1.43 eV, 6; (*3*) 1.4 eV, 1.7; (*4*) 1.38 eV, 0.7.

Now in a fairly large neighborhood of the anode the distribution $E(x)$ is a smooth function, which increases with a small positive curvature.

The general conclusion is that the coordinate dependence of the field $E(x)$ in the vicinity of the dark electrode does not have a clearly pronounced positive curvature in a pure high-resistivity crystal illuminated by nonmonochromatic light. This conclusion qualitatively differentiates these distributions from the experimentally measured fields and therefore provides an additional basis for the assumption that the space charge of deep impurity levels in the crystals investigated in Refs. 11 and 12 significantly influences the form of the field distribution in the presence of illumination.

6. STEADY-STATE FIELD DISTRIBUTIONS IN CRYSTALS WITH DEEP IMPURITY LEVELS

6.1. The goal of our subsequent numerical calculations is to analyze the influence of various spectral compositions of the incident light on the electric fields in high-resistivity structures with uniform dark field distributions obtained by compensation of the free and bound charges. We use a solitary-level model embodying four characteristics: the energy of the level $\varepsilon_t=E_c-E_t$, the density of impurity levels N_t, and the capture cross sections σ_n and σ_p for the impurity trapping of carriers. The spectrum of the incident radiation represents the sum of two monochromatic sources with absorption coefficients $\alpha_1=10^4\,\mathrm{cm}^{-1}$ and $\alpha_2=10\,\mathrm{cm}^{-1}$. Strongly absorbed light is assumed to have an intensity $I_1=10^{16}\,\mathrm{cm}^{-2}\cdot\mathrm{s}^{-1}$, and the intensity of the weakly absorbed pulse is varied in the interval $I_2=0-7\times10^{13}\,\mathrm{cm}^{-2}\cdot\mathrm{s}^{-1}$. This approach can yield a hypothetical answer as to the influence of the long-wavelength part of the spectrum on the distribution $E(x)$, along with an interpretation of the experiment reported in Refs. 11 and 12, without the need for precise data on the spectral composition of the incident light. It can be assumed, in addition, that the field distribution is
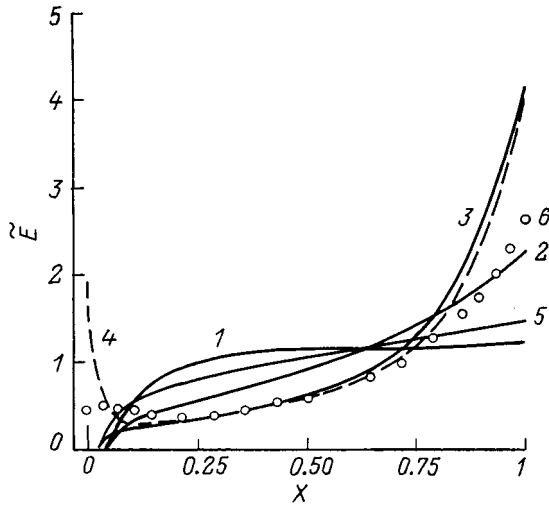
FIG. 2. Distribution of the electric field $\tilde{E} = E/E_e$ in a structure with impurity levels, illuminated by two monochromatic light pulses, for various weakly absorbed light intensities I_2 ($\alpha d = 3$, $p_* = 10^8$ cm^{-3}): (*1*) $I_2 = 0$; (*2*) 0.01×10^{13} cm$^{-2} \cdot$ s^{-1}; (*3*) 1×10^{13} cm$^{-2} \cdot$ s^{-1}; (*4*) 7×10^{13} cm$^{-2} \cdot$ s^{-1}; (*5*) 1×10^{13} cm$^{-2} \cdot$ s^{-1}; (*1–4*) calculated for $\sigma_n = 10^{-13}$ cm^{-2}; (*5*) $\sigma_n = 5 \times 10^{-14}$ cm^{-2}; (*6*) experimental[11] at a luminous intensity $I = 15$ mW/cm^2.
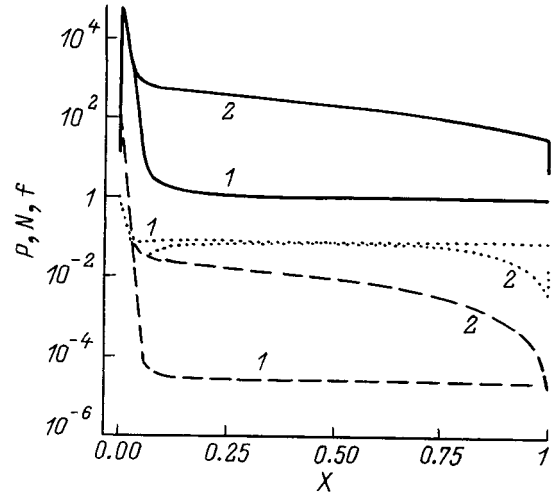

FIG. 3. Distributions of the densities of electrons $N = n/p_*$ (dotted curves) and holes $P = p/p_*$ (solid curves) and the degree of filling of a deep impurity with electrons f (dashed curves) with or without frequencies corresponding to optical thicknesses of the order of unity in the spectrum. Intensity of weakly absorbed light: (*1*) $I_2 = 0$; (*2*) 10^{13} cm$^{-2} \cdot$ s^{-1}.

significantly influenced by the very region of the spectrum with an optical thickness close to unity. This assumption stems from the fact that the exact form of the spectral density of the radiation is not all that important for photon energies $h\nu > E_g$, where the condition $\alpha d \gg 1$ holds, and photogeneration is negligible at photon energies lower than E_g by a factor of several times kT.

To achieve a significant effect, the initial data are chosen close to the parameters associated with the analytical curves of Fig. 4 in Ref. 15, where for values of φ_{B_n} different from φ_{cr} dark field distributions with a distinct positive curvature have been obtained. The following values are assigned to the main parameters: $p_* = 10^8$ cm^{-3}, $e\varphi_{B_n} = 0.865$ eV, $N_t = 10^{13}$ cm^{-3}, $\varepsilon_t = 0.8$ eV, $\sigma_n = 10^{-13}$ cm^2, $\sigma_p = 10^{-16}$ cm^2.

The steady-state field distributions for various intensities I_2 are shown in Fig. 2 (curves *1–5*). One of the experimental distributions is also shown here for comparison (curve *6*). It is evident from Fig. 2 that the field distribution in illumination by ambient light ($I_2 = 0$, curve *1*) has negative curvature and resembles the field profiles corresponding to a deep trapping level (see Fig. 5 in Refs. 17 and 15). The addition of weakly absorbed radiation with an optical thickness of the order of unity significantly affects the field distribution. It decreases in the middle part of the bulk and increases around the dark electrode. The distribution already exhibits positive curvature at an intensity $I_2 = 10^{11}$ cm$^{-2} \cdot$ s^{-1} (Fig. 2, curve *2*); with a further increase in the intensity, the field acquires a characteristic form (curve *3*) very similar to the experimentally measured electric field distributions (curve *6*). At a sufficiently high intensity, $I_2 = 7 \times 10^{13}$ cm$^{-2} \cdot$ s^{-1}, when the contribution to photogeneration of the second pulse in the vicinity of the anode is comparable with the contribution of the first pulse, new phenomena begin to appear (see curve *4*). The trapping by impurity levels of photoelectrons generated in the bulk by the weakly absorbed component of the spec-

trum forms a negative-charge region in the vicinity of the anode, with a marked increase in the field around the anode. This region is followed by a fairly broad zone in which the field varies only slightly. Such a distribution curve qualitatively resembles the case of the dark distribution for $\varphi_{B_n} < \varphi_{cr}$ (Fig. 1 in Ref. 15 or curve *5* in Fig. 2 in Ref. 2). It should be noted that the marked increase in the field close to the anode can result in additional carrier injection due to lowering of the energy barriers at the interface.

Figure 3 shows the variation of the distributions of the electron and hole densities and the degree of filling of the impurity levels when a radiation component with an optical thickness of the order of unity is introduced in the spectrum. A comparison of the curves proves conclusively that the reason for the onset of field distributions with a distinct positive curvature near the cathode is an increase in the hole density in the bulk and a decrease in the degree of filling of the deep impurity levels below the equilibrium value in the cathode part of the structure.

The influence of the spectral region with $\alpha d \simeq 1$ weakens and vanishes altogether when the hole capture cross section increases (curve *5* in Fig. 3 for $I_2 = 10^{13}$ cm$^{-2} \cdot$ s^{-1} and $\sigma_p = 5 \times 10^{-14}$ cm^2). In this case holes are trapped near the anode, the degree of filling of the levels in the cathode part tends to the equilibrium value, and the positive charge of the deep levels decreases. This effect is clearly illustrated for the dark profiles of the electric field in Fig. 6 in Ref. 15 and for the light field distributions in Fig. 7 in Ref. 18. On the other hand, to achieve the positive curvature effect, it is not necessary to specify the level energy, which can be varied over a range spanning several hundred electron-volts.

Since the density of equilibrium holes in the interior of the samples is known only very approximately in the experiment described in Refs. 11 and 12, it is necessary to estimate the sensitivity of the resulting field distributions to the choice of p_*. To do so, we have run a series of calculations for
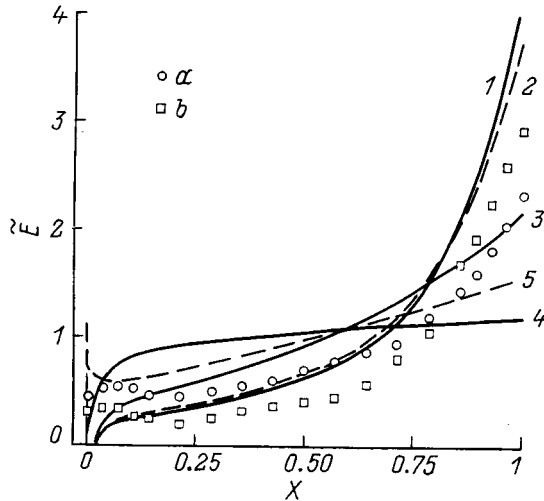
FIG. 4. Distribution of the electric field $\tilde{E} = E/E_e$ in illumination by two monochromatic light pulses: (1–4) $I_2 = 10^{13}$ cm$^{-2} \cdot$s^{-1}; (5) $I_2 = 5 \times 10^{13}$ cm$^{-2} \cdot$s^{-1}, and for various equilibrium hole densities in the bulk: (1) $p_* = 10^8$ cm^{-3}; (2) 10^9 cm^{-3}; (3) 10^{10} cm^{-3}; (4, 5) 10^{11} cm^{-3}. The experimental curves are plotted for luminous intensities $I = 6$ mW/cm^2 (a) and $I = 95$ mW/cm^2 (b) (Ref. 11).

various values of p_* in the interval $p_* = 10^8 - 10^{11}$ cm^{-3}. To preserve a uniform dark field distribution, the height of the Schottky barrier φ_{B_n} in each case is chosen with a view toward compensating the space charge in the structure according to Eq. (2). It is also necessary to preserve the influence of the variation of the impurity space charge in illumination, because the bound-charge contribution is small for $f_* \ll 1$ or $1 - f_* \ll 1$. Consequently, as the density p_* is varied, the level energy ε_t varies in such a way as to maintain the equilibrium degree of filling of the impurity $f_* = p_1/(p_1 + p_*)$ of the order of several hundred. The calculations are carried out for the following groups of parameters:

(1) $p_* = 10^9$ cm^{-3}, $e\varphi_{B_n} = 0.923$ eV, $\varepsilon_t = 0.86$ eV;

(2) $p_* = 10^{10}$ cm^{-3}, $e\varphi_{B_n} = 0.983$ eV, $\varepsilon_t = 0.92$ eV;

(3) $p_* = 10^{11}$ cm^{-3}, $e\varphi_{B_n} = 1.043$ eV, $\varepsilon_t = 0.98$ eV.

The density of impurity levels $N_t = 10^{13}$ cm^{-3}, the intensity $I_2 = 10^{13}$ cm$^{-2} \cdot$s^{-1}, and the cross sections σ_n and σ_p are the same as in the preceding case with $p_* = 10^8$ cm^{-3}. Figure 4 shows the variation of the field distributions as the ratio of the densities of free and bound charges is varied with the structure illuminated by light having a complex spectral composition. Also shown are two experimental curves (a and b) for different incident luminous intensities. It is evident from Fig. 4 that at low densities $p_* = 10^8$ cm^{-3} and $p_* = 10^9$ cm^{-3} the field distributions essentially coincide and have a characteristic form qualitatively consistent with the experimental. As the density of equilibrium holes is increased (and the relative contribution of the bound charge of deep impurity levels decreases), the field near the cathode $\tilde{E}_d = E_d/E_e$ decreases, and the distribution in the bulk becomes more uniform (curve 3). For $p_* = 10^{11}$ cm^{-3} (curve 4)

the $E(x)$ curve is similar to the field profile for strong absorption, and only when the light intensity I_2 is increased to $I_2 = 5 \times 10^{13}$ cm$^{-2} \cdot$s^{-1} (dashed curve 5) do we witness the formation of a region of high positive bound charge and restoration of the positive curvature of the profile in the cathode part of the structure. Consequently, field distributions $E(x)$ with positive curvature ($d^2E/dx^2 > 0$) exist over a wide range of densities p_*. We also note that the existence of a region of low space charge near the anode, as is clearly evident from experiment, and the rather weak dependence of the field in this part of the structure on the intensity (Figs. 2 and 4; see also Figs. 2, 4a, and 4b in Ref. 11) are attributable to the formation of a compensating negative charge in absorption of the part of the spectrum with an optical thickness close to unity. In a pure crystal with strong light absorption the field near the anode at a total radiation intensity $I_i = 10^{16}$ cm$^{-2} \cdot$s^{-1} is close to zero.[14]

6.2. The significant influence of the frequency interval with an optical thickness of the order of unity, established in the preceding section, is a motive for studying the field distributions formed when a structure is illuminated by a non-monochromatic light pulse, which generates photocarriers with different densities throughout the entire depth of the structure. The calculations are carried out for $p_* = 10^9$ cm^{-3} using the numerical values given in the previous section for the parameters of the structure and the impurity. The total flux of the incident light over the entire spectrum is $I_i = 5 \times 10^{15}$ cm$^{-2} \cdot$s^{-1}. The spectral density is specified in the form of a Gaussian distribution and is characterized by two parameters: the position of the maximum of the spectrum $h\nu_m$ and the "half-width" Δ, which characterizes the energy interval in which the spectral density decreases by $1/e$. According to previous data,[11] the position of the spectral maximum is fixed at $h\nu_m = 1.56$ eV ($\lambda = 0.8$ μm). The contribution of the long-wavelength region of the spectrum is varied by varying the half-width Δ.

Figure 5 shows steady-state field distributions for various values of Δ. Curve 1 indicates the distribution for the case $\Delta = 10^{-4}$ eV and corresponds to monochromatic light with an absorption coefficient $\alpha = 1640$ cm^{-1}. For a half-width $\Delta < (h\nu_m - E_g)/2$ the field distributions are scarcely distinguishable from the case of strong absorption (curve 2, $\Delta = 0.03$ eV). As the half-width Δ increases, a frequency interval $h\nu < E_g$ is introduced in the spectrum, and photocarriers begin to be generated throughout the structure. The region of quasi-neutrality near the anode broadens, and at a certain distance from it there appears a zone in which the field is observed to increase more and more at an accelerated rate [positive curvature of the distribution $E(x)$]. Simultaneously the field increases in the cathode part of the structure and near the dark electrode. Finally, for $\Delta = 0.07$ eV the field distribution has positive curvature in the entire structure. In this range of Δ the field at the anode becomes highly sensitive to the half-width of the pulse (the spectral density of the radiation). With only a slight increase in the contribution from the spectrum in the long-wavelength region, a region of negative space charge emerges near the anode, with very high values of the field at the anode; the field is essentially invariant in the cathode part of the structure in this case. The
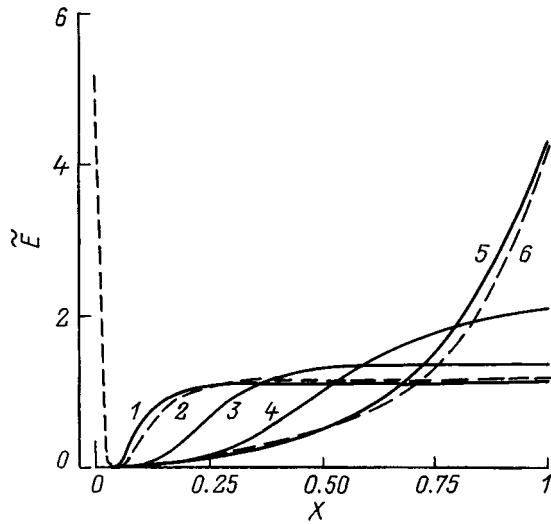
FIG. 5. Steady-state distributions of the electric field $\tilde{E} = E/E_e$ in illumination by nonmonochromatic light whose spectrum is described by a Gaussian distribution with various half-widths Δ: (*1*) $\Delta = 0$; (*2*) 0.03 eV; (*3*) 0.04 eV; (*4*) 0.05 eV; (*5*) 0.07 eV; (*6*) 0.08 eV.

FIG. 6. Distribution of the electric field $\tilde{E} = E/E_e$ in illumination by nonmonochromatic light ($I = 5 \times 10^{15}$ cm$^{-2} \cdot$ s^{-1}) whose spectral density is described by a Gaussian distribution with half-width $\Delta = 0.07$ eV for various equilibrium hole densities in the bulk p_*: (*1*) $p_* = 10^9$ cm^{-3}; (*2*) 10^{10} cm^{-3}; (*3*) 10^{11} cm^{-3}; (*4*) experimental, for a luminous intensity $I = 95$ mW/cm^2 (Ref. 11).

effect is similar to that discussed in the preceding section, when increasing the flux of light with an optical thickness of the order of unity above a certain limit began to influence the field distribution near the anode. We note that at times of the order of the hole drift transit time $t_{dr}^p = d/(\mu_p E_e)$ there is no observable difference in the field distributions for any value of Δ. The effects of positive curvature of the field begin to set in already at $t = 0.02\tau_t$, where τ_t is the impurity ionization time.[19] All these facts demonstrate the decisive influence of the bound charge on the evolution of the field distribution. The decrease in its relative contribution with an increase in the density of equilibrium holes p_* diminishes the positive curvature of the field distribution in the bulk and causes the field near the cathode to decrease (Fig. 6). This result proves that field distributions with positive curvature in illumination by nonmonochromatic light are inherent only in high-resistivity MSM structures with a sufficiently high density of deep impurity levels.

7. CONCLUSIONS

We now briefly summarize the most important results.

1. In a crystal with deep impurity levels the dark distribution of the electric field is uniform if the height of the Schottky barrier, the equilibrium hole density in the bulk, and the tunneling transmissivity of the interface satisfy the condition for compensation of the free and bound charges, i.e., relation (2).

2. In pure crystals the field distribution depends relatively weakly on the spectral composition of the incident light. As the photon energy (absorption coefficient) decreases, the coordinate dependence of the field tends to a uniform distribution and changes the curvature from negative to positive.

3. In high-resistivity crystals containing a moderate density of deep impurity levels the electric fields are not only light-sensitive but also spectrally sensitive. In illumination
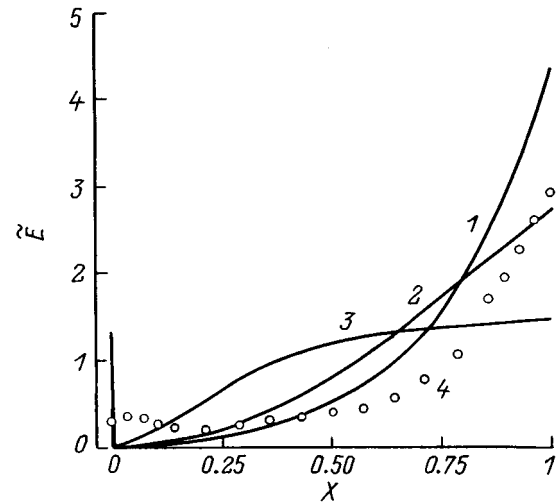
by light of complex spectral composition the energy interval corresponding to optical thicknesses of the order of $\delta_0 = \alpha d \simeq 1$, even at fluxes of the order of μW/cm^2 in this region of the spectrum, significantly influences the distribution of a field of the order of 10^3 V/cm. The reason for such influence is the decisive contribution of spectral components with $\delta_0 \simeq 1$ to the generation function in the bulk and the formation of a positive space charge when holes are trapped by an impurity. The field distributions calculated with allowance for the weakly absorbed part of the spectrum are close to the experimentally measured distributions and exhibit the most distinct features recorded in experiments (a region of positive curvature near the cathode and a region of weak space charge near the anode).

4. The field increases considerably in the vicinity of the electrodes, owing to the high negative space charge density of the deep impurities. This effect can lead to additional carrier injection from the electrodes in connection with the lowering of the energy barriers at the metal-semiconductor interface and also with the superlinear current-intensity curves.

[1] M. P. Petrov, S. I. Stepanov, and A. V. Khomenko, *Photosensitive Electrooptical Media in Holography and Optical Data Processing* [in Russian], Nauka, Leningrad, 1983.

[2] I. T. Ovchinnikov and É. V. Yanshin, Pis'ma Zh. Tekh. Fiz. **8**, 355 (1982) [Sov. Tech. Phys. Lett. **8**, 153 (1982)].

[3] V. V. Bryksin, L. I. Korovin, V. I. Marakhonov, and A. V. Khomenko, Pis'ma Zh. Tekh. Fiz. **9**, 385 (1983) [Sov. Tech. Phys. Lett. **9**, 165 (1983)].

[4] V. N. Astratov and A. V. Il'inskiĭ, Fiz. Tverd. Tela (Leningrad) **24**, 108 (1982) [Sov. Phys. Solid State **24**, 61 (1982)].

[5] N. F. Mott and W. Gurney, *Electronic Processes in Ionic Crystals*, 2nd ed. [Dover, New York, 1964; 1st ed., IL, Moscow, 1950].

[6] V. V. Bryksin, L. I. Korovin, and Yu. K. Kuz'min, Fiz. Tverd. Tela (Leningrad) **28**, 2728 (1986) [Sov. Phys. Solid State **28**, 1528 (1986)].

[7] V. N. Astratov and A. V. Il'inskiĭ, FTI Preprint No. 1091 [in Russian]

(A. F. Ioffe Physicotechnical Institute, Academy of Sciences of the USSR, Leningrad, 1986).

[8] V. N. Klimova, Mikroelektronika **10**, 457 (1981).

[9] E. N. Arkad'eva, L. V. Maslova, O. A. Matveev, S. V. Prokof'ev, S. M. Ryvkin, and A. Kh. Khusainov, Dokl. Akad. Nauk SSSR **221**, 77 (1975) [Sov. Phys. Dokl. **20**, 211 (1975)].

[10] P. G. Kasherininov, A. V. Kichaev, Yu. N. Perepelitsin, Yu. O. Semenov, and I. D. Yaroshetskiĭ, Élektrosvyaz, No. 10, 27 (1990).

[11] P. G. Kasherininov, A. V. Kichaev, and A. A. Tomasov, Fiz. Tekh. Poluprovodn. **29**, 2092 (1995) [Semiconductors **29**, 1092 (1995)].

[12] A. V. Kichaev, ''Structural transformation of the electric field in high-resistance semiconductor structures,'' Candidate's Dissertation [in Russian], A. F. Ioffe Physicotechnical Institute, Russian Academy of Sciences, St. Petersburg, 1995.

[13] P. G. Kasherininov, A. V. Kichaev, and I. D. Yaroshetskiĭ, Zh. Tekh. Fiz. **65**(9), 193 (1995) [Tech. Phys. **40**, 970 (1995)].

[14] P. G. Kasherininov, B. I. Reznikov, and G. V. Tsarenkov, Fiz. Tekh. Poluprovodn. **26**, 1480 (1992) [Sov. Phys. Semicond. **26**, 832 (1992)].

[15] B. I. Reznikov and G. V. Tsarenkov, Fiz. Tekh. Poluprovodn. **29**, 2189 (1995) [Semiconductors **29**, 1147 (1995)].

[16] B. I. Reznikov, Fiz. Tekh. Poluprovodn. **30**, 1497 (1996) [Semiconductors **30**, 787 (1996)].

[17] B. I. Reznikov and G. V. Tsarenkov, Fiz. Tekh. Poluprovodn. **28**, 1788 (1994) [Semiconductors **28**, 991 (1994)].

[18] B. I. Reznikov and G. V. Tsarenkov, Fiz. Tekh. Poluprovodn. **29**, 1430 (1995) [Semiconductors **29**, 743 (1995)].

[19] B. I. Reznikov, Fiz. Tverd. Tela (St. Petersburg) **39**, 1775 (1997) [Phys. Solid State **39**, 1582 (1997)].

[20] A. E. Iverson and D. L. Smith, IEEE Trans. Electron Devices **ED-34**, 2098 (1987).

[21] N. A. Kudryashov, S. S. Kucherenko, and Yu. I. Syts'ko, Mat. Model. **1**(12), 1 (1989).

[22] B. I. Reznikov, Fiz. Tekh. Poluprovodn. **31**, 1003 (1997) [Semiconductors **31**, 857 (1997)].

[23] S. M. Sze, *Physics of Semiconductor Devices*, 2nd ed. [Wiley–Interscience, New York, 1981; Mir, Moscow, 1984].

[24] L. A. Bovina and V. I. Stafeev, *Physics of II–VI Compounds* (Mir, Moscow, 1971).

[25] B. M. Morozov, Yu. B. Bolkhovitinov, R. S. Gabaraev, A. F. Kravchenko, and V. I. Yudaev, Fiz. Tekh. Poluprovodn. **14**, 1486 (1980) [Sov. Phys. Semicond. **14**, 883 (1980)].

[26] K. Zanio, *Semiconductors and Semimetals*, Vol. 13: *Cadmium Telluride* (Academic Press, New York–London, 1978).

Translated by James S. Wood

Heterojunctions utilizing CuIn$_x$Ga$_{1-x}$Te$_2$ thin films

V. Yu. Rud'*)

St. Petersburg State Technical University, 195251 St. Petersburg, Russia

Yu. V. Rud' and R. N. Bekimbetov

A. F. Ioffe Physicotechnical Institute, Russian Academy of Sciences, 194021 St. Petersburg, Russia

V. F. Gremenok, I. A. Viktorov, I. V. Bodnar', and D. D. Krivolap

*Institute of Solid-State and Semiconductor Physics, National Academy of Sciences of Belarus,
220072 Minsk, Belarus*

Polycrystalline CuIn$_x$Ga$_{1-x}$Te$_2$ thin films are prepared by pulsed laser evaporation. The room-temperature hole densities and mobilities of the films are determined. It is established that direct optical contact of the postgrowth surface of such films with the surface of a cleaved InSe wafer exhibits the photovoltaic effect. The spectra of the relative quantum efficiency of photoconversion of the heterojunctions are investigated as a function of the composition of the CuIn$_x$Ga$_{1-x}$Te$_2$ films and the photodetection geometry. It is concluded that the fabricated heterojunctions have potential applications in photodetectors of unpolarized radiation. © *1999 American Institute of Physics.* [S1063-7826(99)01307-1]

Ternary A^{I}B^{III}C$_2^{VI}$ compounds and their solid solutions have gained widespread applications in developments of high-efficiency, thin-film devices for the photoconversion of solar energy.[1–4] The efficiency of superior solar cells utilizing Cu(In,Ga)Se$_2$ has already attained 18% (Ref. 5). Further optimization of such photoconverters can be pursued through detailed physicotechnological studies of the interconnection between technological processes and the properties of specific types of structures, and also through assimilation of the numerous systems of solid solutions based on A^{I}B^{III}C$_2^{VI}$ semiconductors. Here we give the results of first-time investigations of the photoelectric properties of heterojunctions constructed by forming an optical contact between natural chips of the lamellar semiconductor InSe and the outer surface of thin polycrystalline CuIn$_x$Ga$_{1-x}$Te$_2$ films.

1. PREPARATION OF CuIn$_x$Ga$_{1-x}$Te$_2$ FILMS

The targets used for spray deposition of the films were crystals synthesized by oriented crystallization from the melt.[6,7] Initial components of semiconductor-rated purity were used for synthesis. X-ray examination showed that the grown crystals had a large-block (12 mm in diameter and 40 mm in length) structure and were homogeneous.

The Cu(In,Ga)Te$_2$ films were vacuum-evaporated (10^{-5} Torr) by means of an industrial free-running laser (λ = 1.06 μm, $t_{\text{pulse}} = 10^{-3}$ s, $F_{\text{pulse}} = 150-180$ J).[8] The substrates were chemically cleaned glass maintained at a temperature $T_s = 470-490$ °C. The thicknesses of the final films in the active area of 2 cm^2 were $0.3-1.0$ μm.

The composition of the thin films was monitored by microprobe x-ray spectral analysis and was reproduced in the diagnostics of different sections of the films (within ± 5%

methodological error limits). X-ray examinations showed that only the system of lines associated with a chalcopyrite structure is observed in the diffraction patterns of the pulverized crystals and the films obtained from them by vacuum evaporation.

2. ELECTRICAL PROPERTIES OF THE THIN FILMS

Investigations of the resistivity and the Hall effect have shown that the method used here is capable of yielding electrically homogeneous films of CuIn$_x$Ga$_{1-x}$Te$_2$ solid solutions. Table I shows typical values of the resistivity ρ, the density p, and the Hall mobility μ of free holes for the samples. It is evident from Table I that the solid solutions preserve the p-type conductivity inherent in the initial compounds. The reduction of the Hall mobility in the solid solutions of the relatively ordered phases can be the result of both scattering by the random potential and variations in the hole density. It is important to emphasize that the resistivity of the solid solution thin-film samples does not increase relative to the ternary compounds from which they are formed. On this basis it is justifiable to expect the quantum efficiency

TABLE I. Electrical properties of CuIn$_x$Ga$_{1-x}$Te$_2$ thin films at $T = 300$ K.

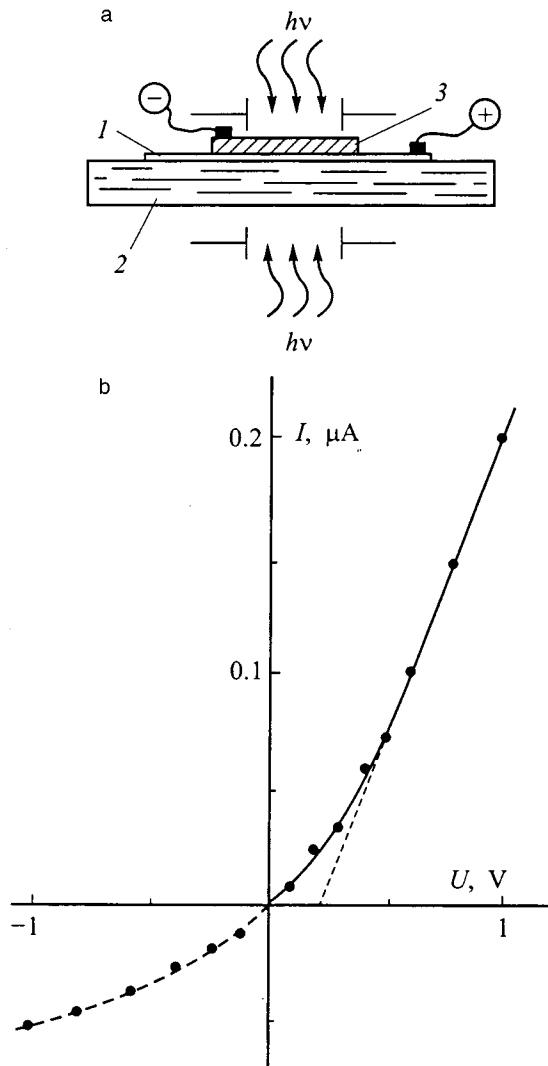| x, mol. %	T_s, °C	d, μm	$\rho \cdot 10^2$, $\Omega \cdot$cm	$p \cdot 10^{-18}$, cm^{-3}	$U p$, cm^2/(V$\cdot$s)
1.0	470	0.32	2.9–3.7	5.5–5.7	34–38
0.27	480	0.72	1.1–7.8	4.1–5.9	14–18
0.5	480	0.58	2.4–3.2	4.8–6.7	16–27
0.6	480	0.54	3.4–3.6	6.8–13	20–43
0.87	480	0.63	1.3–2.2	3.1–16	41–60
0.0	480	0.50	1.4–2.1	4.4–10	67–91

FIG. 1. (a) Structure of a heterojunction utilizing a $CuIn_xGa_{1-x}Te_2$ thin film (*1*) and an InSe wafer (*3*) deposited on the surface a glass substrate (*2*); (b) steady-state I–V characteristic of a p-$CuIn_{0.5}Ga_{0.5}Te_2$/n-InSe heterojunction at $T=300$ K.

of photoconverters utilizing thin films of the solid solutions not to be any lower than analogous $CuInTe_2$ or $CuGaTe_2$ structures because of degradation of the current-transport properties.

3. FABRICATION OF PHOTOSENSITIVE STRUCTURES AND THEIR PROPERTIES

It has been established on the basis of investigations of contact effects of the prepared films with various metals (In, Cu, Au, Mo, etc.) and the lamellar semiconductor InSe that the reproducible observation of a pronounced photovoltaic effect occurs only for a p-$CuIn_xGa_{1-x}Te_2$/n-InSe heterojunction.

The structure of the fabricated heterojunctions is shown in Fig. 1a. A freshly cleaved wafer of indium selenide 3 of thickness ≈ 50 μm and area ranging from 2×2 mm to 5×5 mm is pressed uniformly onto the outer surface of a thin film of the solid solution 1, which is deposited on a glass substrate 2. All the heterojunctions constructed in this way exhibit the rectification effect with reproducible consistency. A typical steady-state current-voltage (I-V) characteristic for one such heterojunction is shown in Fig. 1b. The direction of the through current corresponds to negative polarity of the external bias on the n-InSe wafer in this case. The forward branch of these curves obeys the equation

$$U = U_0 + R_0 \cdot I, \tag{1}$$

where U_0 is the cutoff voltage, and R_0 is the residual resistance of the structures, which is shown in Table II. It is evident that the residual resistance for the prepared heterojunctions is fairly high and weakly dependent on the quantity x characterizing the composition of the solid solution. Taking the resistivity of $CuIn_xGa_{1-x}Te_2$ films into account (Table I), we can assume that the high values of R_0 in the fabricated heterojunctions are governed by the resistance of the heterocontact of films of different compositions with the cleaved indium selenide surface.

When the prepared heterojunctions are illuminated either from the InSe side or from the glass substrate side, a photovoltage is created as a result of separation of the photogenerated pairs of the active zone of the structures. The sign of the photovoltaic effect does not depend on where the radiation is incident on the surface of such structures or on the energy of the incident photons; here a negative potential always corresponded to indium selenide; this result, in turn, is consistent with the direction of rectification in such heterojunctions.

The maximum values of the voltage (S_U) and current (S_I) photosensitivities of $CuIn_xGa_{1-x}Te_2$/InSe are listed in Table II for both geometries of their illumination by ambient

TABLE II. Photoelectric properties of heterojunctions based on $CuIn_xGa_{1-x}Te_2$ thin films at $T=300$ K.

| Structure type	$R \cdot 10^{-5}$, Ω	Substrate illumination				InSe wafer illumination			
		S_U, V/W	S_I, μm/W	$h\nu$, eV	$\delta_{1/2}$, meV	S_U, V/W	S_I, μm/W	$h\nu$, eV	$\delta_{1/2}$, meV
$CuInTe_2$/InSe	1.3	10	1	1.23	500	10	0.5	1.21	50
$CuIn_{0.87}Ga_{0.13}Te_2$/InSe	3.3	6	0.5	1.24	550	20	40	1.21	27
$CuIn_{0.6}Ga_{0.4}Te_2$/InSe	2.0	4	60	1.22	150	1	10	1.21	25
$CuIn_{0.5}Gs_{0.5}Te_2$/InSe	3.3	1	3	1.24	340	20	0.2	1.21	25
$CuIn_{0.27}Ga_{0.73}Te_2$/InSe	2.8	1	0.1	1.22	100	28	10	1.21	40
$CuGaTe_2$/InSe	2.0	20	5	1.23	200	10	1	1.21	50
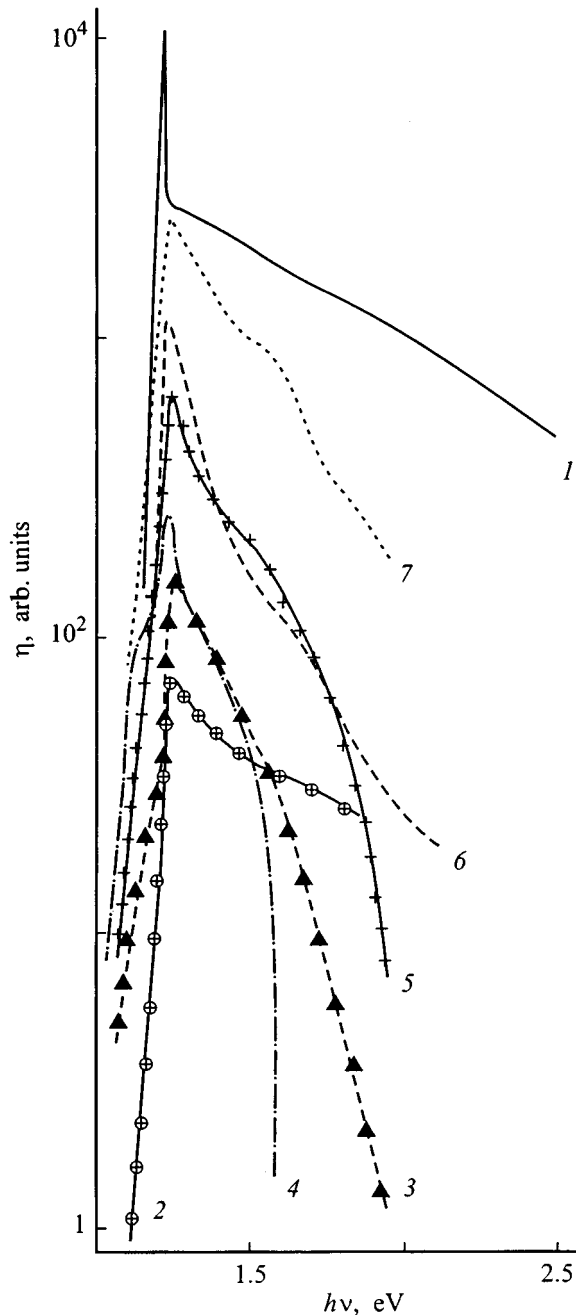
FIG. 2. Spectral curves of the relative quantum efficiency of $CuIn_xGa_{1-x}Te_2/InSe$ heterojunctions at $T = 300$ K in ambient light. Illumination geometry: (*1*) from the InSe side; (*2–7*) from the $CuIn_xGa_{1-x}Te_2$ side: (*2*) $x = 1.0$ mole %; (*3*) 0.27 mole %; (*1, 4*) 0.5 mole %; (*5*) 0.6 mole %; (*6*) 0.87 mole %; (*7*) 0. The spectral resolution is at least 1 meV.

junctions. The resulting spectra exhibit the following features. The spectra are similar when heterojunctions utilizing solid solutions of any composition is illuminated from the side of the InSe film. The long-wavelength exponential edge of η and its spectral position are determined by direct interband transitions in InSe,[9] and the narrowly selective maximum of the photosensitivity is attributable to the influence of absorption of the incident radiation by the film of direct-gap $CuIn_xGa_{1-x}Te_2$ solid solutions. This is what causes the very steep short-wavelength decay of η followed by a monotonic decrease of the photosensitivity. It is evident from Table II that the energy position of the photosensitivity peak ($h\nu$) in illumination from the side of the InSe wafer, which is identical for all structure, is identical. The photosensitivity band in the given photodetection geometry is found to have a small FWHM (full width at half-maximum of the quantum efficiency) $\delta_{1/2}$, its value varying in the interval 25–50 meV, which can be attributed to differences in the quality of the heterointerface. The fact that the photosensitivity of the heterojunction is determined mainly by absorption in the indium selenide can be identified with the predominant localization of the active zone of these heterojunctions in the InSe film. The latter condition is dictated by differences in the doping levels of the InSe and the $CuIn_xGa_{1-x}Te_2$ solid solutions.

When the illumination of the heterojunctions is changed to the side of the $CuIn_xGa_{1-x}Te_2$ films, the maximum of the quantum efficiency shifts 2−3 meV into the short-wavelength region and is situated at 1.22–1.24 eV, which corresponds to the width of the InSe band gap.[9] This shift is also found to be insensitive to the composition of the solid solution films. In comparison with illumination of the heterojunctions from the InSe side, the long-wavelength edge of η is not as steep, and a number of heterojunctions exhibit a long-wavelength photosensitivity peak (Fig. 2, curves *3* and *4*) associated with increased absorption in the $CuIn_xGa_{1-x}Te_2$ film. Another noticeable characteristic is an increase in the width of the photosensitivity bands of the heterojunctions when they are illuminated from the side of the $CuIn_xGa_{1-x}Te_2$ film, which is thinner than the InSe; this effect is also attributable to the reduction of absorption in the InSe wafer. Finally, in illumination from the side of the solid solution films the spectra of η acquire in the vicinity of 1.5 eV a steeper decay of the photosensitivity than in illumination from the InSe side. This effect is probably caused by the influence of absorption in the solid solution film itself.[10,11]

On the whole, it is probably reasonable to conclude from a comparison of the photosensitivity spectra of the fabricated heterojunctions that the widths of the band gaps in the films of the $CuIn_xGa_{1-x}Te_2$ solid solutions and the InSe are close to one another. This most likely accounts for our not having detected any appreciable differences in the spectra of η for the two given photoexcitation geometries.

In summary, we have used $CuIn_xGa_{1-x}Te_2$ thin films grown by pulsed laser deposition, establishing optical contact between them and InSe cleavage surfaces, to construct photosensitive heterojunctions with good potential applications as wide-gap, narrowly selective photodetectors of natural radiation. At the same time, it is important to note the

light. It should be noted that we did not detect any distinct local dependence of S_U and S_I when the placement of the InSe wafer was shifted along the surface of the $CuIn_xGa_{1-x}Te_2$ films, demonstrating good homogeneity of the solid solution films. It is similarly essential to note the absence of any kind of degradation effects in the photosensitivity of the structures formed by establishing direct optical contact between the postgrowth surfaces of the solid solution thin films and the natural cleavage planes of the InSe.

Figure 2 shows typical spectral curves of the relative quantum efficiency η of $CuIn_xGa_{1-x}Te_2$ thin-film hetero-

possibility of using the movable optical contact of lamellar semiconductors to evaluate the quality of polycrystalline thin films of chalcopyrite semiconductor compounds as materials for photovoltaic radiation converters.

*)E-mail: rudvas@uniys.hop.stu.neva.ru

---

[1] L. Stolt, J. Hedström, J. Kessler, M. Ruckh, K. O. Velthaus, and H. W. Schock, Appl. Phys. Lett. **62**, 597 (1993).

[2] N. N. Konstantinova, M. A. Magomedov, V. Yu. Rud', and Yu. V. Rud', Fiz. Tekh. Poluprovodn. **26**, 558 (1992) [Sov. Phys. Semicond. **26**, 317 (1992)].

[3] F. Guastavino, M. Berghol, U. Sudibyo, G. Masse, and K. Djessas, Cryst. Res. Technol. **31**, 489 (1996).

[4] M. Hornung, K. W. Benz, L. Marguliu, D. Schmid, and H. W. Schock, J. Cryst. Growth **154**, 315 (1995).

[5] H. W. Schock, Appl. Surf. Sci. **92**, 606 (1996).

[6] I. V. Bondar', V. F. Gremenok, I. A. Viktorov, and D. D. Krivolap, Pis'ma Zh. Tekh. Fiz. **24**(3), 18 (1998) [Tech. Phys. Lett. **24**, 89 (1998)].

[7] I. V. Bodnar and N. S. Orlova, Cryst. Res. Technol. **21**, 1091 (1986).

[8] I. V. Bodnar, V. F. Gremenok, E. P. Zaretskya, and I. A. Victorov, Thin Solid Films **207**, 54 (1992).

[9] T. Walter, V. Yu. Rud', Yu. V. Rud', and H. W. Schock, Fiz. Tekh. Poluprovodn. **31**, 806 (1997) [Semiconductors **31**, 681 (1997)].

[10] *Physicochemical Properties of Semiconductor Materials: Handbook* [in Russian], Nauka, Moscow, 1978).

[11] C. Rincon, S. M. Wasim, G. Marin, and G. Sanches-Perez, J. Appl. Phys. **32**, 4550 (1997).

Translated by James S. Wood

LOW-DIMENSIONAL SYSTEMS

Intraband light absorption in quasi-two-dimensional systems in external electric and magnetic fields

É. P. Sinyavskiĭ and S. M. Sokovnich

Institute of Applied Physics, Moldovan Academy of Sciences, MD-2028 Kishinev, Moldova

Intraband light absorption in parabolic quantum wells is studied with an electric field directed along the spatial quantization axis and a magnetic field parallel to the plane of the size-confined system. In such a geometry direct optical transitions between the quantum-well levels are possible, the peak light absorption coefficient reaches large values ($\sim 3 \times 10^2 \, \text{cm}^{-1}$), and the frequency of the absorption maximum depends on magnetic field strength. It is shown for the normal incidence of electromagnetic waves that the level of absorption decreases with increasing electric field strength and that it is incorrect to confine the calculations to the Born approximation in strong magnetic fields. © *1999 American Institute of Physics.*
[S1063-7826(99)01407-6]

1. The great interest in research on intraband optical transitions (for example, transitions between quantum-well conduction-band states) in quantum wells (QW's) is due to the possible creation of far-infrared detectors,[1] emitters, and high-speed modulators, as well as quantum cascade lasers.[2] The possibility of creating QW's of various width permits variation of the working wavelength of the detector, making quantum-well systems promising for optoelectronics. Intense absorption via intraband transitions was first observed in GaAs/AlGaAs QW's in Ref. 3. The strong infrared intraband absorption at a wavelength of 8.2 μm in doped GaAs/AlAs QW's was investigated in Ref. 4. The peak absorption at room temperature reached a value of $1.6 \times 10^4 \, \text{cm}^{-1}$. The intraband absorption of light in indirect semiconductor QW's has been studied extensively in recent years.[5–10]

Si/Si$_{1-x}$Ge$_x$ (Refs. 5–8), GaSb/Ga$_{0.6}$Al$_{0.4}$Sb$_{0.9}$Al$_{0.1}$ (Ref. 6), and Ga$_{1-x}$Al$_x$Sb/AlSb quantum wells (Ref. 9) can exhibit intense intravalley absorption ($L1 \rightarrow L2$) in the [100] direction, which can serve as a firm basis for employing them as infrared detectors. Owing to the strong effective-mass anisotropy for normal incidence, the peak absorption reaches high values ($\sim 9 \times 10^3 \, \text{cm}^{-1}$).

This paper describes an investigation of the features of the intraband light absorption in parabolic QW's in external electric and magnetic fields.

Parabolic QW's are very attractive quantum-confined systems, since equidistant quantum-well states appear in them when the thickness of the well layer d_0 is fairly large. For example, for GaAs/Al$_x$Ga$_{1-x}$As parabolic QW's with $d_0 = 1000$ Å the quantum-well step reaches 14 meV, and these quantum levels can, therefore, easily be observed experimentally at $T < 100$ K. Thus, it is not surprising that the optical properties of parabolic QW's have been investigated experimentally in structures with $d_0 > 2000$ Å.[11,12] Just such broad QW's can be very promising for optoelectronics, since

they permit relatively simple investigations of the intense intraband absorption of light incident parallel to the surface of the system (with the polarization vector directed parallel to the spatial quantization axis). The presence of external electric and magnetic fields makes it possible to control the working frequency of an infrared (IR) detector and the level of intraband light absorption.

2. Let us consider a parabolic QW immersed in a uniform electric field, whose intensity vector **F** is directed along the spatial quantization axis z, while the vector of the external magnetic field H is parallel to the QW surface. In the field configuration under consideration the sought-for Hamiltonian for an electron can be written in the form

$$\hat{H} = \frac{1}{2m}\left(\hat{P} + \frac{e}{c}\mathbf{A}\right)^2 + eFz + \frac{1}{2}m\omega^2 z^2. \tag{1}$$

Here m is the electron effective mass, $\hbar\omega$ is the spatial quantization energy, and **A** is the vector potential. In the gauge for the vector potential $\mathbf{A}(0,Hz,0)$, if the vector of the external magnetic field is directed along the x axis [$\mathbf{H}(H,0,0)$], the wave functions and eigenvalues of the Hamiltonian can be found directly:

$$\Psi_\alpha(\mathbf{r}) = \frac{1}{\sqrt{L_x L_y}}\left(\frac{\lambda}{\pi}\right)^{1/4}\exp[i(K_x + K_y)]$$

$$\times \exp\left[-\frac{1}{2}\lambda(z + \tilde{z}_0)^2\right]H_n[\sqrt{\lambda}(z + \tilde{z}_0)], \tag{2}$$

$$E_\alpha = \frac{1}{2m}\hbar^2 K_x^2 + \frac{1}{2m}\left(\frac{\omega}{\omega_0}\right)^2$$

$$\times (K_y - K_0)^2 + \hbar\omega_0\left(n + \frac{1}{2}\right) - \frac{e^2 F^2}{2m\omega^2}. \tag{3}$$

Here

$$\lambda = m\omega_0/\hbar, \quad \omega_0^2 = \omega^2 + \omega_c^2, \quad \omega_c = eH/mc,$$

$$-\tilde{z}_0 = (eF + \hbar\omega_c K_y)/m\omega_0^2, \quad K_0 = eF\omega_c/\hbar\omega^2,$$

$H_n(x)$ are Hermite polynomials, $\alpha(n, K_x, K_y)$ are the quantum numbers specifying the quantum states, K_x and K_y are the projections of the electron wave vector, and L_x and L_y are the lengths of the QW in the x and y directions, respectively.

Let linearly polarized light with a frequency Ω be incident parallel to the surface of the parabolic QW, and let the polarization vector be directed along the spatial quantization axis. In this case direct optical transitions are possible between the lower state with $n=0$ and the next state with $n=1$, and the light absorption coefficient is specified by the relation

$$K(\Omega) = \frac{4\pi e^2 \lambda \hbar}{c\sqrt{\varepsilon_0}m^2\Omega} n_e \frac{\gamma}{\gamma^2 + (\omega_0 - \Omega)^2}. \tag{4}$$

Here n_e is the electron concentration in the size-confined system; ε_0 is the dielectric constant of the semiconductor QW; and the quantity $2\hbar\gamma$ specifies the intraband absorption half-width and, with allowance for the scattering of electrons on acoustic modes in the elastic-scattering approximation at temperatures where $k_0 T/\hbar\omega_0 < 1$, has the form

$$2\gamma\hbar = \sqrt{\frac{m\omega}{2\pi\hbar}} \frac{k_0 T m E_1^2}{\rho\hbar^2 v^2} \left(\frac{\omega_0}{\omega}\right)^{3/2}, \tag{5}$$

where E_1 is the deformation potential constant, ρ is the density of the crystal, and v is the speed of sound. For the typical parameters of a GaAs/AlGaAs parabolic QW $E_1 = 7$ eV, $\rho = 5.4$ g/cm^3, $v = 3 \times 10^5$ cm/s, $m = 0.06m_0$, and $\hbar\omega$ [eV] $= 14/d_0$ [Å], at $T = 300$ K we have $\omega_0/\omega = 12$, $d_0 = 10^3$ Å, and $2\gamma\hbar \approx 5$ meV. According to (4), the absorption coefficient at the maximum ($\omega_0 = \Omega$) has the form

$$K_m(\omega_0) = 4\pi e^2 n_e / c\sqrt{\varepsilon_0}m\gamma, \tag{6}$$

and for $n_e = 2 \times 10^{15}$ cm^{-3} and $\varepsilon_0 = 8.2$, $K_m(\omega_0) = 3 \times 10^2$ cm^{-1}.

Since the energetic distance between the electron states, which is equal to $\hbar\omega_0$, increases with magnetic field strength, there is a unique possibility for controlling the working frequency of an IR detector over a broad range by varying the external field.

3. If an electromagnetic wave is incident perpendicularly to the surface of the quantum-well system, intraband light absorption is possible when a ''third body,'' which alters the quasimomentum of the carrier, participates in the absorption process. Let us investigate indirect optical transitions, where electron scattering occurs on an impurity center, which we shall describe in the zero-range potential model.[13] According to the solution of the Lippman–Schwinger equation, in this model the wave function of a band carrier with an energy E_α has the form

$$\Psi_\alpha(\mathbf{r}) = \Psi_\alpha^{(0)}(\mathbf{r}) + \frac{V_0}{1 - V_0 \tilde{G}_\alpha(z_0, z_0)} \tilde{\Psi}_\alpha^{(0)}(\mathbf{r}) G_\alpha(\mathbf{r}, z_0). \tag{7}$$

The Green's function $G_\alpha(\mathbf{r}, z_0)$ is defined by the relation

$$G_\alpha(\mathbf{r}, z_0) = \sum_{\alpha'} \frac{\Psi_{\alpha'}^{(0)}(\mathbf{r}) \Psi_{\alpha'}^{*(0)}(z_0)}{E_\alpha - E_{\alpha'} + i\delta}, \quad \delta \to +0, \tag{8}$$

V_0 describes the power of the impurity center and is related to the energy of the localized state E_0 ($E_0 = -2\pi^2\hbar^6/V_0^2 m^3$), and

$$\tilde{A}(z_0) = \left[1 + x\frac{\partial}{\partial x} + y\frac{\partial}{\partial y} + (z - z_0)\frac{\partial}{\partial z}\right] A(\mathbf{r}) \Big|_{\substack{x=y=0, \\ z=z_0}}.$$

In writing formula (7) it was assumed that the impurity is localized at a point with the coordinates $\mathbf{r}_0(0,0,z_0)$.

If the polarization vector of the light wave is directed along the magnetic field strength vector ($\mathbf{H}\|0x$), the matrix element of the momentum operator acting on the wave functions (7) can be calculated directly. As a result, with consideration of the energy conservation law $E_{\alpha'} - E_\alpha = \hbar\Omega$ we obtain

$$\int \Psi_\alpha^*(\mathbf{r}) \hat{P}_x \Psi_{\alpha'}(\mathbf{r}) \, d\mathbf{r}$$

$$= \frac{V_0}{L_x L_y} \left(\frac{\lambda}{\pi}\right)^{1/2} \frac{1}{\Omega} \frac{1}{\sqrt{2^n n! 2^{n'} n'!}} \exp\left[-\frac{\lambda}{2}(\tilde{z}_0 + z_0)^2\right]$$

$$\times \exp\left[-\frac{\lambda}{2}(\tilde{z}_0' + z_0)^2\right] H_n[\sqrt{\lambda}(\tilde{z}_0 + z_0)] H_{n'}$$

$$\times [\sqrt{\lambda}(\tilde{z}_0' + z_0)] \left\{ -\frac{K_x'}{1 - V_0 \tilde{G}_\alpha^*(z_0, z_0)} \right.$$

$$\left. + \frac{K_x}{1 - V_0 \tilde{G}_{\alpha'}(z_0, z_0)} \right\}. \tag{9}$$

We shall henceforth consider the case where $\beta\hbar\omega_0 \gg 1$, in which the electrons are in the lowest conduction band ($n = 0$). Processes with the absorption of light followed by scattering on an impurity [the second term in (9)] are less probable than processes with scattering on an impurity potential followed by the absorption of electromagnetic radiation [the first term in (9)]. Using the approximations indicated above, we can represent the absorption of light in the form

$$K(\Omega) = \frac{8\pi e^2 V_0^2 N_c}{c\sqrt{\varepsilon_0}m^2\Omega^3} \frac{\lambda}{(L_x L_y)^2} \sum_{\alpha', K_x, K_y} f_{K_x K_y}^{(0)} \frac{1}{2^{n'} n'!}$$

$$\times \exp[-\lambda(\tilde{z}_0 + z_0)^2] \exp[-\lambda(\tilde{z}_0' + z_0)^2]$$

$$\times H_{n'}^2[\sqrt{\lambda}(\tilde{z}_0' + z_0)] \frac{K_x'^2}{|1 - V_0 \tilde{G}_\alpha^*(z_0, z_0)|^2}$$

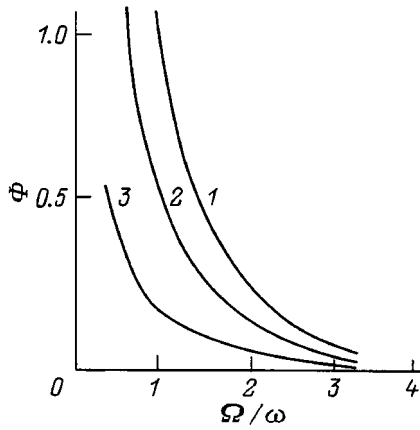$$\times \delta[E_{\alpha'} - E_\alpha - \hbar\Omega], \tag{10}$$

FIG. 1. Frequency dependence of the light absorption coefficient (in relative units): 1–3 — $\xi^2 = 0, 1, 2$, respectively.

FIG. 2. Temperature dependence of $J_0(\beta, \delta)$. 1–4 — $\delta = 0.25$, 1, 4, 10, respectively.

where N_c is the concentration of impurity centers.

For nondegenerate semiconductor QW's

$$f^{(0)}_{K_x K_y n} = n_e^0 \left(\frac{\omega}{\omega_0} \right) \frac{\pi \beta \hbar^2}{m}$$

$$\times \exp \left\{ -\beta \left[\frac{\hbar^2 K_x^2}{2m} + \frac{\hbar^2}{2m} \left(\frac{\omega}{\omega_0} \right)^2 (K_y - K_0)^2 \right] \right\},$$

where $n_e^0 = N/L_x L_y$ is the surface concentration of electrons.

Let us consider some particular cases, which permit an analytical investigation of the behavior of $K(\Omega)$ in external fields. If there is no magnetic field ($\omega_c = 0$, $\omega_0 = \omega$), the intraband light absorption takes the form

$$K(\Omega) = K^{(B)}(\Omega) J(\xi, \beta). \qquad (11)$$

Here we have introduced the notation

$$K^{(B)}(\Omega) = \frac{e^2 V_0^2 N_c n_e m}{c \hbar^4 \omega \sqrt{\varepsilon_0}} \exp(-\xi^2) \Phi(\xi, \Omega),$$

$$\xi^2 = \left(z_0 + \frac{eF}{m\omega^2} \right)^2 \lambda_0, \quad \lambda_0 = \frac{m\omega}{\hbar},$$

$$\Phi(\xi, \Omega) = \exp(-\xi^2) \sum_n \frac{H_n^2(\xi)}{2^n n!} \left(1 - \frac{\hbar\omega}{\hbar\Omega} n \right) \left(\frac{\omega}{\Omega} \right)^2,$$

$$J(\xi, \beta) = \int_0^\infty \frac{\exp(-x)}{|1 - \widetilde{G}_x(z_0, z_0)|^2} dx. \qquad (12)$$

As follows directly from the energy conservation law, $1 - n\omega/\Omega \geqslant 0$. The function $J(\xi, \beta)$ describes the deviation of $K(\Omega)$ from the absorption in the Born approximation $K^{(B)}(\Omega)$. The Green's function $\widetilde{G}_x(z_0, z_0)$ is calculated by the usual procedure used in the zero-range potential model.[13] The expression for $\widetilde{G}_x(z_0, z_0)$ is not presented here because of its cumbersomeness. An analysis reveals that at temperatures where $\hbar\omega/k_0 T \gg 1$, $\exp(-\xi^2) J(\xi, \beta)$ is essentially temperature-independent and decreases with increasing ξ^2.

Figure 1 presents the dependence of $\Phi(\xi, \Omega)$ on Ω/ω for various values of ξ^2. As the calculations show, the contribution of the high-energy states with $n \neq 0$ to $\Phi(\xi, \Omega)$ is
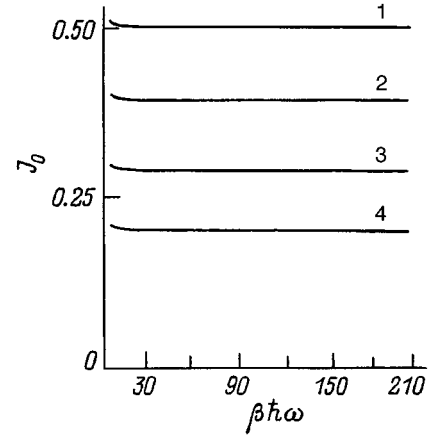
insignificant; therefore, it can be assumed that $\Phi(\xi, \Omega) \approx \exp(-\xi^2)(\omega/\Omega)^2$, i.e., that $\Phi(\xi, \Omega)$ decreases with increasing ξ^2.

If the impurity is located at the midpoint of the size-confined system, $z_0 = 0$, and $\xi^2 = (e^2 F^2/m^2 \omega^4) \lambda_0$, then in the absence of an electric field the minimum of the electron potential energy $[U(z) = (1/2) m\omega^2 z^2]$ is located above the localized state. In an electric field whose intensity vector $\mathbf{F}$ is directed along the spatial quantization axis, the minimum of the potential energy $[U(z) = (1/2) m\omega^2 z^2 + eFz]$ moves away from the impurity, and the electron-impurity interaction consequently weakens. The latter circumstance also causes the intraband light absorption to decrease with increasing ξ^2. A somewhat different situation arises when the dopant atom is not located at the center of the QW. If the impurity is located at the point $-z_0$, then $\xi^2 = \lambda(-z_0 + eF/m\omega^2)$ and the potential energy minimum approaches the impurity as F increases (ξ^2 decreases), causing enhancement of the electron-impurity interaction, i.e., an increase in intraband light absorption. If $z_0 = eF/m\omega^2$, $\xi^2 = 0$ and a further increase in F [with movement of the minimum of $U(z)$ away from $-z_0$] leads to an increase in ξ^2, i.e., to a decrease in $K(\Omega)$. The appreciable variation of intraband light absorption as a function of the magnitude and direction of the electric field intensity and the site of the dopant atom can be important in optoelectronics.

Let us consider the case where the scattering centers are located at the midpoint of the QW ($z_0 = 0$) and there is no electric field ($\xi^2 = 0$). At low temperatures ($\hbar\omega/k_0 T \gg 1$), $(\omega_c/\omega)^2 (k_0 T/\hbar\omega_0) \ll 1$ and the expression (10) for $\hbar\Omega \leqslant \hbar\omega_0$ (in the sum over n' we retain the term with $n' = 0$) takes the form

$$K(\Omega) = K_0 (\omega_0/\Omega)^2 J(\beta, \delta) \exp(-\gamma) \{I_0(\gamma) + I_1(\gamma)\}. \qquad (13)$$

Here $K_0 = 2e^2 V_0^2 n_e N_c m/c \sqrt{\varepsilon_0} \hbar^4 \omega$, $\gamma = \delta(\Omega/\omega_0)$, $\delta = (\omega_c/\omega)^2$, $I_0(\gamma)$, and $I_1(\gamma)$ are the modified Bessel functions of order zero and of first order, respectively; and $J_0(\beta, \delta)$ is described by Eq. (12), in which the Green's function $\widetilde{G}_x(z_0, z_0)$ is calculated for $\xi = 0$, but $\delta \neq 0$, by the usual methods used in the zero-range potential theory.[13]
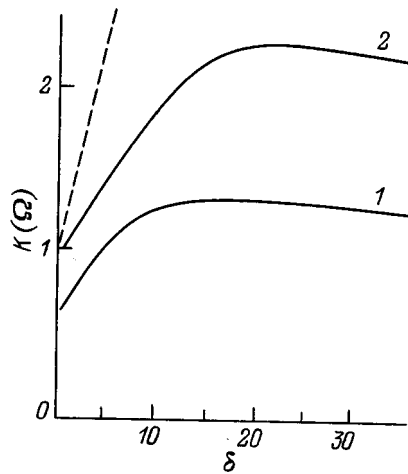
FIG. 3. Dependence of the light absorption coefficient on magnetic field (in relative units): *1, 2* — $\Omega/\omega=1,0.8$, respectively. Dashed line — Born approximation for $\Omega/\omega=1$.

Figure 2 presents the dependence of $J_0(\beta,\delta)$ on $\beta\omega\hbar$ for various values of the magnetic field. Curves *1–4* were obtained for $\delta=0.25$, 1, 4, and 10, respectively, in the case where $\Delta=(\hbar\omega/2\pi E_0)^{1/2}=0.1$. As follows directly from Fig. 2, at low temperatures $J_0(\beta,\delta)$ is essentially temperature-independent, but decreases appreciably with increasing magnetic field strength. This means that in strong magnetic fields the electron-impurity interaction intensifies appreciably, and it is incorrect to confine the calculation of $K(\Omega)$ to the Born approximation $[J_0(\beta,\delta)=1]$.

Figure 3 presents the dependence of the intraband light absorption (in relative units) on magnetic field strength for various values of Ω/ω. As can be seen from the figure, the absorption exhibits nonmonotonic behavior as the magnetic field strength increases. We note that in the Born approximation (the dashed line in Fig. 3, which was obtained for $\Omega/\omega=1$) $K(\omega)$ increases with increasing H. Therefore, the level of intraband light absorption in quantum-confined systems exhibits an appreciable dependence on the strength of the external electric and magnetic fields, which can be very important for the operation of IR detectors.

[1] B. F. Levine, K. K. Choi, C. G. Bethea, J. Walker, and R. J. Malik, Appl. Phys. Lett. **50**, 1092 (1987).
[2] J. Faist, F. Capasso, D. L. Sivco *et al.*, Science **264**, 553 (1994).
[3] L. C. West and S. J. Eglash, Appl. Phys. Lett. **46**, 1156 (1985).
[4] B. F. Levine, R. J. Malik, J. Walker, K. K. Choi, C. G. Bethea, D. A. Kleinman, and J. M. Vandenberg, Appl. Phys. Lett. **50**, 273 (1987).
[5] C. -L. Yang, D. -S. Pan, and R. Samoano, J. Appl. Phys. **65**, 3253 (1989).
[6] Y. Zhang, N. Baruch, and W. I. Wang, Appl. Phys. Lett. **63**, 1068 (1993).
[7] R. Misra, D. W. Greve, and T. E. Schlesinger, Appl. Phys. Lett. **67**, 2548 (1995).
[8] E. R. Brown and S. J. Eglash, Phys. Rev. B **41**, 7559 (1990).
[9] H. Xie, J. Piao, J. Katz, and W. I. Wang, J. Appl. Phys. **70**, 3152 (1991).
[10] F. Namavar and R. A. Soref, J. Appl. Phys. **70**, 3370 (1991).
[11] A. C. Gossard, in *Institute of Physics Conference Series, Vol. 69*, Institute of Physics, Bristol (1983), p. 1.
[12] S. M. Wang, G. Treideris, W. Q. Chen, and T. G. Andersson, Appl. Phys. Lett. **62**, 61 (1993).
[13] Yu. N. Demkov and V.N. Ostrovskiĭ, *Zero-Range Potentials and Their Applications in Atomic Physics* [Plenum Press, New York (1988); Izd. LGU, Leningrad (1975)].

Translated by P. Shelnitz

Polar state of a particle with a degenerate band spectrum in a quantum dot

I. P. Ipatova,*) A. Yu. Maslov, and O. V. Proshina

A. F. Ioffe Physicotechnical Institute, Russian Academy of Sciences, 194021 St. Petersburg, Russia

The energies of electron and hole polarons in spherical quantum dots based on materials with a high degree of ionicity are found. It is established that consideration of the valence-band degeneracy causes the hole polaron binding energy to be greater than the electron polaron binding energy. The polaron effects increase with decreasing quantum dot radius. Interband optical transitions are accompanied by partial compensation of the polaron effects, because the emergent electron and hole tend to create polarization potential wells with opposite signs. It is shown that complete compensation of the polaron effects does not occur when the valence-band degeneracy is taken into account. Therefore, interband transitions are accompanied by polarization of the medium. Such polarization is manifested by the appearance of a series of intense phonon replicas of the lines for the electronic transitions. © *1999 American Institute of Physics.* [S1063-7826(99)01507-0]

1. ELECTRON STATES IN QUANTUM DOTS

The confinement of charged particles and excitons in quantum dots leads to significant enhancement of the interaction of these particles with one another and with longitudinal-optical phonons. In materials with a high degree of ionicity the enhancement of the interactions in a quantum dot leads to an increase in the polaron effects in comparison to bulk materials.

It was shown in Refs. 1 and 2 that polaron effects become stronger as the dot size decreases. The enhancement parameter is the ratio of the radius of the polaron state a_0 to the dot radius R:

$$\frac{a_0}{R} \gg 1. \tag{1}$$

In this case a strong confinement regime is realized for carriers in a dot. The condition (1) means that the binding energy of a polaron is smaller than the quantum-well energy of the particle in the dot. Then the electron (hole) wave function $\psi_{e,h}$ in the zeroth approximation is specified by the Schrödinger equation for a quantum dot without electron-phonon coupling:

$$\hat{H}_{e,h}\psi_{e,h} + V_{e,h}(\mathbf{r})\psi_{e,h} = E_{e,h}\psi_{e,h}, \tag{2}$$

where $\hat{H}_{e,h}$ is the kinetic energy operator and $V_{e,h}(\mathbf{r})$ is the potential energy of the particle in the quantum dot. The kinetic energy operator of electrons in direct-gap semiconductors has the form

$$\hat{H}_e = -\frac{\hbar^2}{2m_e}\nabla^2 = \frac{\hat{p}^2}{2m_e}, \tag{3}$$

where m_e is the electron effective mass.

The energy and wave function corresponding to the solution of the Schrödinger equation (2) with the kinetic energy (3) for an arbitrary spherical potential $V_{e,h}(\mathbf{r})$ depend on the orbital quantum number l and the radial quantum number n (Ref. 3). They were found for a spherical quantum dot with infinite walls in Ref. 4:

$$E_{ln} = \frac{\hbar^2}{2m_e R^2}C_n^2(l),$$

$$\psi_{ln} = \frac{J_l[C_n(l)r/R]Y_{lm}(\theta,\varphi)}{\sqrt{J_{l+1}[C_n(l)]}}, \tag{4}$$

where $C_n(l)$ is the nth root of the lth spherical Bessel function $J_l(x)$, and $Y_{lm}(\theta,\varphi)$ are spherical functions. The dependence of the wave function ψ_{ln} on the projection of the momentum onto the quantization axis (i.e., the quantum number m) is not significant for calculating the polaron binding energy. Therefore, the index m is not added to the wave function in Eq. (4) or anywhere below.

If the spin-orbit split-off band is disregarded, the hole band in typical semiconductors is quadruply degenerate at the Γ point of the Brillouin zone. This degeneracy can be taken into account if the spherical Luttinger Hamiltonian serves as the hole kinetic energy operator $\hat{H}_h$:

$$\hat{H}_h = \left(\gamma_1 + \frac{5}{2}\gamma\right)\frac{\hat{p}^2}{2m_0} - \frac{\gamma}{m_0}(\hat{p}\hat{j})^2, \tag{5}$$

where $\hat{j}$ is the momentum operator with $j=3/2$, m_0 is the free-electron mass, and the parameters γ_1 and γ are related to the heavy- and light-hole masses m_h and m_l by the expression

$$m_{l,h} = \frac{m_0}{\gamma_1 \pm 2\gamma}. \tag{6}$$

Equation (2) with the kinetic energy operator (5) has the following properties. The hole wave functions for a spherically symmetric quantum-dot potential $V_h(\mathbf{r})$ are classified according to the value of the momentum $\hat{F} = \hat{l} + \hat{j}$, where $\hat{l}$ is

the orbital angular momentum. The wave function of a hole with a total momentum $\hat{F}$ is expressed in terms of the wave functions for $\hat{l}$ and $\hat{j}$ (Ref. 3, Sec. 106). For $j=3/2$ we have

$$\psi_{FN}=\sqrt{2F+1}\sum_l(-1)^{l-3/2+M}R_{F,l}(r)$$

$$\times\sum_{m,\mu}\begin{pmatrix} l & 3/2 & F \\ m & \mu & -M \end{pmatrix}Y_m(\theta,\varphi)\chi_\mu. \qquad (7)$$

Here M is the projection of the momentum $\hat{F}$ onto the quantization axis, χ_μ is the projection of the matrix eigenvector $|j_z|$, μ is the eigenvalue corresponding to that eigenvector ($|j_z|\chi_\mu=\mu\chi_\mu$), and

$$\begin{pmatrix} l & 3/2 & F \\ m & \mu & -M \end{pmatrix}$$

is a Wigner $3j$ symbol. The summation in (7) is carried out over all values of the quantum number l in the range $|F-3/2|\le l\le F+3/2$ and over the values of m and μ which satisfy the condition $m+\mu=M$. The hole ground state in a quantum dot corresponds to the momentum $F=3/2$. The energy E_{FN} of an arbitrary quantum-well level and its wave function ψ_{FN} depend on the total momentum $\hat{F}$ and the radial quantum number N. The dependence of the hole wave function on the momentum projection M, like the dependence of the electron wave function on m, is insignificant for calculating the polaron binding energy. Therefore, the index M has been omitted in (7).

In the expression for the hole wave function (7) the angular dependence is given in an explicit form, and the radial wave functions $R_{F,l}$ depend on the specific form of the potential $V(r)$. The equations for $R_{F,l}$ in the case of an arbitrary spherical potential were found in Refs. 5 and 6. Éfros[7] found the radial functions for a quantum dot with infinite walls in the case of $F=3/2$. They have the form

$$R_{3/2.0}\equiv R_0=A(\beta)\left[J_0(kr)-\frac{J_0(kR)}{J_0(k\sqrt{\beta}R)}J_0(k\sqrt{\beta}r)\right],$$

$$R_{3/2.2}\equiv R_2=A(\beta)\left[J_2(kr)+\frac{J_0(kR)}{J_0(k\sqrt{\beta}R)}J_2(k\sqrt{\beta}r)\right], \quad (8)$$

where $A(\beta)$ is the normalization factor, $\beta=m_l/m_h$, and k is the solution of the transcendental equation following from the condition that the wave functions (8) vanish on the infinite walls of the well:

$$J_0(kR)J_2(k\sqrt{\beta}R)+J_0(k\sqrt{\beta}R)J_2(kR)=0. \qquad (9)$$

The parameter k is related to the hole ground-state energy E_h in the following way:

$$k=\frac{1}{\hbar}\sqrt{2m_hE_h}. \qquad (10)$$

The dependence of k on the mass ratio $\beta=m_l/m_h$ was given in Refs. 7 and 8. As β increases in the range $0\le\beta\le1$ the dimensionless parameter kR decreases in the range

$$C_2(1)\ge kR\ge C_0(1), \qquad (11)$$

where $C_2(1)=5.76$ is the first root of the second-order spherical Bessel function J_2, and $C_0(1)=\pi$ is the first root of the zero-order Bessel function J_0.

When the light- and heavy-hole masses coincide ($\beta=1$), the angle-dependent part of the wave function $\psi_{3/2,N}$ from (7) vanishes, and R_0 from (8) coincides with the radial part of the wave function ψ_{01} from relations (4) for a nondegenerate band.

2. ELECTRON AND HOLE POLARONS

In quantum dots based on materials with a high degree of ionicity the strong electron-phonon interaction leads to the appearance of polaron states. Polaron states are manifested by appreciable variation of the electron and hole quantum-well energies in a quantum dot.

Let us find the binding energy of a polaron in a quantum dot. For this purpose, the electron-phonon coupling energy and the phonon self-energy should be added to the Schrödinger equation (2). We thus obtain

$$\left[\hat{H}_{e,h}+V_{e,h}+\sum_q\hbar\omega_qa_q^+a_q+e\sqrt{\frac{2\pi\hbar}{V\varepsilon}}\right.$$

$$\left.\times\sum_q\sqrt{\omega_q}\frac{1}{q}(a_qe^{i\mathbf{q}\cdot\mathbf{r}}+a_q^+e^{-i\mathbf{q}\cdot\mathbf{r}})\right]\psi=E\psi, \qquad (12)$$

where a_q and a_q^+ are the phonon annihilation and creation operators and $\varepsilon^{-1}=\varepsilon_0^{-1}-\varepsilon_\infty^{-1}$ is the optical dielectric constant. The parameter (1) permits the use of the adiabatic approximation, under which the motion of the electron (hole) in the quantum dot is fast and the polaron motion is slow, in the calculation of the polaron energy. Averaging Eq. (12) over the fast-motional wave functions (4) or (7), we obtain the equation for a particle in a phonon polarization well, which depends on the slow phonon variables:

$$\hat{H}^{(ln)}=E_{ln}+\sum_q\hbar\omega_qa_q^+a_q+e\sqrt{\frac{2\pi\hbar}{V\varepsilon}}$$

$$\times\sum_q\frac{\sqrt{\omega_q}}{q}[\rho_{ln}(q)a_q+\rho_{ln}^*(q)a_q^+], \qquad (13)$$

where

$$\rho_{ln}(q)=\int e^{i\mathbf{q}\cdot\mathbf{r}}\psi_{ln}^2(\mathbf{r})\,d^3r. \qquad (14)$$

Here $\rho_{ln}(q)$ is the Fourier component of the electron density of states at the level with the quantum numbers l and n.

Equation (13) can be brought into diagonal form with respect to the operators a_q^+ and a_q using the unitary transformation

$$U_{ln}=\exp\left[\sum_q\frac{e}{q}\sqrt{\frac{2\pi}{V\varepsilon\hbar\omega_q}}(\rho_{ln}(q)a_q^+-\rho_{ln}^*(q)a_q)\right]. \qquad (15)$$

Applying the unitary transformation (15) to Eq. (13), we obtain

$$\hat{H}^{(ln)} = E_{ln} - \frac{2\pi e^2}{V\varepsilon} \sum_q \frac{|\rho_n(q)|^2}{q^2} + \sum_q \hbar\omega_q a_q^+ a_q. \quad (16)$$

The second term on the right-hand side of Eq. (16) is the electron binding energy $\Delta E^{(ln)}$ at level (ln) in a polarization well. Such a state is called a polaron.[9] Substituting the expression for $\rho_{ln}(q)$ from (14) into (16) and going over from summation over q to integration, we obtain

$$\Delta E^{(ln)} = -\frac{2\pi e^2}{V\varepsilon} \sum_q \frac{|\rho_{ln}(q)|^2}{q^2}$$

$$= -\frac{e^2}{2\varepsilon} \int \frac{\psi_{ln}^2(\mathbf{r})\psi_{ln}^2(\mathbf{r}')}{|\mathbf{r}-\mathbf{r}'|} d^3r\, d^3r'. \quad (17)$$

The expression for the energy of a hole polaron is obtained in a similar manner. It differs from (17) only in that it contains the integral of the squares of the hole wave functions $\psi_{FN}^2(\mathbf{r})$ from (7). To find the polaron binding energy, we substitute the wave functions (4) and (7) into (17) and calculate the corresponding integrals.

In the case of a simple band with the wave function (4), for an electron polaron we obtain

$$\Delta E_e^{(ln)} = -\frac{e^2}{2\varepsilon R} B_e^{(ln)}, \quad (18)$$

where $B_e^{(ln)}$ are numerical coefficients, which differ for different quantum-well levels (ln). For the ground state of an electron in a quantum dot the respective coefficient $B_e^{(01)}$ is

$$B_e^{(01)} = 2\left(1 - \frac{\mathrm{Si}(2\pi)}{2\pi} + \frac{\mathrm{Si}(4\pi)}{4\pi}\right) \approx 1.79,$$

where $\mathrm{Si}(x)$ is the sine integral. When the potential energy of the quantum dot is described by a well with infinite walls, the electron wave functions (4) and the electron polaron binding energy (18) do not depend on electron mass. When the finite height of the barrier is taken into account, such a dependence on mass appears.

To find the hole polaron binding energy in the case of a degenerate valence band, the wave functions (7) should be plugged into Eq. (17). We thus obtain

$$\Delta E_h^{(FN)} = -\frac{e^2}{2\varepsilon R} B_h^{(FN)}(\beta), \quad (19)$$

where the dimensionless multiplier $B_h^{(FN)}(\beta)$ depends on the number of the quantum-well level (FN) and on the ratio between the light- and heavy-hole masses β. Since the angular dependences of the wave functions (7) are known exactly, the integration over the angles can be performed analytically to find the hole polaron energy. As a result, for the hole ground state we obtain

$$B_h^{(3/2,1)} = R\left\{ \int_0^R r^2\, dr\, [R_0^2(r) + R_2^2(r)] \right.$$

$$\times\left[\frac{1}{r}\int_0^r r_1^2\, dr_1\, [R_0^2(r_1) + R_2^2(r_1)] \right.$$

$$\left. + \int_r^R r_1\, dr_1\, [R_0^2(r_1) + R_2^2(r_1)] \right]$$

$$+ \frac{4}{5}\int_0^R r^2\, dr\, R_0(r)R_2(r)$$

$$\times\left[\int_0^r \frac{r_1^4}{r^3} dr_1\, R_0(r_1)R_2(r_1) \right.$$

$$\left.\left. + r^2 \int_r^R \frac{dr_1}{r_1} R_0(r_1)R_2(r_1) \right] \right\}. \quad (20)$$

In the region $\beta \approx 1$ the degeneracy of the energy bands has a weak influence on the form of the radial part of the wave function. The function $R_2(r)$ is small, and the parameter $B_h^{(3/2,1)}$ is close to the value of $B_e^{(0,1)}$ for a nondegenerate band. The values of $B_h^{FN}(\beta)$ for an arbitrary mass ratio can be found only numerically. A plot of $B_h^{(3/2,1)}(\beta)$ obtained by numerically integrating Eq. (20) is presented in Fig. 1. The maximum deviation of the polaron binding energy in a degenerate band from the polaron energy in a simple band is observed at $\beta \approx 0.2$. Several features in the behavior of the hole binding energy in a spherical quantum dot[7] and in the splitting of the hole energy levels in a quantum dot in the presence of an aspherical perturbation[8] have previously been obtained for just such values of β.

3. POLARON EXCITONS

Interband optical transitions in a quantum dot are accompanied by the simultaneous appearance or disappearance of an electron and a hole. In ionic materials each particle tends to create its own polarization well, and the potential energies of these wells have opposite signs. Partial compensation of
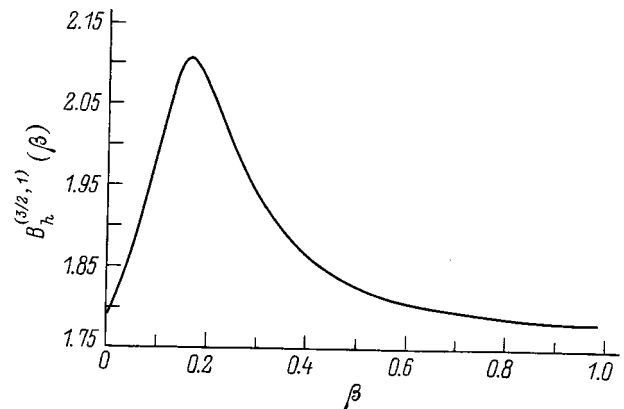

FIG. 1. Dependence of the dimensionless coefficient $B_h^{(3/2,1)}$ from the expression for the hole polaron binding energy (20) on the ratio between the light- and heavy-hole masses β.

the polaron effects occurs as a result. This compensation is complete, if both the electron and the hole are described in a nondegenerate band model. However, the difference between the electron and hole charge density distributions appearing as a consequence of valence-band degeneracy precludes complete compensation of the polaron effects.

When there are two charged particles, viz., an electron and a hole, in a quantum dot, the Schrödinger equation can be written with allowance for the interaction of the particles with polar optical phonons and their Coulomb interaction by analogy with (12):

$$
\left\{ \hat{H}_e + \hat{H}_h + V_e + V_h - \frac{e^2}{\varepsilon_0 |\mathbf{r}_e - \mathbf{r}_h|} + \sum_q \hbar \omega_q a_q^+ a_q \right.
$$

$$
+ e \sqrt{\frac{2\pi\hbar}{V\varepsilon}} \sum_q \sqrt{\omega_q} \frac{1}{q} [(a_q e^{i\mathbf{q}\cdot\mathbf{r}_e} + a_q^+ e^{-i\mathbf{q}\cdot\mathbf{r}_e})
$$

$$
\left. - (a_q e^{i\mathbf{q}\cdot\mathbf{r}_h} + a_q^+ e^{-i\mathbf{q}\cdot\mathbf{r}_h})] \right\} \psi(\mathbf{r}_e, \mathbf{r}_h) = E\psi(\mathbf{r}_e, \mathbf{r}_h).
$$

$$(21)$$

When the strong confinement condition (1) holds for both the electron and the hole, the energy of the Coulomb interaction of the particles with one another, as well as the energy of their interaction with polar optical phonons, are smaller than the gap between the quantum-well levels in the dot. The wave function of the electron-hole pair then reduces to the product of the wave functions of the electron and the hole in certain quantum-well levels, i.e.,

$$
\psi(\mathbf{r}_e, \mathbf{r}_h) = \psi_{ln}(\mathbf{r}_e)\psi_{FN}(\mathbf{r}_h), \tag{22}
$$

and the wave functions $\psi_{ln}(\mathbf{r}_e)$ and $\psi_{FN}(\mathbf{r}_h)$ are specified by Eqs. (4) and (7), respectively.

Averaging Eq. (21) over the fast-motional wave functions (22), we obtain the dependence of the polaron exciton energy on the slow phonon variables:

$$
\hat{H}_{ex}^{(ln,FN)} = E_{ln,FN} + \sum_q \hbar \omega_q a_q^+ a_q + e\sqrt{\frac{2\pi\hbar}{V\varepsilon}}
$$

$$
\times \sum_q \frac{\sqrt{\omega_q}}{q}(\rho_{ln,FN}(q)a_q + \rho_{ln,FN}^*(q)a_q^+), \quad (23)
$$

where

$$
\rho_{ln,FN}(q) = \rho_{ln}(q) - \rho_{FN}(q) \tag{24}
$$

is the Fourier component of the difference between the charge distribution densities for the electron and the hole. The quantity $E_{ln,FN}$ is the energy of the optical transition without allowance for the electron-phonon interaction and contains the energy of the Coulomb interaction of the electron and the hole averaged over the wave function (22).

Equation (23) is structurally similar to Eq. (13) for an electron polaron. Applying a unitary transformation analogous to (15),

$$
U_1 = \exp\left[\sum_q \frac{e}{q}\sqrt{\frac{2\pi}{V\varepsilon\hbar\omega_q}}(\rho_{ln,FN}(q)a_q^+ - \rho_{ln,FN}^*(q)a_q) \right],
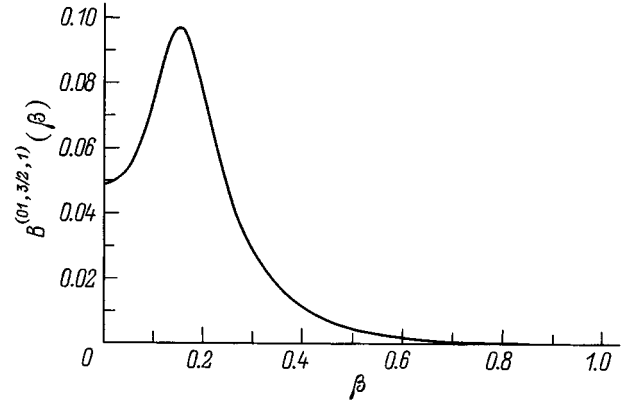$$

$$(25)$$

FIG. 2. Dependence of the dimensionless coefficient $B^{(01,3/2,1)}$ from the expression for the polaron exciton ground-state binding energy (27) on the ratio between the light- and heavy-hole masses β.

where $\rho_{ln,FN}(q)$ includes the density for both the electron and the hole, we obtain the polaron exciton binding energy $\Delta E_{ln,FN}$ in the form

$$
\Delta E_{ln,FN} = -\frac{e^2}{2\varepsilon}\int \frac{d^3r\, d^3r'}{|\mathbf{r}-\mathbf{r}'|}[\psi_{ln}^2(\mathbf{r}) - \psi_{FN}^2(\mathbf{r})]
$$

$$
\times [\psi_{ln}^2(\mathbf{r}') - \psi_{FN}^2(\mathbf{r}')]. \tag{26}
$$

This energy can be represented in a form similar to (19):

$$
\Delta E_{ln,FN} = -\frac{e^2}{2\varepsilon R}B^{ln,FN}(\beta). \tag{27}
$$

Here the dimensionless coefficients $B^{(ln,FN)}(\beta)$ depend on the ratio between the light- and heavy-hole masses β. A plot of $B^{(01,3/2,1)}(\beta)$ for the optical transition between the electron ($l=0$, $n=1$) and hole ($F=3/2$, $N=1$) ground states is shown in Fig. 2. The magnitude of the polaron shift $\Delta E_{ln,FN}$ increases upon variation of the dimensions of the dot in proportion to R^{-1}.

It can be seen from Fig. 2 that the interaction with phonons is significant for the electron-hole pair only at a fairly small ratio between the light- and heavy-hole masses $\beta < 0.6$. When $\beta \approx 1$, the function R_2 from (8) is small, and R_0 reduces to the electron wave function ψ_{01} from (4). In this case there is essentially complete compensation of the polaron effects from the electron and the hole.

4. INTRABAND OPTICAL TRANSITIONS

The polaron states in quantum dots are manifested in two effects accompanying interband optical transitions. First, intense phonon replicas of the line for the interband electronic transition appear because of the polarization of the medium by the charged particles. Second, the difference between the polarizations of the initial and final states produces a large Stokes shift between the absorption and emission lines.

When light is absorbed, there is only a photon in the initial state, and there is no electron in the conduction band or hole in the valence band. The wave function of such an initial state can be written approximately in the form

$$\Psi_i = \delta(\mathbf{r}_e - \mathbf{r}_h)\Phi_{\text{vib}}^i. \qquad (28)$$

Here the presence of the multiplier $\delta(\mathbf{r}_e - \mathbf{r}_h)$ means that the electron is still in the valence band, i.e., where a hole appears after absorption, and Φ_{vib}^i is the vibrational wave function of the initial state.

The wave function of the final state is

$$\Psi_f = \psi_{ln}(\mathbf{r}_e)\psi_{FN}(\mathbf{r}_h)\Phi_{\text{vib}}^f. \qquad (29)$$

Here the first two multipliers correspond to the wave function of the electron-hole pair from Eq. (22), and Φ_{vib}^f is the vibrational wave function of the final state. It is next shown that because of the difference between the polarizations of the medium in the initial and final states, Φ_{vib}^f has an equilibrium position displaced relative to Φ_{vib}^i.

The probability of the absorption of a photon in a dipole transition has the form

$$W_{ln,FN}^{\text{abs}} = \frac{2\pi}{\hbar}|P_{cv}|^2|I_{ln,FN}|^2\sum_f W_{if}\delta(E_{ln,FN}-E_f-\hbar\omega). \qquad (30)$$

Here P_{cv} is the interband transition matrix element in Bloch modulating functions, $I_{ln,FN}$ is the overlap integral of the envelopes of the electron wave functions (4) and the hole wave functions (7), W_{if} is the square of the overlap integral of the vibrational wave functions with shifted equilibrium positions, and E_f is the vibrational energy of the final state of the system. Let us examine the case of the fairly low temperatures $T \ll \hbar\omega_0$, where ω_0 is the threshold optical phonon frequency, and therefore disregard any processes with phonon absorption in (30). The energy conservation law corresponding to the δ function reflects the fact that, due to the displacement of the equilibrium position of the vibrational states, the electronic transition is accompanied by the emission of any number K of optical phonons, whose total energy equals E_f already in first-order perturbation theory. It has been taken into account in the energy conservation law in (30) that the absorption process takes place in the absence of polarization of the medium, because there were no charged particles in the system before absorption of the photon.

The matrix element P_{cv} for an allowed interband transition is nonzero. The overlap integral of the envelopes of the electron and hole wave functions

$$I_{ln,FN} = \int d^3r\,\psi_{ln}(\mathbf{r})\psi_{FN}(\mathbf{r}) \qquad (31)$$

determines the selection rules for the electron and hole quantum-well levels in a quantum dot. It follows from the form of the wave functions (4) and (7) that a larger number of transitions between excited electron and hole states are allowed with consideration of the degeneracy of the valence band than in the case of nondegenerate bands.

For the transition between the ground electron ($l=0$, $n=1$) and hole ($F=3/2$, $N=1$) states we obtain

$$I_{01,3/2,1}(\beta) = A(\beta)\frac{\sqrt{2}\pi}{R^{3/2}}\int_0^R r^2\,dr\,R_0 J_0(\pi r/R). \qquad (32)$$

At $\beta=1$ we have $I_{01,3/2,1}=1$, and the limit $\beta\to 0$ corresponds to

$$I_{01,3/2,1}(0) = \frac{A(0)\sqrt{2}C_1(2)\sin C_1(2)}{\pi[\pi^2 - C_1(2)^2]} \approx 0.335.$$

It can be seen that $I_{01,3/2,1}(\beta)$ varies fairly slowly with the ratio between the light- and heavy-hole masses β.

Displacement of the equilibrium position of the vibrational wave functions appears in our calculations of the transition probability (30) as a consequence of the unitary transformation (25), which was applied to the Hamiltonian (23). In fact, the probability of multiphonon transitions is specified by the integral over the vibrational coordinates x_q in (30):

$$W_{if} = \left|\int dx_q\,\Phi_{\text{vib}}^i\Phi_{\text{vib}}^f\right|^2$$

$$= \left|\int dx_q\,\Phi_i(\ldots x_q \ldots)e^{U_1}\Phi_f(\ldots x_q \ldots)\right|^2. \qquad (33)$$

The functions $e^{U_1}\Phi_f(\ldots x_q \ldots)$ and $\Phi_i(\ldots x_q \ldots)$ are nonorthogonal and, as was shown by Huang and Rhys,[10] thus lead to multiphonon transitions.

Let us find the displacement of the equilibrium positions of the oscillators in response to the canonical transformation (25). We plug the usual expressions for the creation and annihilation operators for the qth harmonic oscillator in terms of the coordinate $(\hat{x}_q)$ and momentum $(\hat{p}_q)$ operators into (25):

$$a_q = \frac{1}{2}\sqrt{\frac{2M_0\omega_q}{\hbar}}\left(\hat{x}_q + i\frac{\hat{p}_q}{M_0\omega_q}\right),$$

$$a_q^+ = \frac{1}{2}\sqrt{\frac{2M_0\omega_q}{\hbar}}\left(\hat{x}_q - i\frac{\hat{p}_q}{M_0\omega_q}\right), \qquad (34)$$

where M_0 is the oscillator mass. Taking into account that the Fourier component of the electron density $\rho_{ln,FN}(q)$ is a real quantity and substituting (34) into (25), we obtain

$$\hat{U}_1 = \exp\left[-i\sum_q \frac{e}{q\hbar\omega_q}\sqrt{\frac{2\pi}{M_0 V\varepsilon}}\rho_{ln,FN}(q)\hat{p}_q\right]. \qquad (35)$$

As we know from quantum mechanics,[3] the operator $\hat{U}_1$ from (35) for an oscillator with the coordinate x_q is the operator of parallel transfer to the final state, which is

$$s_q = -\frac{e}{\omega_q q}\rho_{ln,FN}(q)\sqrt{\frac{2\pi}{M_0 V\varepsilon}}.$$

As a result, the probability of multiphonon transitions W_{if} from (33) is equal to the product of the transition probabilities ω_q for each oscillator q:

$$W_{if} = \prod_q \omega_q = \prod_q \left|\int dx_q\,\Phi_i(x_q)\Phi_f(x_q - s_q)\right|^2. \qquad (36)$$

The transition probability $w_q(K_q)$ calculated from the wave functions of an harmonic oscillator for an oscillator with the coordinate x_q upon the emission of K_q optical phonons by it has the form[3]

$$\omega_q(K_q) = \frac{\left(\left|s_q\right|^2 \frac{M_0\omega_q}{\hbar}\right)^{K_q}}{2^{K_q}(K_q)!} \exp\left[-\frac{1}{2}\left|s_q\right|^2 \frac{M_0\omega_q}{\hbar}\right]. \quad (37)$$

The probability of the emission of a certain number of phonons K is obtained by multiplying the probabilities $w_q(K_q)$ of the emission of K_q phonons by the qth oscillator from (37), so that the sum over all the oscillators gives $\Sigma_q K_q = K$. Taking into account all the possible permutations of K_q, we obtain

$$W(K) = \frac{\left(\sum_q \left|s_q\right|^2 \frac{M_0\omega_q}{\hbar}\right)^K}{2^K K!} \exp\left[-\frac{1}{2}\sum_q \left|s_q\right|^2 \frac{M_0\omega_q}{\hbar}\right]. \quad (38)$$

Calculations of the probability (38) with consideration of the phonon dispersion of ω_q are fairly cumbersome. However, for optical phonons, which exhibit weak dispersion ($\omega_q \approx \omega_0$), we obtain

$$W(K) = \frac{S_0^K}{2^K K!} \exp\left(-\frac{1}{2}S_0^2\right), \quad (39)$$

where S_0 is expressed in terms of the polaron exciton binding energy (26):

$$S_0 = \sum_q \left|s_q\right|^2 \frac{M_0\omega_0}{\hbar} = \frac{\Delta E_{ln,FN}}{\hbar\omega_0}. \quad (40)$$

If $K=0$, we obtain the probability for the zero-phonon line, which is

$$W(0) = e^{-S_0^2/2}. \quad (41)$$

When the dispersion of the optical phonons is disregarded, i.e., when $\omega_q = \omega_0$, the final state of the system is determined only by the number of phonons emitted K. Therefore, the sum over the final states of the system appearing in (30) reduces to the sum over all possible values of K, and the energy E_f reduces to $E_f = K\hbar\omega_0$. The photon absorption probability (30) has the form

$$W_{ln,FN}^{\text{abs}} = \frac{2\pi}{\hbar}|P_{cv}|^2 |I_{ln,FN}|^2$$

$$\times \sum_K W(K)\delta(E_{ln,FN} - K\hbar\omega_0 - \hbar\omega). \quad (42)$$

If the polaron energy is greater than the optical phonon energy, then

$$S_0 > 1, \quad (43)$$

and the probability of multiphonon transitions is large. The Kth phonon replica with $K \approx S_0$ has the highest intensity. For each value of K we can select a quantum dot with a value of $\Delta E_{ln,FN}$ from (27), for which the Kth phonon replica should have the greatest intensity upon an interband electronic transition.

When a photon is emitted, an optical electronic transition (recombination of an electron and a hole) occurs within the polarization potential well corresponding to displacement of the electron energy by $\Delta E_{ln,FN}$. After recombination of the electron and the hole in the emission process, the medium remains polarized. Therefore, the energy of the final state exceeds the energy of the ground state. Within our model of dispersionless phonons, this energy difference is equal to the same quantity $\Delta E_{ln,FN}$ from (27). Therefore, the probability of such a transition is

$$W_{(ln,FN)}^{\text{em}}(\omega) = \frac{2\pi}{\hbar}P_{cv}^2 |I_{ln,FN}|^2 \sum_K W(K)$$

$$\times \delta(E_{ln,FN} - 2\Delta E_{ln,FN} - K\hbar\omega_0 - \hbar\omega). \quad (44)$$

A comparison of (42) and (44) reveals that there is a Stokes shift ΔE_s between the absorption and emission lines, which is

$$\Delta E_s = 2\Delta E_{ln,FN}. \quad (45)$$

Thus, the polaron effects accompanying interband transitions in quantum dots should be manifested in the appearance of both intense phonon replicas and a significant Stokes shift. To identify polaron effects, both phenomena must be observed simultaneously. Each of them taken individually can be attributed to other mechanisms.

Large Stokes shifts of the lines of optical transitions[11] and intense phonon replicas[12] have been observed experimentally in II–VI-based quantum dots. However, we do not know of any experiments in which these two phenomena and their dependence on the dimensions of the quantum dots were investigated simultaneously.

*)E-mail: iip.ton@pop.ioffe.rssi.ru; Fax: $+$(7)-(812)-247-1017

[1] I. P. Ipatova, A. Yu. Maslov, and O. V. Proshina, Fiz. Tverd. Tela (St. Petersburg) **37**, 1819 (1995) [Phys. Solid State **37**, 991 (1995)].

[2] I. P. Ipatova, A. Yu. Maslov, and O. V. Proshina, Phys. Low-Dimens. Struct., No **4–5**, 1, (1996).

[3] L. D. Landau and E. M. Lifshitz, *Quantum Mechanics: Non-Relativistic Theory*, 3rd ed., [Pergamon Press, Oxford (1977); Nauka, Moscow (1989)].

[4] Al. L. Éfros and A. L. Éfros, Fiz. Tekh. Poluprovodn. **16**, 1209 (1982) [Sov. Phys. Semicond. **16**, 772 (1982)].

[5] B. L. Gel'mont and M. I. D'yakonov, Fiz. Tekh. Poluprovodn. **5**, 2191 (1971) [Sov. Phys. Semicond. **5**, 1905 (1971)].

[6] A. Baldareschi and N. O. Lipari, Phys. Rev. B **8**, 2697 (1973).

[7] Al. L. Efros, Phys. Rev. B **46**, 7448 (1992).

[8] Al. L. Efros and A. V. Rodina, Phys. Rev. B **47**, 10 005 (1993).

[9] S. I. Pekar, Report AEC-tr-5575, U.S. Atomic Energy Commission (1963).

[10] Kun Huang and A. Rhys, Proc. R. Soc. London, Ser. A **204**, 406 (1950).

[11] G. Scamarcio, V. Spagnolo, G. Ventruti, M. Lugara, and G. C. Regnini, Phys. Rev. B **53**, R10 489 (1996).

[12] V. Yungnickel, F. Henneberger, and J. Puls, in *Proceedings of the 22nd International Conference on the Physics of Semiconductors*, World Scientific, Singapore (1994), Vol. 3, p. 2011; V. Yungnickel and F. Henneberger, J. Lumin. **70**, 238 (1996).

Translated by P. Shelnitz

Transport and optical properties of tin δ-doped GaAs structures

V. A. Kul'bachinskiĭ, V. G. Kytin, R. A. Lunin, V. G. Mokerov, A. P. Senichkin,
A. S. Bugaev, A. L. Karuzskiĭ, and A. V. Perestoronin

M. V. Lomonosov Moscow State University, 119899 Moscow, Russia

R. T. F. van Schaijk and A. de Visser

Van der Waals Laboratory, University of Amsterdam, the Netherlands
(Submitted November 10, 1998; accepted for publication December 1, 1998)
Fiz. Tekh. Poluprovodn. **33**, 839–846 (July 1999)

The transport and optical properties of tin δ layers in GaAs are investigated as functions of the Sn concentration. The Shubnikov–de Haas and Hall effects are measured in the temperature range $0.4-12$ K in magnetic fields up to 38 T. The band diagrams and quantum mobilities of electrons in the quantum-well subbands are calculated. Features associated with electronic transitions from quantum-well levels are found in the photoluminescence spectra of the structures. Oscillations of the resistance are observed in a magnetic field parallel to the δ layer and are attributed to features in the density of states at the Fermi level. © *1999 American Institute of Physics.* [S1063-7826(99)01607-5]

1. INTRODUCTION

One of the effective methods for obtaining a high concentration of two-dimensional electrons in semiconductor structures is δ doping, under which an impurity is concentrated in a very thin layer, which ideally consists of only one sheet of atoms. Silicon is usually used for δ doping. Tin has hitherto been used only to a small extent to δ dope GaAs because of its high capacity for surface segregation,[1] although, as a donor impurity, it is less amphoteric than silicon, which has been used traditionally to create *n*-type δ layers. The use of Sn makes it possible to obtain a high concentration of two-dimensional electrons in the δ layer. In the present work the transport and optical properties of tin δ layers on a singular surface are investigated in GaAs/ GaAs(δ-Sn) structures as a function of the tin concentration. Scrutiny of the results of the tin δ doping of singular surfaces is important for comparison with data on the tin δ doping of vicinal (or high-index) gallium arsenide surfaces, which are promising for creating one-dimensional electron channels.[2,3]

2. SAMPLES AND MEASUREMENT METHOD

Tin δ-doped GaAs structures grown by molecular-beam epitaxy were investigated in this work. An *i*-GaAs buffer layer (240 nm) was grown on a semi-insulating (001) GaAs(Cr) substrate, and then a tin δ layer was deposited on the surface at $T_S \approx 450\,°$C with an increased flow of As and capped by an *i*-GaAs layer with a thickness of 40 nm and a GaAs:Si contact layer (having a silicon concentration of $1.5 \times 10^{18}\,\text{cm}^{-3}$) with a thickness of 20 nm. The tin doping level varied from $N_D = 2.97 \times 10^{12}\,\text{cm}^{-2}$ in sample 1 to $N_D = 2.67 \times 10^{14}\,\text{cm}^{-2}$ in sample 6. Some parameters of the samples are listed in Table I. The measurements were performed both on samples in the form of a double Hall bridge and on square samples.

The temperature dependence of the resistance was measured in the temperature range $0.4 < T < 300$ K. The Hall effect and the magnetoresistance were investigated at $0.4 < T < 12$ K in fixed magnetic fields up to 10 T and in pulsed fields up to 38 T. The pulsed magnetic-field facility of the University of Amsterdam was used for the measurements in magnetic fields up to 38 T. The measurements of the low-temperature photoluminescence spectra were performed at 4.2 K using an MDR-3 spectrometer and a photomultiplier operating in the photon-counting mode with optical excitation by the output of an argon laser (the wavelength was 514.5 nm, the radiated power was 7 mW, and the spot diameter was 1 mm).

3. CONDUCTANCE AND MAGNETORESISTANCE OF THE STRUCTURES INVESTIGATED

The resistance of sample 1 with a relatively small electron concentration increases as the temperature is lowered from room temperature to liquid-helium temperature (Fig. 1). The resistance of the heavily doped samples (4–6) decreases with decreasing temperature to a certain temperature (which decreases with increased doping of the sample) and then increases. As can be seen from Fig. 1, the resistance drops with increasing impurity concentration.

The Hall measurements showed that the Hall coefficient is constant in all of the samples in the range of magnetic fields investigated and does not depend on temperature in the range $0.4 < T < 12$ K. The values of the Hall electron concentration n_H obtained vary from $1.74 \times 10^{12}\,\text{cm}^{-2}$ in sample 1 to $8.35 \times 10^{13}\,\text{cm}^{-2}$ in sample 6 (see Table I), and the Hall mobility equals $1080-1940\,\text{cm}^2/(\text{V}\cdot\text{s})$ in different samples at liquid-helium temperature.

Negative magnetoresistance was observed in all the samples at low temperatures in magnetic fields equal to $B < 0.2$ T. It was quadratic in weak magnetic fields and loga-

TABLE I. Tin concentration N_D, sum of the electron concentrations n_{SdH} in all the subbands determined from the Shubnikov–de Haas effect, and Hall concentration n_H for different samples at $T = 4.2$ K.

Sample No.	N_D, 10^{12} cm^{-2}	Σn_{SdH}, 10^{12} cm^{-2}	n_H, 10^{12} cm^{-2}
1	2.97	2.75	1.74
2	8.91	8.73	3.59
3	26.7	7.30	2.63
4	29.7	7.80	10.4
5	89.1	8.09	8.35
6	267	45.3	83.5

rithmically dependent on magnetic induction in strong fields. The absolute value of the negative magnetoresistance decreases with increasing tin concentration in the δ layer. The Shubnikov–de Haas effect was observed in the structures investigated at low temperatures in strong magnetic fields. As an example, Fig. 2 shows the oscillations of the transverse magnetoresistance of samples 2 and 6, and Fig. 3 shows the Fourier transform of the oscillations of $\Delta R(H)$ in a reversed magnetic field for samples 2 and 4–6. Measurements of the dependence of the oscillation frequency on the tilt angle of the magnetic field showed that the oscillations are observed from two-dimensional carriers.

The two-dimensional electron concentrations in the quantum-well subbands determined from the maxima in the Fourier spectra are presented in Table II. It can be seen from Table I that the free-electron concentration Σn_{SdH} in samples 1 and 2 is approximately equal to the concentration of tin introduced N_D. As the concentration of tin introduced is increased, the free-electron concentration does not vary significantly (samples 3 to 5 in Table I). The positions of the maxima in the Fourier spectra in Fig. 3a are approximately identical for samples 2, 4, and 5, although the amplitudes of the peaks differ because of the different distributions of the electron mobilities among the subbands in these samples. The sum of the two-dimensional concentrations in four size-quantized subbands in samples 2–5 is equal to roughly
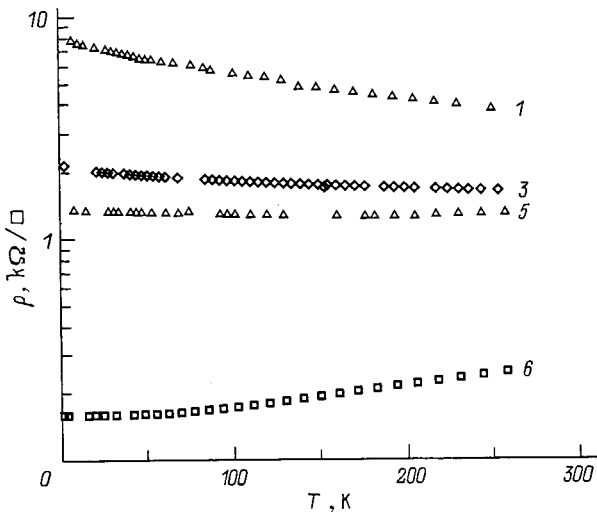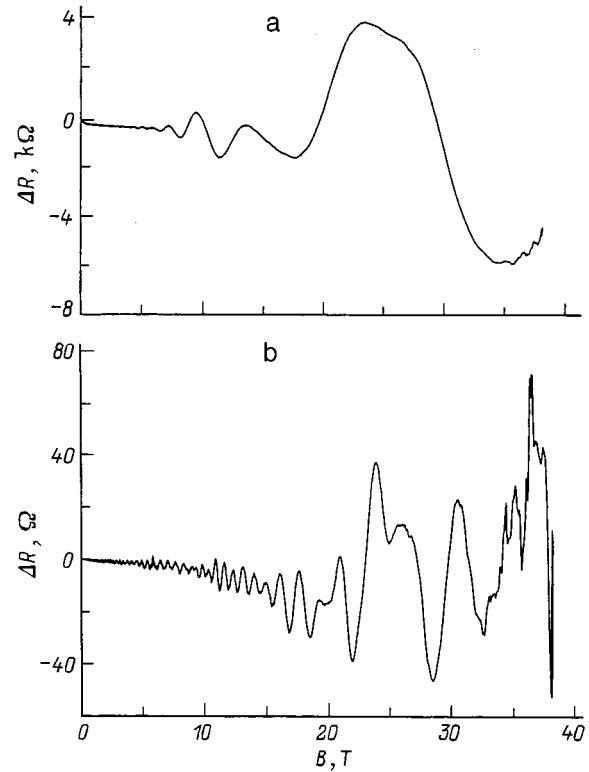

FIG. 2. Dependence of the change in resistance $\Delta R = R(B) - R(0)$ on the magnetic induction B at $T = 4.2$ K for samples 2 (a) and 6 (b).

8×10^{12} cm^{-2}, which is comparable to the limiting electron concentration for silicon δ-doped GaAs structures.[4–6] However, when the concentration of tin introduced is increased further, the free-electron concentration increases significantly (sample 6). The saturation of the concentration of free carriers in GaAs (δ-Si) structures is usually attributed to the filling of DX centers[5,7] or an increase in the number of compensating defects[8,9] as the dopant concentration rises. It can be assumed that the energy of the DX level relative to the Γ conduction band edge increases at doping levels as high as in sample 6 (Refs. 10 and 11) and that different defects roughly compensate for the donor tin atoms.

When the electron mobilities in the quantum-well subbands are determined, it is important to distinguish the transport relaxation times from the quantum relaxation times.[12–14] The transport momentum relaxation time τ_t of an electron is determined by the mean time between events of elastic scattering on impurities that significantly alter the direction of the momentum and can be written in the form

$$\frac{1}{\tau_t} = \int_0^\pi \sigma(\varphi)(1 - \cos\varphi)\, d\varphi, \tag{1}$$

where $\sigma(\varphi)$ is proportional to the probability of scattering into the angle φ per unit time in the plane of the δ layer. The quantum lifetime (one-particle relaxation time) is obtained by averaging the time between any scattering events and is given by the expression

$$\frac{1}{\tau_q} = \int_0^\pi \sigma(\varphi)\, d\varphi. \tag{2}$$

FIG. 1. Temperature dependence of the resistivity ρ (resistance per square) in samples 1, 3, 5, and 6 (see Table I).
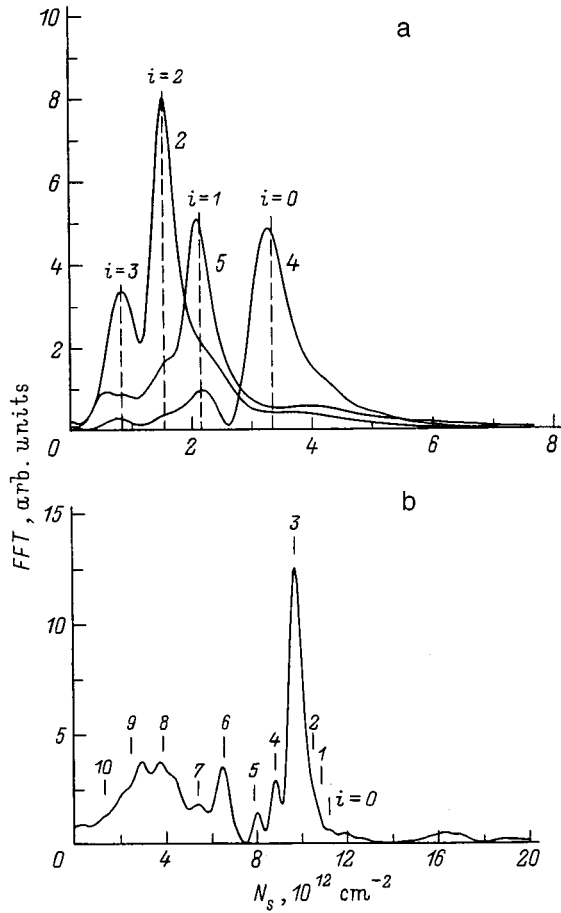
FIG. 3. Fourier spectra of the oscillations of the magnetoresistance in a reversed magnetic field for samples 2, 4, and 5 (a) and sample 6 (b). The arrows in part *b* show the concentrations corresponding to the calculated energies of the quantum-well subbands.

Because of the multiplier $(1-\cos\varphi)$ in the expression for τ_t, the transport scattering time can differ from the quantum analog. For isotropic scattering, for example, on phonons, these scattering times are equal. However, in the case of Coulomb scattering on ionized impurities, the cross section $\sigma(\varphi)$ is large for scattering into small angles; therefore, τ_t can be several times greater than τ_q.

An analysis of the magnetic-field dependence of the amplitude of the Shubnikov–de Haas oscillations makes it possible to determine the quantum mobilities $\mu_q = e/m^* \tau_q$ of electrons in each of the quantum-well subbands.[13] For this purpose, the corresponding frequencies are isolated in the Shubnikov–de Haas oscillations by a digital filter,[15] and a Dingle plot is constructed.[16] The quantum mobilities obtained increase in all the samples from approximately 600 cm^2/(V·s) in the lower quantum-well subbands to 2100 cm^2/(V·s) in the upper subbands (see Table II). These values are consistent with the mobility values obtained for silicon δ-doped GaAs structures.[17,18]

4. ENERGY SPECTRUM AND PHOTOLUMINESCENCE OF GaAs(δ-Sn) STRUCTURES

The band diagrams, wave functions, and electron concentrations in the quantum-well subbands were calculated by finding a self-consistent solution of the Schrödinger and Poisson equations by analogy with the calculations performed in Ref. 17. The nonparabolicity of the Γ conduction band was taken into account by substituting the mean square of the wave vector $\langle k_z^2 \rangle_i = \int_{-\infty}^{\infty} \psi_i(-d^2/dz^2)\psi_i\,dz$ into the dispersion relation according to Ref. 19, permitting a calculation of the density of states in the ith subband. The thickness of the δ layer of ionized tin atoms, which served as a

TABLE II. Electron concentrations n_{SdH} and quantum mobilities μ_q^{SdH} in different subbands determined from the Shubnikov–de Haas effect at 4.2 K, concentrations N_S obtained from self-consistent calculations, quantum mobilities μ_q^t of electrons calculated for scattering on ionized impurities with allowance for intersubband scattering, and experimental ($B_\parallel$) and calculated ($B_\parallel^t$) values of the parallel magnetic induction at which emptying of the subbands occurs.

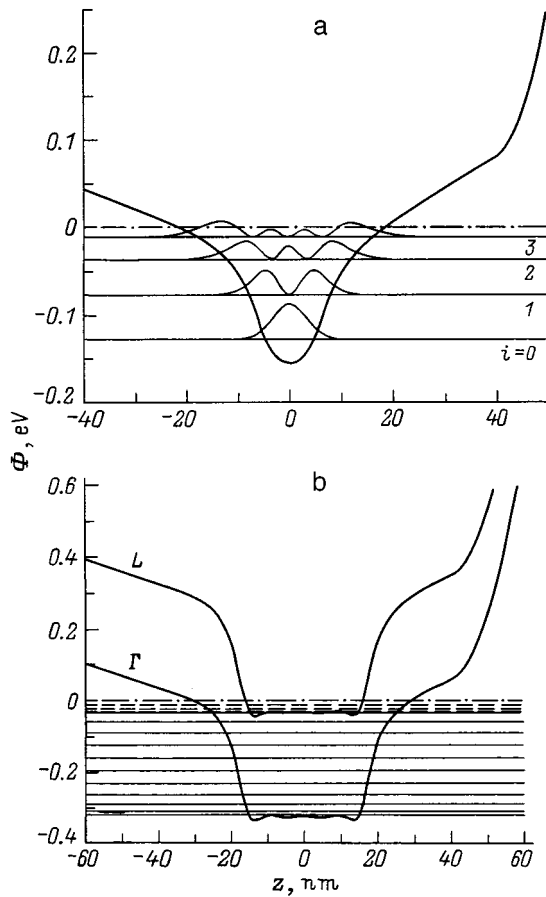| Sample No.	Subband number i	n_{SdH}, 10^{12}cm^{-2}	N_S, 10^{12}cm^{-2}	μ_q^{SdH}, cm^2/(V·s)	μ_q^t, cm^2/(V·s)	$B_\parallel$, T	$B_\parallel^t$, T
	0	1.76	1.75	1340	790	⋯	⋯
1	1	0.99	0.99	1450	900	18.6	20.5
	2	⋯	0.28	⋯	1120	4	7.4
	0	3.91	3.97	570	570	⋯	⋯
5	1	2.12	2.42	1100	740	33.4	41.7
	2	1.49	1.12	1630	1470	18.4	18.1
	3	0.57	0.33	2060	1830	5.6	6.3
	0	⋯	11.06	⋯	217	⋯	⋯
	1	⋯	10.80	⋯	217	⋯	⋯
	2	⋯	10.38	⋯	218	⋯	⋯
	3	9.75	9.75	1370	220	⋯	⋯
	4	8.84	8.87	1590	225	⋯	43.9
6	5	8.04	7.84	1910	236	36.3	34.1
	6	6.54	6.68	1330	258	29.6	28.7
	7	5.39	5.36	−	295	24.7	23.3
	8	3.76	3.91	−	359	19.7	17.8
	9	2.95	2.49	−	461	13.0	12.5
	10	−	1.32	−	509	7.6	8.0

FIG. 4. Band diagrams for samples 5 (a) and 6 (b). The energy is measured relative to the Fermi level (dot-dashed line). The free surface of the samples is located at $z = 60$ nm. The squares of the electronic wave functions in the subbands are also shown for sample 5. The energy levels at the L point in sample 6 are indicated by dashed lines.

fitting parameter in the calculations,[20] was found to be approximately equal to 16 nm for samples 1–5. Although such a δ layer thickness is higher than the values for silicon δ-doped structures,[4,7,21] it is small for tin.[1] The calculated two-dimensional electron concentrations in the quantum-well subbands are listed in Table II. Figure 4a shows the band diagram calculated for sample 5. It was taken into account in the calculations that the Fermi level is pinned on the free surface of the sample at a level 0.74 eV below the bottom of the conduction band[22] and in the semi-insulating substrate at the level for chromium (0.75 eV below the conduction band[23]).

In sample 6, which has the highest tin concentration $N_D = 2.67 \times 10^{14}\,\text{cm}^{-2}$ and a Hall concentration $n_H = 8.35 \times 10^{13}\,\text{cm}^{-2}$, the L conduction band should also be filled with electrons at low temperatures (according to Ref. 5, in the case of an ideally narrow δ layer this occurs when the concentration of the ionized impurity is above $N_D = 1.6 \times 10^{13}\,\text{cm}^{-2}$ and the electron concentration in the lowest subband is greater than $9.3 \times 10^{12}\,\text{cm}^{-2}$). In the case of several filled subbands, the Hall concentration is averaged over all the subbands:

$$n_H = \frac{\left(\sum_i n_i \mu_{ti} \right)^2}{\sum_i n_i \mu_{ti}^2}, \tag{3}$$

where n_i is the electron concentration, and μ_{ti} is the transport mobility in the ith subband. As a result, the value of n_H is less than the total electron concentration in all the subbands determined from the Shubnikov–de Haas effect; therefore, in order to achieve such a high value of n_H, sample 6 must have at least three subbands with a concentration greater than $10^{13}\,\text{cm}^{-2}$, which are weakly manifested in the range of magnetic fields investigated (see Fig. 3b). The electrons at the L point should not make a significant contribution to the value of n_H due to their low mobility. The following parameters of the electron effective masses at the L point for the (001) plane (Ref. 5) were used in the self-consistent calculation: for motion in the quantization direction $m_z = 0.11 m_0$, and for motion in the plane of the layer (the xy plane) $m_x = 0.075 m_0$ and $m_y = 1.29 m_0$. In this case the density-of-states effective mass $m_{ds} = (m_x m_y)^{1/2} = 0.38 m_0$, and there are four equivalent ellipsoids of constant energy (the degree of degeneracy $g_v = 4$). The energies of the size-quantized subbands at the L point were calculated at a potential displaced along the energy scale by $E_{L-\Gamma} = 290$ meV above the Γ point. The X point was neglected in the calculations, since $E_{X-\Gamma} = 460$ meV. The potential curve at the Γ and L points was obtained by solving the Poisson equation for the total charge distribution, which consists of both the filled electronic states at the Γ and L points and the stationary positive charge of the ionized tin donors. The calculated band diagram for sample 6 is presented in Fig. 4b. The electron concentrations at the Γ point obtained for a thickness of a δ layer of ionized impurities equal to 34 nm are roughly equal to the observed concentrations in the Fourier spectrum (Fig. 3b and Table II). The concentrations in the three lowest subbands are very close to one another, and, therefore, the corresponding peaks merge to form a single broad peak near $1.1 \times 10^{13}\,\text{cm}^{-2}$ in Fig. 3b; these peaks therefore cannot be clearly distinguished separately in the Fourier spectrum. The calculated electron concentrations in the three subbands at the L point are equal to 2.0×10^{13}, 1.54×10^{13}, and $7.8 \times 10^{12}\,\text{cm}^{-2}$. The total free-electron concentration in this sample is at least 4 times greater than the maximum achievable concentration for silicon δ-doped GaAs structures[6] when the thickness of the δ layer is small for tin.[1]

Low-temperature photoluminescence provides an important experimental technique for investigating two-dimensional electron systems. However, investigating the photoluminescence of δ-doped structures is complicated by the fact that the potential retaining electrons in the quantum-well subbands is repulsive toward holes. This repulsion can reduce the overlap between the electron and hole wave functions and can consequently lower the photoluminescence intensity.[24,25]

Figure 5 presents the photoluminescence emission spectra of samples 3, 5, and 6, as well as a control sample with-
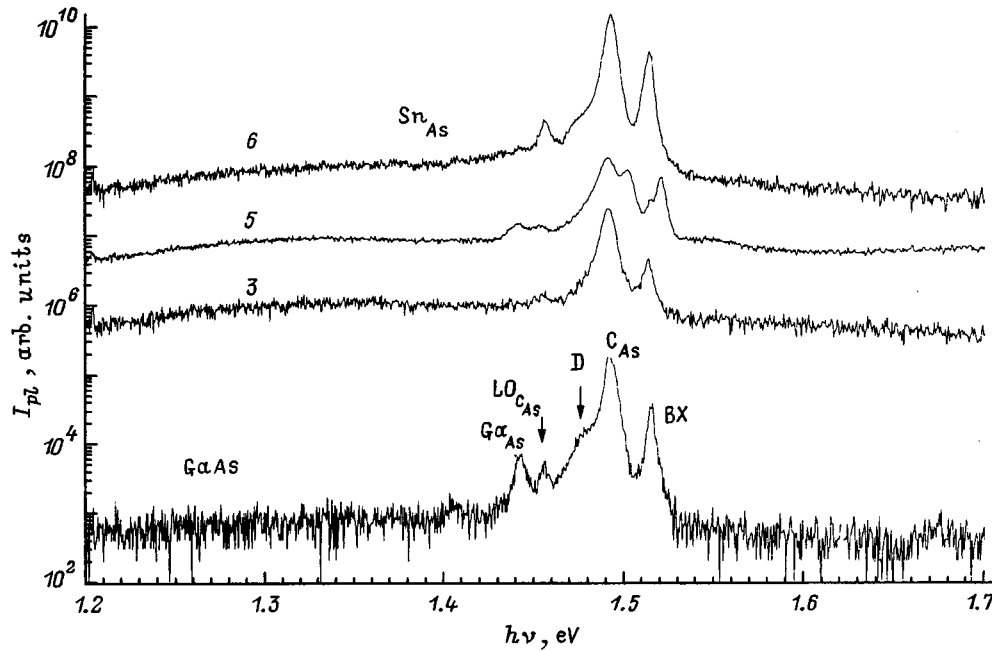
FIG. 5. Photoluminescence spectra of samples 3, 5, and 6 and of the control sample of GaAs without a δ layer at $T = 4.2$ K. The positions of the maxima are explained in the text.

out a δ layer. The control sample was obtained by etching away the upper layers of sample 1, which contains a δ layer, to a depth of 100 nm. The low-temperature photoluminescence spectra of the GaAs sample without a δ layer contains characteristic lines with an energy of 1.514 eV, which corresponds to the recombination of excitons bound to a neutral donor; a line with an energy of 1.492 eV, which corresponds to a radiative electronic transition to a carbon acceptor level, and its LO-phonon replica with an energy of 1.456 eV; and a line with an energy of 1.442 eV (a Ga defect in the As sublattice).[26,27] The spectral feature at 1.478 eV is caused by recombination of a bound exciton involving an LO phonon, as well as recombination at defects appearing during growth by molecular-beam epitaxy.

For structures with δ layers of different concentrations the form of the photoluminescence spectrum varies as the doping level of the δ layer increases. A broad band with a maximum at 1.35 eV (see Fig. 5), which is caused by a radiative transition to a Sn acceptor level localized in the region of the δ layer, appears. The intensity of this band increases with increasing tin concentration. In addition, the ratio between the intensities of the lines characteristic of the sample without a δ layer described above varies, and new spectral features, which can be attributed to the recombination of electrons from quantum-well levels in the δ layer and photogenerated holes localized near the sample surface, appear.[24] The features caused by the quantum-well levels are especially pronounced for sample 5 (Fig. 6, the peaks with energies equal to 1.521 and 1.502 eV). These features can most probably be assigned to electronic transitions from the upper quantum-well levels, since the wave functions of the upper subbands extend far from the midplane of the δ layer and their overlap with the hole wave functions is greater than that for the lower subbands. The energy difference between

the upper $i = 2$ and $i = 3$ subbands obtained for this sample in a self-consistent calculation is equal to 25 meV, which roughly coincides with the difference between the new photoluminescence lines. We also note that, along with the recombination channel just described, the recombination of electrons from the upper $i = 3$ electronic level and holes localized at a carbon acceptor can make a contribution to the line at 1.502 eV.

The wave functions found in the self-consistent calculations were used to calculate the low-temperature quantum mobilities of electrons for multisubband scattering at ionized impurities,[28-30] which are listed in Table II. The screening of the scattering Coulomb potential was taken into account in the random-phase approximation.[28] It can be seen from the
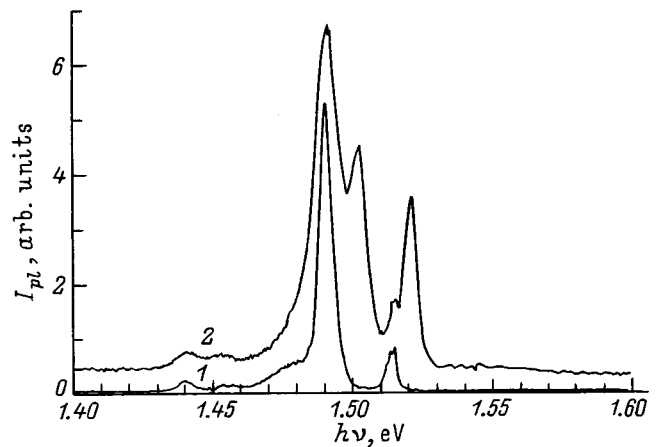

FIG. 6. Isolated parts of the photoluminescence spectra of the control sample without a δ layer (*1*) and sample 5 (*2*) at $T = 4.2$ K. The photoluminescence intensities are the same as in Fig. 5.
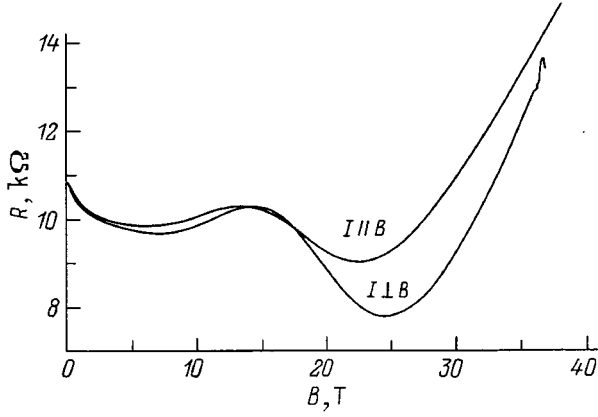
FIG. 7. Resistance of sample 1 in a magnetic field parallel to the δ layer for two orientations of the current through the sample relative to the magnetic field.

FIG. 8. Quantum-well energy subbands in sample 2 in the absence of a magnetic field (dashed lines) and in a field with $B = 18$ T (solid lines).

numerical calculations (see Table II) that the electron mobilities increase with the subband number i, since the mean distance from electrons to impurities is greater in the upper subbands. The calculated quantum mobilities in samples 1–5 were somewhat smaller than the values determined from the Shubnikov–de Haas effect (see Table II) due to the partial correlation in the distribution of the ionized impurities.[31,32] In sample 6 the quantum mobilities of electrons determined from the Shubnikov–de Haas effect are more than six times greater than the calculated quantum mobilities. This is attributable to the strong screening of the ionized impurities by the L-band electrons, which have a large effective mass (this screening was disregarded in the calculations), as well as by stronger correlation of the impurities than in samples 1–5.

5. RESISTANCE OSCILLATIONS IN A MAGNETIC FIELD PARALLEL TO THE δ LAYER

Measuring the Shubnikov–de Haas effect is the principal method for determining the electron concentrations in quantum-well subbands of two-dimensional systems. However, in δ-doped structures the upper subbands have low concentrations of electrons, from which oscillations are difficult to see when the Shubnikov–de Haas effect is measured. The diamagnetic Shubnikov–de Haas effect, under which the magnetic field is directed in the plane of the δ layer, however, permits exact determination of the number of filled subbands[33] and is a useful tool for investigating multisubband two-dimensional systems. As an example, Fig. 7 presents the resistance oscillations of sample 1 in a magnetic field parallel to the surface for currents parallel and perpendicular to the magnetic field.

If the magnetic induction B is directed along the y axis and the vector potential is $\mathbf{A} = (Bz,0,0)$, the Schrödinger equation has the form[34]

$$\left[\frac{p_y^2}{2m^*} + \frac{1}{2m^*}(p_x + ezB)^2 - \frac{\hbar^2}{2m^*} \frac{\partial^2}{\partial z^2} + \Phi(z) \right] \Psi = E\Psi. \tag{4}$$

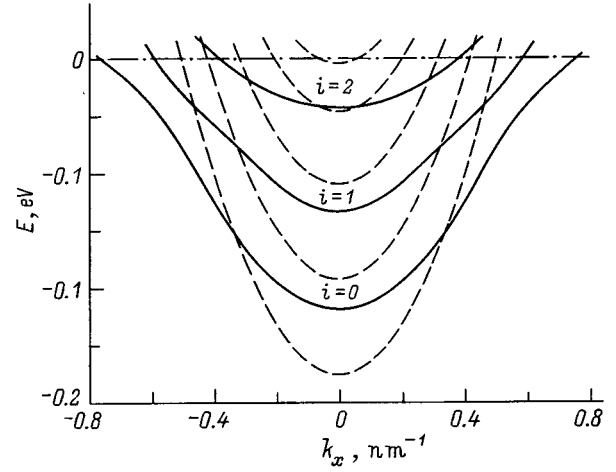Here the potential $\Phi(z)$ is the sum of the electrostatic potential U_H determined from the Poisson equation

$$\frac{d^2 U_H(z)}{dz^2} = -\frac{e^2}{\varepsilon_0 \varepsilon} \left[\sum n_i \psi_i^2(z) - N(z) \right], \tag{5}$$

where $\varepsilon = 13.18$ is the dielectric constant of GaAs, $N(z)$ is the volume concentration of ionized donors, and $n_i = m^*/\pi\hbar^2 (E_F - E_i)$ is the two-dimensional electron concentration in the ith subband, and of the exchange-correlation potential U_{xc} (Ref. 35)

$$U_{xc} = -\left[1 + 0.0545 r_S \ln\left(1 + \frac{11.4}{r_S} \right) \right] \frac{2}{\pi \alpha r_S} Ry^*, \tag{6}$$

where

$$\alpha = \left(\frac{4}{9\pi} \right)^{1/3}, \quad r_S = \left(\frac{4\pi a_B^3 n(z)}{3} \right)^{-1/3},$$

$$a_B^* = \frac{4\pi\varepsilon_0\varepsilon\hbar^2}{m^* e^2}, \quad Ry^* = \frac{e^2}{8\pi\varepsilon_0\varepsilon a_B^*},$$

$n(z)$ is volume concentration of electrons. The self-consistent solution can be written in the form

$$E = E_i(k_x) + \frac{\hbar^2}{2m^*} k_y^2. \tag{7}$$

The calculations were performed for the parabolic case, and the electron effective mass in all the subbands was assumed to be $m^* = 0.07 m_0$. Figure 8 presents plots of $E_i(k_x)$ for $B = 0$ and $B = 18$ T in the case of sample 2. It is seen that in such a magnetic field the $i = 4$ and $i = 3$ subbands are pushed upward above the Fermi level and emptied; here the electrons are redistributed among the remaining three subbands in the varying self-consistent potential $\Phi(z)$. As the magnetic field is increased, the subbands are shifted toward the Fermi level, and the total density of states $g(B)$ increases, but it subsequently drops sharply when the energy of each successive subband passes through the Fermi level. The increase in the density of states and emptying of the subbands lead to oscillations of the magnetoresistance (Fig. 9). The calculated values of the magnetic induction $B_\parallel^t$ at which emp-
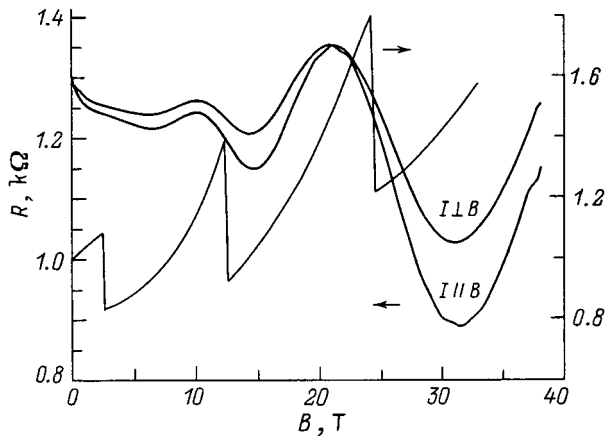
FIG. 9. Dependence of the resistance of sample 2 on the magnetic induction parallel to the δ layer for two orientations of the current through the sample relative to the magnetic field and ratio of the calculated density of states at the Fermi level $g(B)$ to the density of states in the absence of a magnetic field $g(0)$.

tying of the respective quantum-well subbands occurs and the experimental values of $B_\parallel$ determined from the minima of the first derivative of the magnetoresistance[34] closely coincide (see Table II). The small difference between the calculated and experimentally determined values of $B_\parallel$ can be attributed to the fact that the crossing of the Fermi level by the subbands is accompanied by changes not only in the density of states, but also in the electron mobilities due to intersubband scattering.[36] The positions of the resistance maxima depend weakly on the direction of the current flowing through the sample relative to the parallel magnetic field (Figs. 7 and 9), as in the case of thick silicon δ layers.[34]

In sample 6 the energy position of the subbands is determined to a considerable degree by the nonparabolicity of the Γ conduction band: according to the calculations, the electron effective mass increases from $0.083m_0$ in the lowest subband to $0.1m_0$ in the highest. Perturbation theory can be used to estimate the values of the parallel magnetic induction $B_\parallel$ at which emptying of the subbands occurs in this sample. Emptying of a subband occurs when the diamagnetic energy shift $e^2 B_\parallel^2 / 2m^* \langle z_i^2 \rangle$ equals the energy of the bottom of the respective subband $E_i = \pi \hbar^2 / m^* n_i$. We thus obtain

$$B_\parallel = \sqrt{\frac{2 \pi \hbar^2 n_i}{e^2 \langle z_i^2 \rangle}}. \tag{8}$$

Formula (8) does not contain the effective mass and agrees fairly well with the results of the exact calculation.[37] The values of the magnetic induction $B_\parallel$ thus obtained for sample 6 agree well with the experimentally determined values (see Table II), attesting to the correctness of the description of the upper subbands in this sample.

6. CONCLUSIONS

The transport and optical properties of GaAs(δ-Sn) structures have been investigated as a function of the tin concentration. The calculated quantum mobilities of electrons in the quantum-well subbands agree fairly well with the

corresponding values determined from the Shubnikov–de Haas effect. The maximum two-dimensional free-electron concentration obtained exceeds the limiting values for silicon δ-doped GaAs structures when the thickness of the tin δ layer is relatively small. At such high concentrations the L conduction band is filled with electrons. The calculated values of the parallel magnetic induction at which emptying of the subbands occurs closely coincide with the experimentally determined values.

[1] J. J. Harris, D. E. Ashenford, C. T. Foxon, P. J. Dobson, and B. A. Joyce, Appl. Phys. A: Solids Surf. **33**, 87 (1984).

[2] A. de Visser, V. I. Kadushkin, V. A. Kul'bachinskiĭ, V. G. Kytin, A. P. Senichkin, and E. L. Shangina, JETP Lett. **59**, 363 (1994).

[3] V. A. Kulbachinskii, R. A. Lunin, E. V. Bogdanov, V. G. Kytin, and A. P. Senichkin, Physica B **229**, 262 (1997).

[4] A. Zrenner, F. Koch, and K. Ploog, Surf. Sci. **196**, 671 (1988).

[5] A. Zrenner, F. Koch, R. L. Williams, R. A. Stradling, K. Ploog, and G. Weimann, Semicond. Sci. Technol. **3**, 1203 (1988).

[6] J. V. Thordson, T. G. Andersson, G. Swenson, and U. Rodervall, J. Cryst. Growth **175/176**, 234 (1997).

[7] S. P. Wilks, A. E. Cornish, M. Elliot *et al., J. Appl. Phys.* **76**, 3583 (1994).

[8] R. C. Newman, M. J. Ashwin, M. R. Fahy *et al., Phys. Rev. B* **54**, 8769 (1996).

[9] C. Domke, P. Ebert, M. Heinrich, and K. Urban, Phys. Rev. B **54**, 10 288 (1996).

[10] D. K. Maude, J. C. Portal, L. Dmowski *et al., Phys. Rev. Lett.* **59**, 815 (1987).

[11] P. M. Mooney, J. Appl. Phys. **67**, R1 (1990).

[12] P. M. Koenraad, in *Delta Doping of Semiconductors*, E. F. Schubert (Ed.), Cambridge University Press, Cambridge (1996), Chap. 17.

[13] P. M. Koenraad, A. F. W. van de Stadt, J. M. Shi *et al., Physica B* **211**, 462 (1995).

[14] P. T. Coleridge, R. Stoner, and R. Fletcher, Phys. Rev. B **39**, 1120 (1989).

[15] J. F. Kaiser and W. A. Reed, Rev. Sci. Instrum. **49**, 1103 (1978).

[16] P. T. Coleridge, Phys. Rev. B **44**, 3793 (1991).

[17] V. A. Kul'bachinskiĭ, R. A. Lunin, V. G. Kytin, A. S. Bugaev, and A. P. Senichkin, Zh. Éksp. Teor. Fiz. **110**, 1517 (1996) [JETP **83**, 841 (1996)].

[18] R. A. Lunin, V. G. Kytin, V. A. Kul'bachinskiĭ, and G. A. Mironova, Vestn. Mosk. Univ., Ser. 3: Fiz. Astron., No. **4**, 31 (1997).

[19] U. Rössler, Solid State Commun. **49**, 943 (1984).

[20] M. H. Degani, Phys. Rev. B **44**, 5580 (1991).

[21] E. F. Schubert, C. W. Tu, R. F. Kopf *et al., Appl. Phys. Lett.* **51**, 2592 (1989).

[22] T. M. Hsu, W.-H. Chang, D. H. Liao, and W. C. Lee, J. Appl. Phys. **84**, 1074 (1998).

[23] A. Chandra, C. E. C. Wood, D. W. Woodard, and L. F. Eastman, Solid-State Electron. **22**, 645 (1979).

[24] J. Wagner, A. Fischer, and K. Ploog, Phys. Rev. B **42**, 7280 (1990).

[25] J. Wagner and D. Richards, in *Delta Doping of Semiconductors*, E. F. Schubert (Ed.), Cambridge University Press, Cambridge (1996), Chap. 15.

[26] M. S. Skolnick, C. W. Tu, and T. D. Harris, Phys. Rev. B **33**, 8468 (1986).

[27] D. J. Ashen, P. J. Dean, D. T. J. Hurle *et al., J. Phys. Chem. Solids* **36**, 1041 (1975).

[28] G.-O. Hai, N. Studart, and F. M. Peeters, Phys. Rev. B **52**, 8363 (1995).

[29] L. R. Gonzalez, J. Krupski, and T. Szwacka, Phys. Rev. B **49**, 11 111 (1994).

[30] L. C. D. Goncalves and A. B. Henriques, Semicond. Sci. Technol. **12**, 203 (1997).

[31] J. M. Shi, P. M. Koenraad, A. F. W. van de Stadt *et al., Phys. Rev. B* **55**, 13 093 (1997).

[32] R. Shikler, M. Heiblum, and V. Umansky, Phys. Rev. B **55**, 15 427 (1997).

[33] H. Reisinger and F. Koch, Surf. Sci. **170**, 397 (1986).

[34] A. F. W. van de Stadt, R. Bogaerts, P. M. Koenraad *et al.*, Physica B **211**, 458 (1995).

[35] *Theory of the Inhomogeneous Electron Gas*, S. Lundqvist and N. H. March (Eds.) [Plenum Press, New York (1983); Mir, Moscow (1987)].

[36] J. M. Heisz and E. Zaremba, Phys. Rev. B **53**, 13 594 (1996).

[37] A. Zrenner, H. Reisinger, F. Koch, K. Ploog, and J. C. Maan, Phys. Rev. B **33**, 5607 (1986).

Translated by P. Shelnitz

Collective resonances and shape function for homogeneous broadening of the emission spectra of quantum-well semiconductor heterostructures

A. M. Georgievskiĭ, S. V. Zaĭtsev, N. Yu. Gordeev, V. I. Kopchatov, L. Ya. Karachinskiĭ, I. I. Novikov, and P. S. Kop'ev

A. F. Ioffe Physicotechnical Institute, Russian Academy of Sciences, 194021 St. Petersburg, Russia
(Submitted December 3, 1998; accepted for publication December 8, 1998)
Fiz. Tekh. Poluprovodn. **33**, 847–850 (July 1999)

An analytic expression for the shape function for homogeneous broadening of the emission spectra of semiconductor heterostructure lasers is obtained on the basis of simple expressions from the theory of the superradiance of two-level systems. Good agreement between the theory and experimental data is achieved for an InGaAs/GaAs quantum-well heterostructure laser. An estimate of the duration of the superradiance pulse is given. © *1999 American Institute of Physics.* [S1063-7826(99)01707-X]

1. INTRODUCTION

The problem of investigating the mechanisms of homogeneous broadening in semiconductors was examined in Ref. 1 in connection with the need to simulate the emission spectra of injection lasers. A deviation of the shape of the emission spectrum from the classical Lorentzian contour was pointed out in that paper. The need to take into account the coherent interaction of radiation with the medium at times of the order of the coherence loss time was pointed out in Ref. 2. However, when the processes taking place in lasers are described, such effects are ordinarily ignored, and the treatment is confined to the incoherent approximation.

Consideration of the coherent interaction of carriers during emission opens the way to explain a number of phenomena in the physics of semiconductor lasers. For example, the formal similarity of stimulated emission to superradiance was noted in Ref. 3. The possibility of switching a semiconductor laser pumped by a constant current to an undamped pulsation regime was theoretically demonstrated in Ref. 4. Such pulsations have also been observed experimentally. For example, previously performed autocorrelation investigations of injection lasers above the lasing threshold revealed the existence of subpicosecond pulses in the structure of the output under continuous pumping.[5]

The present work was devoted to exploring the influence of the collective interaction of carriers on the shape function for homogeneous broadening of the emission spectra of semiconductor lasers below the lasing threshold. The emission spectra of separate-confinement double heterostructure lasers with a quantum-well active layer were investigated experimentally. Good agreement with the theoretical models was obtained.

2. THEORETICAL MODEL

A. Coherent spontaneous emission of a two-level system

Our theoretical treatment is based on the simple model of coherent spontaneous emission by a polyatomic system.[6] If the concentration of dipoles is sufficiently high, they be-come synchronized during emission with the resultant appearance of a coherent emission component with an intensity proportional to the square of the number of interacting dipoles. Such phenomena were first described theoretically by Dicke[7] and have been termed ''Dicke superradiance.''

If the inhomogeneous broadening is disregarded in comparison to the homogeneous broadening, we can apply the results obtained for two-level systems to the description of emission processes in semiconductors. The time dependence of the radiation intensity for an excited polyatomic system can then be described with sufficient accuracy as

$$I(t) = \frac{\hbar \omega_0}{4 \mu \tau_N} (N\mu + 1)^2 \mathrm{sech}^2\left(\frac{t - t_0}{2\tau_N}\right),$$

$$\frac{1}{\tau_N} = (N\mu + 1)\frac{1}{\tau_1},$$

$$t_0 = \tau_N \ln(N\mu), \tag{1}$$

where N is the number of emitting dipoles in the ensemble, μ is the shape function of the active region, the parameter $N\mu$ characterizes the efficiency of the interaction of the dipoles, τ_N is the collective interaction time or the duration of the superradiance pulse, and t_0 is the dipole accumulation (synchronization) time corresponding to intensity maximum.[6]

Following Ref. 1, the shape function for homogeneous broadening is determined by the kinetics of the emission process and is obtained by Fourier transformation of the wave packet corresponding to the dipole moment of the electron-hole pair. The wave packet [Eq. (1)] clearly corresponds to the expression

$$E(t) \sim \Theta(t + t_0)\mathrm{sech}\left(\frac{t}{2\tau_N}\right)\exp(i\omega_0 t). \tag{2}$$

Here we assume that the emission process began at $t = -t_0$. The shape function for homogeneous broadening can then be written in the form

$$F(\delta = \omega - \omega_0) \sim \int_{-\infty}^{+\infty} E(t) \exp(-i\omega t)\, dt$$

$$= \int_{-t_0}^{+\infty} \frac{\exp(-i\delta t)}{\cosh\left(\dfrac{t}{2\tau_N}\right)}\, dt, \qquad (3)$$

where δ is the frequency mismatch.

For working concentrations of the order of $10^{18}\,\text{cm}^{-3}$ there are of the order of 2×10^4 charge carriers in a volume with linear dimensions equal to the output wavelength of 1 μm. This simple estimate shows that the number of sources in the ensemble is so high that the accumulation time (t_0) can be considered fairly large compared with the emission time (τ_N), especially since t_0 appears in the exponent in (1). Thus, we can expand the integration range to obtain the shape function for homogeneous broadening in an analytic form:

$$F(\delta) \sim \int_{-\infty}^{+\infty} \frac{\exp(-i\delta t)}{\cosh\left(\dfrac{t}{2\tau_N}\right)}\, dt$$

$$= 2\int_{0}^{+\infty} \frac{\cos(\delta t)}{\cosh\left(\dfrac{t}{2\tau_N}\right)}\, dt = 2\pi t_N \operatorname{sech}(\pi\delta\tau_N).$$

$$(4)$$

We note that the shape function for homogeneous broadening of such a form agrees well with the results obtained in Ref. 8.

B. Shape function for homogeneous broadening and corresponding emission spectrum

The final form of the emission spectrum is defined as the convolution of the inhomogeneously broadened spectrum $[R_0(E)]$ and the shape function for homogeneous broadening:[1]

$$R(\hbar\omega) = \int_{0}^{+\infty} R_0(E) F\left(\frac{\hbar\omega - E}{\hbar}\right) dE. \qquad (5)$$

This formula is valid only for cases where the inhomogeneous broadening is much smaller than the homogeneous broadening. Otherwise, the region of applicability of Eq. (5) can be expanded only by introducing the dependence of the shape function on energy. Since the expression for the shape function (4) already contains the dependence on the effective number of interacting dipoles ($N\mu$), expansion of the region of applicability of the theory to the case of a broad carrier energy distribution $[R_0(E)]$ is a fairly simple task.

When the case where the inhomogeneous broadening is much smaller than the homogeneous broadening is considered, the carrier energy distribution operates as a δ function, and the result of the integration in (5) mimics the form of $F(\delta)$. Such a situation is realized, for example, at low temperatures and a pumping level that is not excessively high for the quantum layer. The inhomogeneous broadening can also be ignored when ideal quantum dots are considered as the active layer.

Thus, on the long- and short-wavelength tails of the spectrum, where $\hbar\omega$ is significantly smaller or greater than E_g, the asymptotes of the function (5) [the slope of the function (5) on a logarithmic scale] will be determined exclusively by the shape function for homogeneous broadening (4):

$$R(\hbar\omega) \sim \exp(\pm\pi\omega\tau_N), \qquad (6)$$

under the condition $|\hbar\omega - E_g| > \dfrac{\hbar}{\pi\tau_N}$.

In order for an asymmetric spectrum to be obtained, we must have an asymmetric shape function in the form

$$F(\delta) = \frac{2}{\exp(\delta t_1) + \exp(-\delta t_2)} = \exp(-\delta\Delta t)\operatorname{sech}(\delta\tau_n), \quad (7)$$

where $\tau_n = (t_1 + t_2)/2$ and $\Delta t = (t_1 - t_2)/2$.

There are several physical mechanisms which lead to asymmetry of the shape function for homogeneous broadening.

When the emission spectrum from the end surface of a heterostructure is measured, the absorption (reemission) in the waveguide and the emitters plays a significant role.[9] When the spectra are measured through a lateral surface, the role of reemission in the waveguide of the laser structure is reduced to a minimum, but the presence of an absorption ''tail'' in the emitters and (or) the substrate near the absorption edge makes a contribution to the shape function in the form of the exponential multiplier (7) (Urbach's rule). In addition, distortion of the low-energy part of the spectrum due to radiative recombination through impurity centers is possible.

Thus, if the condition under which the homogeneous broadening is significantly greater than the inhomogeneous broadening associated with the energy distribution of the carriers holds in an experiment, the parameter τ_n in (7) takes on the meaning of the characteristic time of the resonance interaction of the carriers τ_N (the pulse duration) multiplied by π [in accordance with (4)].

3. EXPERIMENTAL RESULTS

A separate-confinement double heterostructure laser was grown in an InGaAs/GaAs system by molecular-beam epitaxy on a silicon-doped n-GaAs(100) substrate. The active region was positioned in the middle of a GaAs layer with a thickness of 200 nm separated from the surface and the substrate by short-period AlAs/GaAs superlattices. The active region was a quantum well, i.e., an In$_{0.15}$Ga$_{0.85}$As layer with a thickness of 100 Å.

The samples were investigated under pulsed excitation (with a pulse duration of 3 μs and a repetition frequency of 5 kHz) at 77 K. For this purpose, the samples were fused in layers to the underside of a thermal conductor and placed in a cryostat. The emission was measured through a special window in the upper contact of each laser structure. Special attention was focused on suppressing the feedback, the mirrors were etched and then covered by a black paint with a
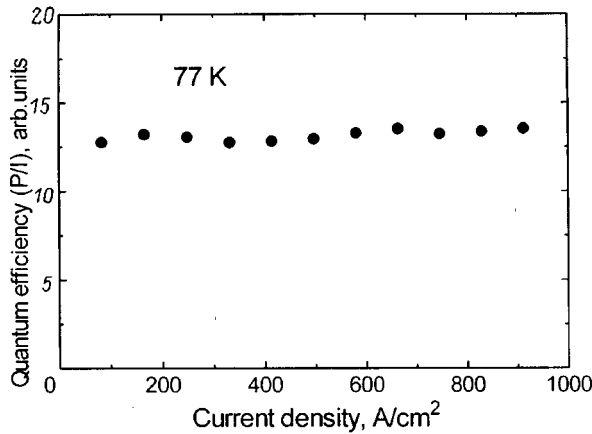
FIG. 1. Dependence of the spontaneous-recombination quantum efficiency on pump current density.

FIG. 3. Dependence of the collective emission time (τ_N) on pump current density.

high refractive index. This method, which permits elimination of the influence of reemission, was described in detail in Ref. 9.

Apart from investigating the emission spectra, the radiated power was measured, enabling us to construct a plot of the external recombination quantum efficiency as a function of pump current density (Fig. 1). The constant value of this parameter attests to the absence of lasing up to a pump current density equal to 900 A/cm^2.

It can clearly be seen in the observed spontaneous emission spectra plotted on a semilogarithmic scale (Fig. 2) that both slopes can be approximated by exponential functions (they are shown as dotted lines). Thus, a case where the homogeneous broadening is much greater than the inhomogeneous broadening is realized. A calculation of the expo-

nential decay times t_1 and t_2 using formula (7) permitted estimation of the collective interaction time τ_N as a function of the pump current density (Fig. 3). In this case τ_N increases from 20 to 35 fs as the current is increased.

4. CONCLUSIONS

It has been shown that consideration of the coherent interaction of the carriers during emission can account for the deviation of the experimentally observed, homogeneously broadened spectrum from the classical Lorentzian contour. The analytic expression obtained for the shape function for homogeneous broadening can be used to simulate the dynamics and emission spectra of semiconductor lasers. The parameters of the spectra have been measured. The dependence of these spectra on the pump current density at low temperatures (77 K) has been investigated, and the characteristic time of the collective interaction has been estimated on its basis.

FIG. 2. Spontaneous emission spectra of a quantum-well heterostructure laser through a window in the substrate (the temperature was 77 K).

[1] P. G. Eliseev and I. V. Akimova, Fiz. Tekh. Poluprovodn. **32**, 478 (1998) [Semiconductors **32**, 428 (1998)].
[2] P. G. Eliseev, *Introduction to the Physics of Injection Lasers* [in Russian], Nauka, Moscow (1983).
[3] D. G. Deppe, Phys. Rev. A **54**, 2506 (1996).
[4] A. A. Belyanin and V. V. Kocharovsky, Quantum Semiclassic. Opt. **10**, L13 (1998).
[5] S. V. Zaitsev and A. M. Georgievski, Jpn. J. Appl. Phys. , Part 1 **36**, 4209 (1997) (Proceedings of the International Conference QDS'96).
[6] L. Allen and J. H. Eberly, *Optical Resonance and Two-Level Atoms*, Wiley, New York–London–Sydney–Toronto (1975).
[7] R. H. Dicke, Phys. Rev. **93**, 99 (1954).
[8] P. G. Eliseev and I. V. Akimova, Fiz. Tekh. Poluprovodn. **32**, 472 (1998) [Semiconductors **32**, 423 (1998)].
[9] Zh. I. Alferov, D. Z. Garbuzov, S. V. Zaĭtsev, A. B. Nivin, A. V. Ovchinnikov, and I. S. Tarasov, Fiz. Tekh. Poluprovodn. **21**, 824 (1987) [Sov. Phys. Semicond. **21**, 503 (1987)].

Translated by P. Shelnitz

Electron-beam-induced conductivity in self-organized silicon quantum wells

A. N. Andronov and S. V. Robozerov

St. Petersburg State Technical University, 195251 St. Petersburg, Russia

N. T. Bagraev, L. E. Klyachkin, and A. M. Malyarenko

A. F. Ioffe Physicotechnical Institute, Russian Academy of Sciences, 194021 St. Petersburg, Russia
(Submitted November 20, 1998; accepted for publication December 8, 1998)
Fiz. Tekh. Poluprovodn. **33**, 851–857 (July 1999)

Electron-beam diagnostics are used to study self-organized quantum wells which form within ultrashallow silicon p^+-n junctions under the conditions of nonequilibrium boron diffusion. The energy dependence and current-voltage characteristics of the electron-beam-induced conductivity are investigated with relative dominance of both longitudinal and transverse quantum wells, which are oriented parallel and perpendicularly to the $p-n$ junction plane, respectively. Current-voltage characteristics of the electron-beam-induced conductivity are exhibited for the first time with both reverse and forward biasing of the silicon p^+-n junction. This became possible because of the presence of self-organized transverse quantum wells within the ultrashallow p^+ diffusion profile, while self-organized longitudinal quantum wells promote the appearance of electron-beam-induced conductivity only when the p^+-n junction is reverse-biased. The distribution of the probability for the separation of electron-hole pairs across the thickness of the crystal derived from the energy dependences of the electron-beam-induced conductivity reveals effects of the avalanche multiplication of the nonequilibrium carriers as a result of the spatial separation of electrons and holes in the field of a p^+-n junction that contains self-organized transverse quantum wells. © *1999 American Institute of Physics.* [S1063-7826(99)01807-4]

1. INTRODUCTION

The practical utilization of the gettering of dopants by excess fluxes of vacancies or intrinsic interstitial atoms within planar silicon diffusion technology has made it possible to obtain ultrashallow ($5-20$ nm) diffusion profiles of boron and phosphorus with a sharp boundary.[1,2] The doping level, depth, and properties of ultrashallow diffusion profiles depend on the crystallographic orientation of the single-crystal silicon, the diffusion temperature, and the thickness of the preliminarily deposited oxide, whose interface with silicon (Si/SiO_2) is a source for the generation of intrinsic interstitial atoms and vacancies, which activate the *kick-out* and vacancy mechanisms of impurity diffusion, respectively.[1–6]

The study of the cyclotron resonance and quantized conductivity features have shown that the ultrashallow $p-n$ junctions obtained on the surface of single-crystal silicon under the conditions of a strong exchange interaction between the dopant and intrinsic interstitial atoms (the kick-out diffusion mechanism) consist of transverse quantum wells oriented in the [111] crystallographic direction, while the gettering of impurity atoms by vacancies (vacancy diffusion mechanisms) leads to the dominance transverse quantum wells oriented in the [100] direction within ultrashallow diffusion profiles.[1,7,8] Very shallow diffusion profiles (~ 5 nm), which consist predominantly of longitudinal quantum wells oriented parallel to the plane of the $p-n$ junction, have been obtained under the conditions of parity between the kick-out and vacancy diffusion mechanisms.[7,8]

In this paper we present the results of experimental studies of the effect of self-organized transverse and longitudinal quantum wells on the current-voltage characteristics (IVC's) and energy dependence of the electron-beam-induced conductivity generated during the probing of p^+ diffusion profiles by low- and medium-energy electrons. The experimental method employed permits determination of the distribution of the probability for the separation of electron-hole pairs by the field of the $p-n$ junction across the thickness of the crystal, which makes it possible to identify processes leading to the avalanche multiplication of nonequilibrium carriers within self-organized quantum wells, as well as to record IVC's of the electron-beam-induced conductivity with both reverse and forward biasing of the $p-n$ junction.

2. FORMING ULTRASHALLOW p^+-n JUNCTIONS UNDER NONEQUILIBRIUM DIFFUSION CONDITIONS IN SILICON

Ultrashallow p^+-n junctions were obtained from wafers of (111) n-type silicon with a thickness of 350 μm and a resistivity $\rho \cong 90$ $\Omega\cdot$cm. Both sides of each wafer were preliminarily oxidized in an atmosphere of dry oxygen at 1150 °C, and then circular windows with a diameter of 3 mm were cut in the oxide layer on the working side using photolithography to allow the diffusion of boron from the gas
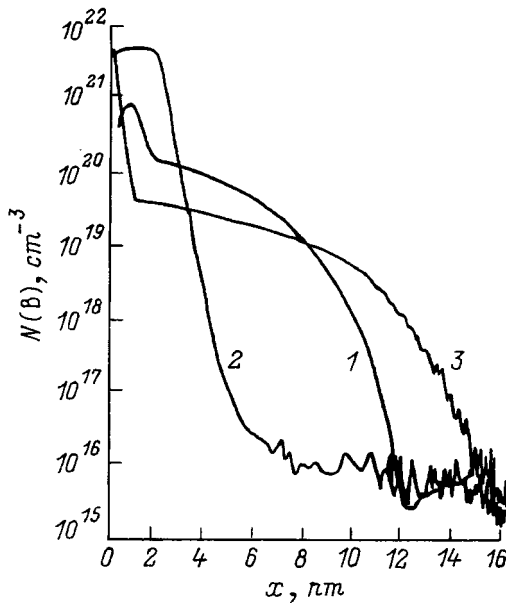
FIG. 1. Boron concentration profiles in silicon $p^+ - n$ junctions formed on a (111) silicon surface doped with phosphorus to a concentration $N(\mathrm{P}) = 5 \times 10^{13}$ cm^{-3} at various diffusion temperatures T_{dif}, °C: *1* — 800, *2* — 900, *3* — 1100.

phase in a brief (4 min) process. The values of the diffusion temperature (800 and 900 °C) were varied during the experiments, while the thickness of the preliminarily deposited surface oxide remained unchanged, permitting simulation of the conditions of the kick-out and vacancy mechanisms of impurity diffusion.[1–6] The thickness of the preliminarily deposited oxide on both sides of the wafers was greater than $d_0 \cong 0.44$ μm, stimulating the additional injection of vacancies by the Si/SiO$_2$ interface during impurity diffusion.[1,9,10] In addition, a high concentration of the nonequilibrium vacancies responsible for the dopant gettering effects was ensured during diffusion by additional saturation of the boron-containing gas phase with dry oxygen and chlorine compounds. In the concluding stage of the technological process, ohmic contacts were formed along the perimeter of the windows and on the reverse side of the wafers. The concentration profiles of the dopant were measured using secondary-ion mass spectrometry (SIMS) (see Fig. 1).[2,11]

At a diffusion temperature $T_{\mathrm{dif}} = 800$ °C boron penetrates into silicon as a result of the gettering of impurity atoms by silicon vacancies.[1,6,9,10] In this case, as in the case of dominance of the kick-out mechanism, acceleration of the impurity diffusion process is observed (Fig. 1, curve *1*). Drastic slowing of boron diffusion is observed at a diffusion temperature $T_{\mathrm{dif}} = 900$ °C (Fig. 1, curve *2*), i.e., in the region of parity between these diffusion mechanisms,[9,10] because of the intense annihilation of the intrinsic interstitial atoms and vacancies near the working surface of the silicon wafer. The diffusion profiles obtained under the conditions of brief nonequilibrium diffusion differ from the classical form; ultrasharp boron profiles are formed in the cases of both the suppression and acceleration of impurity diffusion, indicating the existence of a fractal mechanism of diffusion doping under the conditions of a strong interaction between the

fluxes of impurity atoms and intrinsic defects, whose intensity is determined by the form of the deformation potential on the Si/SiO$_2$ interface.[9,10]

3. METHOD FOR INVESTIGATING THE ELECTRON-BEAM-INDUCED CONDUCTIVITY OF ULTRASHALLOW SILICON $p^+ - n$ JUNCTIONS

The small depth of the p^+ diffusion profile $(5-20$ nm) in ultrashallow silicon $p^+ - n$ junctions is responsible for the use of the conductivity induced by a focused electron beam probing the near-surface region with low- and medium-energy electrons to investigate them.[9,10,12,13] The probing depth can be smoothly varied from 2 to 250 nm by varying the electron beam energy (E_p) in the range from 0.1 to 3.0 keV.[9,10] In order to separate the induced current from the dark current, measurements of the IVC's and energy dependence of the electron-beam-induced conductivity were performed with sinusoidal modulation of the primary electron flux at a frequency of 1 kHz. Control experiments using a constant current confirmed that a stationary value of the electron-beam-induced conductivity γ manages to be established already at such frequencies. The computer-controlled electron beam scanned the surface under study, making it possible to perform measurements of γ at evenly spaced points and, accordingly, to obtain an image of the surface using primary electron beams of different energies. The preliminary experiments[9,10] showed that the ultrashallow $p^+ - n$ junctions obtained with a thick oxide on the single-crystal silicon surface, which ensured dominance of the vacancy mechanisms, are characterized by a high degree of uniformity of the distribution of γ along the surface of the p^+ diffusion profile.

Treatment of the experimental plots of the energy dependence of the electron-beam-induced conductivity $\gamma(E_p)$ using regularizing algorithms from the theory of ill-posed problems permits reconstruction of the unknown nonequilibrium carrier collection functions $f(x)$, which appears in the integral equation

$$\gamma(E_p) = \int_0^\infty \frac{g(E_p, x)}{\Delta\varepsilon} f(x)\, dx, \tag{1}$$

where $g(E_p, x)$ is the one-dimensional distribution function of individual energy losses by primary electrons with respect to the depth in silicon, $\Delta\varepsilon$ is the mean energy expended on the formation of a single electron-hole pair, and $f(x)$ is the collection function of the $p - n$ junction,[12,13] which specifies the number of electron-hole pairs excited at the depth x that are capable of making a contribution to the induced current. When irradiation by electrons with an energy of $0.1-3.0$ keV is employed, the treatment of $f(x)$ is confined directly to the space-charge region of the $p - n$ junction. The behavior of $f(x)$ in this region reflects the probability of the separation of electron-hole pairs by the field of the $p - n$ junction and is determined primarily by the lifetime of the nonequilibrium carriers and the distribution of the electric field, and in the case of nonmonotonic behavior, it permits the identi-
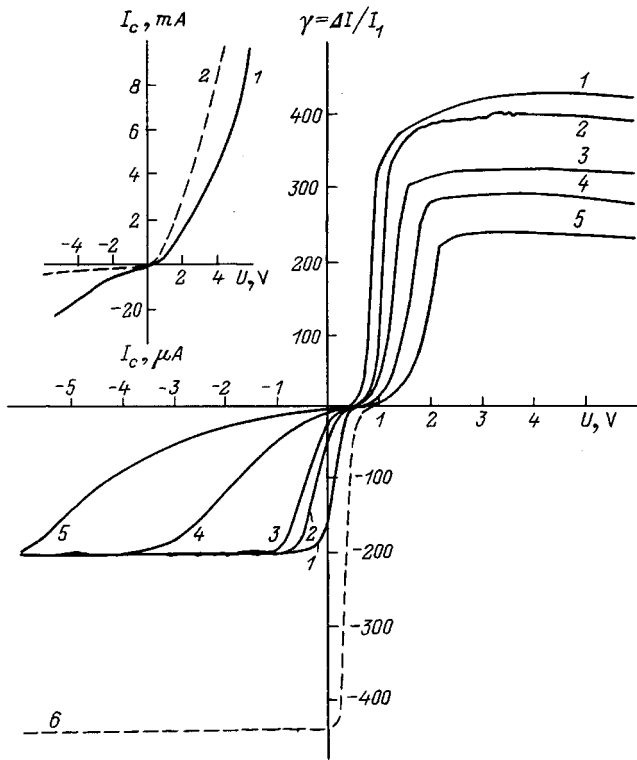
FIG. 2. Current-voltage characteristics of the electron-beam-induced conductivity (γ versus U curves) for p^+-n junctions formed at diffusion temperatures equal to 800 (*1–5*) and 900 °C (*6*) on a (111) silicon surface doped with phosphorus to a concentration $N(\text{P})=5\times10^{13}$ cm^{-3}. Notation adopted in the figure: $\Delta I = I - I_1$, where I_1 is the primary current and I is the stationary current induced by the electron beam. Values of I_1, μA: *1* — 0.5, *2, 6* — 1.0, *3* — 1.9, *4* — 5.0, *5* — 10. Inset — current-voltage characteristics (I_c versus U curves) of the p^+-n investigated for T_{dif}, °C: *1* — 800, *2* — 900.

fication of processes leading to a precipitous increase in γ as a result of the spatial separation of the nonequilibrium electrons and holes.

4. CURRENT-VOLTAGE CHARACTERISTICS OF THE ELECTRON-BEAM-INDUCED CONDUCTIVITY IN SELF-ORGANIZED QUANTUM WELLS ON A (111) SILICON SURFACE

Figure 2 shows IVC's of the electron-beam-induced conductivity [plots of $\gamma=f(U)$] for ultrashallow p^+-n junctions formed at low boron diffusion temperatures on the surface of single-crystal wafers of (111) silicon with n-type conduction. The IVC of the electron-beam-induced conductivity of a p^+-n junction formed at a diffusion temperature $T_{\text{dif}}=900$ °C is observed only when it is reverse-biased. Here the electron-beam-induced conductivity γ does not depend on primary current or on bias voltage. Under forward biasing the electron-beam-induced conduction current drops abruptly to zero as a result of the intense recombination of nonequilibrium carriers on the interface of the p^+-n junction (Fig. 2, curve *6*). An unexpected result was obtained when the IVC of the electron-beam-induced conductivity of a p^+-n junction formed at a diffusion temperature $T_{\text{dif}}=800$ °C was recorded. In this case electron-beam-induced conductivity is detected with both reverse and forward biasing of the

p^+-n junction and does not decrease even when a conduction current of the order of 10 mA flows through the open diode, attesting to a significant increase in the lifetime of the excited carriers (Fig. 2, curves *1–5*). Such lowering of the recombination efficiency is probably caused by the spatial separation of the electron and hole fluxes due to the presence of self-organized quantum wells within the ultrashallow p^+ diffusion profiles.

Measurements of the angular dependence of the cyclotron resonance of electrons and holes, as well as of the crystallographically dependent hole conductivity, showed[1,7,8] that the p^+ diffusion profiles realized under the conditions of parity between the kick-out and vacancy mechanisms of impurity diffusion, which is achieved at $T_{\text{dif}}=900$ °C, consists of self-organized longitudinal quantum wells (Figs. 3a and 3b), while transverse quantum wells were discovered within the silicon p^+-n junctions obtained with dominance of the vacancy diffusion mechanisms ($T_{\text{dif}}=800$ °C) (Figs. 3c and 3d). An analysis of the IVC's of the quantized conductivity[14,15] provides evidence that self-organized n- and p-type quantum wells (Fig. 3) form between the heavily doped two-dimensional layers, which, according to ESR data, consist predominantly of B^+-B^- impurity dipoles with a negative correlation energy and weakly influence the mobility and recombination of the nonequilibrium current carriers.

Ultrashallow silicon p^+-n junctions consisting of longitudinal quantum wells are characterized by a low reverse dark current (curve *2* in the inset) because of the presence of natural potential barriers to the minority carriers (Figs. 3a and 3b). However, spatial separation of the excited electrons and holes does not occur in this case, and, as was noted above, this situation leads to abrupt disappearance of the electron-beam-induced conductivity when the p^+-n junction is forward-biased (Fig. 2, curve *6*).

The presence of transverse quantum wells leads to an increase in the reverse dark current (see curve *1* in the inset in Fig. 2) due to the appearance of natural channels for minority carriers (Figs. 3c and 3d), but, at the same time, it promotes spatial separation of the excited electrons and holes. Therefore, the electron-beam-induced conductivity of p^+-n junctions containing self-organized transverse quantum wells can be detected at both forward and reverse voltages (Fig. 2, curves *1–5*). The potential well created by the transverse quantum wells, which is responsible for the spatial separation of electrons and holes, can be smoothed as the current rises as a result of the ohmic voltage drop on the p^+-n junction interface, which should be most pronounced in structures with a high-resistivity substrate. In fact, when the p^+-n junction is forward-biased, a decrease in γ with increasing values of the primary current I_1 begins to be observed at the point where the carrier excitation current ΔI is comparable to the dark current I_c. This reflects the intensification of carrier recombination processes. At the same time, when the p^+-n junction is reverse-biased, in the absence of a current of majority carriers, the electron-beam-induced conductivity does not depend on the primary current, which influences only the value of the voltage at which the IVC of
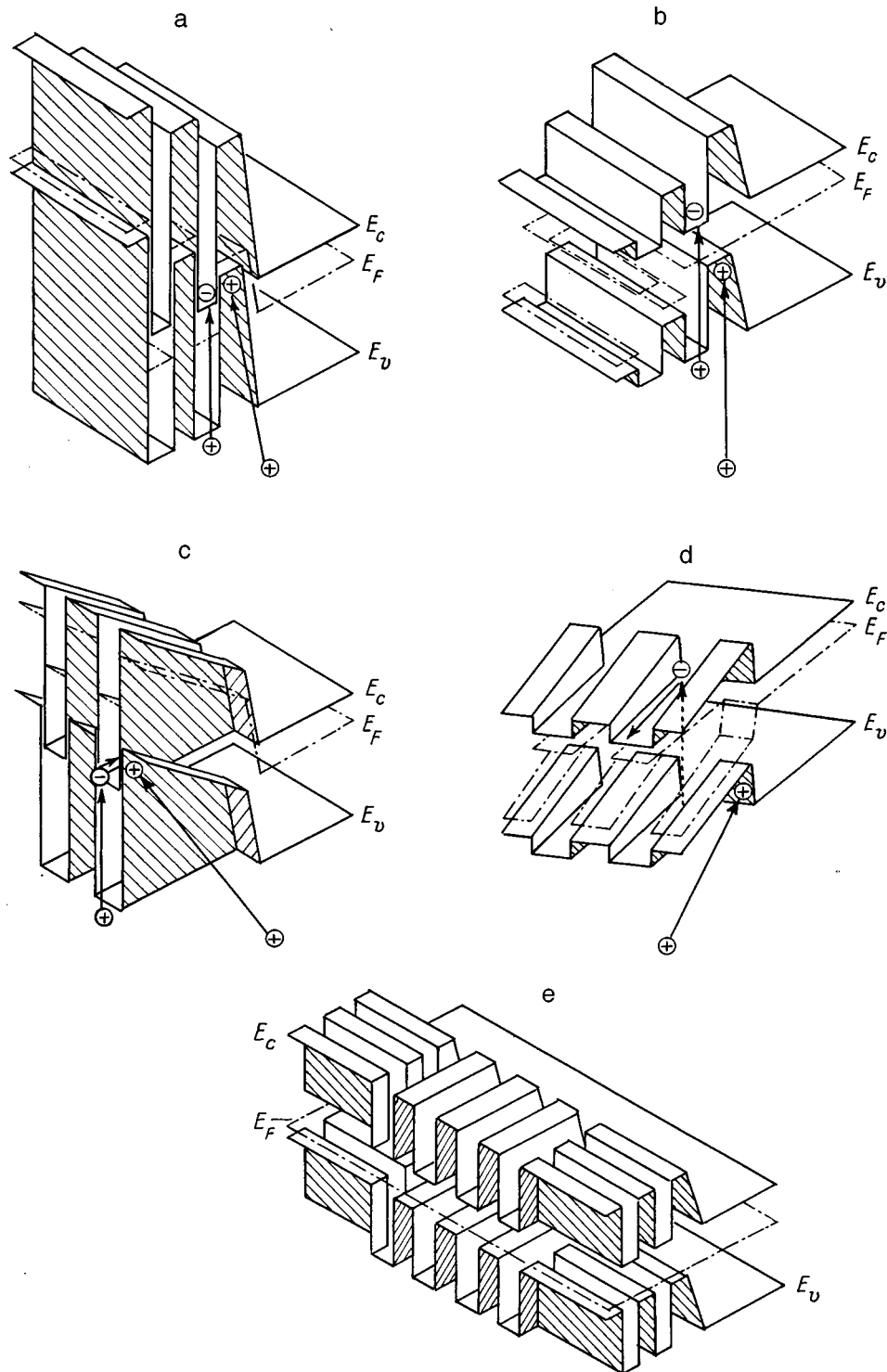
FIG. 3. Three-dimensional image of the one-electron band diagram of p^+-n junctions consisting of longitudinal (a, b) and transverse (c, d) quantum wells, as well as combinations of these wells (e). Bias voltages on the p^+-n junctions: a, c — reverse; b, d — forward; e — zero.

the electron-beam-induced conductivity reaches saturation (Fig. 2, curves *1–5*).

5. ENERGY DEPENDENCES OF THE ELECTRON-BEAM-INDUCED CONDUCTIVITY IN SELF-ORGANIZED QUANTUM WELLS ON A ⟨111⟩ SILICON SURFACE

Plots of the electron-beam-induced conductivity γ as a function of the energy of the primary electrons are shown in

Fig. 4a. The electron-beam-induced conductivity of a p^+-n junction formed at $T_{\text{dif}} = 900\,^\circ\text{C}$ begins to appear at an energy of the primary electrons $E_1 = 200$ eV and rapidly increases as the latter increases further (Fig. 4a, curve *3*). The collection function $f(x)$ calculated from the experimental γ versus E_1 curve exhibits a characteristic stepped form, which confirms the existence of a ''dead layer'' on the
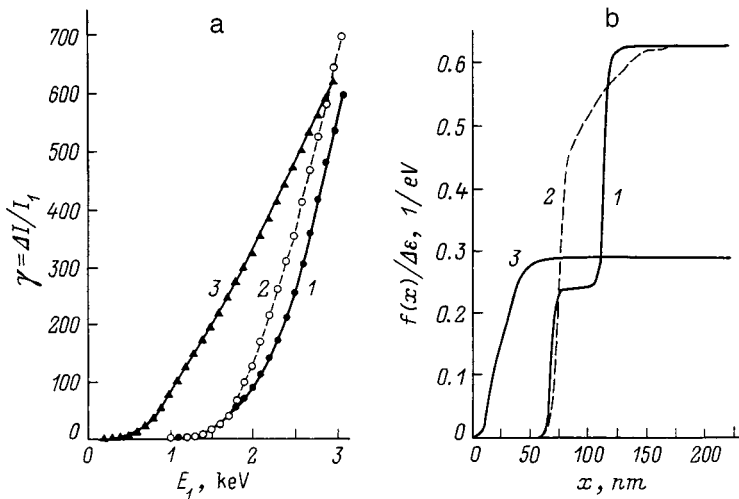
FIG. 4. Dependence of the electron-beam-induced conductivity γ on the energy of the primary electrons (a) E_1 ($I_1 = 2$ μA) and distributions of the collection function $f(x)$ across the thickness of the p^+-n junction calculated from them (b) for reverse (curves *1* and *3* — $U = -5$ V) and forward (curves *2* — $U = 2$ V) biasing of p^+-n junctions formed on a (111) silicon surface doped with phosphorus to a concentration $N(\text{P}) = 5 \times 10^{13}$ cm^{-3} at $T_{\text{dif}} = 800$ (*1*, *2*) and 900 °C (*3*).

p^+-n junction interface, in which the excited electron-hole pairs do not participate in the formation of the electron-beam-induced conductivity either because of the short lifetime of the carriers or because of the potential barriers appearing in the presence of the longitudinal quantum wells.[9,10] The thickness of the dead layer on the interface of the p^+-n junction obtained at $T_{\text{dif}} = 900$ °C does not exceed 10 nm, and the collection function $f(x)$ reaches saturation already at a depth of 50 nm (Fig. 4b, curve *3*). It should be noted that the maximum value of $f(x)$ determined is close to 1, since the typical mean value of the energy $\Delta\varepsilon$ expended on the formation of a single electron-hole pair for silicon is about 3 eV. Taking into account that the p^+-n junctions obtained at $T_{\text{dif}} = 900$ °C are characterized by small reverse dark currents (see curve *2* in the inset in Fig. 2) and a long lifetime for the nonequilibrium carriers, we can conclude that the self-organized longitudinal quantum wells play a fundamental role in the formation of the dead layer at a depth of 50 nm.

Conversely, the lifetime of the nonequilibrium carriers excited in the dead layer of the p^+-n junction formed at $T_{\text{dif}} = 800$ °C, which is a combination of longitudinal and transverse quantum wells, is insufficient for them to make an appreciable contribution to the electron-beam-induced conductivity. In this case the thickness of the dead layer (about 70 nm) is identical for both forward and reverse biasing of the p^+-n junction (Fig. 4a, curves *1* and *2*) and is determined primarily by the concentration of recombination-active centers near its interface.[9,10] In addition, significant differences in the form of the collection function are observed for reverse and forward biasing of the p^+-n junction (Fig. 4b, curves *1* and *2*). Under reverse biasing the collection function $f(x)$ at first increases sharply almost to unity at a depth of 75 nm and then increases again by a factor of 2.5 at a depth of 120 nm. The threshold increase in the collection function, under which $f(x)$ exceeds the limiting value determined by the concentration of excited electron-hole pairs, can be attributed to the avalanche multiplication of holes, which are generated at a large depth and which move toward the surface when the p^+-n junction is reverse-biased (Fig. 3c). At the same time, the value of the collection function,

which reflects the contribution of the carriers excited at a small depth to the electron-beam-induced conductivity, does not exceed 1. Hence it follows that nonequilibrium electrons moving from the working surface toward the substrate do not undergo avalanche multiplication because of the spatial separation of the fluxes of excited electrons and holes. When the p^+-n junction is forward-biased, the holes move toward the substrate, and the collection function exceeds 1 at all depths where electron-hole pairs are excited, which is possible only in the case of avalanche multiplication of carriers in the accelerating field (Fig. 3d). This sharp increase in the electron-beam-induced conductivity is most clearly seen in Si(100) in the case of the creation of a combination of alternating longitudinal and transverse *n*- and *p*-type quantum wells which are crystallographically oriented in equivalent $\langle 100 \rangle$ directions (Figs. 5 and 3e).

6. CONCLUSIONS

Electron-beam diagnostics have been used to study the current-voltage and energy characteristics of the electron-

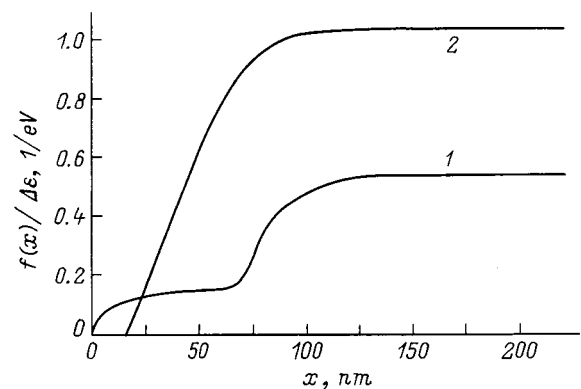FIG. 5. Collection functions $f(x)$ for reverse biasing of p^+-n junctions formed on a (100) silicon surface doped with phosphorus to a concentration $N(\text{P}) = 8 \times 10^{12}$ cm^{-3} at $T_{\text{dif}} = 800$ (*1*) and 900 °C (*2*) under the conditions of a strong deformation potential, which stimulates the formation of combinations of self-organized longitudinal and transverse quantum wells (Fig. 3e).

beam-induced conductivity of self-organized quantum wells, which form spontaneously during the fabrication of silicon p^+-n junctions using nonequilibrium impurity diffusion. Current-voltage characteristics of the electron-beam-induced conductivity have been detected with both reverse and forward biasing of a p^+-n junction consisting predominantly of transverse (perpendicular to the plane of the p^+-n junction) quantum wells, while the presence of longitudinal (parallel to the plane of the p^+-n junction) quantum wells promotes the generation of electron-beam-induced conductivity only when the p^+-n junction is reverse-biased. Plots of the electron-beam-induced conductivity versus the energy of the primary electrons have shown that the self-organized transverse quantum wells within the p^+ diffusion profile stimulate the avalanche multiplication of nonequilibrium carriers as a consequence of the spatial separation of the electrons and holes in the field of an ultrashallow p^+-n junction.

[1] N. T. Bagraev, W. Gehlhoff, L. E. Klyachkin, and A. Naeser, Defect Diffus. Forum **143–147**, 1003 (1997).

[2] N. T. Bagraev, L. E. Klyachkin, and V. L. Sukhanov, Defect Diffus. Forum **103–105**, 192 (1993).

[3] W. Frank, U. Gosele, H. Mehrer, and A. Seeger, *Diffusion in Crystalline Solids*, Academic Press (1984), p. 63.

[4] E. Antoncik, J. Electrochem. Soc. **141**, 3593 (1994).

[5] R. B. Fair, Defect Diffus. Forum **37**, 1 (1984).

[6] N. T. Bagraev, E. V. Vladimirskaya, V. É. Gasumyants, V. I. Kaĭdanov, V. V. Kveder, L. E. Klyachkin, A. M. Malyarenko, and E. I. Chaĭkina, Fiz. Tekh. Poluprovodn. **29**, 2133 (1995) [Semiconductors **29**, 1112 (1995)].

[7] N. T. Bagraev, E. I. Chaikina, L. E. Klyachkin, I. I. Markov, and W. Gehlhoff, Superlattices Microstruct. **23**, 338 (1998).

[8] N. T. Bagraev, W. Gehlhoff, L. E. Klyachkin, A. M. Malyarenko, and A. Naeser, Mater. Sci. Forum **258–263**, 1607 (1997).

[9] A. N. Andronov, N. T. Bagraev, L. E. Klyachkin, and S. V. Robozerov, Fiz. Tekh. Poluprovodn. **32**, 137 (1998) [Semiconductors **32**, 124 (1998)].

[10] A. N. Andronov, N. T. Bagraev, L. E. Klyachkin, A. M. Malyarenko, and S. V. Robozerov, Fiz. Tekh. Poluprovodn. **33**, 46 (1999) [Semiconductors **33**, 51 (1999)].

[11] P. S. Zalm, Rep. Prog. Phys. **58**, 1321 (1995).

[12] E. N. Pyatyshev and D. V. Kuzichev, Izmer. Tekh. No. **9**, 3 (1991).

[13] A. N. Andronov, N. T. Bagraev, L. E. Klyachkin, S. V. Robozerov, and N. S. Faradzhev, Fiz. Tekh. Poluprovodn. **28**, 2049 (1994) [Semiconductors **28**, 1128 (1994)].

[14] N. T. Bagraev, W. Gehlhoff, L. E. Klyachkin, A. M. Malyarenko, and A. Naeser, Mater. Sci. Forum **258–263**, 1683 (1997).

[15] W. Gehlhoff, K. Irmscher, N. T. Bagraev, L. E. Klyachkin, and A. M. Malyarenko, in *Proceedings of the IC–SLCS*, C. A. J. Ammerlaan and B. Pajot (Eds.), World Scientific, Singapore (1997), p. 227.

Translated by P. Shelnitz

Self-organized nanoscale InP islands in an InGaP/GaAs host and InAs islands in an InGaAs/InP host

D. A. Vinokurov, V. A. Kapitonov, O. V. Kovalenkov, D. A. Livshits, Z. N. Sokolova, I. S. Tarasov,[*)] and Zh. I. Alferov

A. F. Ioffe Physicotechnical Institute, Russian Academy of Sciences, 194021 St. Petersburg, Russia

Arrays of strained nanoscale InP islands in an $In_{0.49}Ga_{0.51}P$ host on a GaAs(100) substrate and InAs islands in a $In_{0.53}Ga_{0.47}As$ host on an InP(100) substrate are obtained by metalorganic vapor-phase epitaxy (MOVPE). Their structural and photoluminescence properties are investigated. It is shown that the nanoscale islands that are formed measure 80 nm (InP/InGaP) and $25-60$ nm (InAs/InGaAs). The photoluminescence spectra of the nanoscale islands display bands in the wavelength ranges $0.66-0.72$ and $1.66-1.91$ μm at 77 K with maxima whose position does not vary as the effective thickness of InP and InAs increases. The radiation efficiency of the nanoscale InP islands is two orders of magnitude greater than the luminescence intensity of the InAs islands. © *1999 American Institute of Physics.* [S1063-7826(99)01907-9]

1. INTRODUCTION

The formation of self-organized nanoscale islands (nanoislands) during the heteroepitaxial growth of strongly strained semiconductor layers is attracting attention because of the possibility of achieving three-dimensional (3D) electron confinement in homogeneous and coherent (dislocation-free) islands. In contrast with the nanoscale heterostructures formed when complicated photolithographic procedures are employed, the self-organized heterostructures obtained by molecular-beam epitaxy (MBE) and metalorganic-hydride epitaxy [metalorganic vapor-phase epitaxy (MOVPE)] have a high density of states due to three-dimensional quantization, as well as a high radiation efficiency due to the low defect density.[1]

Our purpose in this work was to obtain two types of heterostructures with nanoscale islands by metalorganic-hydride epitaxy and to investigate them. One of them consists of indium phosphide islands in an $In_{0.49}Ga_{0.51}P$ matrix lattice-matched to a GaAs substrate.[2–4] The other object of investigation consists of InAs nanoislands in an $In_{0.53}Ga_{0.47}As$ matrix lattice-matched to an InP substrate.[5–8]

This paper is divided into five sections. After the introduction, the second section describes the method used to grow the heterostructures, the third section presents the results of an investigation of the heterostructures by transmission electron microscopy (TEM), the fourth section gives the results of a photoluminescence investigation, and the results are discussed in the fifth section.

2. METHOD USED TO GROW THE HETEROSTRUCTURES

In this work self-organized nanoscale InP and InAs islands were grown on GaAs and InP substrates, respectively, by metalorganic-hydride epitaxy on an Epiquip VP 50-RP system at a reduced pressure (100 mbar) in a horizontal reactor of rectangular cross section with high-frequency heating of the substrate-holder.

The starting reagents used were trimethylgallium (TMG), trimethylindium (TMI), arsine (a 20% mixture with hydrogen), and phosphine (a 30% mixture with hydrogen). Hydrogen with a dew point not exceeding $-90\,°C$ served as the carrier gas.

The structures with InP nanoislands in an InGaP host were grown at $T_g = 700\,°C$ on GaAs(100) substrates. These structures contained a layer of InP nanoislands, whose nominal thickness varied from 0.5 to 12 monolayers (ML). The layer with nanoislands was sandwiched between an $In_{0.49}Ga_{0.51}P$ buffer layer with a thickness of 0.5 μm, which was lattice-matched to the substrate, and an upper wide-gap $In_{0.49}Ga_{0.51}P$ layer with a thickness of 0.04 μm.

The structures with InAs nanoislands in an InGaAs matrix were grown on InP(100) substrates at $T_g = 600\,°C$. These structures were similar in geometry to the structures with InP nanoislands and contained from 2 to 10 ML of InAs sandwiched between lower and upper layers of $In_{0.53}Ga_{0.47}As$ with a thickness of 0.25 and 0.04 μm, respectively. The growth rates for both types of structures were 2 Å/s for the binary compounds and 8 Å/s for the ternary solid solutions.

In addition, InAs nanoislands were grown at the reduced temperatures $T_g = 550$ and 500 °C. Therefore, after the lower buffer layer was formed at $T_g = 600\,°C$, the growth was interrupted to lower the temperature for 2 and 2.5 min, respectively. The upper wide-gap layer was grown at the growth temperature of the InAs nanoislands.

3. INVESTIGATION OF THE HETEROSTRUCTURES BY TRANSMISSION ELECTRON MICROSCOPY

The structures with nanoislands were investigated in a planar geometry on a Philips EM 420 high-resolution electron microscope with a voltage equal to 120 kV.

Figure 1 presents the transmission electron micrograph of a portion of a structure with a nominal content of InP equal to 3 ML. The image contains nanoscale islands that are
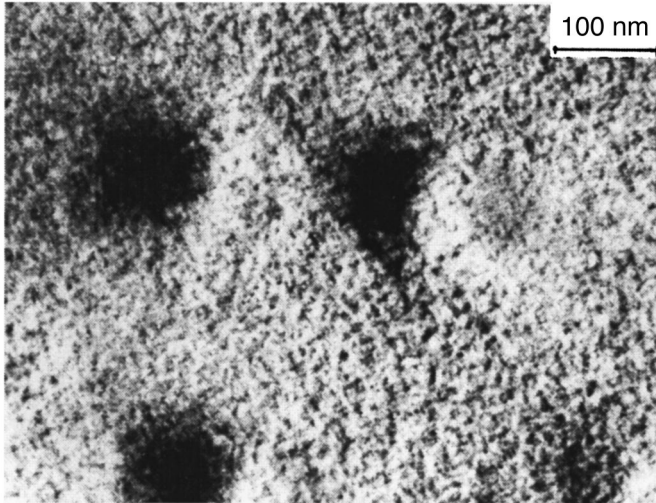
FIG. 1. Transmission electron micrograph of a portion of a structure with a nominal content of InP equal to 3 ML.

fairly uniform in size with a clear pattern of strains around the nanoislands, which can be used to estimate the transverse dimension of the nanoislands (80 nm) with a mean surface density equal to $3 \times 10^9 \, \text{cm}^{-2}$.
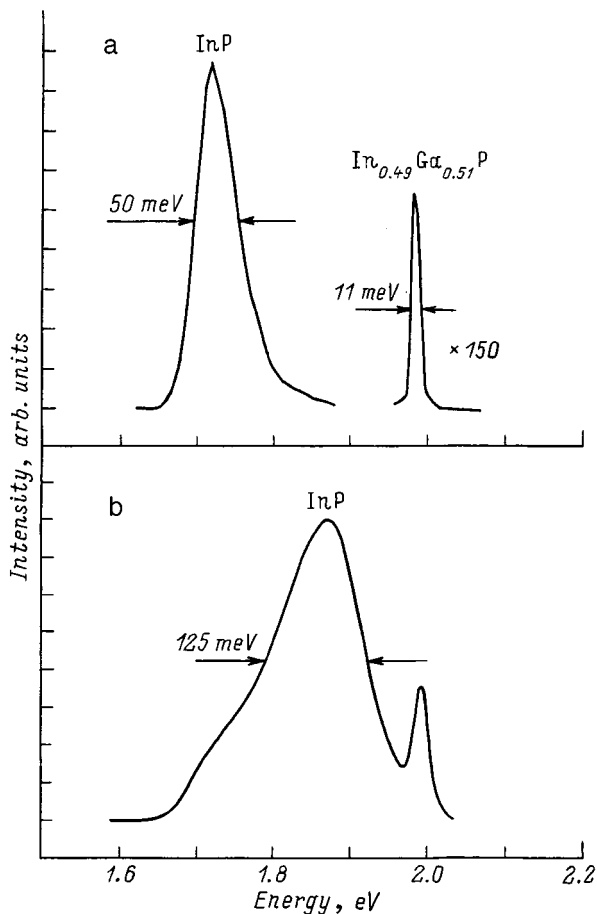

FIG. 2. Photoluminescence spectrum of a structure with InP nanoislands recorded with pump power densities equal to 100 W/cm^2 (a) and 5 kW/cm^2 (b) at $T = 77$ K. The nominal thickness of the InP deposited was 3 ML.
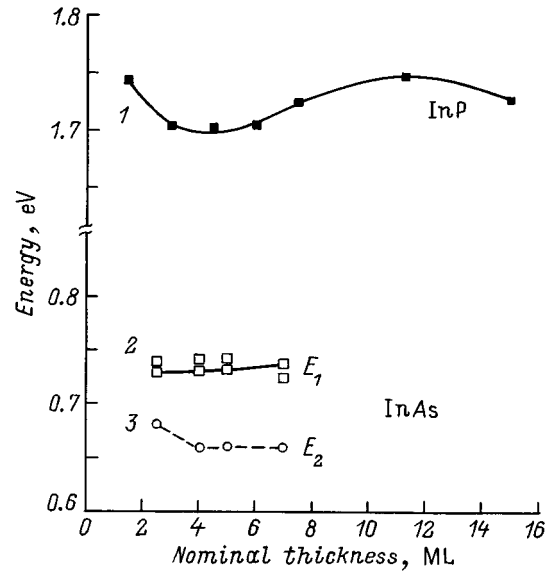
FIG. 3. Energy of the photoluminescence intensity maximum at $T = 77$ K as a function of the nominal thickness of the material deposited for various nanoislands: *1* — InP; *2* — InAs, peak E_1; *3* — InAs, peak E_2.

The TEM image of the InAs nanoislands shows a pattern of strain fields with less contrast than in the case of the InP islands. Nevertheless, two types of nanoislands can be identified on it: islands with mean transverse dimensions equal to 60 and 25 nm with an approximately equal mean density of $(1-2) \times 10^{10} \, \text{cm}^{-2}$.

4. PHOTOLUMINESCENCE INVESTIGATIONS OF THE HETEROSTRUCTURES

An Ar$^+$ laser with an output wavelength of 0.514 μm was used to excite photoluminescence (PL) in the test samples. The signal from each heterostructure was detected by a photomultiplier with a peak spectral sensitivity in the wavelength range $\lambda = 0.35 - 0.9$ μm for the structures containing InP nanoislands and by a GaSb photodiode with a peak sensitivity in the wavelength range $\lambda = 1.3 - 2.4$ μm for recording the long-wavelength spectra of the InAs nanoislands.

The power density of the exciting radiation was usually 100 W/cm^2 for the InP nanoislands and 5 kW/cm^2 for the InAs nanoislands due to the considerably smaller photoluminescence quantum efficiency in the InAs nanoislands.

A. InP nanoislands in an In$_{0.49}$Ga$_{0.51}$P/GaAs host

Figure 2a shows a PL spectrum of a structure containing InP nanoislands with a nominal thickness of the InP deposited equal to 3 ML in an In$_{0.49}$Ga$_{0.51}$P host at $T = 77$ K. The PL spectrum shows two emission bands differing in quantum efficiency by two orders of magnitude. The intense band with a peak energy equal to 1.72 eV and a full width at half-maximum (FWHM) equal to 50 meV probably corresponds to the luminescence of the InP nanoislands. The emission band with a maximum at 1.98 eV and an FWHM equal to 11 meV corresponds to the emission of the In$_{0.49}$Ga$_{0.51}$P host. As the power density of the exciting light
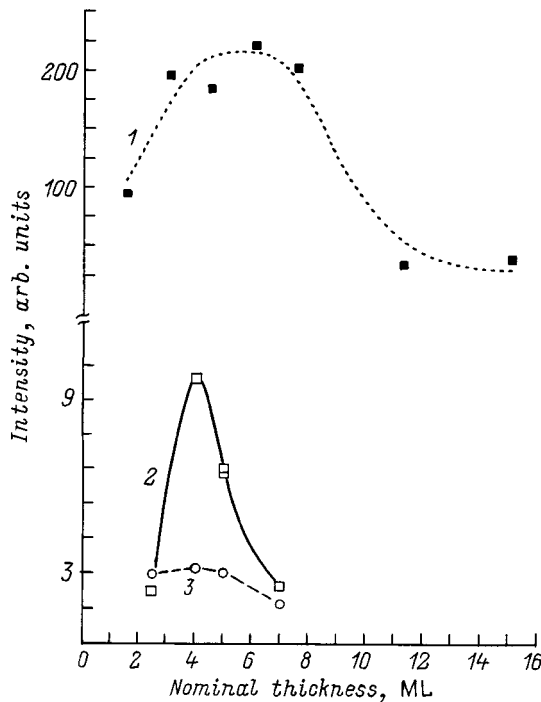
FIG. 4. Dependence of the photoluminescence intensity at $T = 77$ K on the nominal thickness of the material deposited for various nanoislands: *1* — InP; *2* — InAs, peak E_1; *3* — InAs, peak E_2.
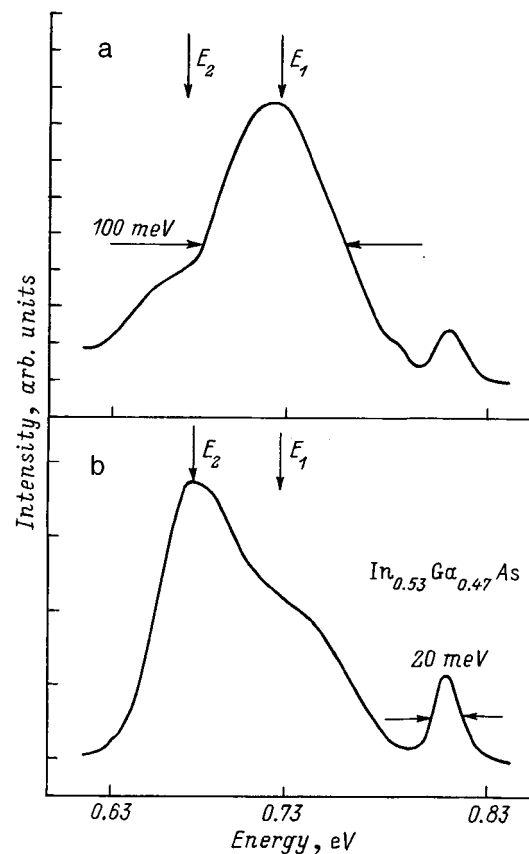

FIG. 5. Photoluminescence spectrum of a structure containing InAs nanoislands with nominal thicknesses of the deposited InAs layer equal to 4 ML (a) and 2.5 ML (b) at $T = 77$ K. The pump power density was 5 kW/cm^2.

is increased, the PL spectrum broadens considerably. When the excitation power density equals 5 kW/cm^2, a high-energy band with an energy at the intensity maximum equal to 1.88 eV and an FWHM equal to 125 meV begins to dominate (Fig. 2b). At this point the PL intensity of the InP nanoislands becomes comparable to the luminescence intensity of the InGaP host. In our opinion, the changes in the PL spectrum at the high pump power density are due to luminescence from the so-called InP wetting layer.

Figure 3 (curve *1*) shows the dependence of the energy at the photoluminescence maximum of InP nanoislands on the number of monolayers of InP deposited. The position of the maximum of the PL band of the InP nanoislands remains essentially unchanged in the range from 2 to 7 ML of material deposited. This differs from the case of quantum wells, where the energy at the maximum of the PL band decreases as the thickness of the layer is increased. The weak dependence of the position of the PL maximum on the amount of InP deposited is probably evidence of the uniformity of the sizes of the nanoislands.

Figure 4 (curve *1*) shows the dependence of the PL intensity on the amount of InP deposited. The maximum PL intensity is observed in the structure containing 6 ML of InP, in which the external quantum efficiency was equal to 30% at $T = 77$ K. Abrupt deterioration of the luminescence characteristics of the heterostructures occurs with an increase in the nominal thickness of InP (above 7 ML) and can be attributed to coalescence of the InP nanoislands and an increase in the number of dislocations.

B. InAs nanoislands in an $In_{0.53}Ga_{0.47}As/InP$ host

Figure 5 shows PL spectra of structures containing InAs nanoislands in an $In_{0.53}Ga_{0.47}As$ host with nominal thicknesses of deposited InAs equal to 4 ML (Fig. 5a) and 2.5 ML (Fig. 5b) at $T = 77$ K. The spectra display a broad band with two maxima at $E_1 = 0.73$ eV and $E_2 = 0.66$ eV. We assign these maxima to the emission of InAs nanoislands having two characteristic diameters (25 and 60 nm). In addition, both spectra contain a band which is several times less intense and narrow (20 meV) and corresponds to the emission of the $In_{0.53}Ga_{0.47}As$ host. It is noteworthy that the luminescence quantum efficiency of the InAs nanoislands is significantly lower than that of the InP nanoislands.

Figure 3 presents plots of the dependence of the energy at the maxima of the two PL bands E_1 and E_2 on the number of monolayers of InAs deposited (curves *2* and *3*). In the range from 2.5 to 7 ML the energies of the two bands depend weakly on the amount of InAs deposited. In addition, the quantum efficiency for the short-wavelength band at $E_1 = 0.73$ eV has a maximum in the vicinity of 4 ML (Fig. 4, curve *2*), and the quantum efficiency for the band with $E_2 = 0.66$ eV (Fig. 4, curve *3*) remains essentially the same for 2.5–7 ML of InAs deposited.

In the heterostructures with InAs nanoislands the intensity of the long-wavelength PL band ($E_2 = 0.66$ eV) exceeds the intensity of the band at $E_1 = 0.73$ eV when the number of

monolayers of material deposited is small (Fig. 4). When the number of monolayers of InAs increases (above 3 ML) the short-wavelength band becomes more intense. Therefore, when the thickness of the material deposited is small (2.5 ML), the InAs nanoislands of larger diameter probably dominate, but as the thickness of the InAs deposited increases, the number of nanoislands of small diameter increases and their contribution to the PL becomes decisive. A similar phenomenon was observed in Ref. 8, in which similar structures were investigated using atomic-force microscopy. The PL spectra of the heterostructures with InAs nanoislands grown at $T_g = 500$ and 550 °C contain long-wavelength emission in the range $\lambda = 1.78 - 1.91$ μm at $T = 77$ K.

5. DISCUSSION OF RESULTS

The investigations performed in this work showed that the structures with InAs nanoislands grown by metalorganic-hydride epitaxy can exhibit luminescence in the range $\lambda = 1.66 - 1.91$ μm at $T = 77$ K. The heterostructures with InP nanoislands emit in the range $\lambda = 0.66 - 0.72$ μm at $T = 77$ K. The luminescence of the InP nanoislands is two orders of magnitude more intense than the luminescence of the InAs nanoislands. One of the reasons for the lower luminescence intensity of the InAs nanoislands is the weak confinement of electrons in the conduction band of the InAs nanoislands. According to our estimates, in a strongly strained $In_{0.49}Ga_{0.51}P/InP$ heterostructure the quantum well for electrons in the region of a nanoisland is at least 100 meV deeper than in the case of InAs nanoislands; therefore, the confinement of electrons in the InP nanoislands is far stronger. A calculation of the exact values of the depth of the potential well in the nanostructures under consideration is complicated by the large spread of the values given in the literature for both the deformation potential constants and the distribution of the potential jump between the conduction band and the valence band.[9]

One special feature distinguishing the nanoislands that we investigated from those obtained by MBE in Ref. 6 is the very weak dependence of the position of the maximum of the PL band on the amount of material deposited in nanoislands (Fig. 3). A similar dependence of the position of the maximum of the PL band in InP nanoislands grown by metalorganic-hydride epitaxy on the amount of material deposited was also observed in Ref. 4. Such behavior can be attributed to the fact that nanoscale islands develop up to their critical size, which corresponds to the minimum energy per unit of surface area of the three-dimensional coherent islands.[1] An increase in the amount of material deposited at first leads only to an increase in the density of the nanoislands. It was shown in Ref. 10 that there is an optimal island size not only for a sparse array of nanoislands, but also for a dense array of interacting islands. As the amount of material deposited increases further, the nanoislands begin to coalesce. This results in the appearance of a large number of nanoislands whose size significantly exceeds the critical value;[6,8] this leads to the formation of dislocations which cause lowering of the PL intensity (Fig. 4).

*)E-mail: tarasov@hpld.ioffe.rssi.ru

[1] N. N. Ledentsov, V. M. Ustinov, V. A. Shchukin, P. S. Kop'ev, Zh. I. Alferov, and D. Bimberg, Fiz. Tekh. Poluprovodn. **32**, 385 (1998) [Semiconductors **32**, 343 (1998)].

[2] O. V. Kovalenkov, D. A. Vinokurov, D. A. Livshits, I. S. Tarasov, N. A. Bert, S. G. Konnikov, and Zh. I. Alferov, in *Proceedings of the 23rd International Symposium on Compound Semiconductors (Institute of Physics Conference Series, No. 155)*, St. Petersburg (1996), Chap. 3, p. 271.

[3] D. A. Vinokurov, V. A. Kapitonov, O. V. Kovalenkov, D. A. Livshits, and I. S. Tarasov, Pis'ma Zh. Tekh. Fiz. **24**(16), 1 (1998) [Tech. Phys. Lett. **24**(8), 623 (1998)].

[4] W. Seifert, N. Carlsson, M.-E. Pistol, and L. Samuelson, Appl. Phys. Lett. **67**, 1166 (1995).

[5] O. V. Kovalenkov, I. S. Tarasov, D. A. Vinokurov, and V. A. Kapitonov, in *Abstracts of the International Symposium ''Nanostructures: Physics and Technology''*, St. Petersburg (1998), p. 268.

[6] V. M. Ustinov, A. E. Zhukov, A. F. Tsatsul'nikov, A. Yu. Egorov, A. R. Kovsh, M. V. Maksimov, A. A. Suvorova, N. A. Bert, and P. S. Kop'ev, Fiz. Tekh. Poluprovodn. **31**, 1256 (1997) [Semiconductors **31**, 1080 (1997)].

[7] V. M. Ustinov, A. R. Kovsh, A. E. Zhukov, A. Yu. Egorov, N. N. Ledentsov, A. V. Lunev, Yu. M. Shernyakov, M. V. Maksimov, A. F. Tsatsul'nikov, B. V. Volovik, P. S. Kop'ev, and Zh. I. Alferov, Pis'ma Zh. Tekh. Fiz. **24**(1), 49 (1998) [Tech. Phys. Lett. **24**(1), 22 (1998)].

[8] M. Taskinen, M. Sopanen, H. Lipsanen, J. Tulkki, T. Tuomi, and J. Ahopelto, Surf. Sci. **376**, 60 (1997).

[9] S. Adachi, *Physical Properties of III–V Semiconductor Compounds*, Wiley, New York (1992).

[10] V. A. Shchukin, N. N. Ledentsov, P. S. Kop'ev, and D. Bimberg, Phys. Rev. Lett. **75**, 2968 (1995).

Translated by P. Shelnitz

AMORPHOUS, GLASSY AND POROUS SEMICONDUCTORS

Photocapacitance relaxation in amorphous As$_2$Se$_3$ films

I. A. Vasiliev and S. D. Shutov

Institute of Applied Physics, Moldavian Academy of Sciences, 2028 Kishinev, Moldavia
(Submitted September 15, 1998; accepted for publication November 23, 1998)
Fiz. Tekh. Poluprovodn. **33**, 863–865 (July 1999)

Studies of the photocapacitance of a-As$_2$Se$_3$ films reveal that its relaxation has a fast and a slow component, leading to two distinct spectra for the density and absorption cross section of deep levels, with different thresholds and magnitudes. The authors associate the fast component of the relaxation with photoemission of holes from D^+ centers, and speculate on the possible nature of the slow component as well. © *1999 American Institute of Physics.* [S1063-7826(99)02007-4]

The characteristics of deep centers (D^+, D^-) in glassy As$_2$Se$_3$ have been studies primarily in bulk samples. The use of spectroscopic methods [photoconductivity, photoluminescence, photoinduced absorption, vibrational modes, and electron spin resonance (ESR)] make it possible to obtain a rather complete picture of the energy spectrum of these deep levels.[1,2] However, the situation in As$_2$Se$_3$ amorphous films is less clear, largely due to difficulties in using these methods to investigate thin films. A useful replacement for them is photocapacitive spectroscopy,[3] although the long Maxwell relaxation time in a-As$_2$Se$_3$ (on the order of 2.4 s at 300 K) requires that measurements be made at ultralow frequencies. In this report we describe the first published study of photocapacitance relaxation from a Al/a-As$_2$Se$_3$ barrier, from which we determine density and cross section spectra for deep levels in the mobility gap of a-As$_2$Se$_3$ films near room temperature.

The samples used in our studies were prepared by vacuum sputtering onto a cold glass substrate the following sequence of layers: a layer of antimony (ohmic contact), an a-As$_2$Se$_3$ film roughly 1 μm thick, and a semitransparent aluminum electrode with area 0.3 cm^2. A Schottky barrier forms at the Al/a-As$_2$Se$_3$ contact with a height of 1.16 eV.[4] The capacitance of the barrier was deteremined in the frequency range $10^{-3} - 5 \times 10^{-2}$ Hz, based on quasistatic measuements of the hysteresis of the displacement current.[4,5] When the sample was illuminated by monochromatic light $(\Delta\lambda \cong 20$ nm) in the range of photon energies $h\nu = 0.83-1.82$ eV, holes that are photoemitted from previously occupied nonequilibrium deep levels into the valence band drift out of the depletion layer, increasing the negative space charge. This increase manifests itself as an increase in capacitance.[3]

In Fig. 1 we plot the increment in the squared photocapacitance $\Delta C^2 = C_{\mathrm{ph}}^2 - C_d^2$ versus time for various values of $h\nu$. C_d and C_{ph} are values of the barrier capacitance in the dark and in the light, determined experimentally at a reverse bias voltage of 0.2 V. The time dependence of the increment can be expressed as a sum of two exponentials in an expansion of the form

$$\Delta C^2(t) = \sum_{i=1}^{2} \Delta C_{si}^2 [1 - \exp(-t/\tau_i)], \qquad (1)$$

where $i=1$ corresponds to the slow relaxation component, and $i=2$ to the fast component. Here ΔC_{si}^2 is the steady-state value of the increment in squared photocapacitance as $t \to \infty$, and τ_i is the characteristic relaxation time. The solid curves plotted in these figures show fits to our experimental data (the symbols in Fig. 1) in the form of the expansion (1). At high photon energies $((h\nu \geqslant 1.51$ eV) (Fig. 1b), both components of (1) are present in the function $\Delta C^2(t)$. With decreasing $h\nu$, the fraction of the fast component decreases, and for photon energies $1.51-1.29$ eV the relaxation is described only by the slow component (Fig. 1a, curve 7). At still lower energies $(h\nu < 1.29$ eV) (Fig. 1a) only the initial
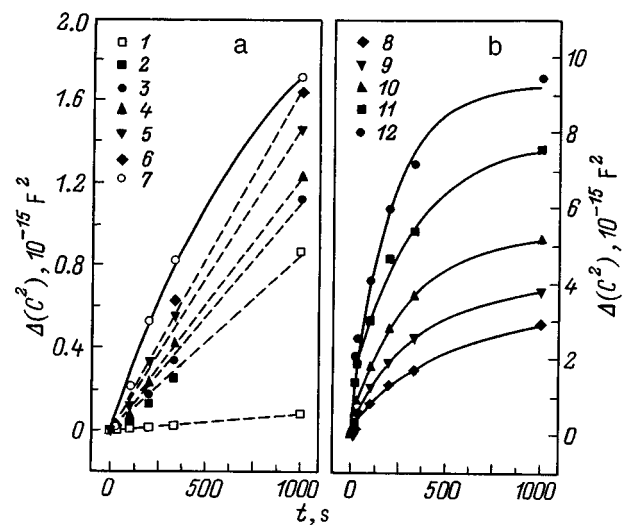

FIG. 1. Relaxation of the photocapacitance $\Delta C^2(t)$ at $T = 289$ K and a reverse bias voltage of 0.2 V. Curve 1 corresponds to relaxation of the dark capacitance; values of the photon energy $h\nu$, eV: $2 - 0.886$, $3 - 1.03$, $4 - 1.13$, $5 - 1.24$, $6 - 1.29$, $7 - 1.38$, $8 - 1.55$, $9 - 1.59$, $10 - 1.63$, $11 - 1.72$, $12 - 1.77$. The solid curves are the results of best fits of the function $\Delta C^2(t)$ using one (a) and two (b) exponentials in Eq. (1).

portion of the relaxation is visible during our measurement time interval (Fig. 1a, the dashed curves). In the analysis that follows, we assume that the process characterized by the decomposition (1) is photoemission of holes, because the relaxation of the dark capacitance (curve *1*) has a considerably larger time constant. The parameters of the photoemission processes ΔC_{si}^2 and τ_i are determined by the densities of states N_{ti} excited by the light and the absorption cross sections σ_i^0 at photon energy $h\nu$:[3]

$$\Delta C_{si}^2 \propto N_{ti}, \quad \tau_i^{-1} = \Phi\sigma_i^0, \tag{2}$$

where Φ is the flux density of the light incident on the sample.

Figure 2 shows spectra of the steady-state values ΔC_{si}^2 for the slow (curves *1* and *1'*) and fast (*2* and *2'*) components of the photocapacitance relaxation at temperatures 289 and 315 K. The fast component is observed only for energies $h\nu \geq 1.51$ eV; the energy 1.51 eV marks a transition in the spectrum of the slow component from a more mildly sloping low-energy segment (visible in the relaxation only at low temperatures; see curve *1'*) to one with a steeper slope. The right-hand scale in the figure gives upper-bound estimates of the concentration of states excited by the light based on Eq. (2). It is clear that $N_{t1} > N_{t2}$ over the entire spectral range.

Figure 3 shows spectra of the absorption cross section for both components at the same temperatures as in Fig. 2, calculated from the relaxation time constants deduced from fitting to Eq. (2). For $T = 289$ K the experimental data are well rectified in Lukovsky coordinates $(\sigma_1^0)^{2/3}(h\nu)^2 = f(h\nu)$ (see the inset in Fig. 3). In these coordinates, the extrapolated threshold values 1.3 and 1.5 eV, and more notably the values of the absorption cross sections, differ significantly for the two components (the values of the cross sections by more than a factor of 30). Increasing the temperature to 315 K allows us to identify a very small ($\leq 10^{-18}$ cm^2) cross section σ_1^0 for the slow component in the energy range 0.8–1.3 eV.
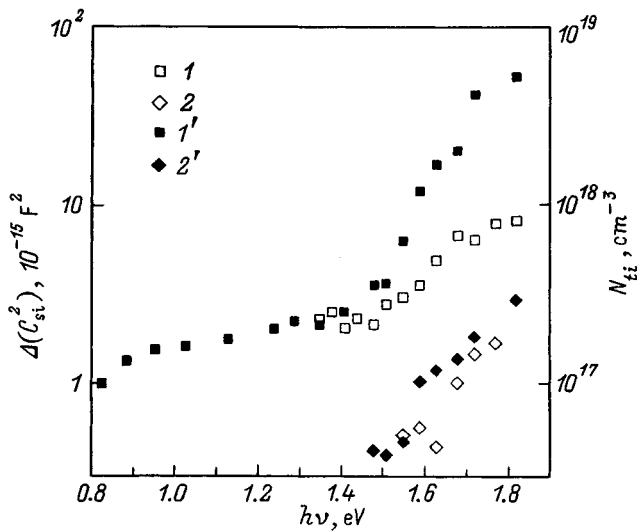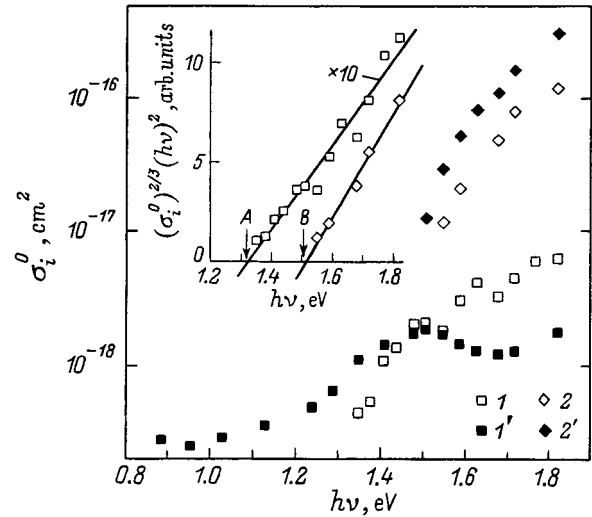

FIG. 3. Spectral dependence of the absorption cross section σ_i^0 for the slow ($i = 1$, curves *1*, *1'*) and fast ($i = 2$, curves *2*, *2'*) components of the relaxation; temperature T, K: *1, 2* — 289, *1', 2'* — 315. The inset shows the dependence of σ_i^0 on $h\nu$ for $T = 289$ K and $i = 1$ (curve *1*), $i = 2$ (curve *2*), in Lukovsky coordinates. The arrows indicate the thresholds of the functions $(\sigma_i^0)^{2/3}(h\nu)^2 = f(h\nu)$ in eV: A — 1.3, B — 1.5.

According to these data, the spectra of the dc increment of the squared photocapacitance and absorption cross section contain features associated with states of at least two different deep levels, with energies located in the upper half of the semiconductor band gap. According to the level scheme for charged defects in a-As$_2$Se$_3$ postulated in Refs. 1 and 2, levels A^+ and $O^+(O^-)$, located at energies 1.4 and 0.8 (0.9) eV from the top of the valence band, respectively, lie in the range of photon energies under discussion. These levels are responsible for two processes by which holes are photoemitted into the valence band:

$$D^+ \overset{h\nu}{\to} D^0 + h, \tag{3}$$

$$D^0 \overset{h\nu}{\to} D^- + h. \tag{4}$$
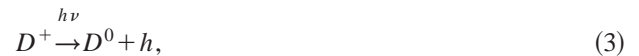
According to the model derived by Street[6] these charged defects, transition (3) causes the tail in the region of weak absorption and low-energy photoconductivity. Once a temperature-dependent shift is included ($\sim 2.4 \times 10^{-3}$ eV $\cdot$ K^{-1}; see Ref. 7), the 1.51-eV threshold we find in this paper agrees with the location of the A^+ level as revealed by the photoelectric measurements of Ref. 2 in bulk samples of a-As$_2$Se$_3$. Our estimates of the concentration ($\sim 5 \times 10^{17}$ cm^{-3}), cross section ($\sim 10^{-16}$ cm^2), and character of its spectrum are typical of deep centers in chalcogenide glasses, and are confirmed by data from low-temperature measurements of induced absorption and ESR.[1] These features allow us to assign the fast component of the photocapacitance relaxation to transitions of type (3) with high probability.

It is considerably more difficult to identify the second, slow relaxation process shown in Figs. 2 and 3. The states involved in it are present in high concentrations (10^{17}–

FIG. 2. Spectral dependence of the dc value of the squared photocapacitance increment ΔC_{si}^2 for the slow ($i = 1$, curves *1*, *1'*) and fast ($i = 2$, curves *2*, *2'*) components of the relaxation; temperature T, K: *1, 2* — 289, *1', 2'* — 315.

10^{19} cm^{-3}), have an anomalously low absorption cross section σ_1^0 ($\lesssim 7 \times 10^{-18}$ cm^2), and make the spectra of ΔC_1^2 broad, strong, and temperature-dependent. Process (4) cannot possibly be responsible for all the peculiarities of these centers. Previous studies of a-As$_2$Se$_3$ have also noted the presence of a mechanism that allows absorption with a very low cross section.[6,8,9] In their analysis of the kinetics of photoinduced absorption over a wide temperature range, Monroe and Kastner[10] observed that the absorption cross section at room temperature increases almost linearly from 2.5×10^{-19} to 7×10^{-19} cm^2 in the energy range $h\nu =$ 0.8–1.4 eV. These data are in good agreement with our results (Fig. 3, curve $1'$). It is clear from Fig. 3 that the cross section remains less than 7×10^{-18} cm^2 above the energy $h\nu =$ 1.4 eV as well. The authors of Ref. 10 also showed that deep levels in the tail of the conduction band also participate in the absorption along with states of charged defects, since the threshold energy for the absorption cross section spectrum follows a thermalization law ($E_p = kT \ln(\nu_0 t)$, where $\nu_0 = 10^{-12}$ s). This prompts us to consider a number of other phenomena as possible reasons for the small value of the cross section: correlation effects,[9] low quantum efficiency,[6] or barriers created by the Coulomb or electron-phonon interaction that can trap free charge carriers.[10]

As evidence of a role for defects in the slow relaxation process, we note that the character of the spectral distribution of the density of states N_{t1} in As$_2$Se$_3$, which we estimate here from ΔC_{si}^2 (see Fig. 2), is analogous to that of the same quantity inferred from data on optically induced ESR in As$_2$S$_3$.[11] In both cases, the function $N_{t1}(h\nu)$ exhibits a transition from mildly to steeply sloping function at a photon energy corresponding to the beginning of the Urbach absorption edge. According to ESR data, the mildly sloping portion of the spectrum is caused by defects at chalcogen atoms, whereas the steep portion is associated with the formation of metastable paramagnetic states on arsenic atoms.

An alternate interpretation of the small absorption cross section is based on the possible existence in a-As$_2$Se$_3$ films of a high concentration of so-called close-pair defects[1] with variable valence (D^+D^-). In this case, optical excitation of holes into the valence band takes place either directly or by a two-step process: first an optical transition takes place within the pair, and then the hole is thermally ejected. The probability of this process is limited by the second step, and can be quite small. As evidence for a stage of thermal excitation we point to the strong temperature dependence of the slow relaxation component.

[1] *Electronic Phenomena in Chalcogenide-Glass Semiconductors*, edited by K. D. Tsendin [in Russian], A. F. Ioffe Physicotechnical Inst. Publ., Russ. Acad. Sci., St. Petersburg, 1996.

[2] G. J. Adriaenssens, Philos. Mag. B **62**, 79 (1990).

[3] L. S. Berman and A. A. Lebedev, *Capacitive Deep-Level Spectroscopy in Semiconductors* [in Russian], Nauka, Leningrad, 1981.

[4] S. D. Shutov and A. A. Simashkevich, J. Non-Cryst. Solids **176**, 253 (1994).

[5] M. Kuhn, Solid-State Electron. **13**, 873 (1970).

[6] R. A. Street, Phys. Rev. B **17**, 3984 (1978).

[7] G. J. Adriaenssens, M. Hammam, H. Michiel, and J. M. Marshall, Solid State Commun. **45**, 465 (1983).

[8] S. G. Bishop, U. Strom, and P. C. Taylor, Phys. Rev. B **15**, 2278 (1977).

[9] J. Tauc and A. Menth, J. Non-Cryst. Solids **8–10**, 569 (1972).

[10] D. Monroe and M. A. Kastner, *Physics of Disordered Materials* (N. Y. – London, 1985) p. 553.

[11] J. A. Freitas, Jr., U. Strom, and S. G. Bishop, Phys. Rev. B **35**, 7780 (1987).

Translated by Frank J. Crowne

Controlling the U^--center density in Se−As chalcogenide-glass semiconductors by doping with metals and halogens

L. P. Kazakova and K. D. Tsendin

A. F. Ioffe Physicotechnical Institute, Russian Academy of Sciences, 194021 St. Petersburg, Russia
(Submitted December 28, 1998; accepted for publication December 30, 1998)

Temperature dependences of the drift mobilities of electrons and holes are investigated in chalcogenide-glass semiconductors with composition $Se_{95}As_5$, both without impurities and with the impurities Ag and Br. The data obtained indicate that the localized states that control the transport of charge carriers are U^--centers, and that the change in the magnitude of the drift mobility after doping is caused by a change in the concentration of these centers. Estimates of the concentrations of positive and negatively charged intrinsic defects show that their values are similar, equalling $\sim 10^{16}$ cm^{-3} in impurity-free glasses with the composition $Se_{95}As_5$ and lying in the range 10^{13}–10^{17} cm^{-3} when these glasses are doped with Ag, Br, and Cl. It is established that halogen impurities change the concentration of U^--centers most strongly (by two to three orders of magnitude). Analysis of the data obtained shows that the percentage of electrically active Br and Cl impurity atoms is 1%, while for Ag atoms it is 10^{-2}%. © *1999 American Institute of Physics.* [S1063-7826(99)02107-9]

INTRODUCTION

At this time we may consider it established that the predominant type of intrinsic defect in chalcogenide-glass semiconductors (CGS) is a defect with negative correlation energy (U^-- centers).[1–7] In the ground state, U^--centers exist in the form of charged point defects D^+ and D^-. This implies that their concentration can be changed by doping the CGS with impurities capable of forming charge states.[3–5] By affecting the concentration of U^--centers we can control such vitally important properties of the CGS as its electrical conductivity, photoconductivity, and luminescence.[1–7]

Recently, the problem of how to vary the concentration of U^--centers has become interesting for another reason. A topic of current interest in the literature[8–12] is the possibility that systems of small bipolarons can enter the superconducting state. It is believed that the ability of such a system to become superconducting is sensitive above all else to the bipolaron concentration. Now, the two charge states of the U^-- center (D^+ and D^-) are by their nature classical examples of small bipolarons. Moreover, in contrast to other material systems (e.g., materials with high-temperature superconductivity), in which the very existence of small bipolarons has not been established unambiguously, the presence of U^--centers, i.e., small bipolarons, in CGS is no longer questioned. Therefore, the possibility of controlling the concentration of U^--centers with the help of doping encourages one to hope that a model material based on CGS could be created for the express purpose of investigating the problem of superconducting transitions in a system of small bipolarons.

In this work, we have measured the drift mobility of charge carriers in glasses with the composition $Se_{95}As_5$ over a wide range of temperatures $T = 290$–360 K in order to determine the concentration of U^--centers and their energy position in the CGS system Se−As.

EXPERIMENTAL METHOD

The choice of the CGS with composition $Se_{95}As_5$ as our object of investigation was made because its mobile charge carriers include both holes and electrons.[13–16]

We used Ag (an electrically positive impurity) and Br, Cl (electrically negative impurities) as dopants. The impurities were introduced into the material during its synthesis, in concentrations that ranged from 10^{16} to 10^{21} cm^{-3}.

The samples we used for measurements had a ''sandwich'' structure, consisting of layers with thickness $\sim 1.5 -2.2$ μm prepared by thermal evaporation in vacuum at a residual pressure of 10^{-6} Torr. As substrates we used polished glass plates on which we first deposited a lower electrode made of aluminum or In_2O_3. As the upper electrode we used a semitransparent film of aluminum sputtered in vacuum onto the layer of material under study. The concentration of impurities in the films was set equal to their content in the batch. The temperature of the samples was monitored by a thermocouple.

In order to study the drift mobility we used the method of time-of-flight measurement.[17] Charge carriers were injected into the sample by a pulse of strongly absorbed light with wavelength 0.33 μm and duration ~ 8 ns obtained from a LGI-21 laser.

The time-of-flight t_T of the charge carriers through the sample was deduced from the dependence of the photocurrent on time. The drift mobility was calculated from the expression $\mu = L/t_T F$, where L is the sample thickness, and F is the electric field intensity.

If the charge carrier transport is monitored by capture of carriers at a discrete trap level located at a distance ΔE from
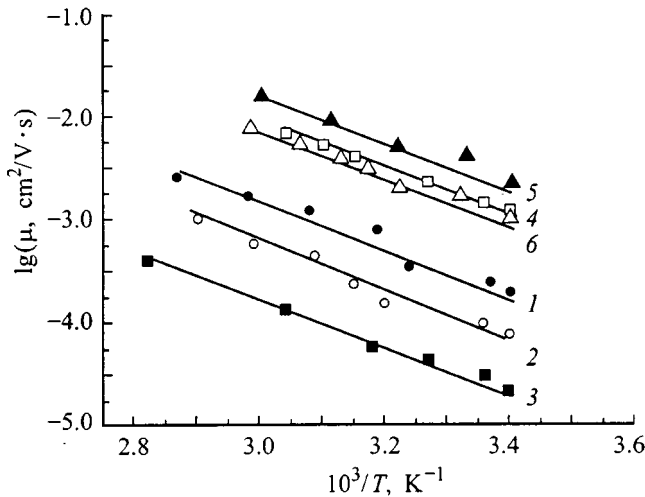
FIG. 1. Dependence of the drift mobility of holes (*1,3,5*) and electrons (*2,4,6*) on temperature for glasses with the composition $Se_{95}As_5$ without impurities (*1,2*), with 5.7 at. % Ag impurities (*3,4*), and 10^{-4} at. % Br impurities (*5,6*). The field intensity was 1×10^4 V/cm.

the edge of the band gap, then the expression for the drift mobility is written in the form

$$\mu = \mu_0 (N_c / N_t) \exp(-\Delta E / kT), \tag{1}$$

where μ_0 is the mobility of the charge carriers in the allowed band, and N_c and N_t are the effective densities of states in the allowed band and the density of localized states, respectively.[18] This expression can be used to determine the concentration of traps that control the transport.

EXPERIMENTAL RESULTS AND DISCUSSION

Figure 1 shows experimental data obtained from our studies of the temperature dependence of the drift mobility, both in a material without impurities and in doped materials with concentrations 5.7 at. % of silver and 10^{-4} at. % of bromine. It is clear from the figure that the values of activation energy for the drift mobility of electrons (ΔE_e) and holes (ΔE_h) in samples with silver and bromine impurities are similar ($\Delta E_e \simeq \Delta E_h \simeq$ 0.44– 0.46 eV), and do not differ significantly from values of the corresponding activation energies found in undoped material ($\Delta E_e \simeq \Delta E_h \simeq$ 0.46– 0.48 eV). At the same time, it is clear from these data that the value of drift mobility for charge carriers changes after doping. When 5.7 at. % Ag is introduced, for example, the electron mobility (μ_e) increases by more than an order of magnitude, while the hole mobility (μ_h) decreases by approximately the same amount. We note that a similar type of change in charge carrier mobility is observed in glassy As_2Se_3 as well, when Ag impurities or other metals are introduced.[19–21]

Behavior of the drift mobilities corresponding to an increase in the mobility of charge carriers of one sign with simultaneous decrease in the mobility of charge carriers of the other sign is also observed when glasses with the composition $Se_{95}As_5$ are doped by halogens (Br and Cl).[22] For example, when the impurity Br is introduced, starting at a

concentration $[Br] \simeq 10^{-4}$ at. % the concentration dependence of the drift mobility exhibits a segment on which μ_h increases and μ_e decreases.

Our investigations have shown that the values of activation energy for the charge carrier drift mobilities practically coincide in our doped and undoped CGS samples. This fact allows us to associate changes in the drift mobilities with changes in the concentration of localized states that control the transport, and to explain our experimental data in terms of the model of charged intrinsic defects developed in Refs. 1–5.

According to this model, charge carrier transport in CGS is controlled by U^-- centers, which consist of the charged defects D^+ and D^-. These defects are formed from an initially neutral defect D^0 according to the reaction

$$2D^0 \rightarrow D^+ + D^-. \tag{2}$$

Since the D^+- and D^--centers are traps for electrons and holes, according to Eq. (1), the values of the drift mobilities are inversely proportional to the concentration of these centers:

$$\mu_e \sim 1/[D^+], \qquad \mu_h \sim 1/[D^-]. \tag{3}$$

Impurities affect the concentrations of D^+- and D^--centers in the following way. When negative (or positive) charged impurities $A^-(A^+)$ are introduced into the material, the law of electrical neutrality must be satisfied:

$$[A^-]+[D^-]=[D^+] \quad \text{or} \quad [A^+]+[D^+]=[D^-]. \tag{4}$$

According to the law of mass action, we can write the following quantitative relation between the concentrations of charged centers generated by the reaction (2):

$$[D^+][D^-]=[D^0]^2 = \text{const.} \tag{5}$$

From Eqs. (4) and (5) it follows that as the concentration $[A^-]$ increases, the concentration of D^+-centers should increase, while the concentration of D^--centers should decrease. When a positively charged impurity A^+ is introduced, we observe the reverse process: $[D^+]$ decreases, while $[D^-]$ increases. According to Eq. (3), such a change in the concentration of charged U^--centers leads to a corresponding change in the value of the charge-carrier drift mobility similar to what we observe experimentally.

Based on these ideas, we estimate the concentrations of D^+- and D^--centers in layers of CGS with the composition $Se_{95}As_5$ doped with Ag, Br, and Cl. For these estimates we will use Eq. (1) and the assumption that $\mu_0 = 10$ cm^2/(V·s) and $N_c = 10^{19}$ cm^{-3}. As a result, we find that when 5.7 at. % Ag is introduced into the material, the concentration of D^--centers increases to $\sim 10^{17}$ cm^{-3}, while the concentration of D^+-centers decreases to $\sim 10^{15}$ cm^{-3}. Doping with halogens causes $[D^-]$ to decrease to $\sim 10^{13}$ cm^{-3} and $[D^+]$ to increase to $\sim 10^{17}$ cm^{-3} (Fig. 2).

Using the fact that in impurity-free $Se_{95}As_5$ we estimate the concentrations of D^+- and D^-- centers to be $[D^+] \simeq [D^-] \simeq 10^{16}$ cm^{-3}, we obtain from Eq. (5) the value $[D^+][D^-] \simeq 10^{32}$ cm^{-6}, i.e., $[D^0] \simeq 10^{16}$ cm^{-3}. This result agrees with data obtained from silver doping, since in this case we also have $[D^+][D^-]=[D^0]^2 \simeq 10^{32}$ cm^{-6}.
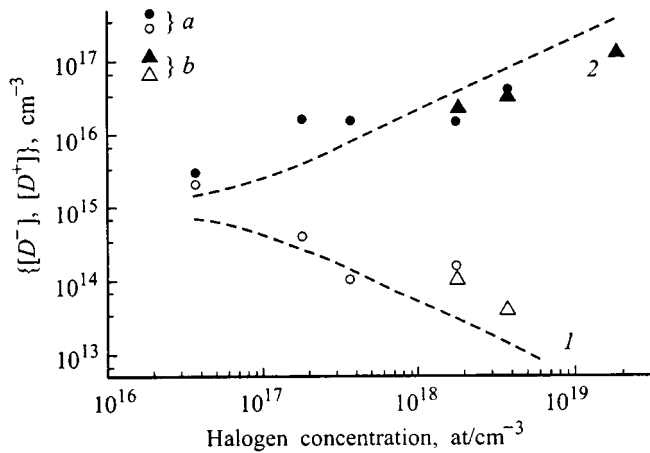
FIG. 2. Dependence of the concentrations of negatively (*1*) and positively (*2*) charged intrinsic defects in glasses with the composition $Se_{95}As_5$ on the content of Br (a) and Cl (b) impurities. The dots correspond to values determined from experimental data using Eq. (1). Data on values of the drift mobility for concentrations of Br and Cl impurities in the range 10^{17} to 10^{19} cm^{-3} are taken from Ref. 22. The dashed lines are theoretical dependences: *1*— calculated from expression (7), *2*— calculated from expression (8).

Based on these data we can estimate the concentration of positively charged silver impurity centers $[A^+]$. Assuming that $[A^+] \gg [D^+]$, from Eq. (4) we obtain $[A^+] \simeq [D^-] \simeq 10^{17}$ cm^{-3}, so that the total concentration of silver introduced is $\sim 10^{21}$ cm^{-3}. Thus, only one out of 10^4 silver atoms appears in $Se_{95}As_5$ as a positively charged center. The majority of impurity atoms are not electrically active, and probably are incorporated into the host material by satisfying all of its valence requirements according to the ''$8-N$ rule,'' where N is the number of valence electrons of the atom.[6,7]

As for the material with halogen impurities, in order to estimate the concentration of D^+- and D^--centers in this case we use values μ_e and μ_h obtained by us and in Ref. 22. In this case we assume that the activation energy for the charge-carrier drift mobility in the samples with Cl impurities does not differ significantly from that of samples doped with Br found in our work.

We see clearly from Fig. 2 that in samples with bromine contents in the range 3.7×10^{16} to 3.7×10^{18} cm^{-3} the concentration $[D^-]$ decreases from $\sim 10^{15}$ to $\sim 10^{14}$ cm^{-3}, while $[D^+]$ increases from $\sim 10^{15}$ to $\sim 10^{16}$ cm^{-3}. In this case the product $[D^+][D^-] \simeq 10^{30}$ cm^{-6}, so that $[D^0] \simeq 10^{15}$ cm^{-3}, i.e., an order of magnitude smaller than in the original undoped material. The same value of the product $[D^+][D^-] \simeq 10^{30}$ cm^{-6} was obtained from analysis of experimental data obtained from samples doped with chlorine.

The reason why the concentration of D^0- centers decreases in material doped with halogens is not entirely clear. We can probably explain this fact by invoking the mechanism of ''healing'' of intrinsic defects proposed in Ref. 22. It is also possible that the concentration of intrinsic defects is affected by certain features of the process by which material with halogen impurities is synthesized. This process includes two steps at which the melt is held at constant temperature – at $T_1 = 700\,°C$ and $T_2 = 430\,°C$ – in contrast to the process in which the melt is held once at a fixed temperature $T_1 = 700\,°C$, which is used to synthesize impurity-free material.

In order to calculate the dependence of the concentration of charged U^--centers on the total concentration of halogen atoms $[A]$ we use Eqs. (4) and (5) and assume that

$$[A^-] = k[A]. \qquad (6)$$

Substituting the expression for $[D^+]$ from Eq. (4) into Eq. (5), we obtain the following quadratic equation: $[D^-]^2 + [D^-][A^-] - [D^0]^2 = 0$. This equation, along with Eq. (6), imply that

$$[D^-] = -(k[A]/2) + (k[A]/2)\{1 + [D^0]^2/(k[A]/2)^2\}^{1/2}, \quad (7)$$

$$[D^+] = (k[A]/2) + (k[A]/2)\{1 + [D^0]^2/(k[A]/2)^2\}^{1/2}. \qquad (8)$$

Figure 2 shows theoretical plots corresponding to Eqs. (7) (curve *1*) and (8) (curve *2*), setting $k = 0.02$. The agreement of the theoretical functions (7) and (8) with values of $[D^-]$ and $[D^+]$ obtained from the experimental data at $k = 0.02$ suggests that when the material is doped with bromine and chlorine, 1 out of 50 impurity atoms in $Se_{95}As_5$ become negatively charged, i.e., the coefficient k in this case is two orders of magnitude higher than the value established previously for silver doping.

We also note that for high impurity concentrations and values of $[A^-]$ that exceed $[D^-]$ by two to three orders of magnitude (i.e., $[Br] \gtrsim 10^{18}$ cm^{-3}, $[Cl] \gtrsim 10^{19}$ cm^{-3}), trapping at negatively charged impurity centers probably begins to limit the hole drift mobility, since its value decreases as the impurity concentration increases.[22] Since in this range of impurity concentrations the value of $\Delta E_h \simeq 0.4$ eV (which is somewhat lower than the energy level of the D^--centers that limit μ_h for $[A] = 10^{16} - 10^{18}$ cm^{-3}), and since $[A^-] \gg [D^-]$, we may conclude that the probability of capture of holes by negatively charged impurity centers is considerably lower than it is for capture by D^--centers.

CONCLUSIONS

Our studies have shown that introducing the impurities Ag, Br, and Cl into a CGS with composition $Se_{95}As_5$ leads to a considerable change in the magnitude of the drift mobility of electrons and holes, while leaving their activation energy practically unchanged. The data obtain by us indicate that the localized states that control the transport of charge carriers in CGS from the system Se–As are associated with U^-- centers, and the change in magnitude of the drift mobility after doping is due to the change in the concentration of these centers.

Our estimates of the concentrations of positively and negatively charged intrinsic defects show that the values of $[D^+]$ and $[D^-]$ are similar and equal $\sim 10^{16}$ cm^{-3} in impurity-free glasses with the composition $Se_{95}As_5$, and vary from 10^{13} to 10^{17} cm^{-3} after doping with Ag, Br, and Cl. We have established that halogen impurities cause the largest change (by two to three orders of magnitude) in the concentration of U^--centers.

Analysis of our data shows that the percentage of electrically active Br and Cl impurity atoms in $Se_{95}As_5$ is 1%, while for Ag it is 10^{-2}%.

[1] P. W. Anderson, Phys. Rev. Lett. **37**, 953 (1975).

[2] R. A. Street and N. F. Mott, Phys. Rev. Lett. **35**, 1293 (1975).

[3] N. F. Mott, E. A. Davis, and R. A. Street, Philos. Mag. B **32**, 961 (1975).

[4] M. Kastner, D. Adler, and H. Fritzsche, Phys. Rev. Lett. **37**, 1504 (1976).

[5] H. Fritzsche and M. Kastner, Philos. Mag. B **37**, 285 (1978).

[6] N. F. Mott and E. A. Davis, *Electronic Processes in Non-Crystalline Materials* (Clarendon Press, Oxford, 1971; Mir, Moscow, 1982).

[7] *Electronic Phenomena in Chalcogenide-Glass Semiconductors*, edited by K. D. Tsendin [in Russian], Nauka, St. Petersburg, 1996.

[8] B. P. Popov and K. D. Tsendin, Tech. Phys. Lett. **24**, 265 (1998).

[9] A. S. Alexandrov and J. Ranninger, Phys. Rev. B **23**, 1726 (1981).

[10] N. F. Mott, Physica C **205**, 191 (1993).

[11] B. K. Chakraverty, J. Ranninger, and D. Feinberg, Phys. Rev. Lett. **81**, 433 (1998).

[12] A. S. Alexandrov, Phys. Rev. B **53**, 2863 (1996).

[13] E. Montrimas, A. Pazera, and J. Viscakas, Phys. Status Solidi A **3**, K199 (1970).

[14] F. D. Fisher, J. M. Marshall, and A. E. Owen, Philos. Mag. B **33**, 261 (1976).

[15] E. A. Lebedev, L. Toth, and L. N. Karpova, Solid State Commun. **36**, 139 (1980).

[16] E. A. Lebedev, and L. P. Kazakova, in *Electronic Phenomena in Chalcogenide-Glass Semiconductors*, edited by K. D. Tsendin [in Russian] Nauka, St. Petersburg (1996), ch. 4, p. 171.

[17] W. E. Spear, J. Non-Cryst. Solids **1**, 197 (1969).

[18] A. Rose, *Concepts in Photoconductivity and Allied Problems* (Interscience, New York, 1963; Mir, Moscow, 1969, under the title *Principles of Photoconductivity Theory*), p. 140.

[19] L. P. Kazakova and E. A. Lebedev, Fiz. Tekh. Poluprovodn. **32**, 803 (1998) [Semiconductors **32**, 714 (1998)].

[20] G. Pfister and M. Morgan, Philos. Mag. B **41**, 209 (1980).

[21] V. L. Aver'yanov, L. P. Kazakova, S. S. Lantratova, E. A. Lebedev, and O. Yu. Prikhod'ko, Fiz. Tekh. Poluprovodn. **17**, 928 (1983) [Sov. Phys. Semicond. **17**, 582 (1983)].

[22] L. P. Kazakova, E. A. Lebedev, A. I. Isaev, S. I. Mekhtieva, N. B. Zakharova, and I. I. Yatlinko, Fiz. Tekh. Poluprovodn. **27**, 959 (1993) [Sov. Phys. Semicond. **27**, 520 (1993)].

Translated by Frank J. Crowne

THE PHYSICS OF SEMICONDUCTOR DEVICES

Theory of photoresistors based on trapezoidal δ-doped superlattices

V. V. Osipov and A. Yu. Selyakov

Russian Science Center ''ORION,'' 111123 Moscow, Russia

M. Foygel

South Dakota School of Mines and Technology, Rapid City, SD 57701-3995, USA

A theory is developed for photoresistors made up of trapezoidal δ-doped superlattices and their sensitivity to long-wavelength infrared light, based on a model proposed previously by the authors. It is shown that despite interband absorption of the infrared light and photogeneration of electron-hole pairs, the photoconductivity of the superlattice is unipolar, and that the photoelectric gain and photosensitivity of a photoresistor incorporating such a superlattice can reach enormous values. It is established that the lifetime of electrons and holes, determined by tunnel-radiative transitions, determines the kinetics of the photoconductivity decay. A paradoxical effect is predicted: the voltage photosensitivity of a trapezoidal superlattice, in contrast to all other types of photoresistors, is nearly independent of the lifetime of the photocarriers and level of doping (i.e., concentration of equilibrium carriers), and can have a gigantic value. The spectral sensitivity $R(\omega)$ is calculated, and it is shown that near the absorption edge $R(\omega)$ increases linearly with increasing photon energy. The spectral density of generation-recombination noise is found, along with the detectivity of such photoresistors. It is noted that this type of photoresistor allows fast erasure of the photoconductivity. © *1999 American Institute of Physics.*
[S1063-7826(99)02207-3]

1. In Refs. 1–4 we discussed a new kind of superlattice—the trapezoidal δ-doped superlattice (TSR). This structure can be grown using any of the well-known homogeneous single-crystal semiconductors (such as Ge, GaAs, InSb, and InAs). Like classical superlattices of $n-i-p-i$-type,[5–8] TSR do not contain heterojunctions and strained layers, and separate electrons and holes in space. In the thin regions of the TSR between differently charged δ-doped layers, superstrong electric fields appear, leading to a band diagram consisting of alternating trapezoidal potential wells for electrons and holes (Fig. 1). The Franz-Keldysh effect predicts that these superstrong electric fields can mediate the efficient absorption of infrared light of any polarization in regions of the TSR where they are present for photon energies $\hbar\omega \ll E_g$ (where E_g is the width of the semiconductor band gap). For example, TSR's based on InSb and InAs with certain parameters can efficiently absorb long-wavelength IR light out to 50–100 μm, while TSR's based on Ge and GaAs can absorb out to 4.5 and 3 μm, respectively.[1–4] Because of the spatial separation of nonequilibrium electrons and holes, their lifetimes τ in the TSR are determined by tunnel-radiative transitions and can be extremely long. Even in TSR based on InSb with its very small effective optical band gap E_g^{eff} (corresponding to a long-wavelength absorption edge, $\lambda_{co} = 25$ μm), τ can reach values on the order of 1 ms. Moreover, in contrast to classically
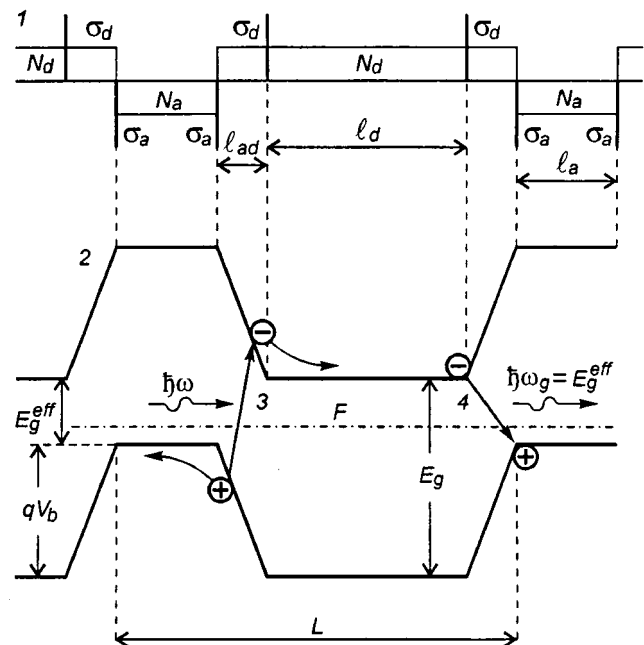

FIG. 1. Trapezoidal δ-doped superlattice: *1*—doping profile, *2*— energy diagram; the arrow *3* shows interband optical transitions that are indirect in real space involving absorption of a photon with energy $\hbar\omega < E_g$; the arrow *4* shows tunneling recombination (indirect in real space) of an electron and a hole with emission of a photon with energy $\hbar\omega \simeq E_g^{\text{eff}}$, where E_g^{eff} is the effective width of the TSR band gap; σ_d and σ_a are surface densities of atoms in the δ-doped layers of donor and acceptor type respectively; N_d and N_a are uncontrolled concentrations of donor and acceptor impurities; and l_d, l_a, and l_{ad} are the TSR layer thicknesses.

doped semiconductors, τ depends only weakly on temperature.[9] It is obvious that in TSR's based on wider-gap semiconductors (such as Ge and GaAs), and also in cases where the built-in electric field intensity of the TSR is not too large, τ can reach extremely large values, and consequently the photosensitivity of the TSR can have gigantic values.

In this paper we consider the spectral dependence of the photosensitivity, generation-recombination noise, and detectivity of longitudinal IR photoresistors based on TSR's.

2. TSR's are created in a single-crystal nondegenerate semiconductor by pairing alternating δ-doped layers of donor and acceptor type, with surface atomic densities equal to σ_d and σ_a, respectively. In such a TSR, regions of superstrong built-in electric field $E = 4\pi q\sigma/\varepsilon$ can appear between oppositely charged δ-doped layers, where q is the electron charge, ε is the dielectric constant of the semiconductor, and $\sigma_d = \sigma_a = \sigma$. In such regions of the TSR, the long-wavelength edge for interband absorption of IR light is determined by the effective width of the band gap $E_g^{\mathrm{eff}} = E_g - qV_b$, where $V_b = El_{ad}$ is the potential difference between differently charged δ-doped layers, and l_{ad} is the distance between these layers (Fig. 1).[1–4] The spatially separated electrons and holes, localized in n- and p-type potential wells, respectively, are effectively described by a statistically non-degenerate electron gas in a uniform semiconductor with a band-gap width E_g^{eff}. In particular, an analog to the law of mass action is satisfied in thermodynamic equilibrium:[9]

$$N_0 P_0 = N_c N_v l_d l_a \exp\{-E_g^{\mathrm{eff}}/kT\} \equiv N_i^2, \tag{1}$$

where $N = \int n\,dx$, $P = \int p\,dx$, n and p are the numbers and local concentrations of electrons and holes in the n- and p-type potential wells, respectively (the integration is over the corresponding potential well); N_0 and P_0 are the equilibrium numbers of electrons and holes in the n- and p-type potential wells, respectively, N_c and N_v are the effective densities of states of the semiconductor in the conduction and valence bands, respectively; k is Boltzmann's constant, T is the absolute temperature, l_d and l_a are the distances between identically charged δ-doped layers of donor and acceptor type, respectively (Fig. 1), and N_i is the effective intrinsic carrier concentration.

It is clear from the TSR energy diagram (Fig. 1) that the nonequilibrium electron-hole pairs generated by interband absorption of infrared light with photon energies $\hbar\omega \ll E_g$ in the regions of superstrong electric field are rapidly separated in space: the electrons roll down into the n-type potential wells, while the holes float up into the p-type wells. This leads to an unusual situation: although the absorption of infrared light in a TSR is determined by interband optical transitions accompanied by generation of electron-hole pairs, the photoconductivity of the TSR is unipolar.

Let us clarify this assertion for the example of a longitudinal photoresistor with the structure shown schematically in Fig. 2. Such a photoresistor consists of a TSR with two strongly doped n^+-type regions at a distance $\mathcal{L}$ from one another, which are ohmic contacts to all the n-type layers (potential wells) belonging to the TSR. In other words, current flows along the n-layers, while the p-layers are blocked
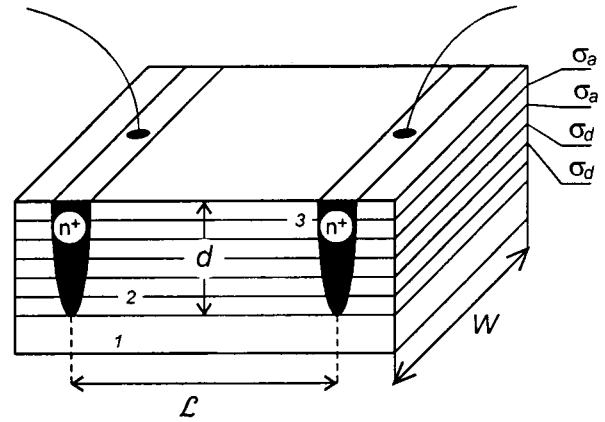

FIG. 2. Structure of a longitudinal TSR photoresistor. *1*—substrate, *2*—trapezoidal δ-doped superlattice; *3*—strongly doped n^+-type regions, i.e., ohmic contacts; $\mathcal{L}$, W, and $d = ML$ are the length, width, and thickness of the TSR photoresistor, respectively.

by $p-n^+$-type blocking contacts. Since photoelectrons accumulate in the n-regions, the photoconductivity of such a photoresistor is unipolar in character.

Note that in bipolar photoresistors the value of the photoelectric gain K is limited due to extraction of minority carriers in the contact. Thus, for photoresistors with n-type photoconductivity $K \leq (\mu_n/\mu_p + 1)/2$, where μ_n and μ_p are mobilities of electrons and holes, respectively.[10] In a unipolar photoresistor the phenomenon of extraction of minority carriers does not occur, and $K \propto V$, where the maximum value of voltage V applied to the photoresistor is limited only by breakdown (electrical, thermal, or tunneling). We emphasize that the electric and tunneling breakdown fields of a longitudinal TSR photoresistor can be quite high, since their values are determined by the width of the band gap of the semiconductor used to make the TSR.

The voltage photosensitivity of a unipolar photoresistor $R_v \propto \Delta N/N$, where ΔN is the number of photocarriers.[11] Therefore, the quantity R_v for a TSR photoresistor will be high if the number of electrons in the n-type conductivity layers is small. In the majority of II–V semiconductors, effective masses of electrons and heavy holes differ strongly: $m_c \ll m_{hh}$. Therefore, the number of equilibrium nondegenerate holes in the p-type wells can greatly exceed the number of equilibrium nondegenerate electrons in n-type wells. This implies that according to Eq. (1) the number of electrons in a p-type TSR can be made much smaller than the number of holes in an n-type TSR. This justifies choosing n^+-type contacts for such a TSR photoresistor.

A high concentration of holes is realized in a TSR photoresistor, e.g., when $\sigma_a > \sigma_d$. Actually, in a TSR that efficiently absorbs IR light,[1–4] the quantities σ_d and σ_a are usually much larger than $N_d l_d$ and $N_a l_a$, where N_d and N_a are uncontrolled concentrations of donor and acceptor impurities in the regions of the TSR between the donor and acceptor δ-doped layers. Therefore, the condition of electrical neutrality over one period of the TSR implies that $P = 2(\sigma_a - \sigma_d) \gg N_i$. For example, in a TSR based on InSb the quantities σ_a and σ_d come to $(2-5)\times10^{12}\,\mathrm{cm}^{-2}$, while for the thickness of the p-type well[1–4] we have $l_a \simeq 100\,\text{Å}$. Therefore, the

concentration of holes in the *p*-type wells can have a value of order 10^{18} cm^{-3}, i.e., close to the value of N_v for InSb. It thus follows that when the condition $N_d, N_a < 10^{18}$ cm^{-3} holds, the equilibrium electron concentration N_0 and hole concentration P_0 in the TSR does not depend on the quantities N_d and N_a.

In order to analyze the photoconductivity let us consider the continuity equation

$$\frac{\partial n}{\partial t} = g + g_T - r + \frac{1}{q}\frac{\partial J_n}{\partial x}, \tag{2}$$

where g_T and g are rates of thermal generation and photogeneration of electrons, *r* is the recombination rate, and J_n is the electron current density. Following Ref. 5, let us integrate Eq. (2) over one period of the superlattice *L*. We note that in a TSR the condition $\alpha_{\text{eff}}L \ll 1$ is satisfied. Here α_{eff} is the effective absorption (i.e., averaged over a period) of IR light in the TSR.[1] This implies that the optical generation within many adjacent periods can be treated as uniform. In this case, the electron current density is a periodic function; more accurately, we can assume that $\int_L (\partial J_n/\partial x)dx = 0$. Since $\int_L n\, dx = N$ to exponential accuracy, we find from Eq. (2) that for each period of the superlattice *L* the following equation holds:

$$\frac{\partial N}{\partial t} = G + G_T - R, \tag{3}$$

where $G = \int_L g\, dx$, $G_T = \int_L g_T dx$, and $R = \int_L r\, dx$ are the integrated rates of photogeneration, thermal generation, and recombination, respectively.

For small deviations from thermodynamic equilibrium ($\Delta N \ll N_0$), Eq. (3) can be rewritten in the form

$$\frac{\partial \Delta N}{\partial t} = G - \frac{\Delta N}{\tau}, \tag{4}$$

where τ is the lifetime of nonequilibrium carriers. From Eq. (4) it is clear that τ determines the decay of the number of nonequilibrium electrons after the illumination of a TSR by IR light ends, and consequently it determines the decay of the photoconductivity. In TSR's that efficiently absorb long-wavelength IR light, the lifetime of nonequilibrium carriers τ_R is determined by tunneling-radiative transitions of electrons from the *n*-type potential wells to the *p*-type potential wells,[9] and can become quite large (on the order of 1 ms for InSb). Note, however, that the photoconductivity of a TSR photoresistor can also be quenched. Accordingly, it is necessary to make not only ohmic contacts to the layers of one conductivity type, but also one or two additional ohmic contacts to the layers of the opposite conductivity type (Fig. 3). When a voltage is applied across ohmic contacts to layers of different conductivity types with a polarity that decreases the height of the potential barrier between the donor and acceptor δ-doped layers (Fig. 1), nonequilibrium electrons and holes can be extracted from the corresponding potential wells.

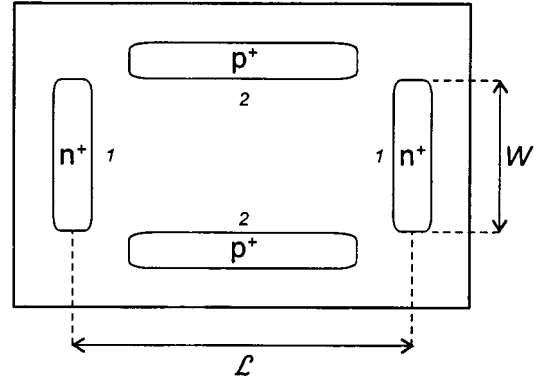**3.** The photocurrent in an *n*-type TSR photoresistor can be written in the form

FIG. 3. Structure for quenching photoconductivity in a TSR photoresistor. *1*—ohmic contact to the *n*-type layers, *2*—additional ohmic contacts for the *p*-type layers.

$$I = q\mu_n E_{\mathcal{L}} W \sum_{j=1}^{j=M} \Delta N_j, \tag{5}$$

where $E_{\mathcal{L}}$ is the longitudinal electric field in the TSR photoresistor, *W* is its width (Fig. 2), *M* is the number of superlattice periods, and ΔN_j is the number of nonequilibrium electrons in the *j*th potential well of the TSR. The latter is determined from Eq. (4), and in the steady state it is

$$\Delta N_j = \tau_R G_j, \tag{6}$$

where the rate of photogeneration in the *j*th period of the TSR is

$$G_j = (1 - \widetilde{R})\exp[-\alpha_{\text{eff}}(j-1)L]J\int_L \alpha_{\text{eff}}\exp(-\alpha_{\text{eff}}x)dx,$$

$\widetilde{R}$ is the reflection coefficient, and *J* is the photon flux density of the light incident on the photoresistor. Using the condition $\alpha_{\text{eff}}L \ll 1$, the rate of photogeneration in the *j*th period of the TSR can be rewritten in the form

$$G_j = (1 - \widetilde{R})\alpha_{\text{eff}}L\, J\exp[-\alpha_{\text{eff}}(j-1)L]. \tag{7}$$

Substituting Eqs. (6) and (7) into Eq. (5), we obtain

$$I = q\eta JAK. \tag{8}$$

Here $A = \mathcal{L}W$ is the area of the photosensitive region; $\mathcal{L}$ is the length of the TSR photoresistor; $K = \tau_R/t_r$ is the photoelectric gain; $t_r = \mathcal{L}^2/\mu_n V$ is the time of flight of an electron through the *n*-region of the TSR; $V = E_{\mathcal{L}}\mathcal{L}$ is the voltage applied to the TSR photoresistor; and η is the quantum efficiency, which is

$$\eta = (1 - \widetilde{R})\alpha_{\text{eff}}L\sum_{j=1}^{j=M}\exp[-\alpha_{\text{eff}}(j-1)L] = (1 - \widetilde{R})\alpha_{\text{eff}}d, \tag{9}$$

where $d = ML$ is the thickness of the TSR. In Eq. (9) we have included the fact that the number of periods of the TSR is limited by diffusive spreading of the δ-doped layers, and the most realistic situation is one where $\alpha_{\text{eff}}d \ll 1$.
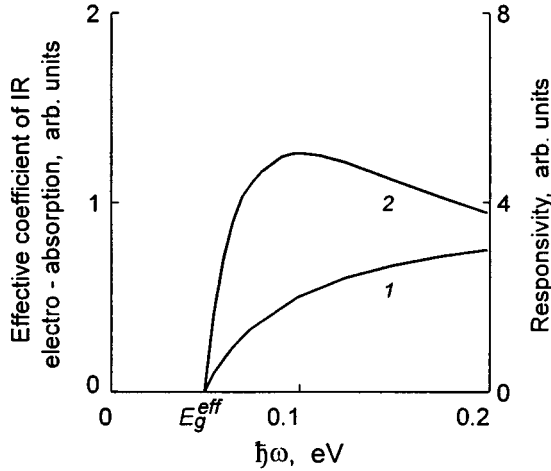
FIG. 4. Spectral dependence of the photosensitivity of a TSR photoresistor. *1*—effective absorption coefficient for IR light in the TSR; *2*—spectral dependence of the photosensitivity. The calculations were made for a TSR photoresistor based on InSb with a long-wavelength absorption edge $\lambda_{co} = 25$ μm; the parameters of this structure were given in Ref. 9.

4. By definition the current sensitivity of a photoresistor is $R_I = I/P$, where $P = \hbar\omega JA$ is the incident monochromatic optical power.[10] According to Eq. (8), the current photosensitivity of a TSR is

$$R_I = q\eta K/\hbar\omega. \tag{10}$$

From Eqs. (10) and (9) it is clear that the spectral current photosensitivity $R_I(\hbar\omega) \propto \alpha_{\text{eff}}(\omega)/\omega$, where the effective absorption of light in TSR with photon energy $\hbar\omega < E_g$ (see Refs. 1 and 4) is

$$\alpha_{\text{eff}}(\hbar\omega) = 2\alpha(\hbar\omega)(\hbar\omega - E_g^{\text{eff}})/qEL. \tag{11}$$

Here $\alpha(\hbar\omega)$ is the electroabsorption, which for the limiting case of a superstrong electric field is

$$\alpha(\hbar\omega) = \Gamma^2(2/3)\,\mathcal{R}\sqrt{\hbar\omega_E}/4\pi, \tag{12}$$

and $\mathcal{R} = (2\mu/\hbar^2)^{3/2}(2q^2 P_{cv}^2)/(m^2 c\tilde{n}\omega)$, $\omega_E = (qE)^{2/3}/(2\mu\hbar)^{1/3}$, $\mu^{-1} = m_c^{-1} + m_{hh}^{-1}$, m is the free electron mass, c is the velocity of light in vacuum, P_{cv} is the interband matrix element of the momentum operator, $\tilde{n}$ is the refractive index of the semiconductor, and $\Gamma(x)$ is the gamma-function . Expression (12) is conveniently written in the form $\alpha(\hbar\omega) = \alpha_g E_g^{\text{eff}}/\hbar\omega$, where $\alpha_g = \alpha(E_g^{\text{eff}})$.

Substituting this formula and Eq. (11) into (9), and taking into account that $\alpha_{\text{eff}}d \ll 1$, we find from Eq. (10) that the spectral dependence of the TSR photosensitivity takes the form

$$R_I(\omega) = \left\{\frac{2(1-\tilde{R})MK\alpha_g E_g^{\text{eff}}}{E}\right\}\left\{\frac{\hbar\omega - E_g^{\text{eff}}}{(\hbar\omega)^2}\right\}. \tag{13}$$

The function $R_I(\omega)$ is shown in Fig. 4. In this figure, the maximum of the photosensitivity corresponds to a photon energy $\hbar\omega_{\max} = 2E_g^{\text{eff}}$; this maximum is $R_I^{\max} = (1-\tilde{R})MK \times \alpha_g/2E$.

The voltage sensitivity of the photoresistor is determined by the expression $R_V = R_I/Y$, where Y is the photoconductivity of the photoresistor, which for a TSR is

$$Y = q\mu_n W(MN_0 + \eta J_b\tau_R)/\mathcal{L}, \tag{14}$$

where J_b is the flux density of background photons. In writing Eq. (14) we have used Eqs. (6), (7), and (9), and have assumed that the intensity of the signal light is much smaller than the background, i.e., $J \simeq J_b$.

For low background intensities ($\eta J_b\tau_R \ll N_0$) it follows from Eqs. (10) and (14) that

$$R_V = \left\{\frac{\eta V}{\hbar\omega AM}\right\}\left\{\frac{\tau_R}{N_0}\right\}. \tag{15}$$

The lifetime of nonequilibrium carriers in the TSR is determined by tunneling-radiative transitions given by[9]

$$\tau_R = N_i^2/\{G_T(N_0 + P_0)\}, \tag{16}$$

where the rate of thermal generation G_T is determined by the expression

$$G_T = \left\{\frac{2(\tilde{n}kTE_g^{\text{eff}})^2}{\pi^2 c^2\hbar^3 qE}\right\}\alpha_g\exp\left\{-\frac{E_g^{\text{eff}}}{kT}\right\}. \tag{17}$$

Substituting Eq. (16) into (15), and taking into account that in our case $P_0 \gg N_0$, we obtain

$$R_V = \{(1-\tilde{R})\alpha_{\text{eff}}\hbar\omega LV\}/\{\hbar\omega AG_T\}. \tag{18}$$

It is well known[10–12] that in impurity and intrinsic photoresistors the voltage sensitivity is proportional to the lifetime and inversely proportional to the concentration of majority carriers, which determines the conductivity of the photoresistor. Let us turn our attention to the nontrivial nature of our results. As we have already mentioned, in TSR photoresistors the absorption of IR light is attributed to the interband transitions in strong electric fields and is accompanied by generation of electron-hole pairs; nevertheless, according to Eq. (15), the TSR voltage sensitivity is $R_V \propto 1/n_0$, where $n_0 = N_0/l_d$ is the effective concentration of minority carriers in the TSR, which for $P_0 \gg N_0$ depends exponentially, according to Eq. (1), on temperature with an activation energy E_g^{eff}. Moreover, from Eqs. (15) and (18) it follows that the quantity R_V is independent of the lifetime and increases exponentially as the temperature decreases, essentially because of the decrease in the number of equilibrium electrons N_0. Thus, a TSR photoresistor can have a high speed while preserving a large voltage sensitivity.

For high background intensities ($\eta J_b\tau_R \gg N_0$), it follows from Eqs. (10) and (14) that $R_V = V/\hbar\omega J_b A$, i.e., the expression for the voltage sensitivity of a TSR photoresistor coincides with the standard formula of Ref. 11 for a unipolar photoresistor in the BLIP regime.

5. Over a wide range of frequencies, the noise in a photoresistor is usually determined by fluctuations in the number of carriers caused by randomness of the generation-recombination processes.[10,12] Therefore, let us consider the threshold characteristics of TSR photoresistors determined by generation-recombination noise. The basic parameter that

characterizes properties of threshold detectors is the specific detectivity, which by definition is (see, for example, Refs. 10 and 12)

$$D^* = R_I \sqrt{A \Delta f} / \sqrt{\overline{\delta I^2}}, \tag{19}$$

where Δf is the frequency bandwidth of the measurement circuit, $\overline{\delta I^2} = S_i \Delta f$ is the dispersion of the noise current, and S_i is the spectral density of the noise.

Using Eq. (5), let us write the current fluctuation in a TSR photoresistor as follows:

$$\delta I = \frac{q \mu_n V}{\mathcal{L}^2} \sum_{j=1}^{j=M} \delta \tilde{N}_j = \frac{q}{t_r} \sum_{j=1}^{j=M} \delta \tilde{N}_j, \tag{20}$$

where $\delta \tilde{N}_j = A \, \delta N_j$ is the fluctuation in the number of carriers in the jth potential well of the TSR, which occurs as a result of generation and recombination processes.

Let us assume that fluctuations in the carrier numbers of different potential wells of the TSR are uncorrelated, and use the Wiener-Khinchine theorem.[13] From Eq. (20) we find that the spectral density of the noise current is

$$S_i = \frac{q^2}{t_r^2} \sum_{j=1}^{j=M} S_{\tilde{N},j}, \tag{21}$$

where $S_{\tilde{N},j}$ is the spectral density of fluctuations of the number of carriers in the jth potential well of the TSR. Following the Langevin method,[13,6] we introduce random sources into Eq. (4) that describe thermal-generation, photogeneration, and recombination noise. In the case under study we assume that these random sources of noise are δ-correlated and write the spectral densities of fluctuations of the random noise sources connected with thermal generation, recombination, and background photogeneration as $S_g = S_r = 2 G_T$, $S_b = 2 G_j$, respectively. Solving Eq. (4), which is linearized with respect to small fluctuations, with the random sources introduced by us, we find that for frequencies $\omega \tau_R \ll 1$ the spectral density of the fluctuations in the number of carriers in the jth potential well of the TSR is

$$S_{\tilde{N},j} = 4 \tau_R^2 A (G_T + G_j). \tag{22}$$

The sum on the right side of Eq. (21) can be transformed to

$$\sum_{j=1}^{j=M} S_{\tilde{N},j} = 4 \tau_R^2 A (M G_T + \eta J_b).$$

Substituting the latter expression into Eq. (21), we obtain

$$S_i = 4 q^2 K^2 A (M G_T + \eta J_b). \tag{23}$$

From Eqs. (23) and (19) it is clear that the conditions for the BLIP regime of a TSR photoresistor are determined by the obvious inequality $\eta J_b \gg M G_T$. In other words, the temperature for BLIP operation of a TSR, like its voltage sensitivity, is determined by E_g^{eff}, i.e., the effective width of the band gap of the TSR, which determines the long-wavelength absorption edge.[1–4]

Substituting Eq. (23) into Eq. (19), we find that for low background intensity $M G_T \gg \eta J_b$ the specific detectivity is

$$D^* = \eta / 2 \hbar \omega \sqrt{M G_T}, \tag{24}$$

i.e., it also is determined by E_g^{eff}.

For the strong-background case $M G_T \ll \eta J_b$, the specific detectivity of the TSR photoresistor is determined by the usual expression $D^* = \sqrt{\eta} / 2 \hbar \omega \sqrt{J_b}$ for specific detectivity of intrinsic and impurity photoresistors in the BLIP regime.[10]

6. Thus, we have shown that by incorporating only δ-doped layers into classical single-crystal semiconductors we can create ultra-high sensitivity photoresistors with spectral sensitivities ranging from mid- to far-IR (up to 50–100 μm for InSb and InAs and 3–4 μm for GaAs and Ge). An additional unique feature of the TSR photoresistor is the fact that its voltage sensitivity does not depend on lifetime. In other words, such a photoresistor can have high speed while maintaining a high voltage sensitivity. This feature of TSR photoresistors allows us to use them to make photodetector line arrays with high values of the parameters for optoelectronic systems with image scanning. TSR photoresistors can have long photosignal accumulation times, which along with a high photosensitivity makes them very promising candidates for use as elements of large-format staring arrays for the mid-IR, far-IR, and ultra-far-IR regions, with the highest possible threshold characteristics.

[1] V. V. Osipov, A. Yu. Selyakov, and M. Foygel, Fiz. Tekh. Poluprovodn. **32**, 221 (1998) [Semiconductors **32**, 201 (1998)].

[2] V. V. Osipov and A. Yu. Selyakov, in *Abstracts from the Proceedings 3rd All-Russia Conf. On Semiconductor Physics* [in Russian], RIIS FIAN, Moscow (1997), p. 81.

[3] V. V. Osipov, A. Yu. Selyakov, and M. Foygel, in *Proceedings of the 1997 Int. Semicond. Dev. Res. Symp.* (Charlottesville, USA, 1997), p. 277.

[4] V. V. Osipov, A. Yu. Selyakov, and M. Foygel, Phys. Status Solidi B **169**, 223 (1998).

[5] L. N. Neustroev, V. V. Osipov, and V. A. Kholodnov, Fiz. Tekh. Poluprovodn. **14**, 939 (1980) [Sov. Phys. Semicond. **14**, 553 (1980)].

[6] L. N. Neustroev and V. V. Osipov, Fiz. Tekh. Poluprovodn. **14**, 1186 (1980) [Sov. Phys. Semicond. **14**, 701 (1980)].

[7] L. N. Neustroev and V. V. Osipov, Microelectronics **9**, 99 (1980).

[8] L. N. Neustroev and V. V. Osipov, Fiz. Tekh. Poluprovodn. **15**, 1068 (1981) [Sov. Phys. Semicond. **15**, 615 (1981)].

[9] V. V. Osipov, A. Yu. Selyakov, and M. Foygel, Fiz. Tekh. Poluprovodn. **33**, 13 (1999) [Semiconductors **33**, 10 (1999)].

[10] *Photodetectors for the IR and Visible Bands* (Radio I Svyaz', Moscow, 1985) [a translation of: *Optical and Infrared Detectors,* edited by R. J. Keyes (Berlin, Heidelberg, N. Y., Springer Verlag, 1980)].

[11] R. L. Petritz, Proceedings IPE **47**, 1458 (1959).

[12] A. A. Drugova and V. V. Osipov, Fiz. Tekh. Poluprovodn. **15**, 2384 (1981) [Sov. Phys. Semicond. **15**, 1384 (1981)].

[13] A. van der Ziel, *Noise in Measurements* (Mir, Moscow, 1979).

Translated by Frank J. Crowne

A comparison of the temperature dependences of photoeffect quantum efficiencies in GaAs $p-n$ structures and Schottky diodes

Yu. A. Goldberg, O. V. Konstantinov, V. M. Lantratov, O. I. Obolensky, T. V. Petelina, E. A. Posse, and M. Z. Shvarts

A. F. Ioffe Physicotechnical Institute, Russian Academy of Sciences, 194223 St. Petersburg, Russia
(Submitted December 9, 1998; accepted for publication December 15, 1998)
Fiz. Tekh. Poluprovodn. **33**, 876–879 (July 1999)

A comparison is made of how the quantum efficiencies for photoelectric conversion in $p-n$- and $m-s$-structures based on GaAs depend on temperature. For photon energies less than or the same order as the width of the band gap, the temperature dependences of the $p-n$- and $m-s$- structures are similar. In the range of photon energies larger than the width of the band gap, the quantum efficiency of $p-n$- structures is temperature independent, whereas the quantum efficiency of $m-s$- structures exhibits a strong temperature dependence. A qualitative explanation of this phenomenon is given. © *1999 American Institute of Physics.* [S1063-7826(99)02307-8]

1. At this time, semiconductor devices based on GaAs are widely used as photodetectors. In the visible region of the spectrum, the most widely used devices are those based on $p-n$-structures (see, e.g., Ref. 1), while in the ultraviolet region Schottky diodes are used ($m-s$-structures) (see, e.g., Ref. 2).

In Ref. 3 we investigated how the quantum efficiencies for photoelectric conversion in GaAs Schottky diodes depend on temperature, in order to identify the photocurrent mechanism in these structures. We observed that the photocurrent increases with increasing temperature. This phenomenon was explained by the presence of imperfections in the surface layer. The combined analysis of the temperature and field dependences of the quantum efficiency of these structures given in Ref. 4 led us to conclude that these imperfections manifest themselves only in the photoelectric properties of the structure and cannot be identified as either shallow or deep impurity levels (charged or not). In the electric field of the space- charge layer they become traps and capture photoelectrons and photo-holes at the same time. We described the dependence of the quantum efficiency of photoelectric conversion on temperature within the framework of an activation model: with increasing temperature, a portion of the carriers liberated from traps contributes to the photocurrent.

In this paper we continue our investigations. Our goal is to compare the temperature dependences for quantum efficiency of $p-n$- and $m-s$- photodetectors based on GaAs. This comparison shows that when the photon energy $h\nu$ is larger than the band gap E_g, the photocurrent in $p-n$-structures based on GaAs shows no temperature dependence. Thus, we may conclude that the photosensitive layer near the $p-n$- junction contains no traps for photocarriers, whereas in $m-s$-structures their concentration is very large.

2. The solar-cell elements we investigated, which were GaAs $p-n$- junctions, had the following structure: n- GaAs (substrate)–Bragg reflector–n-GaAs- -p-GaAs–p-AlGaAs.

They were made by gas-phase epitaxy from metal-organic compounds (MOC-hydride epitaxy) at low pressure in a horizontal reactor.[5] The n- and p-GaAs layers were made by doping with donors and acceptors from silane and Cp$_2$Mg, and had the respective thicknesses $d=$ 1.6, 0.4 μm and carrier concentrations $n=10^{15}$ cm^{-3}, $p=10^{19}$ cm^{-3} at a temperature $T=$ 300 K. The p-Al$_{0.8}$Ga$_{0.2}$As layer consisted of an optical window of thickness $d=0.05\mu$m. The Bragg reflector consisted of 12 pairs of AlAs/GaAs layers. The area of the illuminated surface was 0.1258 cm^2. Figure 1 shows the spectrum of the quantum efficiency for photoelectric conversion (γ) for these $p-n$-structures in the range $h\nu=1.35-3.65$ eV.

The Schottky diodes had the structure n^+-GaAs (substrate)–n-GaAs– Ni (Ref. 3). The n^+-GaAs substrate had a thickness of 200 μm and was doped to an electron concentration of $\sim 10^{17}$ cm^{-3} ($T=$ 300 K), while the n-GaAs layer had a thickness of $\sim 10\mu$m and electron concentration of 10^{15} cm^{-3}. The barrier contact was made by chemical evaporation of nickel onto the epitaxial n-layer. The area of illuminated surface was 0.06 cm^2. Figure 2 shows the quantum efficiency spectrum for photoelectric conversion (γ) of these $m-s$-structures in the range $h\nu=$ 1–5 eV.

Our subject of investigation was the temperature dependence of the quantum efficiency for $p-n$- and $m-s$- structures based on GaAs in the temperature range $T=$ 80–360 K and in the photon energy range $h\nu=$ 1–5 eV. Our measurements were made in the short-circuit photocurrent regime, and the quantum efficiency was defined by the standard expression $\gamma=Ih\nu/P$, where I is the photocurrent (A), P is the incident light flux (W), and $h\nu$ is the incident photon energy (eV).

3. The results of these experiments are shown in Figs. 3 and 4, and reduce to the following.

3.1. In the range of photon energies $h\nu$ less than the width of the band gap E_g (for GaAs $E_g=1.425$ and 1.5 eV at
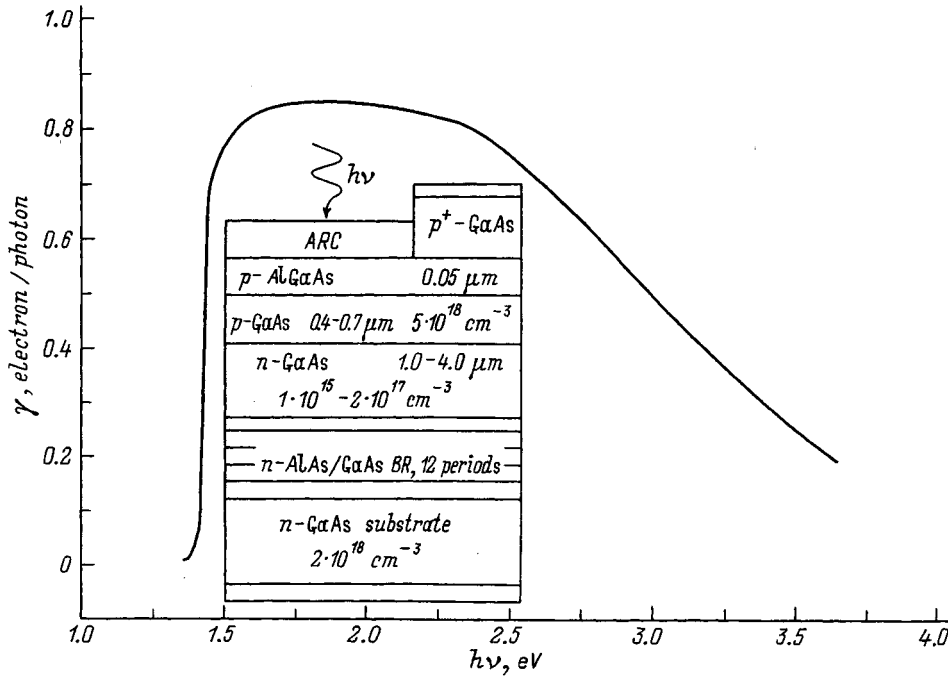
FIG. 1. Quantum efficiency for photo-electric conversion of $p-n$- structures based on GaAs versus photon energy. BR—Bragg reflector, ARC— antireflection coating.

300 and 100 K, respectively), the temperature dependences of the quantum efficiency γ for $p-n$- and $m-s$-structures were the same. With increasing temperature, the quantum efficiency increased because of a decrease in the width of the band gap E_g and an increase in the absorption of light.

We note that the photosensitivity of $m-s$-structures begins at lower photon energies (1.33 eV) than for $p-n$- structures (1.36 eV), which is explained by the presence of a ''Fowler'' segment of the photosensitivity curve for $m-s$-structures (emission of electrons from the metal and their ejection into the semiconductor).

3.2. In the range of photon energies $h\nu$ close to the band gap, the low-temperature quantum efficiency increased appreciably with increasing temperature for both types of structures when $E_g > h\nu$. At high temperatures, i.e., $E_g \simeq h\nu$ and $E_g < h\nu$, the quantum efficiency was nearly constant.

3.3. In the range of photon energies $h\nu$ above the band gap E_g, the temperature dependences of the quantum efficiencies γ for $p-n$- and $m-s$-structures are quite different.

For $p-n$-structures, the quantum efficiency γ is practically temperature-independent, whereas for $m-s$-structures the quantum efficiency increases with increasing tempera-
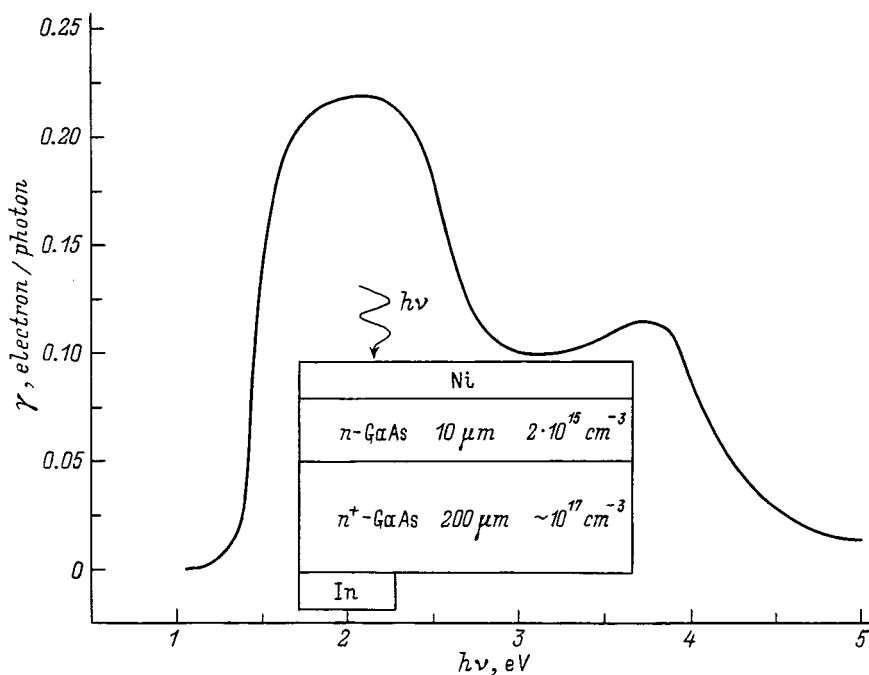

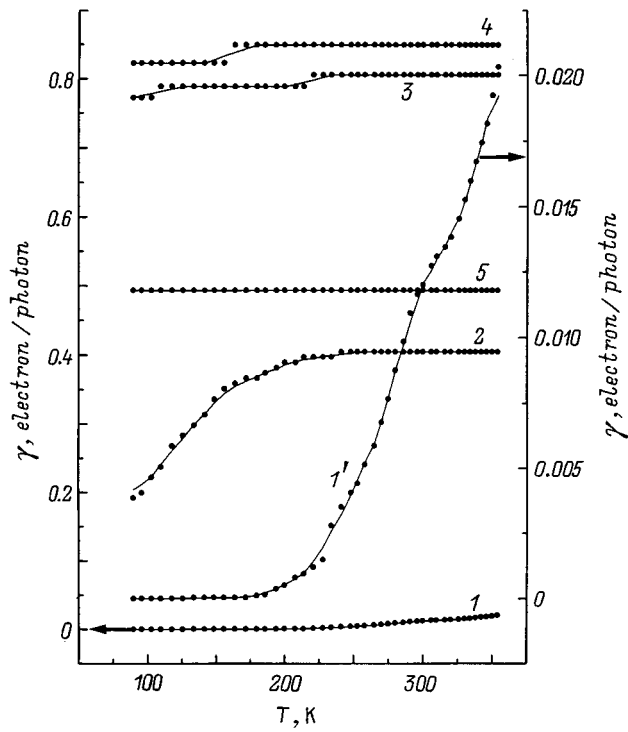FIG. 2. Quantum efficiency for photo-electric conversion of $m-s$- structures based on GaAs versus photon energy.

FIG. 3. Temperature dependence of the quantum efficiency for photoelectric conversion of $p-n$-structures based on GaAs for several photon energies $h\nu$, eV: *1, 1'* — 1.36, *2* — 1.42, *3* — 1.54, *4* — 1.77, *5* — 3.00. Curve *1'* — right-hand scale; other curves — the left-hand scale.

ture. At high photon energies and high temperatures, the function $\gamma = \gamma(T)$ has a tendency to saturate.

In the range $h\nu > 2.5$ eV the photosensitivity of $p-n$-structures decreases. This decrease is attributable to a strong absorption of light near the surface. In contrast, $m-s$-structures exhibit photosensitivity even at very high photon energies ($h\nu \simeq 5$ eV).

4. The main difference in the temperature dependences of the quantum efficiencies for GaAs $p-n$ structures and Schottky diodes lies in the fact that in the region of intrinsic absorption of the semiconductor the quantum efficiency is temperature-independent for $p-n$- structures but increases with temperature for Schottky diodes.

We claim that this difference is connected with imperfections that always appear in the surface region of a semiconductor. In the space-charge layer, i.e., in the presence of an electric field, these imperfections can act as traps for charge carriers which are capable of capturing electrons and holes. With increasing temperature, the charge carriers can be liberated and make a contribution to the photocurrent.
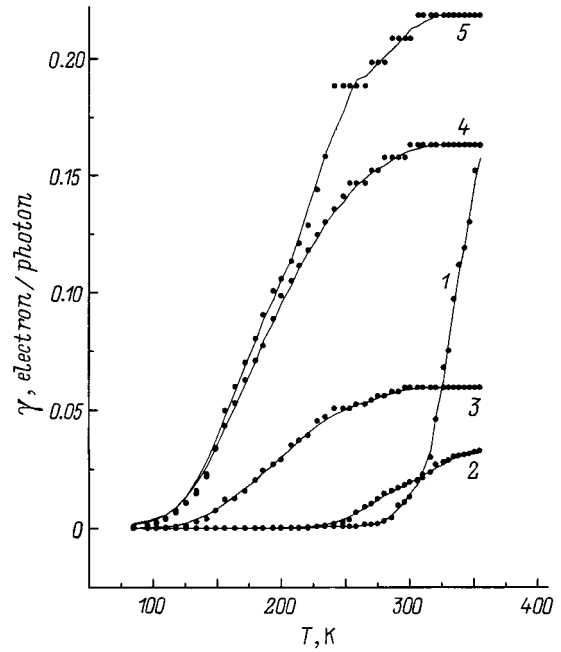

FIG. 4. Temperature dependence of the quantum efficiency for photoelectric conversion of $m-s$-structures based on GaAs for several photon energies $h\nu$, eV: *1, 1'* — 1.33, *2* — 1.36, *3* —1.42, *4* — 1.54, *5* — 1.77.

Since in Schottky diodes the space-charge layer is in the skin layer, this effect is especially characteristic of Schottky diodes. In $p-n$-structures the space-charge layer is deep in the crystal, and the effect of surface traps is not large. Therefore, the quantum efficiency is nearly independent of the temperature.

Thus, $p-n$-structures based on GaAs have a higher temperature stability than $m-s$- structures, whereas Schottky diodes have a higher photosensitivity in the short- wavelength region of the spectrum than $p-n$-structures.

[1] V. M. Andreev, V. V. Komin, I. V. Kochnev, V. M. Lantratov, and M. Z. Shvarts, *Proceedings of the First World Conference on Photovoltaic Energy Conversion* (Hawaii, 1994), p. 1824.

[2] Yu. A. Goldberg, O. V. Konstantinov, E. A. Posse, and B. V. Tsarenkov, Sens. Actuators A A **58**, 121 (1997).

[3] Yu. A. Gol'dberg, O. V. Konstantinov, O. I. Obolenskiĭ, E. A. Posse, and B. V. Tsarenkov, Fiz. Tekh. Poluprovodn. **31**, 563 (1997) [Semiconductors **31**, 473 (1997)].

[4] Yu. A. Goldberg, O. V. Konstantinov, O. I. Obolensky, T. V. Petelina, and E. A. Posse, J. Phys.: Condens. Matter **10** (1999) [to be published].

[5] M. Z. Shvarts, O. I. Chosta, I. V. Kochnev, and V. M. Lantratov, *Proceedings of the Fifth European Space Power Conf. (ESASP-416)* (Tarragona, 1998), p. 513.

Translated by Frank J. Crowne

Fabrication of discrete $p-n$ junctions separated by an insulating layer using direct wafer bonding

E. G. Guk, B. G. Podlaskin, N. A. Tokranova, V. B. Voronkov, and V. A. Kozlov

A. F. Ioffe Physicotechnical Institute, Russian Academy of Sciences, 194021 St. Petersburg, Russia

Three types of fabrication cycle based on the use of direct wafer bonding are developed for making pairs of discrete $p-n$-junctions separated by an insulating layer. The forward and reverse branches of the I–V characteristics of the resulting diodes are investigated. For all three fabrication cycles, the differential resistance of the forward branch of the discrete $p-n$- junctions is $\sim 0.01\,\Omega$, the reverse breakdown is ~ 400 V, and the width of the aperture region for the back-to-back diodes is 0.22 V. Taken as a whole, these data, along with the high integrated photosensitivity of the diodes, indicate that direct wafer bonding produces no oxide barrier between the p- and n-regions and forms high-quality interfaces. © *1999 American Institute of Physics.* [S1063-7826(99)02407-2]

The method of direct wafer bonding (DWB) was developed for making various types of interfaces, e.g., Si–Si, Si–SiO$_2$, etc., by creating direct covalent bonds between atoms of the materials being bonded. This is done by compressing the materials together at high temperatures.[1–3] DWB is used most often to make silicon devices on an insulating substrate with electrical parameters that are characteristic of single-crystal material, the so-called SOI (silicon on insulator) technology.[4] In this case some very unique types of interfaces can be created: from the joining of oxidized and unoxidized Si films with subsequent fabrication on the latter of a device with required topology to the use of a silicon film with prefabricated structures on its surface, e.g., transistor mesas with $p-n$-junctions perpendicular or parallel to the interface, as the second substrate.[5–7]

The fabrication of $p-n$-junctions (i.e., to form Si–Si interfaces) by DWB has until now involved only the bonding of pure silicon films with different conductivity types. Thus, the authors of a number of papers have described technologies for simple and rapid creation of large-area power silicon diode structures, created by bonding perfect single-crystal layers with prespecified electrical parameters. It has been shown that the electrical characteristics of such structures are not inferior to those of analogous high-power semiconductor devices made by the diffusion method, and that with regard to breakdown uniformity over the area of the film they are better than their traditional analogs.[3,8,9]

However, when it comes to fabricating separate elements with specific topologies, bonding has been used only to create contact layers, i.e., $p-p^+$ and $n-n^+$ boundaries,[10,11] although the most important task is clearly to create discrete $p-n$-junctions by DWB. A solution to this problem would allow us not only to avoid the energy-consuming and ecologically contaminating SOI technology,[12] but also to improve the parameters of traditional semiconductor devices. Moreover, DWB technology opens up the possibility of moving to a new level of complexity, allowing us to "construct" three-dimensional integration schemes with active vertical connection between layers while preserving electrical characteristics corresponding to single-crystal material within the built-in elements.

As an example of the use of discrete $p-n$- junctions, we turn to photodiode matrices, in particular, multielement "multiscan" photoreceivers,[13] whose principles of operation are based on the properties of pairs of back-to-back photodiodes.

The traditional planar technology for fabricating a multiscan uses an SOI structure to isolate the back-to-back diodes of each pair from one another (Figs. 1a and 1b). The equivalent circuit of the multiscan is shown in Fig. 1c. However, there are other approaches to realizing this equivalent circuit without using SOI technology, approaches that do not depend on the use a planar structure, which lead to high-quality $p-n$-junctions with high breakdown voltage and narrow knee regions of the I–V characteristics. One possible "three-dimensional" realization of a back-to-back photodiode structure, made using DWB, is shown in Fig. 2.

From Fig. 2 it is clear that the key technological step in fabricating such a structure is the creation of a "columnar" interface layer consisting of discrete $p-n$-junctions separated by insulating layers (Fig. 3).

The goal of this paper is to develop a basic fabrication cycle using direct wafer bonding that leads to the creation of isolated $p-n$-junctions. By repeating this cycle many times in various combinations, we can create multilayer semiconductor structures with discrete elements incorporated into the bulk.

This technological cycle is based on two key operations: direct wafer bonding and precision exposure, i.e., removing a portion of the profiled silicon film until the regions separating the discrete $p-n$- junctions are exposed. The first operation imposes strict requirements on the quality of the surfaces to be bonded, and impacts all the technological operations used to obtain these surfaces prior to the bonding.
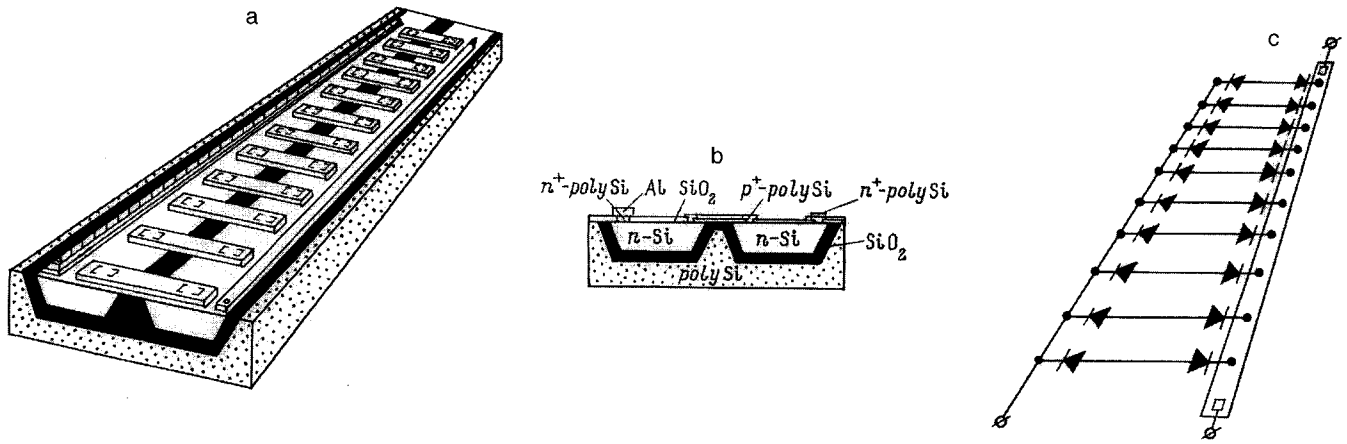
FIG. 1. a—Overall view of a multiscan photodetector; b— cross section of the multiscan structure; c—equivalent circuit of the multiscan; polySi denotes polycrystalline silicon.

The amount of effort required to implement the second operation is dictated by the choice of a method for precisely generating the profiled ''columnar'' layer. It is necessary to strictly maintain a prespecified height of the ''columns,'' which form part of the diodes, not only to obtain specified electric parameters of these structures, but also for subsequent DWB operation. In this case not only is the absolute value of the column height important, but also the scatter in heights over the area of the film. The proposed use of in situ fabricated diodes as cells of a multielement photodiode matrix makes uniformity with respect to height especially critical, since such devices require small scatter in the parameters of the $p-n$- junctions over the entire device structure.

We tested several technological approaches to making structures with discrete $p-n$- junctions separated by insulating layers in order to choose the best one. Since the structure we want to make is analogous to a photoreceiver, we faced the problem of making an asymmetric $p-n$-junction. For this two films were used, with carrier concentrations that differed by five orders of magnitude (both were industrial-grade mirror-polished films: a low-resistance film with p-type conductivity, $\langle 100 \rangle$ orientation, diameter 60 mm, and thickness 350 μm, and a high-resistance KEF-7.5 film with n-type conductivity, $\langle 100 \rangle$ orientation, diameter 60 mm, and thickness 500 μm).

The surface profiling was done on the films with p-type conductivity. In order to comply with our ultimate structural design (Fig. 2), the height of the profiled layer (the etched-

out columns) was kept no less than 2 μm, so as to avoid diffusive coupling between $p-n$-junctions of each pair when DWB is used to make the back-to- back diodes, but no more than 10 μm in order to preserve the mechanical strength of the structure. In all cases the columns had a diameter of 250 μm, with a distance between them of 5 mm.

High-temperature DWB was then used to bond the profiled layer of silicon with p-type conductivity (on the etched side) to a film of pure silicon with n-type conductivity.

Just before the bonding, all the films were etched in hydrofluoric acid, and then subjected to a standard cycle of acid-peroxide washes, at the final stage of which they were processed in a 2% water solution of HF with subsequent hydrophilization of the surface in a solution of NH_4OH: H_2O_2: H_2O (0.05: 1: 5) and then washed in deionized water with a resistivity of $\sim$ 18 M$\Omega\cdot$cm. The films were also joined together while in the deionized water, according to the method described in Ref. 14, which obviated the need for a dust-free atmosphere, and then subjected to preliminary thermal processing to remove moisture and to bond the films. The high-temperature thermal processing of the joined pairs was carried out in air at 1200 °C for one hour without applying external pressure.

In order to study the electrical parameters of the resulting structures, we made ohmic contacts (to the n-type silicon by chemical nickel plating, to the p-type silicon by brazed-in deposited aluminum).

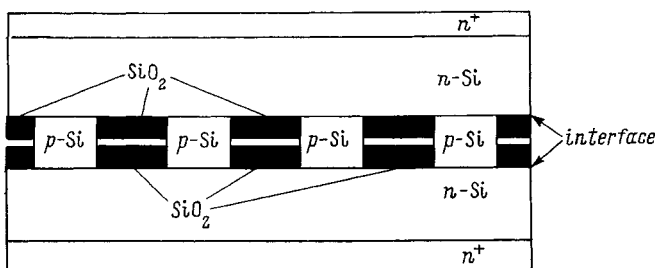The type-I fabrication cycle specified etching-out of col-

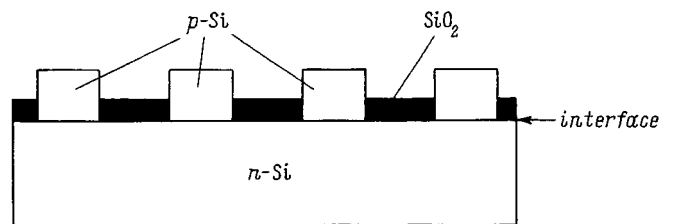FIG. 2. One type of possible realization of a multiscan using DWB.

FIG. 3. Basic structure, including an interface layer consisting of discrete $p-n$-junctions separated by insulating SiO_2 layers.

umns with height 10 μm on a low-resistance film of *p*-type silicon (KDB-0.005). After the growth operation, a portion of the profiled film was removed by precision grinding and polishing of the silicon until the region separating the $p-n$-junctions was exposed.

In the type-II cycle, we decided to replace the technically most difficult operation of polishing with etching down to a stop.

Using the dependence of the etch rate for silicon on the concentration of doping impurities is common practice in semiconductor technology, especially in making membranes.[15] Thus, for example, in Ref. 16 an etching method, which makes use of a stop layer consisting of a boron-diffused layer with concentration $\sim 10^{20}$ cm^{-3}, is described. Because the diffusion front is with high accuracy parallel to the film surface, the authors were able to obtain uniform layers of silicon with thicknesses of a few microns.

In the type-II cycle, in order to use the stop-layer etching technique we needed layers of *p*-type silicon with an initial boron concentration of $\sim 10^{16}$ cm^{-3} (KDB-1). First, columns were formed in these layers with a height of 10 μm, followed by oxidation and photolithography. Boron was then diffused into them at 1250 °C in air for one hour, from a polymer source deposited on the surface[17] with a high boron concentration, generating a surface impurity concentration of $\sim 10^{21}$ cm^{-3}. At the end of the anneal, the diffusion layer was buried at a depth $x_j \sim 10 \mu$m.

However, there are some problem with bonding silicon films containing diffusion layers with high levels of doping by shallow impurities, because the diffusion degrades the quality of the surface of the silicon films. The authors of Ref. 18 demonstrated that direct wafer bonding of films with a diffused *p*- or *n*-layer made in an oxidizing medium and having a high surface concentration of impurities is possible if after the diffusion the films are oxidized with subsequent removal of the oxide. However, since its use results in surface boron concentrations that do not exceed 10^{20} cm^{-3}, this method cannot solve our problem. Since for us what is important is not so much the concentration of boron in the skin layer that forms during growth of the interface as its value at a depth of $\sim 10 \mu$m, we invesgated the possibility of removing the defective surface layer by polishing.

The authors of Ref. 19 attempted to bond silicon films with p^+-n-junctions at a depth of 100 μm after Ga diffusion (in an inert atmosphere) or combined diffusion of B and Al (in air). After diffusion, these films were subjected to chemical-mechanical polishing, because their surfaces were eroded. The authors found that they could bond only those films previously subjected to Ga diffusion. Polishing the surface after boron diffusion with aluminum revealed microroughness which prevented bonding of the film. Obviously, the reason why the microroughness was preserved was the chemical-mechanical character of the polishing used, which is accompanied by unavoidable selective etching along defects. For this reason, we used only mechanical polishing of the profiled surfaces of our films, removing $\sim 1 \mu$m of the surface strongly boron-doped layer as a result of this operation.
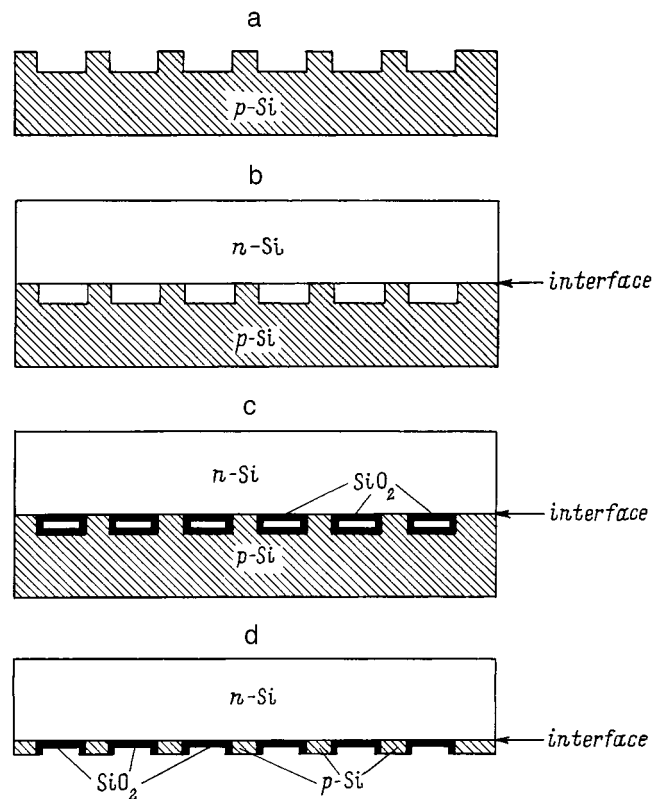
After DWB and a preliminary removal of 200 μm of the

FIG. 4. Fabrication cycle I for making discrete $p-n$-junctions separated by an insulating layer using DWB. a—creation of a profile (columns) on an initial industrially polished film of *p*-type silicon using photolithography with chemical etching; b—high-temperature (1250 °C for 1 hour) direct wafer bonding of the first film (on the etched side) to a pure polished silicon film; c— oxidation in dry oxygen at 1100 °C for 1 hour with subsequent oxidation in water vapor at 1250 °C for 4 hours in order to form the required insulating layer; d— mechanical grinding and subsequent precision polishing in order to remove most of the silicon *p*-layer until the cavities separating discrete $p-n$-junctions are exposed.

structure from the *p*-silicon film, the structure was subjected to processing in a hot KOH + isopropanol + water etch, whose action ceased when the *p*-region was reached.[16]

In our third fabrication cycle, we used SiO$_2$ as the stop layer for the operation of precision polishing. To this end, columns were fabricated on an original *p*-type silicon layer (KDB–0.005) by etching, whose height was 2 μm, and the spacings between them were overgrown by a thermal oxide with thickness 1.8 μm. The oxide was then etched away from the columns themselves after photolithography. Chemical-mechanical polishing, after removing the silicon lying on top of the oxide, was stopped by the oxide layer. The isolated $p-n$-junctions were then exposed by preliminary mechanical polishing, with a final precision polishing down to the oxide stop layer.

Figures 4–6 illustrate schematically the three different fabrication cycles for making discrete $p-n$-junctions separated by insulating layers with the help of DWB.

Infrared photometry is a standard method for monitoring the continuity of bonding.[20] In our case, however, this method could give only rough results due to the high concentration of shallow impurities in the *p*-silicon, which causes intense absorption in the IR region. However, the
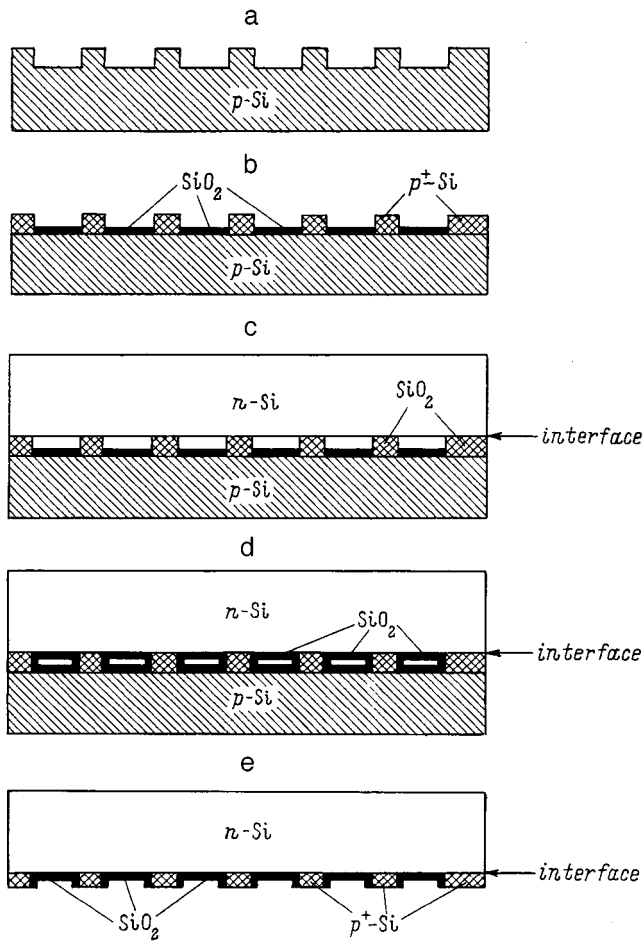
FIG. 5. Fabrication cycle II for making discrete $p-n$-junctions separated by isolating layers using DWB. a—creation of a profile (columns) on an initial industrially polished p-type silicon layer using photolithography with chemical etching; b—diffusion of boron directly into the columns after preliminary oxidation and photolithography at 1250 °C for 1 hour; c—high-temperature (1250 °C for 1 hour) direct wafer bonding of the first film (on the etched side) of a pure polished silicon film; d—oxidation in dry oxygen at 1100 °C for 1 hour with subsequent oxidation in water vapor at 1250 °C for 4 hours in order to create the required insulating layer; e—preliminary removal of 200 μm of the p-silicon layer by mechanical polishing and subsequent etching of the p-layer down to its stop layer in order to expose the cavities separating the discrete $p-n$ junctions.

FIG. 6. Fabrication cycle III for making discrete $p-n$-junctions separated by an insulating layer using DWB. a—creation of a profile (columns) on an initial industrially polished film of p-type silicon using photolithography with chemical etching; b—oxidation in dry oxygen at 1100 °C in order to fill the gaps between columns with a thermal oxide having a thickness of 1.8 μm; c—removal of oxide from the columns; d—chemical-mechanical polishing which removes the silicon protruding above the oxide and the remaining layer of oxide; e—high-temperature (1250 °C for 1 hour) direct wafer bonding of the first layer (on the etched side) to a pure polished silicon film; f—exposure of the $p-n$ junctions by preliminary mechanical grinding completed by precision polishing down to the oxide stop layer.

grinding and polishing operations used to remove the layer of p-silicon, by creating strong shear loads at the interface, allowed us to estimate its mechanical strength and thereby the quality of the bonding. In the course of grinding all the samples, and also when the structures were polished in fabrication cycles I and III or etched in cycle II, partial destruction of the unbonded columns took place. Cycle I had the smallest area ($\sim$ 15%) occupied by damaged regions, while in the two other cycles the area of the defective regions was as large as $\sim$ 40–45%. Because a characteristic feature of the fabrication process in these latter cycles (II and III) is polishing of the p-type silicon from the profiled side before the DWB operation, we can assume that our use of polishing lowered the quality of the surface over a considerable part of the silicon film. However, the results obtained after using fabrication cycle 2 are of interest in their own right, in that we have demonstrated for the first time that direct wafer
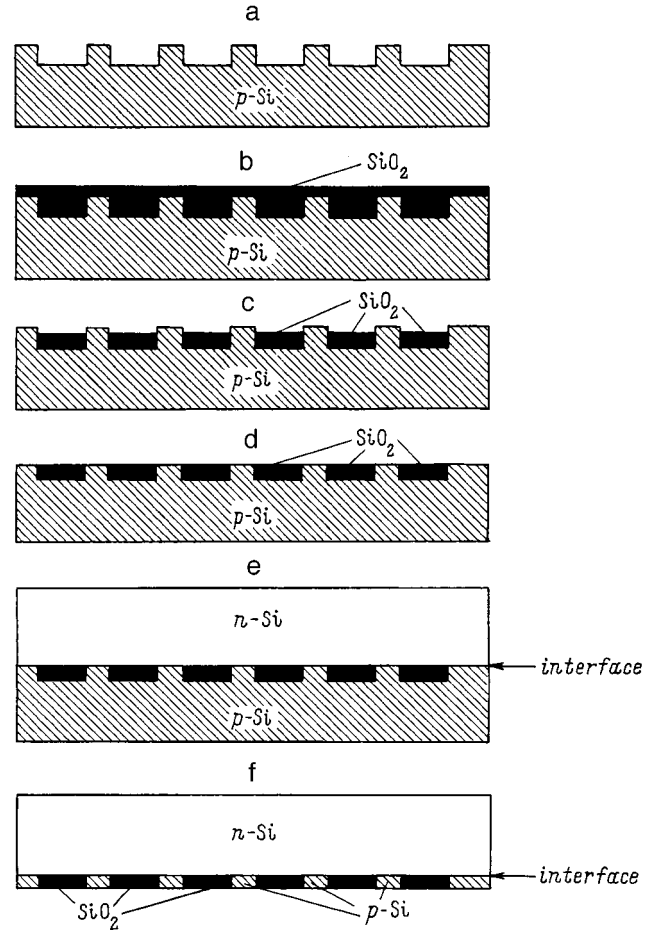
bonding of surfaces can be used after mechanical polishing. It seems to us that further experiments with the grain size of the polishing paste and with polishing regimes should allow us to increase the high-quality area.

It is also noteworthy that exposure of the profiled surface by etching with a stop layer (cycle III) ensured the most uniform column height ($\pm$ 0.3 μm), whereas the scatter in heights generated by cycles I and II were $\pm$ 1.5 and $\pm$0.8 μm, respectively.

The most important conclusions about the quality of the $p-n$-junctions obtained during these growth processes were arrived at by studying the forward (Fig. 7) and reverse branches of the current-voltage characteristics of the resulting diodes. For all three basic fabrication cycles, the differential resistance of the forward branch of the best $p-n$-junctions was $\sim$0.01 Ω, indicating high growth quality. As for the reverse branch of the current-voltage characteristics, the leakage current did not exceed 10 μA at a re-
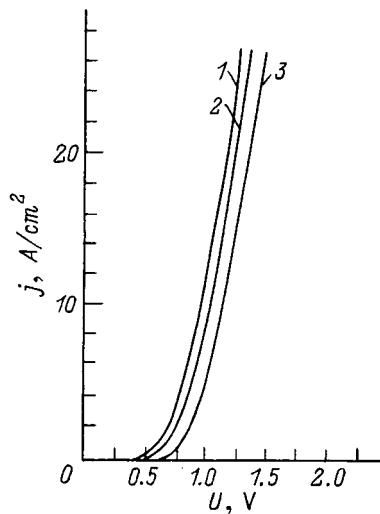
FIG. 7. Forward branch of the current-voltage ($j-U$) characteristics of discrete $p-n$-junctions separated by an insulating layer. *1−3* corresponds to fabrication types I–III.
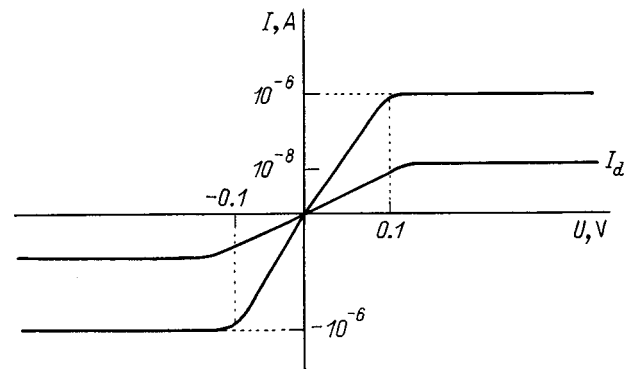

FIG. 8. Current-voltage ($I-U$) characteristic of two diodes obtained by direct wafer bonding, connected back-to-back. I_d is the dark current.

verse bias of 130 V, and the breakdown voltage had a value of $\sim$ 400 V for all three variants. However, the number of such $p-n$-junctions without an oxide barrier between the *p*- and *n*-regions was different for the different cycles. Thus, in the first cycle, the number of $p-n$-junctions with such characteristics was around 60%, in the second around 30%, and in the third around 20%.

For back-to-back diodes used as elementary cells in photodiode matrices and multiscans, which have unipolar I–V characteristics, an important figure of merit is the width of the transition region of the I–V characteristic between the two regions of current saturation (the aperture). In the aperture region the photodiodes switch from the shorted state to the open state and conversely. The main property of this portion of the I–V characteristics is the width of the transition interval, which in multiscan operation determines the spatial width of the transition zone within which the photocurrent of the $p-n$-junctions changes sign.[21] The width of the aperture in the I–V characteristics of a diode-diode cell is the most important parameter, since it determines such characteristics of the photodetector as its spatial resolution in the scanning regime, coordinates sensitivity in the positioning regime, and others. When an optical signal falls in the ''aperture zone'' of the photodetector layers of the device, a decrease in the conversion of the optical signal to electric current is observed. The possibility of narrowing the aperture depends above all on the possibility of applying a sufficiently high voltage to the $p-n$-junction, since the working aperture of the multiscan decreases its spatial value with increasing applied voltage.

Figure 8 shows experimental I–V characteristics for back-to-back $p-n$- junctions for the three fabrication cycles used to make them. It is clear that the width of the aperture is 0.22 V. A theoretical value of the half-width of the voltage aperture can be obtained from an expression for the I–V characteristics of an isolated pair of back-to-back diodes, based on the Shockley equation for an ideal silicon diode,[22]

and comes to $8kT/q$. Assuming an ideal $p-n$-junction, the computed value of the total width of the aperture at a temperature of 300 K comes to 0.21 V, which nearly coincides with the experimental values we obtained for all the fabrication types, indicating strongly that the $p-n$-junctions we fabricated are ''ideal.''

During operation, a multiscan made using SOI technology has a spatial value of the aperture of $\sim$400 μm, determined largely by the value of its applied voltage, here 10 V. In contrast, the high breakdown voltage of our devices allows us to operate at values of the applied voltage above 100 V, which can lower the spatial value of the aperture to 40 μm or less.

Furthermore, the discrete $p-n$-junctions separated by insulating layer that we have fabricated are distinguished by high photosensitivity, indicating the absence of oxide barriers between the *p*- and *n*- regions, and a low dark current (at 30 V the dark current did not exceed 5×10^{-8} A for all the cycles). The measured integrated photosensitivity for fabrication cycles I and III was 0.3 A/W, while for variant II it was 0.25 A/W.

Thus, by estimating the electrical characteristics of isolated diodes made by our processes, we have confirmed the effectiveness of DWB in making high-quality $p-n$-junctions in all three fabrication cycles. However, in choosing a fabrication cycle we must take into account that cycle I is the simplest, that it contains the lowest number of operations, and that it yields the highest percentage of bonded diode structures for the lowest height uniformity of the profiled layer. This cycle can be effectively used when strict uniformity of the parameters is not required. For problems where the requirements on uniformity of the profiled layer are strict, we recommend fabrication cycle II, whereas cycle III will find application only for solving a restricted set of problems requiring complete filling of the volume within the bonded structure by a SiO₂ layer.

[1] J. B. Lasky, Appl. Phys. Lett. **48**, 78 (1986).
[2] M. Shimbo, K. Furukawa, K. Fukuda, and K. Tanzava, J. Appl. Phys. **50**, 2987 (1986).
[3] S. Bengtsson, J. Electron. Mater. **21**, 841 (1992).
[4] H. Gotoi, J. de Phys. **49**, 4 (1988).
[5] B. Mazhari, S. Cristoloveanu, D. E. Ioannou, and A. L. Caviglia, IEEE Trans. Electron Devices **ED-38**, 1289 (1991).

[6] K. Watanabe, T. Hashimoto, M. Yoshida, M. Usami, Y. Sakai, and T. Ikeda, *Ext. Abstr. Electrochem. Soc. Fall Mtg.* (1991) 91-2, p. 774.

[7] A. L. Caviglia, R. C. Potter, and L. J. West, IEEE Electron. Dev. Lett. **EDL-12**, 26 (1991).

[8] R. Wilson, H. S. Gamble, and S. J. N. Mitchell, *Ext. Abstr. Electrochem. Soc. Fall Mtg.* (1991) 91-2, p. 742.

[9] V. M. Volle, V. B. Voronkov, I. V. Grekhov, and V. A. Kozlov, Pis'ma Zh. Tekh. Fiz. **16**, 6 (1990) [Sov. Tech. Phys. Lett. **16**, 602 (1990)].

[10] I. Rhee, F. M. Casparini, A. Petrou, and D. J. Bishiop, Rev. Sci. Instrum. **61**, 1528 (1990).

[11] K. Tsuruta, M. Katada, S. Fujino, and T. Hattori, *IEICE Trans. Electron.* (1992) E75-C, p. 1459.

[12] N. A. Bryukhno, E. M. Zharkovskiĭ, Yu. A. Kontsevoĭ, and Yu. G. Sakharov, *Electrical Engineering Reviews. Ser. 3: Microelectronics* **4** (1987).

[13] K. F. Berkovskaya, N. V. Kirillova, B. G. Podlaskin, V. M. Stolovitskiĭ, and N. A. Tokranova, *Achievements in Science and Engineering* [in Russian], VIMI, Moscow (1992), Vol. 2, p. 22.

[14] I. V. Grekhov, V. A. Kozlov, V. M. Volle, and V. B. Voronkov, *Best of Soviet Semicond. Phys. and Technol. 1989– 1990*, edited by M. Levinstein and M. Shur (World Scientific, 1995) p. 597.

[15] K. Sangval, *Etching of Crystals: Theory, Experiment, Applications* (Mir, Moscow, 1990), ch. 11, p. 426.

[16] G. I. Kuhn and C. J. Rhee, J. Electrochem. Soc. **120**, 1563 (1973).

[17] E. G. Guk, A. V. El'tsov, V. B. Shuman, and T. A. Yurre, *Photoresists– Diffusants in Semiconductor Technology* (Nauka, Leningrad, 1984), p. 76.

[18] V. B. Voronkov, E. G. Guk, V. A. Kozlov, and V. B. Shuman, Pis'ma Zh. Tekh. Fiz. **24**, 1 (1998) [Tech. Phys. Lett. **24**, 3 (1998)].

[19] V. A. Kozlov, V. K. Eremin, I. L. Shulpina, V. B. Voronkov, A. M. Ivanov, V. V. Eliseyev, and V. V. Chibirkin, in *High Purity Silicon IV*, edited by C. L. Claeys, P. Rai-Choudhury, P. Stallhofer, and J. E. Maurits [*The Electrochem. Soc. Ser.* (Pennington, 1996) v. PV 96-13, p. 369].

[20] R. D. Black, S. D. Arthur, R. S. Gilmore *et al.*, J. Appl. Phys. **63**, 2773 (1988).

[21] B. G. Podlaskin, E. P. Romanova, and V. S. Yuferev, Zh. Éksp. Teor. Fiz. **62**, 126 (1992) [Sov. Phys. JETP **37**, 303 (1992)].

[22] V. F. Zolotarev, *Vacuumless Analogues of Television Tubes* (Energiya, Moscow, 1972).

Translated by Frank J. Crowne

Polarization selection in VCSELs due to current carrier heating

B. S. Ryvkin and A. M. Georgievskiĭ

A. F. Ioffe Physicotechnical Institute, Russian Academy of Sciences, 194021 St. Petersburg, Russia

The problem of polarization switching of light from a vertical cavity surface emitting laser (VCSEL) is discussed. It is shown that heating of holes in the *p*-type distributed Bragg reflector and of electrons and holes in the quantum wells of the active region lead to switching of the polarization of the VCSEL. The model developed here makes it possible to explain the results of experiments on switching of the polarization of VCSELs at fixed active region temperatures. © *1999 American Institute of Physics.* [S1063-7826(99)02507-7]

INTRODUCTION

The polarization characteristics of light from vertical cavity surface emitting lasers (VCSEL's) differs significantly from the corresponding characteristics of ''end- fire'' semiconductor lasers.[1–5] This is attributable to the cylindrical symmetry of the VCSEL geometry, in which the directions of the light and the carrier injection are both perpendicular to the plane of the active layer and directed along the axis of cylindrical symmetry.

Usually, VCSEL's are grown on a substrate of *n*-GaAs with (100) orientation, i.e., the emission and carrier injection are directed along one of the cubic [100] axes. Nevertheless, it has been shown experimentally that proton-implanted VSCEL's (Fig. 1) generate linearly polarized light. The direction of polarization of this light in the (100) plane usually coincides with one of the equivalent crystallographic directions [110] or [1$\bar{1}$0]. It has also been shown that for injected currents above threshold by 10–50 % (i.e., in the range where the fundamental Gaussian transverse mode forms) the initial polarization of the light can switch to the orthogonal direction. The frequencies of light in the orthogonal polarizations **1** and **2** differ by a small amount $\Delta f = $ 1–40 GHz. The corresponding difference in wavelength of the two orthogonal polarizations is associated with birefringence in the resonator of the VSCEL, which is caused by stresses and strains unintentionally introduced during the fabrication process,[6] and (or) the electrooptic effect associated with internal electric fields in the VSCEL.[7] When birefringence is present, the refraction indices n_1 and n_2 for the two orthogonal polarizations are slightly different. Thus, light with two different polarizations and slightly different wavelengths (λ_1 and λ_2) can in principle be generated in the VSCEL resonator.

Current analyses of the polarization properties of VSCEL's assume that while current injection pulses pass through the VSCEL, the temperatures of holes and electrons in the passive and active regions coincide with the lattice temperature. It is also assumed that the gain in the VSCEL is wavelength selective, while losses are not selective, in which case the polarization of the VSCEL emission is determined only by the gain selectivity.

Our goal in this paper is to show that heating of electrons and holes relative to the lattice in the active and passive regions of a VSCEL can lead to rapid switching of the polarization of the VSCEL emission. We will also show that wavelength selectivity of the losses due to absorption by free carriers and holes in the Bragg reflector can be important in determining the polarization of VSCEL light. A qualitative comparison of the model developed here with the results of experiments involving rapid switching of the polarization of VSCEL light with the active region held at constant temperature[8] shows that our mechanism could be responsible for the polarization switching observed in Ref. 8.

1. SELECTIVITY OF LOSSES IN VSCELS

The polarization of VSCEL light depends on the gain ratio (g_1 and g_2) for the two orthogonal polarizations and on the loss ratio (α_1 and α_2) for these polarizations. The terms ''gain'' and ''loss'' are understood to mean mode gain and mode loss. This distinction is relevant because differences in
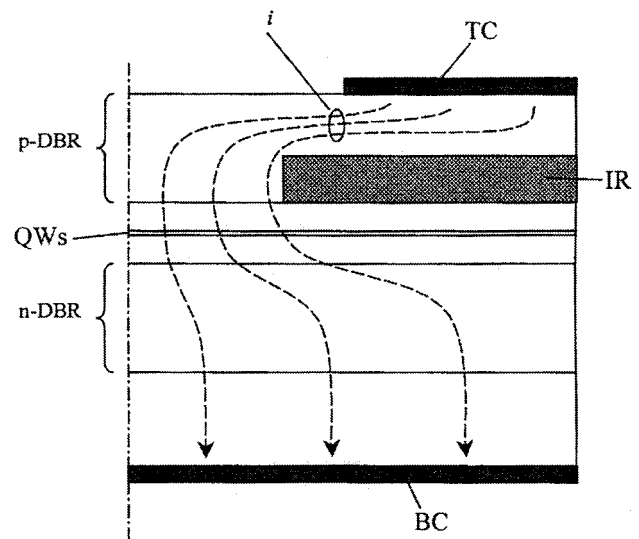

FIG. 1. Schematic diagram of a quantum well VSCEL; *p*-DBR, *n*-DBR denote the distributed Bragg reflectors; QW the quantum wells in the active region; IR are the implanted regions; tc, bc are the top and bottom contacts.

the field distributions of modes with different polarizations (and slightly different wavelengths λ_1 and λ_2) in the plane of the active layer can in certain cases turn out to affect the polarization properties of a VSCEL significantly.[5,9] In what follows, however, we assume that in our case the difference in field distribution of these modes in the plane of the active layer does not significantly affect the polarization properties of the VSCEL, i.e., we will ignore it. It is also known that the difference in reflectivity of modes with two orthogonal polarizations by multilayer semiconductor Bragg reflectors in which absorption is absent can be ignored. Thus, we will assume that the behavior of the gains g_1 and g_2 in the material of the active layer and the loss coefficients for light α_1 and α_2 in the passive portion of the VSCEL determines its polarization properties.

Figure 2a shows schematically the dependence of the gain on photon energy $g(\hbar\omega)$ for the active region of a heterojunction laser. Suppose that the losses of the VSCEL are independent of photon energy. In this case the polarization of the light (**1** or **2**) will be determined by the position of the emission lines $\hbar\omega_1$ and $\hbar\omega_2$ with respect to the maximum of the gain line shape $g(\hbar\omega)$. If the gain line shape shifts with respect to energy, due to a shift in the band edge brought on by changes in the temperature of the active region as the injection current changes, the polarization of the VSCEL can switch to the orthogonal direction.[2]

Figure 2b shows schematically the dependence of the losses on photon energy $\alpha_l(\hbar\omega)$ when light is absorbed in the passive part of a heterojunction laser and $(E_g < E_g')$ $> \hbar\omega$, where E_g and E_g' are the band gap widths in the active region and the very narrow-gap regions located in the passive portions of the heterojunction laser, respectively. When $\hbar\omega \ll E_g'$, $\alpha_l(\hbar\omega)$ is determined by free-carrier absorption of the light, which decreases with increasing $\hbar\omega$. For $\hbar\omega \lesssim E_g'$ the absorption increases exponentially as $\hbar\omega$ approaches E_g' (the Urbach rule). Let the absorption of light occur primarily in the Bragg reflectors of the VSCEL. In this case the optical loss function $\alpha_l(\hbar\omega)$ due to the decrease in reflection coefficient from the reflectors as the absorption in them increases will schematically have the same form as shown in Fig. 2b [see Eq. (4) of this paper]. Taking into account the dependence $\alpha_l(\hbar\omega)$, a steady-state oscillation regime with predominantly polarization **2** will occur if the following condition holds when $G_0 = \alpha_{l0}$:

$$\frac{G_2}{\alpha_{l2}} > \frac{G_1}{\alpha_{l1}} \quad or \quad \frac{g_2}{g_1} > \frac{\alpha_{l2}}{\alpha_{l1}}, \quad or \quad \frac{dG}{d(\hbar\omega)}\bigg|_{\hbar\omega_0} > \frac{d\alpha_l}{d(\hbar\omega)}\bigg|_{\hbar\omega_0},$$
$$(1)$$

where $G = (a/L)g$, a is the thickness of the active region, and L is the effective thickness of the VSCEL resonator. The energy $\hbar\omega_{1,2}$ of the emitted photons is determined by the resonator parameters and is constant for a given VSCEL. Conversely, if the reverse inequalities hold:

$$\frac{G_2}{\alpha_{l2}} < \frac{G_1}{\alpha_{l1}} \quad or \quad \frac{g_2}{g_1} < \frac{\alpha_{l2}}{\alpha_{l1}}, \quad or \quad \frac{dG}{d(\hbar\omega)}\bigg|_{\hbar\omega_0} < \frac{d\alpha_l}{d(\hbar\omega)}\bigg|_{\hbar\omega_0},$$
$$(2)$$

then the VSCEL will emit light that is predominantly polarized with polarization **1**.

Let us consider the situation shown in Fig. 2, where the losses in the VSCEL are determined by free-carrier absorption. Let the emission line be located at the low-energy (long-wavelength) edge of the gain line shape. In this case, it is obvious that inequality (1) is always satisfied, and that light is generated with polarization **2**. We now assume that the emission line is located at the high-energy (short-wavelength) edge of the gain line shape. In this case both inequality (1) (light generated with polarization **2**) and inequality (2) (light generated with polarization **1**) can be satisfied.

For $\hbar\omega \lesssim E_g'$ (polarization determined by the Urbach rule) emission with polarizations **1** or **2** can be generated when the emission line is located at the low-energy (long-wavelength) edge of the gain line shape. In principle this can happen when the Bragg reflector is strongly heated.

In proton-implanted VSCELs (Fig. 1) free-carrier absorption is an important factor in the n-type, and even more so in the p-type, distributed Bragg reflectors. We assume that it is only the optical losses in the p-type distributed Bragg reflector that are important, and we will discuss only them.[1] In this case we also assume that the absorption due to free
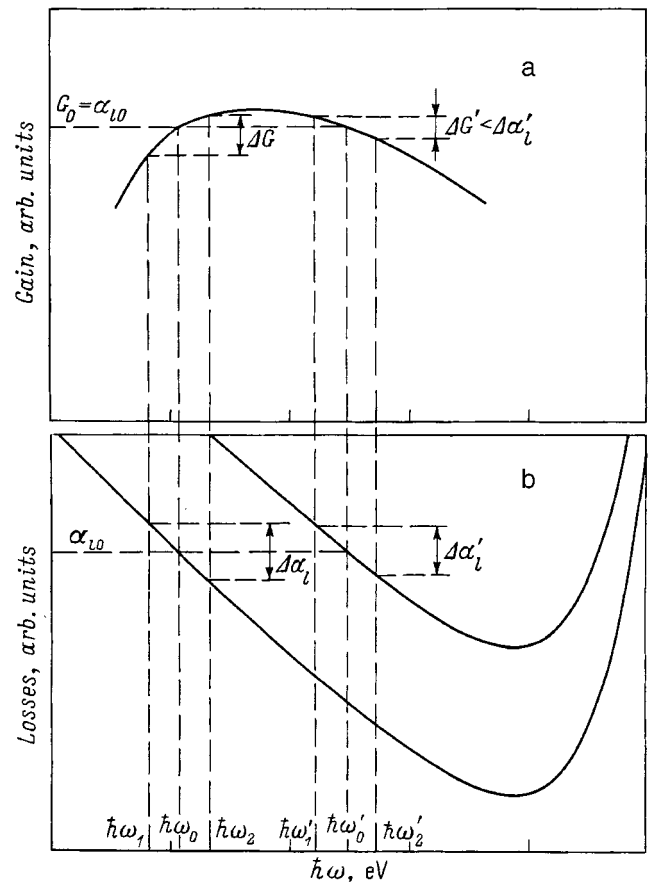

FIG. 2. Schematic plots of the gain (a) and loss (b) versus photon energy. Two possible situations are shown: the oscillator line $\hbar\omega_0$ is located at the low-energy edge of the gain line shape and the oscillator line $\hbar\omega_0'$ is located at the high-energy edge of the gain line shape, corresponding to different dependences of the loss on photon energy.
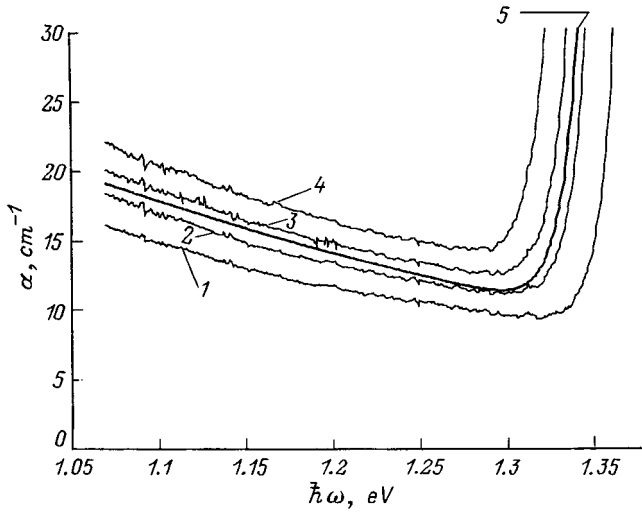
FIG. 3. Experimental dependences of the absorption coefficient of p-GaAs ($p \approx 1.5 \times 10^{18}$ cm^{-3}) on photon energy at various lattice temperatures T, K: 1 — 295, 2 — 318, 3 — 346, 4 — 370. 5—calculated function $\alpha(\hbar\omega)$ constructed using Eq. (3).

holes in the p-AlGaAs does not depend on the Al content of the AlGaAs, because the structure of the AlGaAs valence band does not depend on Al content.

We could not find data in the literature on the absorption of p-GaAs for $\hbar\omega \leqslant E_g'$ at temperatures above room temperature. Our experimental results for the dependences of the absorption on photon energy $\alpha(\hbar\omega)$ in p-GaAs with carrier concentrations $p = (1-2) \times 10^{18}$ cm^{-3} at various temperatures are shown in Fig. 3.

At energies $\hbar\omega < 1.3$ eV, at room temperature and above the absorption for holes is determined by transitions from the heavy-hole subband 1 to the split-off hole subband 3. In this case, the absorption coefficient α_{13} is determined by the occupancy of states in the heavy-hole band by holes, from which direct transitions to the split-off subband take place.[11,12] With increasing photon energy, the energy of these states increases and the absorption coefficient correspondingly decreases to photon energies where interband transitions become important.

Using expressions for the absorption α_{13} associated with transitions from the heavy-hole subband to the split-off subband[11,12] and the exponential dependence of the absorption near the absorption edge (α_U) (the Urbach rule), we can approximate experimental dependences very well by the expression (Fig. 3)

$$\alpha = \alpha_{13} + \alpha_U = \frac{A}{\hbar\omega}\left[\frac{\hbar\omega - \Delta}{kT}\right]^{3/2} \exp\left[-B\frac{\hbar\omega - \Delta}{kT}\right]$$
$$+ C\exp\left[D\frac{\hbar\omega - E_g(T)}{kT}\right] \qquad (3)$$

for values of the coefficients $A = 1.85$ eV/cm and $B = 0.096$, where $\Delta = 0.34$ eV. The function $E_g(T)$ for GaAs was taken from Ref. 13.

In order to determine the reflection coefficients of the Bragg reflectors when absorption of light in them is taken into account, we can use the expressions given in Refs. 14

and 15. These expressions simplify when the number of layers is large. It can be shown that when the absorption in the reflector layers is not too large, i.e., $\alpha\lambda \ll 1$ and $\alpha\lambda \ll |n_{ng} - n_{wg}|$, in the many-layer approximation the dependence of the magnitude of the reflection on the absorption for the case of absorption by free holes is determined by the expression[15]

$$R \approx 1 - \frac{\lambda(n_{ng}^2 + n_{wg}^2)}{2n_0(n_{ng}^2 - n_{wg}^2)}\alpha_{13} = 1 - K\alpha_{13}, \qquad (4)$$

where n_{wg} and n_{ng} are the refractive indices of the wide-gap and narrow-gap layers of the interference reflector, and n_0 is the refractive index of the resonator material. Assuming that the deviations from unity of the reflection for the n- and p-type distributed Bragg reflectors is determined primarily by the magnitudes of the absorption in them, and assuming that the absorption in the n-type distributed Bragg reflector equals zero, we have the following expression when $R_n = 1$:

$$\alpha_l = \frac{1}{L}\ln\left[\frac{1}{\sqrt{R_n R_p}}\right] \approx \frac{1}{2L}(1 - R_p) \approx \frac{K}{2L}\alpha_{13}. \qquad (5)$$

Equation (5) can be used when the composition of the Bragg reflectors is chosen in such a way that $\hbar\omega_0 \ll E_g$ even for the narrow-gap layer of the reflector. In this case

$$\frac{d\alpha_l}{d(\hbar\omega)} \sim \alpha_l(\hbar\omega, T)\left[\frac{B}{kT} - \frac{3}{2}\frac{1}{\hbar\omega - \Delta} + \frac{1}{\hbar\omega}\right]. \qquad (6)$$

For an AlGaAs / AlAs distributed Bragg reflector, the derivative $d\alpha_l / d(\hbar\omega)$ is nearly temperature-independent.

A dependence analogous to Eq. (3) for the optical losses can occur in VSCELs with contacts within the resonator (intercavity-contacted VSCELs)[16] in the strongly doped contact layer.

Near the gain maximum, the quantity $d\alpha_l / d(\hbar\omega)$ can easily exceed the value of $dG / d(\hbar\omega)$, and thus selectivity of the losses will significantly affect the polarization properties of the VSCEL. Thus, for example, the authors of Ref. 9 showed that the initial polarization of light from a proton-implanted VSCEL oscillating at the high-energy (short-wavelength) edge of the gain line shape is determined not only by the thermal-lens mechanism but also by the loss-selectivity mechanism with respect to photon energy. If increasing the injection current leads to heating of the Bragg reflector and the active region, the behavior of the VSCEL polarization can be derived from Eqs. (1), (2), and (6), and from the results of Ref. 9 if the thermal lens effect is important.

2. CARRIER HEATING IN A VSCEL

Here we will consider only the most interesting situation, where switching of the optical polarization is connected with inertia-free local heating of holes and electrons in the active region and the p-layers of the VSCEL without corresponding heating of the crystal lattice when injection current flows through the latter. Such a mechanism can be efficient because the heat capacity of a hole gas (C_p) and electron gas (C_n) with concentrations of order 10^{18} cm^{-3} is five orders of

magnitude smaller than the heat capacity of the crystal lattice (C_l). Therefore, heating of holes and electrons can greatly exceed the lattice heating if (C_n/τ_r, C_p/τ_r)$<C_l/\tau_l$, where $\tau_r \sim 10^{-12}$ s is the relaxation time for the temperature of the overall bulk of heated carriers due to emission of optical phonons, and τ_l is the smaller of the two times: the relaxation time for temperature of the crystal lattice or the duration of the injection pulse.

The heating of electrons and holes relative to the lattice is local. An important question is: what is the ratio of the temperature change for hot carriers in the p-type distributed Bragg reflector to that for hot carriers in the quantum wells of the active layer? A lower bound on the heating of carriers relative to the lattice temperature $\Delta T = T - T_0$ (where T_0 is the lattice temperature) can be estimated from the energy balance equation, assuming the holes are nondegenerate.

For the quantum wells of the active layer,

$$\frac{3}{2}k\Delta T_{\text{QW}} \sim \frac{\Delta j(\Delta E/q)}{d_{\text{QW}}p_{\text{QW}}}\tau_r, \qquad (7)$$

where Δj is the increment in the density of pulsed injection current, which heats the carriers relative to the lattice (the maximum value of $\Delta j_{\max} \sim 5\,\text{kA/cm}^2$); $\Delta E \approx \Delta E_c + \Delta E_v \sim 0.25$ eV is the energy imparted to a carrier pair relaxing from the quantum well barriers with the effective mass of thermalized carriers[17] (ΔE_c and ΔE_v are heights of these barriers in the conduction and valence bands, respectively); $p_{\text{QW}} \sim 10^{19}\,\text{cm}^{-3}$ is the variable concentration of holes in the quantum well during heating; and $d_{\text{QW}} \sim 80$ Å is the width of the quantum well layer. In writing Eq. (7), we took into account that the heat capacity of a strongly degenerate electron gas is a few times smaller than the heat capacity of a strongly degenerate hole gas.

For the p-type distributed Bragg reflector we have

$$\frac{3}{2}k\Delta T_{\text{DBR}} \sim \frac{\Delta j \cdot V}{d_{\text{DBR}} \cdot p_{\text{DBR}}}\tau_r', \qquad (8)$$

where V is the voltage drop across the p-type distributed Bragg reflector (maximum value $V_{\max} \sim 5$ V), $d_{\text{DBR}} \cdot p_{\text{DBR}} \sim 2 \times 10^{14}\,\text{cm}^{-2}$ is the total density of holes for all the layers of the distributed Bragg reflector which is modulation-doped,[15] and $\tau_r' \sim 3 \times 10^{-12}$ s is the temperature relaxation time for holes with concentrations greater than $10^{19}\,\text{cm}^{-3}$ which accumulate near the heterojunction barriers of the distributed Bragg reflector.

For a current density $\Delta j \sim 5\,\text{kA/cm}^2$ the heating $\Delta T_{\text{QW}} \approx 5$ K and $\Delta T_{\text{DBR}} \approx 20$ K.[2] Assume that effective heating of electrons and holes takes place in the quantum wells of the VCSEL active region above the threshold for oscillations. Carrier heating leads to a decrease in the distance between the quasi-Fermi levels (F_p and F_n). In this case the gain $g(\hbar\omega)$ decreases. In order to maintain the gain at energy $\hbar\omega_0$ equal to the losses ($G_0 = \alpha_{l0}$) as the temperature of the carriers in the quantum well changes, the concentration of hot carriers in the quantum well ($n_{\text{QW}}^h = p_{\text{QW}}^h$) must increase relative to the concentration of ''cold'' carriers ($n_{\text{QW}}^c = p_{\text{QW}}^c$) by an amount determined from the condition

$$G(\hbar\omega_0, T_{\text{QW}}^h, p_{\text{QW}}^h) = G(\hbar\omega_0, T_{\text{QW}}^c, p_{\text{QW}}^c).$$

Here T_{QW}^h is the temperature of the hot carriers in the quantum well, T_{QW}^c is the temperature of the cold carriers in the quantum well, and the term ''cold'' applied to carriers implies that their temperature equals the lattice temperature. In this case the gain line shape returns essentially to its previous position.

As the holes in the p-type distributed Bragg reflector are heated, their temperature increases to T_{DBR}^h, and the absorption in the p-type distributed Bragg reflector increases, which leads to a further increase in the concentration of hot carriers in the quantum well such that the condition $G(\hbar\omega_0, T_{\text{QW}}^h, p_{\text{QW}}^h) = \alpha_l(\hbar\omega_0, T_{\text{DBR}}^h)$ is satisfied.

The increased carrier concentration in the active region leads to a decrease in the width of the band gap by an amount[18]

$$\Delta E_g\,[\text{eV}] \approx -0.032\,[\text{eV}]$$
$$\times \frac{(p_{\text{QW}}^h\,[\text{cm}^{-3}])^{1/3} - (p_{\text{QW}}^c\,[\text{cm}^{-3}])^{1/3}}{10^6\,[\text{cm}^{-1}]}. \qquad (9)$$

As will be clear from our subsequent discussion, at high levels of injection carrier heating in the VSCEL causes the maximum of the gain line shape to shift towards lower energies.

For the gain of the material in the active region g we have[19]

$$g(\hbar\omega, T_{\text{QW}}, p_{QW}) = \alpha_{\text{QW}}(\hbar\omega)[f_n(E_n, T_{\text{QW}}, n_{\text{QW}})$$
$$+ f_p(E_p, T_{\text{QW}}, p_{\text{QW}}) - 1], \qquad (10)$$

where $\alpha_{\text{QW}}(\hbar\omega)$ is the absorption coefficient of the active region material at those concentrations of carriers where filling of band states can be ignored but the Coulomb interaction between electrons and holes is screened, $f_n(E_n, T_{\text{QW}}, n_{\text{QW}})$ and $f_p(E_p, T_{\text{QW}}, p_{\text{QW}})$ are distribution functions for electrons and holes in the active region of the laser when an injected current flows, and E_n and E_p are the energies of electrons and holes between which optical transitions take place at the photon energy $\hbar\omega_0$.

We assume that optical transitions in the quantum well obey the selection rule with respect to wave vector (the **k** selection rule; see Ref. 18), and that these transitions take place only between quantum-well subbands with the same quantum numbers ($n_c = n_v$, where the labels c and v denote, respectively, the conduction band and the valence band). In this case, in the neighborhood of the absorption edge for optical transitions between states with $n_c = n_v = 1$ we see that $\alpha_{\text{QW}}(\hbar\omega)$ begins to increase linearly, and then saturates (Fig. 4) at the energy where transitions between states with $n_c = n_v = 2$ are possible. The range of energies for which $\alpha_{\text{QW}}(\hbar\omega)$ increases is determined by homogeneous broadening of the absorption line. The function $\alpha_{\text{QW}}(\hbar\omega)$ shown in Fig. 4 is close to that calculated in Ref. 18 for a typical quantum well in the active region of the heterojunction laser.

At high injection levels, which were realized experimentally in Ref. 8, $f_n \approx 1$, $df_n/d(\hbar\omega) \approx 0$ near the maximum of the gain. Therefore, we have

$$g(\hbar\omega, T_{\text{QW}}, p_{\text{QW}}) \approx \alpha_{\text{QW}}(\hbar\omega)f_p[B'(\hbar\omega - E_g), T_{\text{QW}}, p_{\text{QW}}],$$
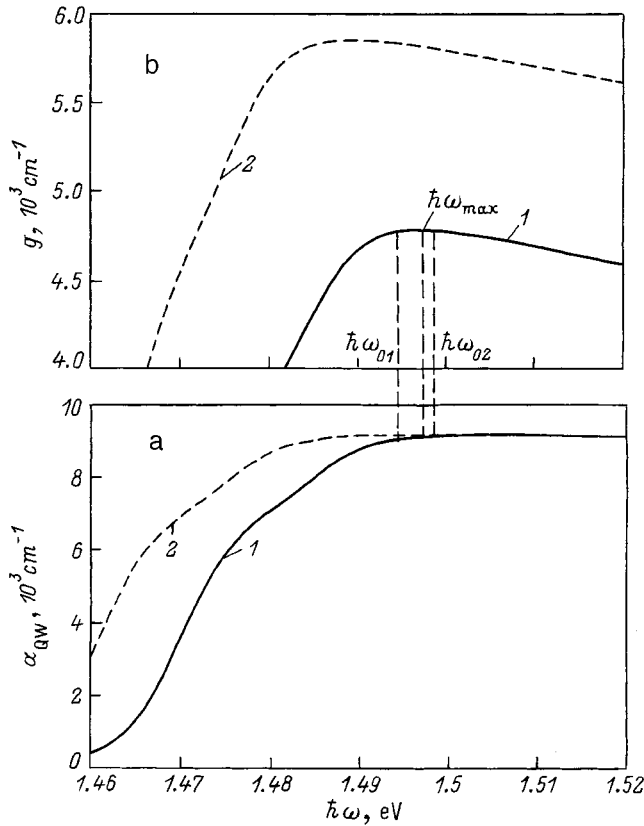$$(11)$$

FIG. 4. a—Dependence of the absorption coefficient on $\hbar\omega$ in a typical quantum well active region of a heterojunction laser in the absence of injection. b—the corresponding dependence of the gain on $\hbar\omega$. 1—low heating of injected carriers relative to the lattice (cold carriers); 2—hot carriers injected into the active region: $\Delta T_{QW} = 10$ K, $\Delta T_{DBR} = 40$ K. $\hbar\omega_{01}$ and $\hbar\omega_{02}$ are the two possible positions of the oscillator line near the maximum of the gain $\hbar\omega_{max}$ for the case of cold carriers.
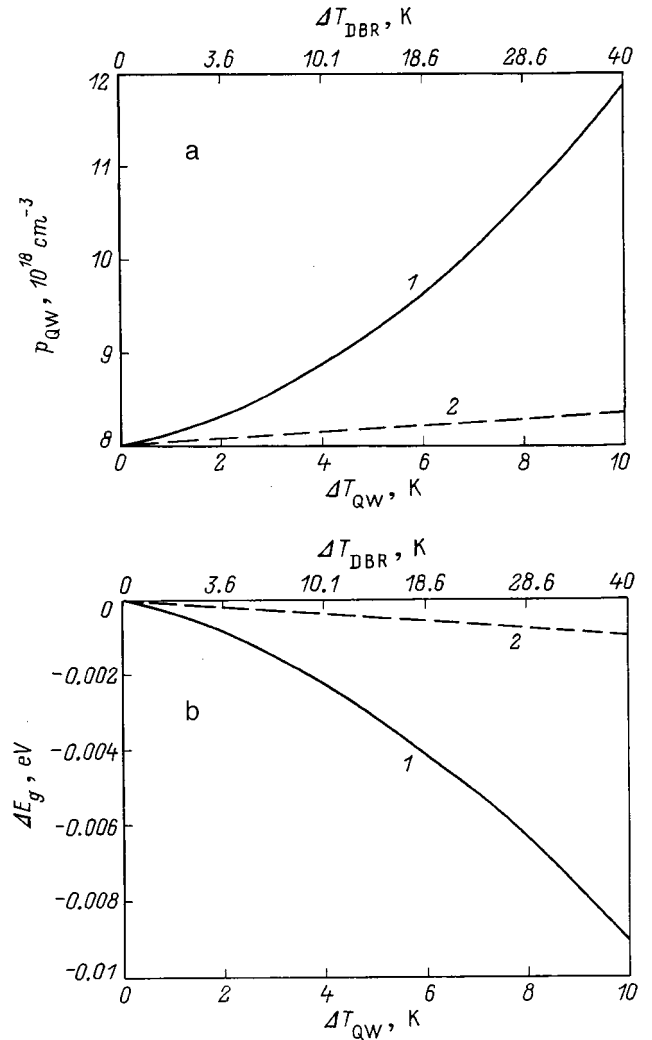

FIG. 5. Dependence of the concentration of heated carriers (a) and ΔE_g (b) on the magnitude of carrier heating in the quantum well (ΔT_{QW}) and in the p-type distributed Bragg reflector (ΔT_{DBR}). 1— including heating of holes in the p-type distributed Bragg reflector, 2—disregarding it. In the entire range of temperature variation the condition $g(\hbar\omega_0) = (L/a)\alpha_l(\hbar\omega_0)$ holds due to increases in the carrier concentration in the quantum wells.

$$\frac{dg}{d(\hbar\omega)}\Big|_{\hbar\omega_0} \approx f_0 \left[\frac{d\alpha_{QW}}{d(\hbar\omega)}\Big|_{\hbar\omega_0} - B' \alpha_{QW}(\hbar\omega_0)\frac{1-f_0}{kT_{QW}} \right], \tag{12}$$

where $f_0 = f_p[B'(\hbar\omega_0 - E_g), T_{QW}, p_{QW}]$; the quantity $B' \approx 0.1$ is determined by the ratio of effective masses of electrons and holes.

As for the function $\alpha_{QW}(\hbar\omega)$ shown in Fig. 4, at high concentrations of cold carriers in the quantum well (p^c) the maximum of $g(\hbar\omega)$ is located in the transition region where $\alpha_{QW}(\hbar\omega)$ switches over from linear increase to saturation.

The carrier heating in the quantum well and in the p-type distributed Bragg reflector (denoted by ΔT_{QW} and ΔT_{DBR}, respectively) gives rise to a considerable shift in ΔE_g and a corresponding shift in the absorption curve $\alpha_{QW}(\hbar\omega)$ towards lower energies. Figure 5 shows the dependence of the concentration of hot carriers in the quantum well, and ΔE_g on carrier heating in the quantum well (ΔT_{QW}) and heating of holes in the p-type distributed Bragg reflector (ΔT_{DBR}), which increase simultaneously (ΔT_{DBR} superlinearly) with increasing injection current. By definition, the condition $g(\hbar\omega_0) = (L/a)\alpha_l(\hbar\omega_0)$ is satisfied in the entire range of temperature variation due to increasing concentration of carriers in the quantum wells. It is clear from Fig. 5 that heating of holes in the p-type distributed Bragg reflector is impor-

tant, and that the shift (ΔE_g) can reach values on the order of 10 meV for 10 K heating of carriers in the quantum well and 40 K heating of holes in the p-type distributed Bragg reflector. As the absorption curve shifts (Fig. 5), the magnitude of the derivative $[d\alpha_{QW}/d(\hbar\omega)]|_{\hbar\omega_0}$ decreases much faster than $B' \cdot \alpha_{QW}(1 - f_0)/kT$ up to energies corresponding to the region where $\alpha_{QW}(\hbar\omega)$ saturates. Therefore, as the carrier temperature increases in the VSCEL, the magnitude of the derivative $[dG/d(\hbar\omega)]|_{\hbar\omega_0} = (a/L)[dg/d(\hbar\omega)]|_{\hbar\omega_0}$ changes as shown in Fig. 6 for the initial ($\Delta E_g = 0$, $\Delta T_{QW} = 0$) position of $\hbar\omega_0$. In this initial position $[dG/d(\hbar\omega)]|_{\hbar\omega_0}$ is positive, because the oscillation line is located in the low-energy wing of the gain line shape and generates light with polarization **2** [see Eqs. (1) and Fig. (2)]. As the carriers are heated, the derivative G decreases because of the shift in the maximum of the gain line shape towards lower energies together with the shift of the absorption edge. When $\Delta T_{QW} = \Delta T_M$, the maximum of the gain line shape
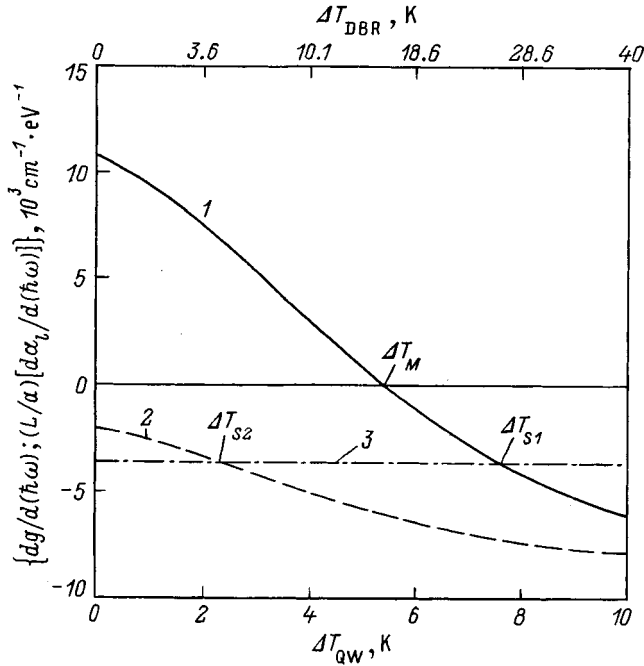
FIG. 6. Functions that clarify the mechanism of VSCEL polarization switching when carriers are heated in a quantum well. *1,2—dg/d(ℏω)* for oscillator lines $\hbar\omega_{01}$ and $\hbar\omega_{02}$, respectively (see Fig. 4). *3*—schematic dependence $(L/a)[d\alpha_1/d(\hbar\omega)]$. ΔT_{S1} and ΔT_{S2} are the temperatures at which the polarization switches, measured relative to the temperature of the active region.

coincides with $\hbar\omega_0$. When $\Delta T_{QW}=\Delta T_S$, even at the high-energy edge of the gain line shape, where $[dG/d(\hbar\omega)]|_{\hbar\omega_0}$ $=[d\alpha_l/d(\hbar\omega)]|_{\hbar\omega_0}$, the polarization will switch. Polarization **2** switches to polarization **1** with the change in photon energy $\hbar\omega_2\rightarrow\hbar\omega_1$ ($\hbar\omega_2>\hbar\omega_1$). In principle, with this type of shift in the absorption edge and $\hbar\omega_0$ located at energies corresponding to the saturation region of $\alpha_{QW}(\hbar\omega)$, further heating of the carriers can cause the polarization of light from the VSCEL to switch back.

We argue that this is the mechanism responsible for the rapid polarization switching of VSCEL's observed at constant temperature of the active layer.[8]

1. Martin–Regalado *et al.*[8] reported that when the pulsed injection current was increased, the initial polarization of light switched to the orthogonal direction with a change in photon energy: $\hbar\omega_2\rightarrow\hbar\omega_1$ ($\hbar\omega_2>\hbar\omega_1$). We describe this switching in the present paper. Note that in the model of Ref. 4, which was used to describe fast polarization switching of a VSCEL, the opposite transition should take place when the temperature of the active region is held constant: $\hbar\omega_1$ $\rightarrow\hbar\omega_2$ ($\hbar\omega_2>\hbar\omega_1$).[20]

2. In Ref. 8 the authors reported that as the temperature of the active region increased as a result of the constant injection current and corresponding shift in the position of the oscillator line on the gain line shape, the difference between values of the pulsed current necessary to switch the polarization decreased along with the threshold current. This is in fact the dependence implied by our model, since increasing the temperature of the active region shifts the maxi-

mum of the gain line shape towards lower energies, which leads to a decrease in the value of the derivative $[dG/d(\hbar\omega)]|_{\hbar\omega_0}$ for $\Delta T_{QW}=0$ and $\Delta T_{S2}<\Delta T_{S1}$, i.e., switching of the polarization takes place at lower injection currents.

3. The process of polarization switching in a VSCEL, according to Ref. 8, takes place in the range where the dependence of the radiated power on injection current saturates. This indicates an increase in losses with increasing injection current. Just such an increase in losses with increasing injection current is predicted by the mechanism for VSCEL polarization switching proposed in this paper.

The polarization properties of VSCELs we have described are based on natural polarization anisotropy. In Ref. 21 it was shown that artificially created polarization anisotropy in the absorption (loss) of a VSCEL connected with anisotropy of the electroabsorption due to the Franz–Keldysh effect, can control the VSCEL polarization.

Both in proton-implanted VSCELs and (especially) in VSCELs with contacts within the resonator,[16] absorption by free holes can bring about strong anisotropy. In fact, the probability of transitions between subbands of heavy holes and the split-off subband is proportional to $\sin^2(\mathbf{e},\mathbf{k})$, where $\mathbf{e}$ is the unit vector for the optical polarization, and $\mathbf{k}$ is a unit vector pointing along the wave vector of holes in the heavy-hole subband.[22] By applying a strong electric field $\mathbf{E}$ to the *p*-type semiconductor, we can create anisotropy in the hole distribution with a preferred direction $\mathbf{k}\|\mathbf{E}$, which leads to a strong polarization anisotropy in the absorption. Experimentally, this effect was observed in *p*-Ge (Ref. 22).

Thus, if the electric field in the plane of the contact layer causes anisotropy, absorption by free carriers will be larger for radiation with $\mathbf{e}\perp\mathbf{E}$ and the VSCEL will generate light with $\mathbf{e}\|\mathbf{E}$.[3] By changing the direction of the electric field we can change polarization of the VSCEL light.

CONCLUSIONS

We have constructed a model of the polarization switching of light from a quantum-well VSCEL at constant temperature of the active region. We have shown that at large injection levels heating of carriers in the quantum wells, and especially holes in the *p*-type distributed Bragg reflector, can lead to a considerable shift in the gain maximum towards lower energies. This shift occurs if the initial position (cold carriers) of the gain maximum is located near the region where the absorption of the quantum well laser saturates in the absence of injection. This shift in the gain maximum towards longer wavelengths causes switching of VSCEL polarization when carriers are heated by the current in the VSCEL. The model developed here allows us to adequately explain the results of experiments on VSCEL polarization switching when the active region temperature is held constant.[8]

[1)]The AlGaAs and AlAs layers of a distributed Bragg reflector are doped to a level of $p \sim n > 10^{18}$ cm^{-3} in order to decrease their electrical resistance. At such high levels of doping the absorption of light by free carriers at room temperature can be quite large. However, the cross section for absorption of light by electrons in the AlAs layers of the n-type distributed Bragg reflector is small, because the effective mass of electrons in n-AlAs is large. On the other hand, in order to obtain a low resistance for both distributed Bragg reflectors, the level of doping for the layers of the p-type distributed Bragg reflector must be higher than for the layers of n-AlGaAs (with a low percentage of Al) in the n-type distributed Bragg reflector. We also note that in layers of n-AlGaAs with a small Al percentage, in the range 0.9–2.0 μm, the absorption by electrons is in fact independent of photon energy.[10]

[2)]Saturation of the watt-ampere characteristics of a VSCEL[8] when the temperature of the active region is held constant indicates an increase in the losses, due primarily to carrier heating in the quantum wells. Thus, estimate (7) is an overestimate of the value of ΔT_{QW}. The increase in ΔT_{QW} in turn leads to the somewhat larger values of p_{QW} and ΔE_g shown in Fig. 5.

[3)]We note that a possible Franz–Keldysh effect in the plane of the contact layer of the VSCEL will facilitate the generation of light with $\mathbf{e} \perp \mathbf{E}$.[21]

---

[1] A. K. Jansen van Doorn, M. P. van Exter, and J. P. Woerdman, Appl. Phys. Lett. **69**, 1041 (1996).

[2] K. D. Choquette, D. A. Richie, and R. E. Leibenguth, Appl. Phys. Lett. **64**, 2062 (1994).

[3] K. D. Choquette, K. L. Lear, R. E. Liebenguth, and M. T. Asom, Appl. Phys. Lett. **64**, 2767 (1994).

[4] J. Martin-Regalado, F. Prati, M. San Miguel, and N. B. Abraham, IEEE J. Quantum Electron. **QE-33**, 765 (1997).

[5] A. Valle, L. Pesquera, and K. S. Shore, IEEE Photon. Technol. Lett. **9**, 557 (1997).

[6] A. K. Jansen van Doorn, M. P. van Exter, and J. P. Woerdman, Appl. Phys. Lett. **69**, 1041 (1996).

[7] M. P. van Exter, A. K. Jansen van Doorn, and J. P. Woerdman, Phys. Rev. A **56**, 845 (1997).

[8] J. Martin-Regalado, J. L. A. Chilla, J. J. Rocca, and P. Brusenbach, Appl. Phys. Lett. **70**, 3350 (1997).

[9] K. Panajotov, B. Ryvkin, J. Danckaert, M. Peeters, H. Thienpont, and I. Veretennicoff, IEEE Photon. Technol. Lett. **10**, 6 (1998).

[10] W. G. Spitzer and J. M. Whelan, Phys. Rev. **114**, 59 (1959).

[11] A. H. Kahn, Phys. Rev. **97**, 1647 (1955).

[12] O. Christensen, Phys. Rev. B **7**, 1426 (1973).

[13] M. Levinshtein and S. Rumyantsen, *Handbook on Semiconductor Parameters* (World Scientific, Singapore– NewJersey–London–Hong Kong, 1998), Ch. 4.2.1, p. 79.

[14] M. A. Kaliteevskiĭ and A. V. Kavokin, Fiz. Tverd. Tela (St. Petersburg) **37**, 2721 (1995) [Phys. Solid State **37**, 1497 (1995)].

[15] T. E. Sale, *Vertical Cavity Surface Emitting Lasers* (J. Wiley & Sons, 1995).

[16] M. H. MacDougal, P. D. Dapkus, A. E. Bond, C. K. Lin, and J. Geske, IEEE J. Selected Topics Quant. Electron. **3**, 905 (1997).

[17] V. D. Pishchalko and V. I. Tolstikhin, Fiz. Tverd. Tela (Leningrad) **24**, 462 (1990) [Sov. Phys. Solid State **24**, 288 (1990)].

[18] L. A. Coldren and S. W. Corzine, *Diode Lasers and Photonic Integrated Circuits* (J. Wiley & Sons, 1995).

[19] R. F. Kazarinov, Fiz. Tekh. Poluprovodn. **7**, 763 (1973) [Sov. Phys. Semicond. **7**, 525 (1973)].

[20] T. Erneux, J. Danckaert, K. Panajotov, and I. Veretennicoff, Phys. Rev. A **59** (6) (1999).

[21] B. Ryvkin, K. Panajotov, J. Danckaert, H. Thienpont, and I. Veretennicoff, *SPIE Int. Conf. on Optics in Computing '98* (Bruges, Belgium, 1998), post-deadline paper P 87.

[22] R. Bray and W. E. Pinson, Phys. Rev. Lett. **11**, 268 (1963).

Translated by Frank J. Crowne